Technische Universität München
Fakultät für Physik

Dissertation

Adsorption of phthalocyanine-complexes on hexagonal boron nitride templates

Mathias Pörtner

Technische Universität München

Lehrstuhl E20 – Molekulare Nanowissenschaft an Grenzflächen

Adsorption of phthalocyanine-complexes on hexagonal boron nitride templates

Mathias Pörtner

Vollständiger Abdruck der von der Fakultät für Physik der Technischen Universität München zur Erlangung des akademischen Grades eines Doktors der Naturwissenschaften (Dr. rer. nat.) genehmigten Dissertation.

Vorsitzender: Prof. Dr. David Egger

Prüfer der Dissertation:
1. Prof. Dr. Willi Auwärter
2. Prof. Christine Papadakis, Ph.D.

Die Dissertation wurde am 05.12.2019 bei der Technischen Universität München eingereicht und durch die Fakultät für Physik am 17.01.2020 angenommen.

Abstract

This thesis presents the study of phythalocyanine-complexes on one atom thick hexagonal boron nitride (hBN) templates on metal surfaces with respect to their electronic and structural properties. These properties are key to get an understanding of the charge state or the catalytic nature of the molecules. The experiments were performed by scanning probe microscopy and X-ray photoelectron spectroscopy and are supported by calculations and simulations using density functional theory. These experiments reveal, that the charge state control of F_{16}CoPc on hBN/Cu(111) is mainly determined by three parameters. The adsorption of the molecule on hBN/Cu(111) will be compared with the adsorption on hBN/Ir(111). In another project the array formation of $CePc_2$ doubledecker molecules along the moiré structure of hBN/Ir(111) was investigated and the appearance of the molecules was compared with theoretical simulations. As a byproduct of the $CePc_2$ doubledeckers, smaller molecules – identified as diiminoisoindolines – adsorb on the hBN/Ir(111) surface and can functionalize the hBN layer. The appearance and dimerization of these molecules will be described and compared with theoretical calculations. By simulating the appearance of different dimers, molecular models will be assigned to the observed molecules. As the last project of this thesis, different multidecker systems were theoretically calculated by density functional theory and will be compared with the experimentally available data.

Zusammenfassung

In dieser Dissertation werden Phthalocyanine-Komplexe auf ein Atom dicken Templaten von hexagonalen Bornitrids (hBN) auf Metalloberflächen im Hinblick auf ihre elektronischen und strukturellen Eigenschaften untersucht. Diese Eigenschaften sind entscheidend, um ein Verständis vom Ladungszustand und der katalytischen Natur der Moleküle zu bekommen. Die Untersuchungen werden mit Hilfe von Rastertunnel- und Rasterkraftmikroskopie und Röntgenphotoelektronenspektroskopie durchgeführt und von Berechnungen und Simulationen mittels Dichtefunktionaltheorie unterstützt. Es wird gezeigt, dass die Kontrolle des Ladungszustandes von F_{16}CoPc auf hBN/Cu(111) wesentlich durch drei Parameter bestimmt wird. Die Adsorption des Moleküls auf hBN/Cu(111) wird mit der auf hBN/Ir(111) verglichen. In einem weiteren Projekt wurde die Anordnung von $CePc_2$ Doppeldecker-Molekülen entlang der Moiré-Struktur von hBN/Ir(111) untersucht. Die Erscheinung der Moleküle wurde mit theoretischen Simulationen verglichen. Als Nebenprodukt der $CePc_2$-Doppeldecker adsorbieren auch kleinere Moleküle, welche als Diiminoisoindoline identifiziert werden, auf der hBN/Ir(111) Oberfläche und können die hBN Lage funktionalisieren. Die Erscheinung und Dimerisierung dieser Moleküle wird beschrieben und mit theoretischen Rechnungen verglichen. Durch Simulationen der Erscheinungen verschiedener Dimere werden Molekülmodelle den beobachteten Molekülen zugeordnet. Als letztes Projekt dieser Dissertation werden verschiedene Multidecker-Systeme mithilfe von Dichtefuntionaltheorie theoretisch berechnet und mit den experimentell vorhandenen Daten verglichen.

Contents

Abstract i

Zusammenfassung iii

Contents iv

List of Abbreviations v

I. Introduction 1

II. Theory and concepts 5

1. Scanning tunneling microscopy 6

1.1. Electron tunneling 6

1.2. Scanning tunneling spectroscopy 11

1.3. STM operation modes 13

1.4. Manipulation modes 14

2. Non-contact atomic force microscopy 15

2.1. Theoretic model of nc-AFM 15

2.2. Tip sample forces 16

3. Density functional theory 21

4. X-ray photoelectron spectroscopy 23

III. Experimental setup, substrates and materials 25

5. Ultra-high vacuum system 26

5.1. Pumping system 27

5.2. Cryogenic system 28

5.3. Vibrational damping system 28

5.4. SPM scanner 30

6. Materials and substrates **33**
6.1. Metal substrates . . . 33
6.2. Hexagonal boron nitride . . . 34
6.3. Molecules . . . 37

IV. Results **39**

7. Charge state control of F_{16}CoPc on *h*BN/Cu(111) **40**
7.1. Template induced gating . . . 43
7.2. Tip induced gating . . . 46
7.3. Screening . . . 50
7.4. High molecular coverage . . . 52
7.5. Second layer growth . . . 57
7.6. DFT calculations of CO adsorption on F_{16}CoPc . . . 58
7.7. Comparison to F_{16}CoPc on *h*BN/Ir(111) . . . 60
7.8. Summary and outlook . . . 65

8. Array formation of Ce-based multideckers on *h*BN/Ir(111) **69**
8.1. Adsorption of pre-synthesized $CePc_2$ molecules on *h*BN/Ir(111) . . . 71
8.2. Adsorption of $CePc_2$ on Ag(111) . . . 75
8.3. In-situ preparation of Ce-based multideckers on *h*BN/Ir(111) . . . 77
8.4. DFT calculations and STM simulations of $CePc_2$ on *h*BN/Ir(111) . . . 81
8.5. Summary and outlook . . . 87

9. Functionalization of *h*BN/Ir(111) by diiminoisoindoline **89**
9.1. Adsorption of 2III on *h*BN/Ir(111) . . . 90
9.2. Irreversible modification of single 2III on *h*BN/Ir(111) . . . 92
9.3. Temperature stability of the bond between 2III and *h*BN . . . 94
9.4. Dimer formation on *h*BN/Ir(111) . . . 98
9.5. Adsorption of 2III on a submonolayer *h*BN/Ir(111) . . . 100
9.6. DFT calculations of the molecular energies . . . 101
9.7. STM simulations of the different molecular species . . . 105
9.8. Summary and outlook . . . 108

10. DFT calculations on novel tetrapyrrol-based double- and multidecker complexes **111**

10.1. Structural analysis of $Gd_{x-1}Pc_x$ multideckers 111

10.2. Adsorption of $Th(TPP)_2$ doubledeckers on Ag(111) 117

V. Summary and outlook **123**

VI. Appendix **129**

A. Calculation of the moiré-pattern of *h*BN/Ir(111) **130**

B. Hexagonal boron nitride on Cu(100) **133**

C. Vacuum distillation of borazine **137**

D. Lab automatization **141**

E. Data processing **143**

F. List of publications **145**

G. List of Figures **147**

H. List of Tables **149**

I. Acknowledgment **151**

List of Abbreviations

2HI diiminoisoindoline

AFM atomic force microscopy

CVD chemical vapor deposition

DBTJ double barrier tunneling junction

DFT density functional theory

DOS density of states

fcc face centered cubic

GUI graphical user interface

***h*BN** hexagonal boron nitride

HOMO highest occupied molecular orbital

IP ion getter pump

KPFM Kelvin probe force microscopy

LDOS local density of states

LHe liquid helium

LJ Lennard-Jones

LM lateral manipulation

LN_2 liquid nitrogen

LSDA local spin density approximation

LUMO lowest unoccupied molecular orbital

MO molecular orbital

nc-AFM non-contact atomic force microscopy

PBE Perdew Burke Ernzerhof

Pc phthalocyanine

SPM scanning probe microscopy

STM scanning tunneling microscopy

STS scanning tunneling spectroscopy

TP turbo pump

TPP tetraphenylporphyrin

TSP titanium sublimation pump

UHV ultra high vacuum

VASP Vienna ab-initio simulation package

vdW van der Waals

VM vertical manipulation

XPS X-ray photoelectron spectroscopy

Part I.
Introduction

The technological progress of the last century was significantly influenced by the development of faster and more powerful computers, whose miniaturization were portrayed in the past by Moore's law [1]. This law presently reached its fundamental physical limits. Therefore, the idea of Richard Feynman "There's plenty of room at the bottom" becomes more and more relevant. The field of nanotechnology [2], which describes the fabrication, manipulation and use of atoms and molecules for nanostructures with a size of 0.1 - 100 nm [3], offers the possibility to produce new materials, used in different technical fields, such as energy harvesting [4–6], data storage [7–10] or quantum computing [11–13] – just to name a few. Organic molecules and materials play an important role in this process, as sustainability becomes more and more important and current devices are usually based on silicon, (rare earth) metals or materials, mined and processed in complex and expensive procedures [14–16].

A promising class of molecules, which could be used to build such devices, based on organic molcules, is the family of the porphyrins [17–19]. Tetrapyrrole-based molecules like phthalocyanines (Pc) or tetraphenylporphyrins (TPP), found in natural and also artificial systems, exhibit a large π-electron system and are often photoreactive, making them suitable candidates for light harvesting materials [4, 6, 20]. Another advantage of these molecules is their functionalizability. On one hand the molecular structure can be modified/extended chemically by replacing/adding subgroups of/to the molecule [21] but on the other hand metal atoms can be incorporated into the organic macrocycle (metalation) [22–26] and therefore change the electronic and magnetic properties of the molecule. Due to this variety of possibilities, they can also be used for applications, such as data storage [13, 27–30] or quantum computing [31].

With the invention of scanning probe microscopy (SPM) in the 1980s [32, 33], atoms and small molecules could be investigated for the first time experimentally on a wide vari-

ety of surfaces. Since then, the invention and application of new materials was driven by science and many breakthroughs could be achieved, like the manipulation of single atoms [34, 35], the growth of ultra-thin layers [36–39] or the fabrication of self-assembled molecular structures [19, 40]. The properties of molecules, adsorbed on metal surfaces depend strongly on the supporting material, since molecular orbitals can hybridize with the electronic bands of the metal [41]. Hence, the molecular properties like the electronic gap, the geometry or the magnetism are influenced [41, 42]. To preserve the intrinsic molecular properties and still be able to investigate them by SPM, a decoupling from the substrate by thin insulating layers is advantageous [38, 43–46].
One example for a thin layer is hexagonal boron nitride (hBN). This one atom thick layer of the insulating bulk material hexagonal boron nitride is isoelectronic and isostructural to graphene but exhibits a large bandgap of about 6 eV [38, 47–49]. In contrast to graphene, which only consists of carbon atoms, in hBN boron and nitrogen atoms sit on the two different sublattices of the honeycomb lattice. Commonly, this layer is grown on (transition) metal surfaces by chemical vapor deposition (CVD) of the precursor borazine on the hot metal surface [38, 50–52]. This growth process is self-limiting to one monolayer since the catalytic properties of hBN are strongly decreased in comparison to the supporting metal surface. Due to its large bandgap the electronic influence of the metal substrates on adsorbates on the hBN is significantly reduced [29, 38, 53–57]. Beside its decoupling properties, hBN on metal substrates can also be an interesting template for adsorbates, a result of the moiré superstructure, arising for most metal surfaces from the lattice mismatch between the metal and the hBN [38, 55–63]. This lattice mismatch can lead to a geometric and electronic corrugation of the hBN layer.

In this thesis the adsorption of different tetrapyrrole-based molecules on hBN/metal surfaces will be analyzed. To get insights into the molecular properties, like the charge state, the structure or the molecular interaction with the metal-insulator-interface, different aspects and consequences of this adsorption will be portrayed. The understanding of these properties is important for the usage of these molecule-insulator-metal-interfaces for future applications.
The main techniques, used for the investigations, are scanning tunneling microscopy (STM), non-contact atomic force microscopy (nc-AFM), density functional theory (DFT) and X-ray photoelectron spectroscopy (XPS). The theoretic background of these techniques will be explained in part II and the setup as well as the used materials will be introduced in part III.

In the first experiment in part IV, it will be revealed, that the charge state of $F_{16}CoPc$ on hBN/Cu(111) can be controlled by three different parameters, *i.e.*, template induced gating, tip induced gating and screening (section 7). These three effects can shift the molecular level of the molecule in a way, that a change of the charge state is possible. This process will also be examined for the adsorption of $F_{16}CoPc$ on hBN/Ir(111).
In section 8 the growth and structure of Ce-based multideckers on hBN/Ir(111) will be investigated. Two different approaches for the growth will be used, *i.e.*, the deposition of pre-synthesized $CePc_2$ doubledeckers and the in-situ growth due to the temperature induced formation of multideckers by metalation of a 2H-Pc multilayer [64, 65]. DFT-based STM image simulations corroborate the appearances of the $CePc_2$ doubledeckers on hBN/Ir(111). The DFT modeling provides additional insights into magnetic properties, adsorption energies and structural details.
As a byproduct of the evaporation of pre-synthesized $CePc_2$ doubledeckers, Pc-fragments, identified as diiminoisoindoline (2III) [66], were found on the hBN/Ir(111) surface. The analysis of the adsorption of this small molecule will be reported in section 9. In addition to the characterization with STM, the functionalization of the hBN layer by 2III will be studied with XPS. 2III were observed on the hBN/Ir(111) surface even after heating to high temperatures, indicating a strong interaction. Furthermore, the heating induced dimerization of the molecules will be demonstrated. The experimental results will be corroborated by DFT calculations, *i.e.*, STM simulations of adsorbed molecules as well as calculations of formation and adsorption energies.
Two additional projects of tetrapyrrole-multidecker systems will be studied by DFT in section 10 to rationalize recent findings results from other projects in the group. First, the structures of gas phase $Gd_{x-1}Pc_x$ will be investigated, focusing on the rotational alignment of the Pc units consisting the multideckers, as well as on the formation energies. The second project will address the structure, energy and magnetism of $ThTPP_2$ on Ag(111). Additionally, STM images were simulated for comparison to experimental results.
A summary and outlook of the thesis will be provided in Part V.

Part II.
Theory and concepts

1. Scanning tunneling microscopy

Scanning tunneling microscopy (STM) is a surface sensitive technique that was invented by Binnig and Rohrer in 1983 [32], for which they were awarded the nobel prize in 1986 [67]. As the name indicates, the surface is scanned to measure its properties. For this purpose, the probe – a sharp, conducting tip, shown in Fig. 1.1 – needs to be very close to the surface. By applying a bias voltage, a current is created, based on the tunneling effect. This current depends sensitively on the tip-surface distance and thus can yield information on the surface topography.

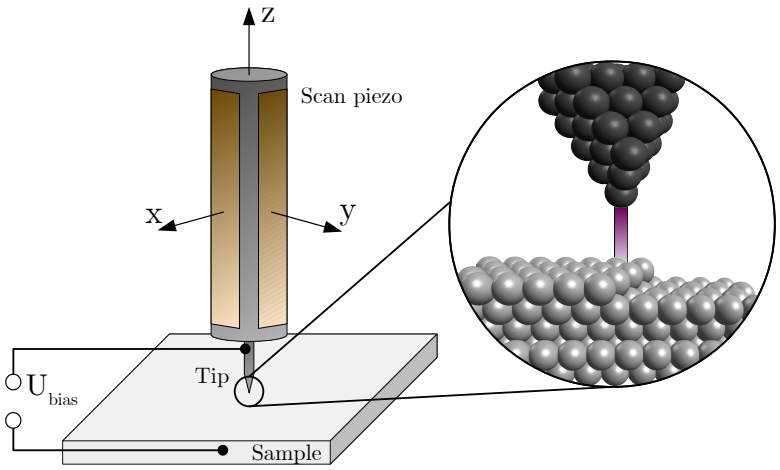

Figure 1.1: *Principle of STM. In STM a piezo-tube with a tip attached is scanning over a sample. In the zoom-in, the tip is close to the surface, resulting in a tunneling current.*

1.1. Electron tunneling

The tunneling effect is a quantum mechanical phenomen, first observed in the early 20^{th} century [68]. Classically, an electron can't propagate through a potential barrier higher than it's own kinetic energy. This problem will be discussed briefly in the following. A detailed desccription can be found in the literature [69–72].

In the classical picture an electron can not overcome a potential barrier if its energy E is smaller than the given potential in this area: $E < V(\boldsymbol{r})$.

In quantum mechanics an electron can be treated as a wave and its wave function $\Psi(\boldsymbol{r}, t)$ is described by the Schrödinger equation

$$-\frac{\hbar^2}{2m}\nabla^2\Psi(\boldsymbol{r},t) + V(\boldsymbol{r},t)\Psi(\boldsymbol{r},t) = \frac{\mathrm{d}}{\mathrm{d}t}\Psi(\boldsymbol{r},t), \tag{1.1}$$

where $\hbar$ is the reduced Planck constant $h/2\pi$. For the restriction to a time-independent and one-dimensional case the Schrödinger equation reduces to

$$-\frac{\hbar^2}{2m}\frac{\mathrm{d}^2}{\mathrm{d}z^2}\Psi(z) + V(z)\Psi(z) = E\Psi(z). \tag{1.2}$$

A potential landscape with an electron propagating in positive z direction, as shown in Fig. 1.2 (a), leads to the solution of Eq. (1.2)

$$\Psi_{\mathrm{I,III}}(z) = \Psi_0 \exp\left[\pm\mathrm{i}\frac{\sqrt{2m(E-V_0)}}{\hbar}z\right] \tag{1.3}$$

in region I and III, where the electron energy is higher than the potential. This means that the electron can propagate back and forth in region I and has a non-vanishing probability to be observed in region III.
Quantum mechanically a solution of the Schrödinger equation can also be found in region II due to the continuity of the functions itself and its first derivative (c.f. Fig. 1.2 (b)). The wave function is given by

$$\Psi_{\mathrm{II}}(z) = \Psi_0 \exp\left[-\frac{\sqrt{2m(V_1-E)}}{\hbar}z\right]. \tag{1.4}$$

Based on these equation, the transmissivity of an electron through a barrier with a height V_1 and a width z_0 can be calculated via

$$T = |\Psi_{\mathrm{II}}(z_0)|^2 = |\Psi_0|^2 \exp\left[-2z_0\frac{\sqrt{2m(V_1-E)}}{\hbar}\right]. \tag{1.5}$$

In order to create a connection to STM, region I and III have to be identified with tip and sample, whereas region II represents the vacuum barrier between tip and sample. This is shown in Fig. 1.2 (c). Without an applied bias voltage, the electrons can tunnel from the tip into the sample and vice versa due to thermal activation. By applying a small bias voltage $eU \ll \phi$, much smaller than the work-function ϕ,[1] electrons with energies $E_{\mathrm{F}}^{\mathrm{S}} - eU < E < E_{\mathrm{F}}^{\mathrm{T}}$ can contribute to a net tunneling current

$$I \approx I_0 \exp\left[-2z_0\frac{\sqrt{2m\phi}}{\hbar}\right]. \tag{1.6}$$

[1] As an simplification, the work-function of tip and sample are assumed to be equal $\phi = \phi^{\mathrm{T}} = \phi^{\mathrm{S}}$.

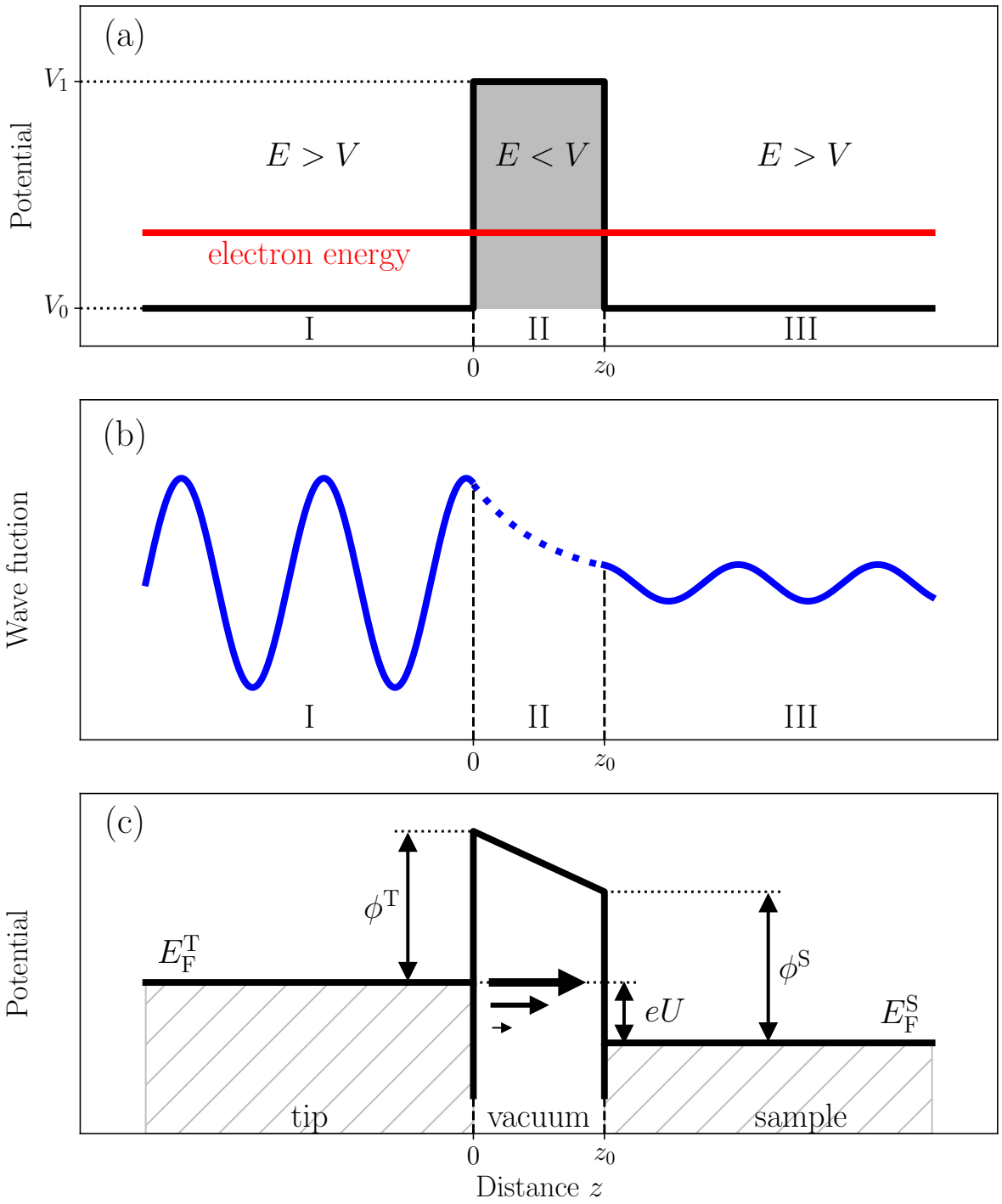

Figure 1.2: *Schematics of an electron tunneling through a potential barrier. The barrier is shown in* **(a)** *and the wave function with its exponential decay can be seen in* **(b)**. *In* **(c)** *the case for electron tunneling in a STM with an applied bias voltage U is portrayed. In the limit of zero temperature and small voltages only electrons with the Fermi energy contribute to the tunneling current.*

In order to develop a better understanding of the quantity I, the tunneling junction should be treated as in Bardeen's approach [69] with restrictions according to Tersoff [70]. The wave function of an electron in the tip and in the sample are called Ψ_T and Ψ_S, respectively. The transition probability T is given by Fermi's Golden Rule

$$T = \frac{2\pi}{\hbar} \left|M_\mathrm{ST}\right|^2 \delta(E_\mathrm{S} - E_\mathrm{T}), \tag{1.7}$$

where the matrix element is for an Hamiltonian $\mathcal{H}$ given by $M_\mathrm{ST} = \langle\Psi_\mathrm{S}| \mathcal{H} |\Psi_\mathrm{T}\rangle$. The tunneling current is therefore given by

$$I = \frac{2\pi e^2}{\hbar} U \sum_\mathrm{T,S} f(E_\mathrm{T})[1 - f(E_\mathrm{S} + eU)] \left|M_\mathrm{ST}\right|^2 \delta(E_\mathrm{T} - E_\mathrm{S}). \tag{1.8}$$

The terms $f(E_\mathrm{T})$ and $[1 - f(E_\mathrm{S} - eU)]$, including the Fermi function $f(E)$, reveal that the summation includes just electrons, tunneling out of occupied states of the tip and into unoccupied states of the sample. This should be taken into consideration regarding the terms of the exclusion principle. For energy conservation (elastic tunneling), the δ-function includes only states with the same energy. For small voltages and low temperatures the Fermi function becomes step-like, resulting in a tunneling current

$$I = \frac{2\pi e^2}{\hbar} U \sum_\mathrm{T,S} \left|M_\mathrm{ST}\right|^2 \delta(E_\mathrm{T} - E_\mathrm{F}) \delta(E_\mathrm{S} - E_\mathrm{F}). \tag{1.9}$$

The δ-functions imply that only electrons with the Fermi energy contribute to the tunneling current. Assuming now that the tip apex is spherical with a radius R, a center $\boldsymbol{r}_0$ and s-shaped tip wave functions, the matrix element can be calculated, creating the following result

$$I = 32\pi^3 \hbar^{-1} e^2 U \phi^2 R^2 k^{-4} \exp[2kR] \rho_\mathrm{T}(E_\mathrm{F}) \sum_\mathrm{S} \left|\Psi_\mathrm{S}(\boldsymbol{r}_0)\right|^2 \delta(E_\mathrm{S} - E_\mathrm{F}), \tag{1.10}$$

with $k = \frac{\sqrt{2m(V_1 - E)}}{\hbar}$. For the assumption that the tip parameters, *i.e.*, the radius R, the work function ϕ and the tip density of states (DOS) $\rho_\mathrm{T}(E_\mathrm{F})$ are constant, the current shows the proportionality

$$I \propto U \cdot \rho_\mathrm{S}(\boldsymbol{r}_0, E_\mathrm{F}) = U \cdot \sum_\mathrm{S} \left|\Psi_\mathrm{S}(\boldsymbol{r}_0)\right|^2 \delta(E_\mathrm{S} - E_\mathrm{F}), \tag{1.11}$$

i.e., the same exponential proportionality as above with the wave function $|\Psi_\mathrm{S}(\boldsymbol{r}_0)|^2 \propto \exp[-2z_0\sqrt{2m\phi}/\hbar]$. This concludes that the current depends strongly on the distance between tip and surface as well as on the local density of states (LDOS) of the sample. Therefore, STM is a suitable technique to measure the electronic as well as the topographic properties of the surface on the atomic scale, as the decay constant is for metals typically in the order of $1\,\text{Å}^{-1}$ [72]. Therefore, the tunneling current changes by one order of magnitude for changing the tip-sample-distance by 1 Å.

1.2. Scanning tunneling spectroscopy

In addition to microscopy, spectroscopy can also be performed by STM. This method is called scanning tunneling spectroscopy (STS) and is able to probe the LDOS of the sample with a high spatial and energetic resolution. Two modes of STS are often applied, *i.e.*, the voltage dependent point spectra $\frac{\mathrm{d}I}{\mathrm{d}U}(U, x = \text{const.}, y = \text{const.})$ with disabled feedback or constant voltage maps $\frac{\mathrm{d}I}{\mathrm{d}U}(U = \text{const.}, x, y)$. STS was first implemented experimentally by Selloni *et al.* [73] as well as Binnig *et al.* [33] and theoretically by Hamers [74]. In the Wentzel-Kramer-Brillouin approximation, the tunneling current is the continuous integral over all states with energies $E_\mathrm{F}^\mathrm{S} < E < E_\mathrm{F}^\mathrm{S} + eU$ of the sample and can be written as

$$I \propto \int_{E_\mathrm{F}}^{E_\mathrm{F}+eU} \rho_\mathrm{S}(\boldsymbol{r}_0, E)\rho_\mathrm{T}(\boldsymbol{r}_0, E - eU)T(\boldsymbol{r}, E, eU)\mathrm{d}E, \tag{1.12}$$

where ρ_S and ρ_T are the LDOS of sample and tip at given energies. The averaged transition probability at low temperatures is given by $T(\boldsymbol{r}, E, eU) = \langle M_\mathrm{ST}\rangle$. A differentiation of Eq.(1.12) with respect to the applied bias voltage U yields the differential conductance

$$\frac{\mathrm{d}I}{\mathrm{d}U} \propto \rho_\mathrm{S}(\boldsymbol{r}_0, eU)\rho_\mathrm{T}(\boldsymbol{r}, 0)T(\boldsymbol{r}_0, eU) + \int_{E_\mathrm{F}}^{E_\mathrm{F}+eU} \rho_\mathrm{S}(\boldsymbol{r}_0, E)\rho_\mathrm{T}(\boldsymbol{r}_0, E - eU)\frac{\mathrm{d}T(\boldsymbol{r}, E, eU)}{\mathrm{d}U}\mathrm{d}E. \tag{1.13}$$

For a voltage-independent transition probability [72] and a constant tip LDOS the differential conductance reveals its important proportionality to the LDOS of the sample

$$\frac{\mathrm{d}I}{\mathrm{d}U} \propto \rho_\mathrm{S}(\boldsymbol{r}_0, eU). \tag{1.14}$$

As a result of the high resolution and the precise positioning of the tip, STS can resolve sub-molecular features in the $\mathrm{d}I/\mathrm{d}V$-signal[2] [76].

Experimentally the STS measurement were acquired by using the lock-in technique. In this method the DC bias voltage is superimposed with a small sinusoidal signal with modulation amplitude U_{mod} and modulation frequency f_{mod}. In the first step the superimposed measurement current signal is intermixed (multiplied) with another modulated signal with the same frequency f_{mod}. Subsequently, the signal is forwarded to a low-pass filter with a cut-off frequency $f_{\mathrm{cut-off}} \ll f_{\mathrm{mod}}$. The signal, passing this filter, is proportional to $\mathrm{d}I/\mathrm{d}U$ [77]. Typical values are $f_{\mathrm{mod}} = 0.2 - 2.5\,\mathrm{kHz}$ and $U_{\mathrm{mod}} = 5 - 50\,\mathrm{mV}$.

1.3. STM operation modes

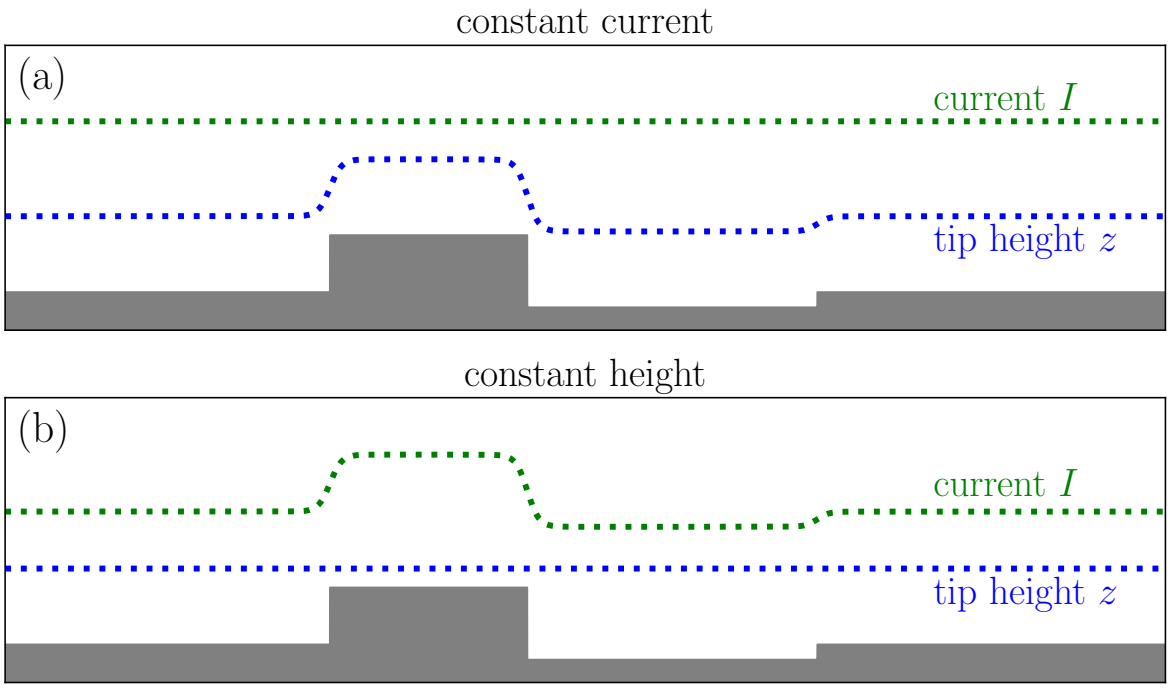

Figure 1.3: *STM modes. In* **(a)** *the constant-current mode with varying tip height is portrayed, whereas in the constant-height mode in* **(b)** *the current is the measurement signal.*

[2]Instead of dI/dU the term dI/dV is also often used, since the letter "U" is only used in Germany for the voltage. Generally, the letter "V" is recommended for the voltage, hence the differential conductance is most of the time called dI/dV [75].

STM can be measured in two different operation modes. The most common one is the constant-current mode, where the tunneling current is kept constant with a feedback loop. Within a measurement, the current is measured continuously and compared to the setpoint value. By amplifying and converting the difference between current and setpoint to a voltage, the z-piezo is driven to the correct height of the tip in a way that it retracts the tip, if the measured current is larger than the setpoint and vice versa. Therefore, the tip follows the surface corrugation – shown in Fig. 1.3 (a) – and gives the imaging information depending on the topography as well as on the LDOS of the sample.
In the constant height measurement the tip height remains constant (see Fig. 1.3 (b)), where the current is the measurement signal, due to its distance dependency. This mode is less often used because it requires flat surfaces, no thermal drift and very good vibrational damping.

1.4. Manipulation modes

In addition to the mentioned surface measurement modes, a STM can also manipulate adsorbates on the surface. This manipulation was pioneered by Eigler *et al.* in 1990, where they positioned Xenon atoms on Ni(111) to write the letters "IBM" on the surface [35]. Later, in 1993, Crommie *et al.* used this technique to position 48 iron atoms in a circular corral on Cu(111) to demonstrate impressively the wave nature of confined surface state electrons [34].
A lateral manipulation (LM) [78] is achieved by the following procedure: The tip is moved closely to the atom or molecule, which should be manipulated. Subsequently, the distance between tip and object is lowered in order to enhance the interaction, which can be attractive as well as repulsive. For attractive interaction the atom/molecule can be pulled by the tip and follows the movements of the tip. Is the interaction repulsive, the object can be pushed over the surface by the tip. By a simple tip retraction the interaction between tip and sample can be reduced.
In addition to the LM, a vertical manipulation (VM) is also possible, where the interaction between tip and surface at the manipulation position is changed either due to a distance of the STM tip to the sample or due to a change the bias voltage, *i.e.*, a change in the electric field. Therefore, atoms or molecules can be picked up or be positioned at the surface.

2. Non-contact atomic force microscopy

Beside STM, there is a second type of scanning probe microscopy (SPM), the atomic force microscopy (AFM). In contrast to STM, where the interaction is measured via the tunneling current, the force between tip and sample is the important quantity in AFM. As a result not only electrically conductive samples can be measured, but also insulating materials.
In a frequency-modulated AFM, the tip is attached at the end of an oscillating cantilever, which is vibrating close to its eigenfrequency. As the name of the method already suggests, in non-contact AFM (nc-AFM) the tip and the sample are not in contact[3], shown in Fig. 2.1 (a). Another type of AFM is contact AFM, where the tip either scratches over the surface or taps in the sample. These types of contact AFM will not be discussed here. In nc-AFM the tip-sample-distance varies and therefore, the force between tip and sample is also oscillating. In this section a brief introduction into the topic of nc-AFM will be provided and an advanced discussion can be found in literature [79–83].

2.1. Theoretic model of nc-AFM

The oscillating tip – represented by an effective mass m^* – can be modeled in nc-AFM by a spring, shown in Fig. 2.1 (b). Without any interaction with the sample, the tip oscillates with a frequency $f_0 = \frac{1}{2\pi}\sqrt{\frac{k_0}{m^*}}$.
By approaching the surface the oscillation frequency of the tip is not only determined by the cantilever but also depends on the interaction with the surface of the sample. The acting force can be modeled by a spring as well with a spring-constant k_{TS} (c.f. Fig. 2.1 (b)). This model assumes that the spring-constant is constant over a full range of oscillation, *i.e.*, the tip-sample force is proportional to the deflection.
Including now both "springs", the resulting spring-constant is according to Hooke's law of small amplitudes $k_{\mathrm{res}} = k_0 + k_{\mathrm{TS}}$, leading to a resulting frequency

$$f_{\mathrm{res}} = \frac{1}{2\pi}\sqrt{\frac{k_{\mathrm{res}}}{m^*}} = \frac{1}{2\pi}\sqrt{\frac{k_0 + k_{\mathrm{TS}}}{m^*}} = \frac{1}{2\pi}\sqrt{\frac{k_0}{m^*}}\sqrt{1 + \frac{k_{\mathrm{TS}}}{k_0}}. \tag{2.1}$$

By comparing the two spring-constants, $k_{\mathrm{TS}} \ll k_0$ is to be observed. A spring-constant for atomic bonds in molecules or crystals, *i.e.*, for atomic interactions is typically in the order of $k_{\mathrm{TS}} = 10\,\mathrm{N/m}$ [84], while the spring-constant of the cantilever of a qPlus sensor

[3] The term "no contact" means, that the sample is not changed due to the approaching and retracting tip.

is $k_0 = 1800\,\mathrm{N/m}$ [82]. Resulting from this difference, the square root in Eq. 2.1 can be Taylor-approximated as $\sqrt{1+\frac{k_{\mathrm{TS}}}{k_0}} \approx 1+\frac{1}{2}\frac{k_{\mathrm{TS}}}{k_0}$. The definition of the spring-constant is usually given by the second derivative of the spring-potential or the negative first derivative of the spring-force. With this definition, the frequency shift, compared to the free cantilever oscillation, results in the proportionality to the force gradient between tip and sample

$$\Delta f(z) = f_{\mathrm{res}} - f_0 = \frac{f_0}{2k_0} k_{\mathrm{TS}} = \frac{f_0}{2k_0}\frac{\partial^2 V_{\mathrm{TS}}}{\partial z^2} = -\frac{f_0}{2k_0}\frac{\partial F_{\mathrm{TS}}}{\partial z}. \tag{2.2}$$

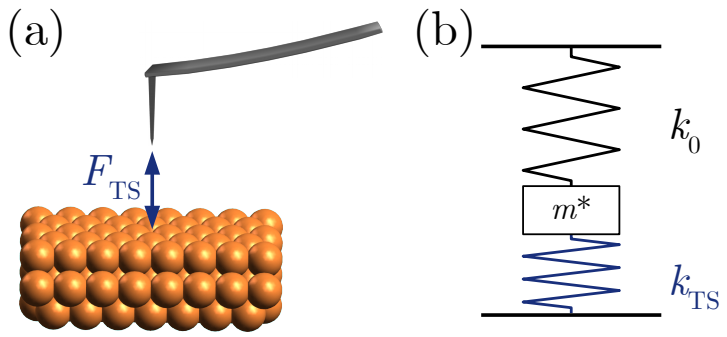

Figure 2.1: *Model of the forces acting in AFM. In* ***(a)*** *the tip and the sample are shown with an acting force F_{TS}.* ***(b)*** *shows the simplified model, where the oscillation of the tip has a spring-constant k_0. The effective mass of the tip is given by m^*. The force between tip and sample is also modeled by a spring with a spring constant k_{TS}.*

2.2. Tip sample forces

As the experimentally observable frequency shift depends on the force gradient, more knowledge, regarding the interactions between tip and sample, is needed. The main forces, which need to be considered are

- Chemical forces
- Electrostatic forces
- Van-der-Waals forces
- Magnetic forces

In this thesis no magnetic tips were used, thus magnetic forces will not be discussed here.

Van der Waals forces

Van der Waals (vdW) forces are the attractive electrostatic forces between induced fluctuating dipoles [85]. These dipoles can stem from the electron cloud of atoms or molecules. As a result, even neutral atoms feel an attractive force between each other at small distances (nanometers). The distance-dependence of the potential of this attractive vdW-force between two particles is given by [85, 86]

$$V_{\mathrm{vdW}} \propto -\frac{1}{z^6}. \tag{2.3}$$

As we are not dealing with point-like particles in AFM but with a tip and a sample, one must differentiate the assumptions regarding this matter. By approximating the tip by a sphere with radius R and the sample by a flat surface, the force between tip and sample can be rewritten as it was done by Hamaker [87]

$$F_{\mathrm{vdW}} = -\frac{A_{\mathrm{H}} R}{6z^2}, \tag{2.4}$$

where A_{H} is the material-dependent Hamaker constant. For noble metals like Au or Ag it has a value of $A_{\mathrm{H}} \approx 4 \cdot 10^{-19}\,\mathrm{J} \approx 2.5\,\mathrm{eV}$ [88].

Chemical forces

The chemical force is present if two atoms approach each other and their wave functions start to overlap as in STM/AFM measurements (see section 1). An empirical description of this scenario is given by the Lennard-Jones (LJ) force [79], where the repulsive term, covering the Pauli repulsion, has a distance dependency of z^{-13}. The attractive term, originating from the above mentioned vdW force acts with a distance dependency of z^{-7}. In combination, the force has the form of

$$F_{\mathrm{LJ}} = -12\frac{E_{\mathrm{bond}}}{z_0}\left[\left(\frac{z_0}{z}\right)^{13} - \left(\frac{z_0}{z}\right)^{7}\right], \tag{2.5}$$

where E_{bond} is the bonding energy and z_0 is the separation in equilibrium.

Electrostatic forces

Electrostatic forces can act between tip and sample and can depend on the applied bias voltage U. This scenario can be modeled macroscopically as an capacitor with capacity

C. This gives an attractive force of the form [81]

$$F_{\mathrm{ES}} = \frac{1}{2}\frac{\mathrm{d}C}{\mathrm{d}z}\left(U + \Delta\phi\right)^2, \tag{2.6}$$

where $\Delta\phi$ is the contact potential difference. By varying the bias voltage, as it is usually done in STS (c.f. section 1.2), the measurement of this local contact potential difference (LCPD) is possible [81, 89, 90]. This can be done either by point spectra or by mapping the surface. This method is called Kelvin Probe Force Microscopy (KPFM).
Eq. 2.6 yields that no bias voltage is needed to introduce an electrostatic force. A single layer of hexagonal boron nitride on different metal substrate exhibits a moiré structure, not only geometrically but also electronically corrugated (c.f. section 6.2) [38, 55, 61]. This corrugation leads to a lateral difference in the work function and therefore in the LCPD.

Effective tip-sample forces

In AFM measurements with a bias voltage of $U = 0$, the potential between tip and sample is the sum of the LJ potential and the approximated vdW potential, shown in Fig. 2.2 (a), and is given by

$$F_{\mathrm{TS}} = -12\frac{E_{\mathrm{bond}}}{z_0}\left[\left(\frac{z_0}{z}\right)^{13} - \left(\frac{z_0}{z}\right)^{7}\right] - \frac{A_{\mathrm{H}}R}{6z^2}. \tag{2.7}$$

The values used in Fig. 2.2 for the LJ potential are a minimal bonding energy of $E_{\mathrm{bond}} = -1\,\mathrm{eV}$, an equilibrium distance between tip and sample of $z_0 = 2\,\text{Å}$, an Hamaker constant of $A_{\mathrm{H}} = 2.5\,\mathrm{eV}$ and a tip radius of $R = 1\,\mathrm{nm}$. The corresponding forces ($F_{\mathrm{TS}} = -\frac{\partial V_{\mathrm{TS}}}{\partial z}$) are shown in (b). In (c) the total potential, the total force and the resulting frequency shift are shown. All curves are normalized to have their minimum at $V = -1$, $F = -1$ or $\Delta f = -1$, respectively. For distances $z \gg z_0$ the frequency shift is in the attractive vdW regime, where the LJ force has nearly no contributions. The distance for imaging with the best resolution is in the repulsive region $z_0 < z < \min(\Delta f)$ [91]. Coming even closer to the sample into the region of bonding distances, the Pauli repulsion is dominating the force, leading to unstable imaging conditions at very short distances.

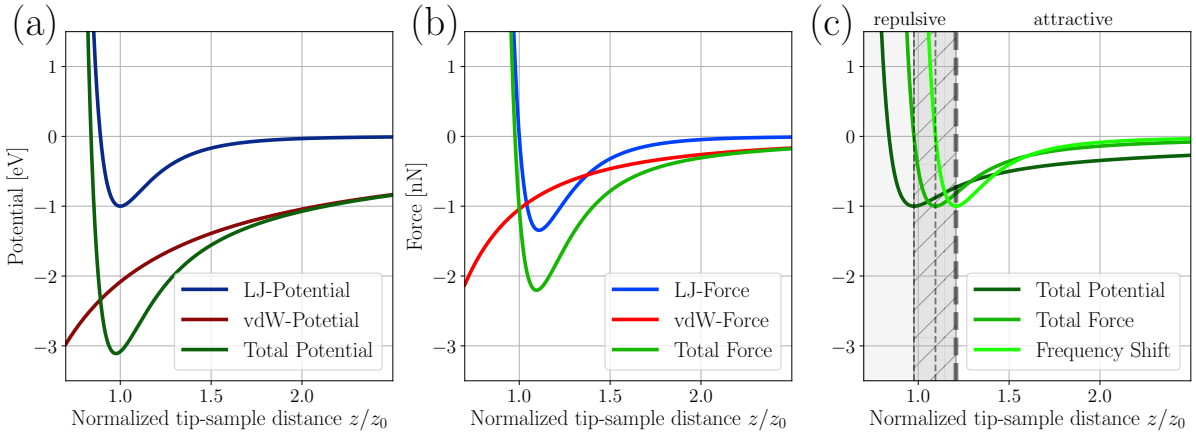

Figure 2.2: *Distance dependencies of the potentials and forces acting in AFM. In* ***(a)*** *the LJ potential (dark blue), the vdW potential (dark red) and the total potential (dark green) are plotted against the normalized tip-sample distance z/z_0.* ***(b)*** *shows the corresponding forces (LJ: blue, vdW: red, total force: green). The connection between the total potential (dark green), the total force (green) and the frequency shift (light green) is shown in* ***(c)****. All curves were normalized to have their minimum at -1. For large distances compared to the equilibrium distance z_0, i.e., the distance, where the total potential has its minimum, the frequency shift is in the attractive regime, otherwise it's in the repulsive regime. Parameters: $E_{\mathrm{bond}} = -1\,eV$, $z_0 = 2\,\text{Å}$, $A_{\mathrm{H}} = 2.5\,eV$, $R = 1\,nm$.*

3. Density functional theory

In addition to the experimental approach, physical properties of materials can also be simulated and calculated. A common method to compute properties such as ground state energies, geometric structures or magnetism is the density functional theory (DFT). The basic idea of this theory is to approach many-electron problems by dealing not with single electrons but with the electron density $n(\boldsymbol{r})$, as in the Thomas-Fermi model [92].
Considering this density, the ground state energy of a many electron system in a potential $V(\boldsymbol{r})$ is according to the Hohenberg-Kohn theorem [93] given by

$$E[n(\boldsymbol{r})] = \int V(\boldsymbol{r})n(\boldsymbol{r})\mathrm{d}\boldsymbol{r} + F[n(\boldsymbol{r})], \tag{3.1}$$

where $E[n]$ and $F[n(\boldsymbol{r})]$ are not ordinary vector functions but functionals of the electron density. The functional $F[n(\boldsymbol{r})]$ includes the kinetic energy of the electrons as well as the energy of electron-electron interactions. The electron-electron interactions are often approximated. Prominent approximations are the general gradient approximation (GGA) [94] or the local density approximation (LDA) [95].
A schematic picture of the reduction of dimensions is shown in Fig. 3.1. The dimension of this N-electron problem is now reduced from $3N$ to 3, *i.e.*, the spatial coordinates. This reduction becomes more important for larger systems like molecules or complex crystals, consisting of many atoms and therefore a huge amount of electrons, which have to be taken into account.

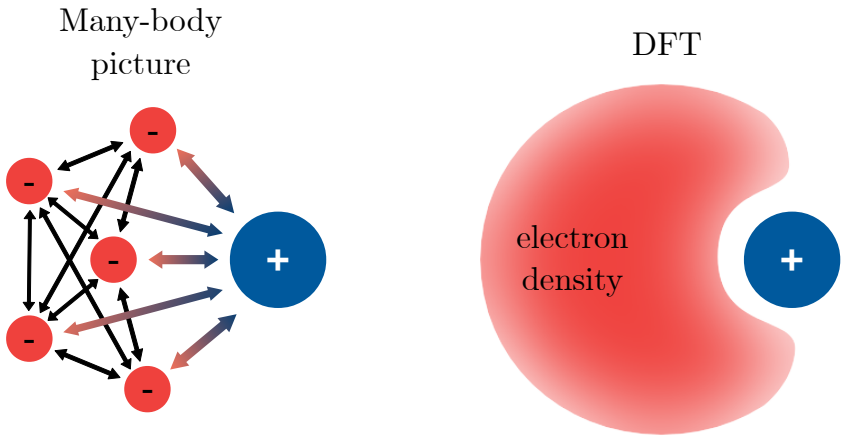

Figure 3.1: *Reduction of the computational dimension for the transition from the many body picture to the density functional picture. Instead of dealing with single electrons the electron density is used in the calculations of desired quantities. Image: c.f. [96]*

Another simplification of DFT is the usage of pseudo-potentials. These potentials mimic a potential created by the core and all closed shells of an atom. With this approximation only the valence electrons need to be taken into account by calculating the total electron wave function.
The iterative process of a DFT calculation is schematically shown in Fig. 3.2.

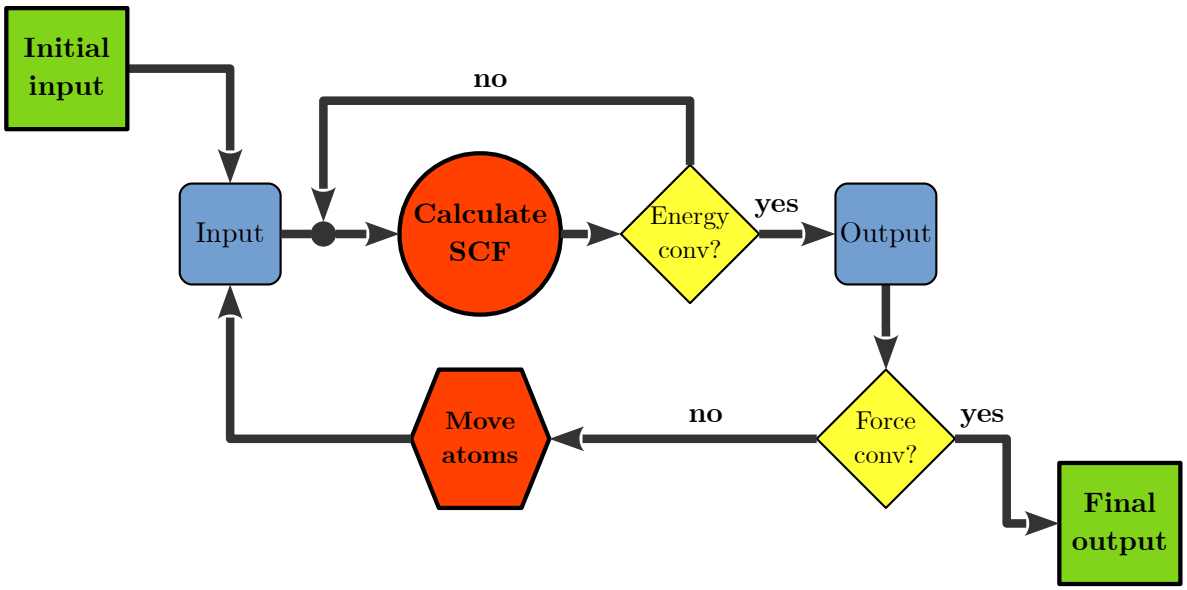

Figure 3.2: *Flowchart of the iterative process in DFT. Based on the input SCFs are calculated in a loop until their energy converges. If the resulting forces on each atom are above a certain threshold, the atomic positions are changed accoring to the acting forces. After the convergence of the forces the structural and energetic information are forwarded to the output.*

The optimization in DFT is an iterative process, starting with initial atomic positions. For this arrangement, the electronic self consistent function (SCF) is calculated in a loop until the energy converges. If so, the force on each atom is calculated. If the force is too high, the atoms are rearranged according to the acting forces. The resulting positions of the atoms are implemented as the new input to start the next loop for the calculation of the electronic SCFs. If the forces are converged below a certain threshold, the structure and energies of this final configuration are forwarded to the output files.
The program package, used in this thesis, is especially designed for solid state and molecular calculation and is the Vienna ab-initio simulation package (VASP) [97, 98].

4. X-ray photoelectron spectroscopy

X-ray photoelectron spectroscopy (XPS) is a surface averaging technique, based on the photoelectric effect. This effect was theoretically explained by Einstein [99], for which he was awarded the nobel prize in 1921 [100]. With the help of this technique, it is possible to get insights into the chemical properties of a materials surface. As schematically shown in Fig. 4.1 (a), the working principle of XPS is the measurement of core electrons, emitted due to the adsorption of X-rays, based on the photoeffect. The measured kinetic energy E_{kin} of the electrons depends on their binding energy E_{b} in the solid, defined relatively to the vacuum level Φ and the energy of the used X-rays $\hbar\omega$:

$$E_{\mathrm{kin}} = \hbar\omega - E_{\mathrm{b}}. \tag{4.1}$$

The X-rays, used for the experiments in this thesis, are emitted from a commercial X-ray source (anode material Mg or Al) and have a fixed photon energy in the range of so-called soft X-rays between $100 - 2000\,\mathrm{eV}$. Within this energy range, photoelectrons have an inelastic mean free path of $\lambda_{\mathrm{mfp}} = 0.5 - 3\,\mathrm{nm}$ [101]. Thus, the first few atomic layers of a material are accessible with XPS.

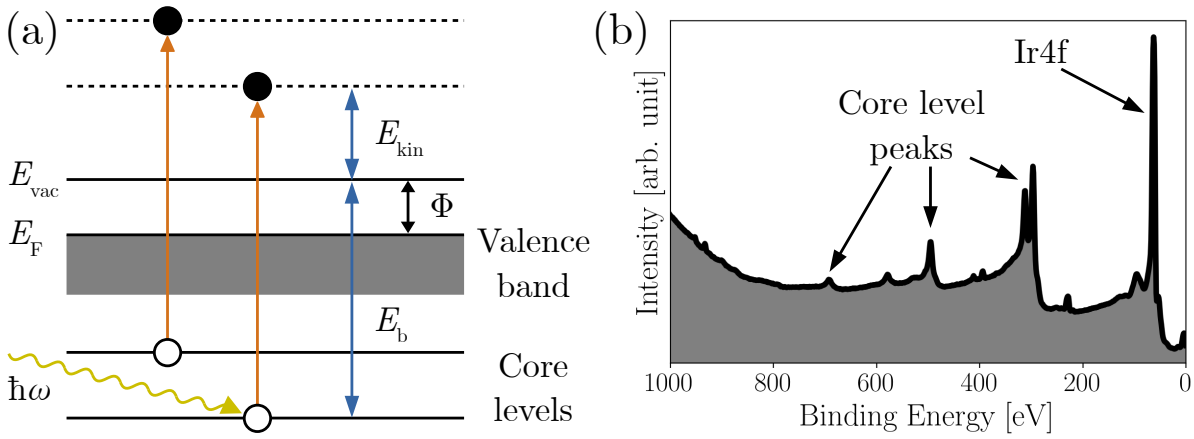

Figure 4.1: *Working principle of XPS. In* ***(a)*** *the emission of core electrons due to the adsorption of X-ray radiation is schematically shown. An exemplary XP spectrum of bare Ir(111) can be seen in* ***(b)****. The background of the spectrum is portrayed in grey. Figure was adapted from [83].*

By the implementation of a fixed photon energy and measuring the kinetic energy of the electrons, the binding energy can be determined with the help of Eq. 4.1. These binding energies are element specific and can provide details about the chemical environment of the measured atomic species [101]. An exemplary XP spectra is shown in Fig. 4.1 (b).

The measured core level peaks are superimposed by a background, portrayed in grey. The binding energy on the x-axis is commonly shown in a reversed order, since it is calculated from the measured kinetic energy and has in contrast to this a negative sign (c.f. Eq. 4.1).

Part III.
Experimental setup, substrates and materials

5. Ultra-high vacuum system

For the experiments, presented in this thesis, two main requirements are essential: an ultra-high vacuum (UHV) to prevent the samples from contamination and low temperatures to freeze out the motion of molecules on the surface.

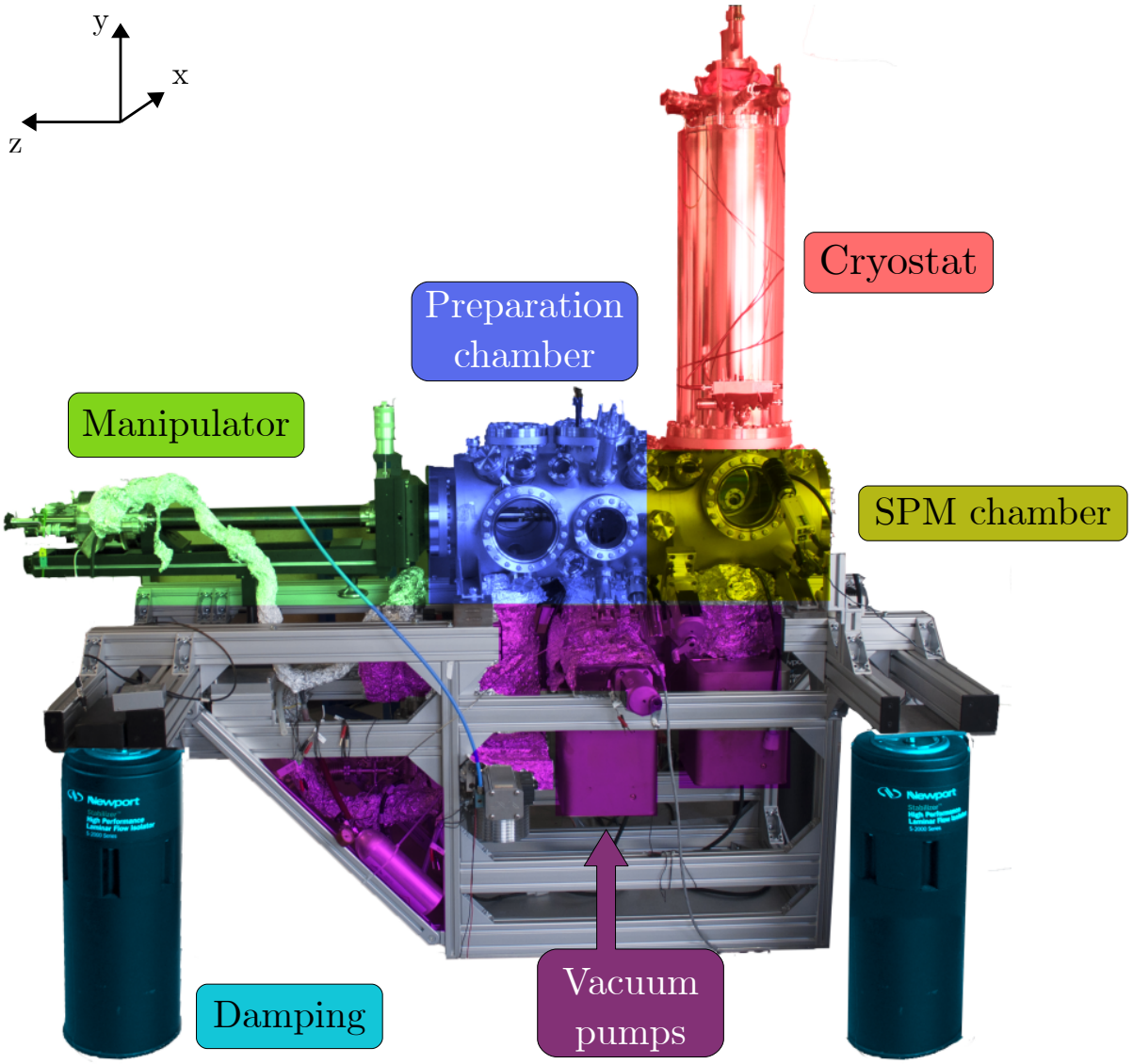

Figure 5.1: *Setup of the UHV system. In the image the different parts of the UHV system are shown, i.e., the manipulator (green) for moving and transferring the samples, the pneumatic damping legs (cyan) to decouple the system from external vibrations, the vacuum pumps (purple) to ensure a stable vacuum, the cryostat (red) for cooling and the two chambers, i.e., the preparation- and the SPM chamber (blue/yellow, respectively). The figure was adapted from [102].*

Three setups, made out of stainless-steel vessels by VAb GmbH [103], similar to the one in Fig. 5.1 with differently colored parts, were used. The manipulator (green) allows a movement of the samples with four degrees of freedom, *i.e.*, translation along all three directions indicated by the coordinate system in the top left corner of Fig. 5.1 as well as rotation around the z direction. Therefore, samples can be placed in various positions for preparation or storage and can be transferred into the microscope.
The two chambers, *i.e.*, the preparation- and the SPM chamber (blue/yellow in Fig. 5.1) can be separated from each other by a gate valve to preserve a low pressure in the SPM chamber while preparing a sample. The difference between the three used setups is mainly the type of sensor in the SPM chamber. One setup, called "LT-STM", is equipped with a normal STM-tip for STM measurements. Another one, called "AFM", is equipped with a qPlus sensor [81, 82, 104] for nc-AFM measurements. A third setup is the room-temperature "XPS-STM". In this setup the samples were measured with STM at room-temperature. In contrast to the other two setups the "XPS-STM" is equipped with a X-ray photoelectron spectrometer in the preparation chamber.

5.1. Pumping system

The base pressure in all UHV-systems is in the order of $p \approx 10^{-10}\,\mathrm{mbar}$. To reach this pressure several pumps are used (shown in purple in Fig. 5.1).

Diaphragm pump At the first stage of pumping, a pressure of $p \approx 1\,\mathrm{mbar}$ can be reached via a diaphragm pump by oscillating a diaphragm.

Turbo molecular pump (TP) The next stage are two TPs mounted in series. Each one consists of alternating rotors and stators, inducing in combination a flow of particles in one direction due to the transfer of momentum by the collision of the rotors and the gas molecules. The rotational frequency is in the order of $f \approx 1\,\mathrm{kHz}$. With the use of such TPs, pressures in the range of $p \approx 10^{-10}\,\mathrm{mbar}$ can be obtained.

Ion getter pump (IP) In addition to the TPs, IPs are also implemented. The working principle here is to ionize particles in between a series of alternating biased metal plates. Between these plates a high voltage ($\sim 3\,\mathrm{kV}$) is applied. Therefore, the ionized particles are accelerated and implanted into the metal plates, where they are trapped.

Titanium sublimation pump (TSP) To trap especially small molecules, like H_2, titanium is evaporated from a resistively heated filament onto the walls of the chamber. The residual gas molecules bind to the Ti, due to its high chemical reactivity.

Cooling trap Temporarily, the pressure can be reduced by filling a reservoir, attached to the chamber wall, with liquid nitrogen (LN_2). Gas can be frozen in the cooling trap as long as the reservoir is filled with LN_2.

While in the SPM chamber an IP is enough to preserve the UHV, in the preparation chamber TPs are additionally needed, because of the temporarily increased pressure due to the preparation of samples, the degassing of evaporators or the usage of high noble gas pressures while cleaning the sample.
Additional advantages of the UHV, beside the minimization of contamination, are on the one hand the extension of the mean free path of atoms and molecules for their deposition and on the other hand the reduced heat conduction, crucial for the cooling of the system.

5.2. Cryogenic system

The low temperatures of $T \approx 5\,\mathrm{K}$ in the microscope are reached by attaching the microscope to a cryostat, filled with liquid gases – shown in red in Fig. 5.1 and in detail in Fig. 5.2.
At this temperature the movement of molecules and the drift of the microscope is highly reduced, allowing for high-resolution measurements. The spectroscopic resolution is most notably enhanced at low temperatures, due to decreased thermal broadening.
The cryostat consists of an outer tank, filled with liquid nitrogen (LN_2, $T \approx 77\,\mathrm{K}$, $V = 15\,\mathrm{l}$) and an inner tank, filled with liquid helium (LHe, $T \approx 4\,\mathrm{K}$, $V = 4\,\mathrm{l}$). The latter one is directly connected to the SPM-head, seen in Fig. 5.2. The SPM head is placed inside of two shields to prevent it from heating up due to radiation. A fully filled cryostat can provide a constant, low temperature of $T \approx 5\,\mathrm{K}$ for a maximum of 50 h.
All STM measurements in this thesis were acquired at these low temperatures of $\sim 5\,\mathrm{K}$, unless stated otherwise.

5.3. Vibrational damping system

Because of the high sensitivity of SPM to height changes, as described in section 1 and 2, the decoupling of the scanner from external vibrations is important for the quality

of the experiment. The total damping is composed of three different stages. First, the whole instrument is placed on pneumatic dampers (cyan in Fig. 5.1). The dampers are also used to adjust the horizontal plane of the instrument. Second, the SPM head is held by three springs and connected to an eddy current damping as shown in Fig. 5.2. Third, the electrical noise of the measurement signal, *i.e.*, the tunneling current, is reduced, due to screened cables, a filtered power supply and a filtered ground.

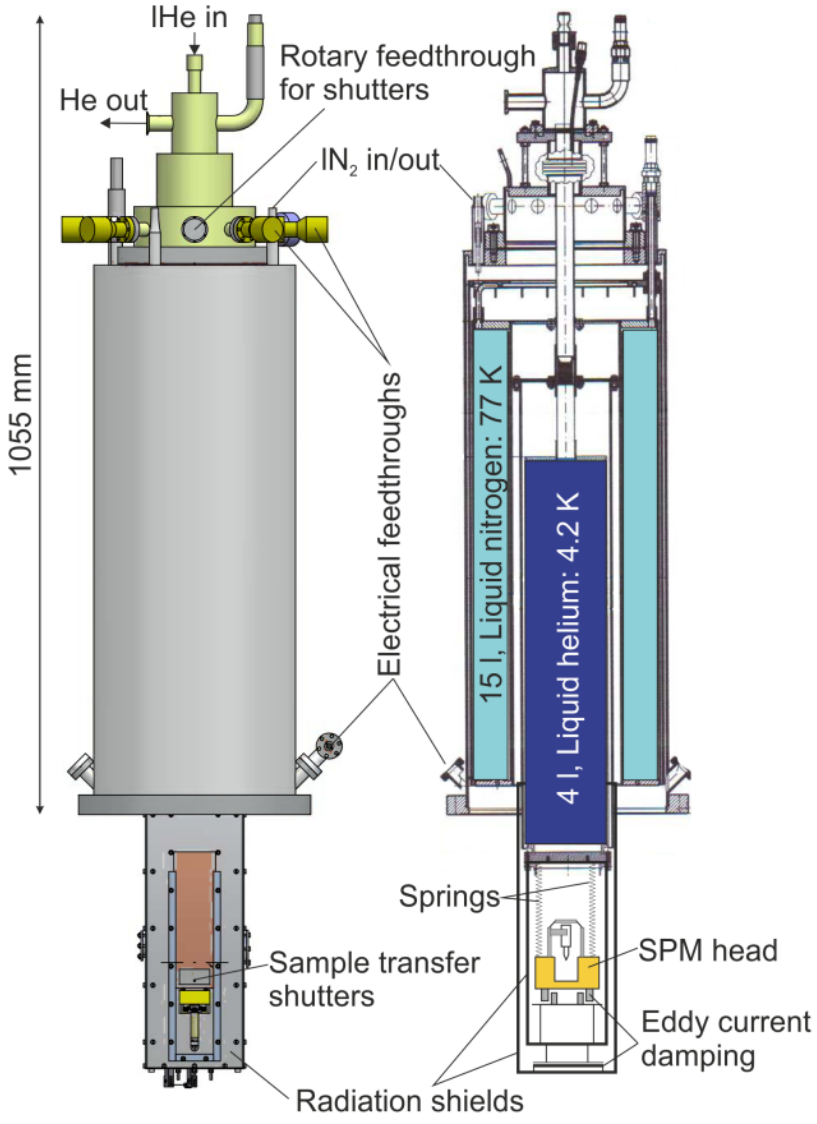

Figure 5.2: *Setup of the cryogenic system. The setup of the cryostat shows two tanks, i.e., the outer tank, filled with LN_2 and the inner tank, filled with LHe. Two radiation shields around the SPM head ensure constant, low temperatures of $T \approx 5\,K$. The figure was adapted from [82, 105].*

5.4. SPM scanner

The heart of the main instrument used in this thesis, *i.e.*, the "LT-STM", is the Createc SPM scanner [105, 106] (also called SPM head), sketched and imaged in Fig. 5.3. This design is called the Besocke-type scanner, where the main piezoelectric actuator (short: piezo) is moved up/down coarsely by movement of three coarse piezos on three segments of the ramp. Another scanner type is the z-slider type, used in the "AFM" and the "XPS-STM" setup. Details about the z-slider can be found in [82, 83, 107] and will not be discussed here. A main difference between the two types of scanners is the range of movement in the z-direction (z-slider: $\sim 20\,\mathrm{mm}$, Besocke: $\sim 2\,\mathrm{mm}$), which needs to be considered when mounting a sample.
The sample fits in the recess of the bottom plate and is contacted by the six pins, shown in Fig. 5.3 (b). Using these pins, the bias voltage for STM measurements is applied to the sample. All STM measurements in this thesis were obtained by applying the bias to the sample. During measurements, the whole scanner is hanging freely on three springs from the bottom of the cryostat and the sample holder is pushed from below onto the bottom plate. The sample can be pulled down into a fixed position for sample transfer. In this position the cooling is more efficient, since the SPM head is in direct contact with the helium cooled radiation shield.

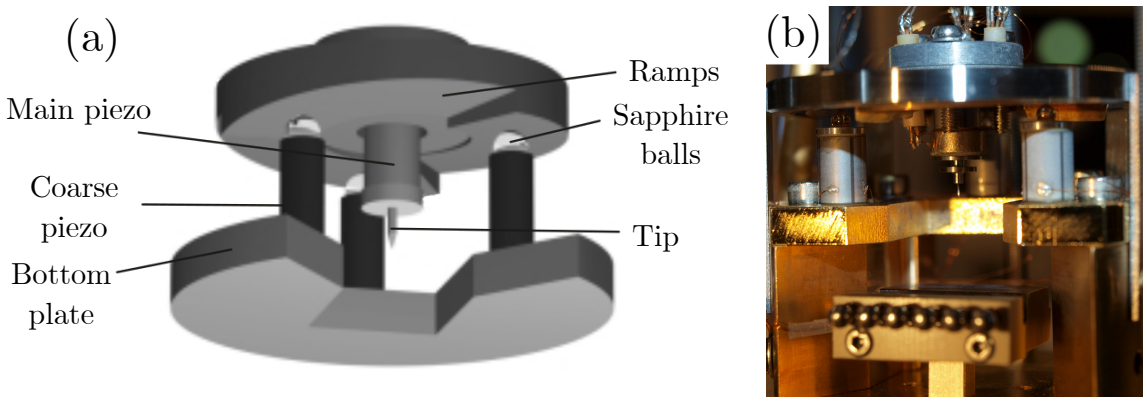

Figure 5.3: *Schematic drawing of the CreaTec SPM scanner. The parts of the Besocke-type scanner are labeled in* ***(a)****. The figure was adapted from [108, 109]. In* ***(b)*** *a photo of the scanner is shown, taken by Knud Seufert.*

The scanner itself consists on the one side of the top part, including the main piezo with the tip and the ramp. On the other side, the bottom part includes the bottom plate and the coarse piezos with attached sapphire balls. The coarse piezos can move with a slip-stick-movement on the ramps to move the main piezo coarsely. By rotating upwards

or downwards on the segments of the ramps the tip-sample-distance can be varied. The slip-stick-movement of the piezos is shown in detail in Fig. 5.4 (a),(b). In step-II the piezos are deformed by a slow change in the drive voltage due to the piezoelectric effect, with respect to the initial position (step-I). During this deformation the piezos stick to the ramps. By switching the applied drive voltage fast to the initial value, as shown in step-III, the piezos slip over the ramps, while returning to their initial position.
For fine movement in the sub-Å range, voltages are applied to the main piezo (shown in Fig. 5.4 (c),(d)). The outer part of the main piezo is divided into four segments, *i.e.*, ±x, ±y for bending the piezo in the xy-direction. The piezos in the inner part are responsible for the fine movement of the tip in z-direction by elongation or contraction, while scanning.

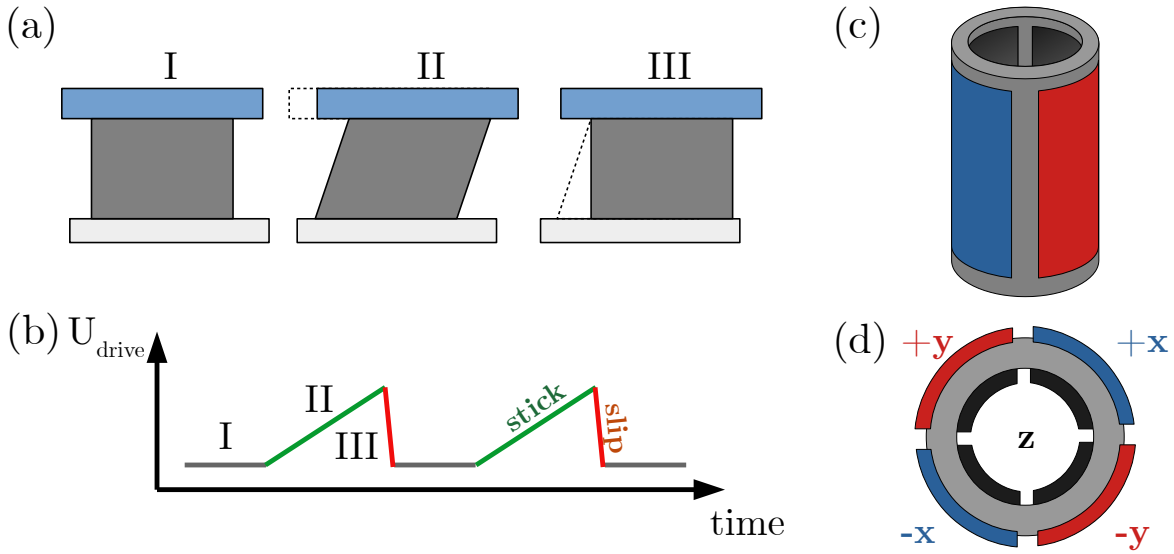

Figure 5.4: *Principle of the slip-stick movement of the piezoelectric actuators. In* ***(a)*** *the movement of a coarse piezo of the scanner is shown with the corresponding drive voltages in* ***(b)****.* ***(c)*** *and* ***(d)*** *show the main piezo, located in the middle of the top part of the scanner. The movement of the main piezo is done by bending, elongation or contraction of the consisting piezos.*

6. Materials and substrates

6.1. Metal substrates

Metal surfaces with different orientations were used in the experiments. All samples have the same crystal structure, *i.e.*, fcc. By cutting these metal single crystals in a certain direction one can obtain surfaces with different symmetries, shown in Fig. 6.1.

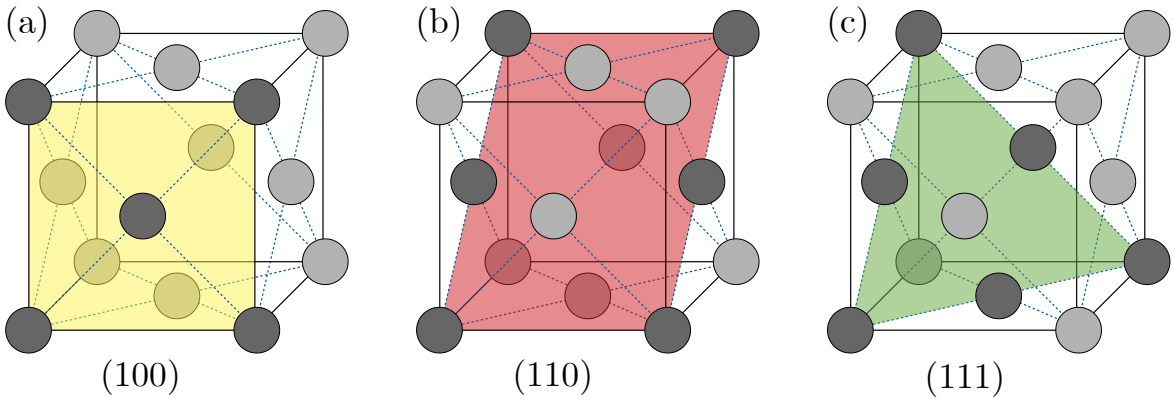

Figure 6.1: *The three high symmetry planes of a fcc crystal. The (100) plane in yellow in* ***(a)*** *has a quadratic, i.e., a fourfold symmetry. The (110) plane in red in* ***(b)*** *has a twofold symmetry and the (111) plane in green in* ***(c)*** *has a hexagonal, i.e., threefold symmetry. The atoms, included in the surface of the corresponding crystal, are highlighted by a darker grey.*

All fcc metal substrates used in the experiments were cleaned by the same procedure: First, the metal was bombarded with noble gas ions, like Ar^+ (sputtering). Due to the high kinetic energy of the ions, surface atoms are kicked out with a certain yield, depending on the masses of ion and target atom, the energy of the ion, the incoming angle of the ion with respect to the target and the temperature of the target. Most commonly the ion beam is perpendicular to the target surface and the target temperature is room temperature. Usual values are a gas pressure of $p_{\mathrm{Ar}} \approx 1 \times 10^{-5}\,\mathrm{mbar}$, a sputter current of $I_{\mathrm{ion}} \approx 5\,\mu\mathrm{A}$ on the sample and an ion energy of $E_{\mathrm{ion}} \approx 1\,\mathrm{keV}$.
After sputtering, the surface is very rough and corrugated. To get a flat surface, the sample is heated to a temperature at which the surface atoms start to diffuse and form flat, extended terraces. Usual annealing temperatures are shown in Tab. 6.1

Material	Cu	Ag	Au	Ir
Temperatur [°C]	500	450	400	1000

Table 6.1: *Heating temperatures of different materials to flatten the surface by surface atom rearrangement after sputtering.*

6.2. Hexagonal boron nitride

The reduction of the influence of the substrate on adsorbed molecules can be achieved by the decoupling of the molecules from the (metal) substrate. This can be fulfilled by a single layer of hexagonal boron nitride (*h*BN).
*h*BN is one form, boron nitride can exhibit. The bulk *h*BN is a layered material similar to graphite [110]. In contrast to graphite, consisting only of carbon atoms, *h*BN consist of alternating boron and nitrogen atoms, shown in Fig. 6.2.

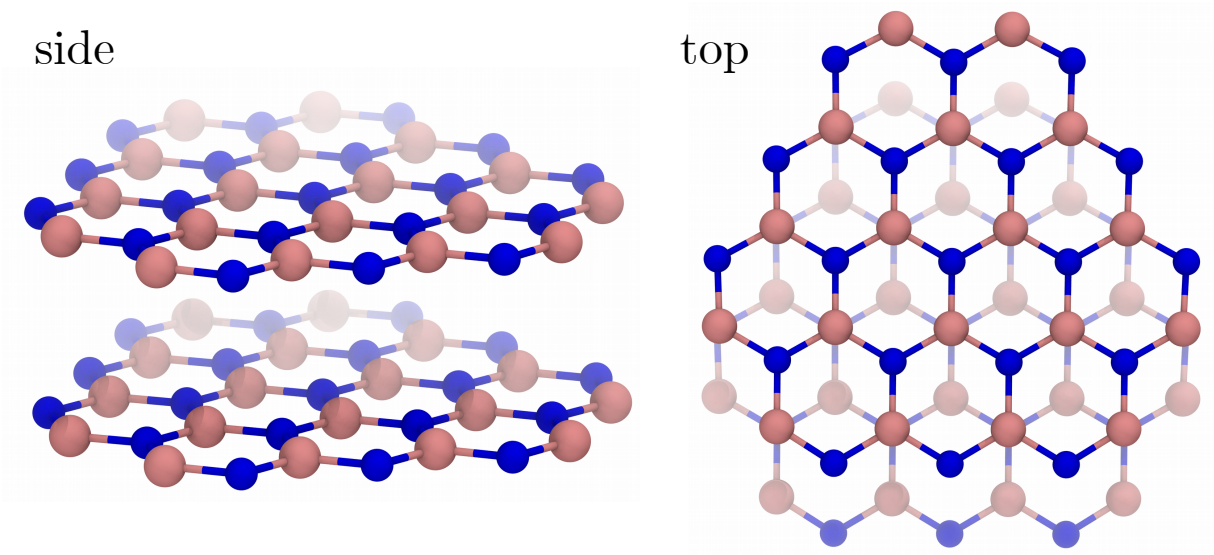

Figure 6.2: *Schematic structure of hBN. In every hexagon the boron (pink) and nitrogen (blue) atoms alternate. In the top view the stacking can be seen, where a boron atom of one layer is placed above a nitrogen atom of the next lower layer.*

The atoms in one layer of *h*BN are covalently bound, while the layers itself are bound by vdW forces to each other. This allows to obtain stable single layers of *h*BN by repeated exfoliation, similar to graphite/graphene [36, 111, 112].
Another method to synthesize single sheet *h*BN on metal surfaces, is to use chemical vapor deposition (CVD) the precursor borazine ($B_3N_3H_6$), shown in Fig. 6.3. Initially, the precursor is evaporated on the hot metal surface.

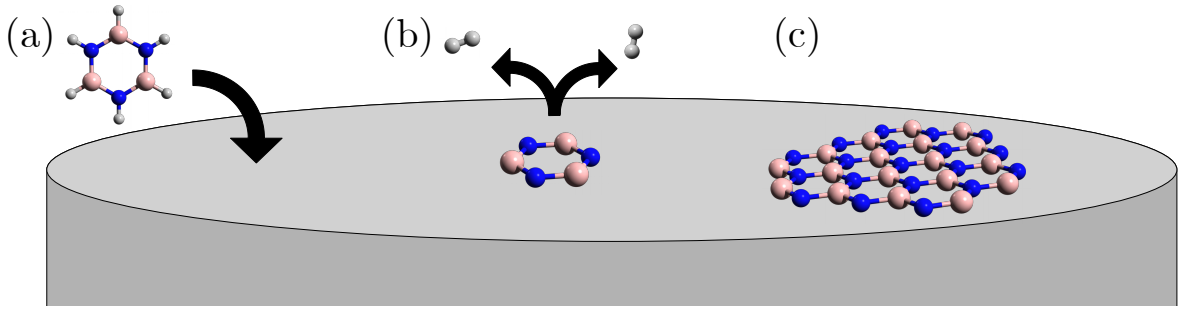

Figure 6.3: *Chemical vapor deposition of borazine to form hBN. In* ***(a)*** *the borazine is evaporated on the hot metal surface. Due to the catalytic nature of the metal the hydrogen atoms are removed from the borazine - shown in* ***(b)****, leading to the growth of a layer of hBN, shown in* ***(c)****.*

On the hot surface the hydrogens of the borazine are removed and desorb as H_2, due to the catalytic nature of the metal surface (Fig. 6.3 (b)) and the borazine ring might be cracked. Subsequently, the growth of the *h*BN layer starts.
An advantage of this procedure is the self limitation to a single layer. After the growth of a full layer of *h*BN, no free metal is available to catalyze the dehydrogenation of additional borazine.
The *h*BN, grown in the experiments in this thesis, is obtained by the following procedure:

1. The metal substrate was cleaned by Ar^+ bombardment.
2. The metal was annealed to a temperature $T_{\text{sample}} = 750 - 1000°\text{C}$.[4]
3. Borazine is introduced into the UHV chamber through a leak valve onto the sample. The pressure and the time of deposition depends on the desired coverage.
   - Monolayer: $p = 7 \times 10^{-7}\,\text{mbar}$, $t = 5\,\text{min}$
   - Submonolayer: $p = 1 \times 10^{-8}\,\text{mbar}$, $t = 5\,\text{s}$
4. The sample is post-annealed for 2 min at the growth temperature.

In ambient conditions borazine is liquid. Exposure to air and heat leads to decomposition. Therefore, it should be kept cool and under static vacuum. To transfer a certain amount of borazine to a vessel, used in experiments, one needs to fill the vessel by vacuum distillation. This process is explained in detail in Appendix C.

[4]The growth temperature depends on the maximum annealing temperature of the substrate (c.f. Tab. 6.1). For Cu the growth temperature is 750°C, for Ir it is 1000°C [38].

The two important substrates used in this thesis are hBN/Cu(111) and hBN/Ir(111) and will be described in the following. A more detailed analysis can be found in literature: [38, 56, 58, 61, 62, 113].

hBN/Cu(111) Due to the missmatch of the lattice constants of hBN and Cu(111) a moiré superlattice is formed. The size of the moiré unit cell depends strongly on the relative rotation of the hBN sheet, with respect to the underlying Cu(111) substrate [38, 56]. Geometrically, the hBN/Cu(111) is adsorbed at an average height of 3.38 ± 0.06 Å, making it a weakly bound system [38, 62]. Electronically, the hBN is corrugated, resulting in a work function difference between pore regions (stronger bound areas, closer to the substrate) and wire regions (weaker bound ares, further away from the substrate). The work function varies from $\phi_{\text{pore}} = 3.8\,\text{eV}$ to $\phi_{\text{wire}} = 4.1\,\text{eV}$ [38, 55, 56]. Molecules usually follow this electronic superlattice upon adsorption and aggregate at the pore regions, due to the higher molecule-metal-interaction [38, 54, 55].

hBN/Ir(111) The moiré superstructure of hBN/Ir(111) shows only one domain in contrast to the one on Cu(111). The periodicity of the hBN/Ir(111) unit cell is 29.1 ± 0.8 Å, corresponding to approximately 12×12 hBN units adsorbed on 11×11 Ir units [58]. The geometric corrugation of this substrate is larger than the one of hBN/Cu(111). The adsorption height varies from 2.2 Å at the strongly bound ares (pore regions) to 3.7 Å at the weakly bound ares (wire regions) [38, 58]. The electronic corrugation of the work function on hBN/Ir(111) is given by $\Delta\phi = \phi_{\text{wire}} - \phi_{\text{pore}} = 4.6\,\text{eV} - 4.2\,\text{eV} = 0.4\,\text{eV}$ [38, 61]. The adsorption of molecules and additional metal atoms follow the template of the substrate: the adsorbates preferentially adsorb on the pore regions [38, 57, 114, 115]. In the case of tetrapyrrolic molecules (see below) the size of the moiré allows the adsorption of roughly one molecule/pore, making it a suitable template for the formation of molecular arrays.

6.3. Molecules

The molecules used in this thesis are (metalated) members of the family of tetrapyrroles, often found in nature. Heme for example consists of iron-porphyrine. Another example is chlorophyll, consisting of magnesium-porphyrine.
An unsubstituted, free base porphyrine (2H-P) is shown in Fig. 6.4 (a). Based on this molecule, other similar ones can be synthesized by either attaching some ligands at different positions of the porphyrine or replacing atoms. If, for example, phenyl-groups

are attached at the linking C-atoms at the meso-positions between the pyrrole groups, tetraphenylporphyrine (TPP) is formed (see Fig. 6.4 (b)). Another example is phthalocyanine (Pc), shown in Fig. 6.4 (c), where the linking C-atoms are replaced by N-atoms. In addition, the pyrroles are replaced by benzopyrrole groups. This molecule is fully synthetic and is extremely stable against temperature, light irradiation and acids [116]. Tetrapyrroles can be metalated. During this process, a metal atom is inserted in the center of the macrocycle of the tetrapyrrole and replaces the two hydrogen atoms [19].

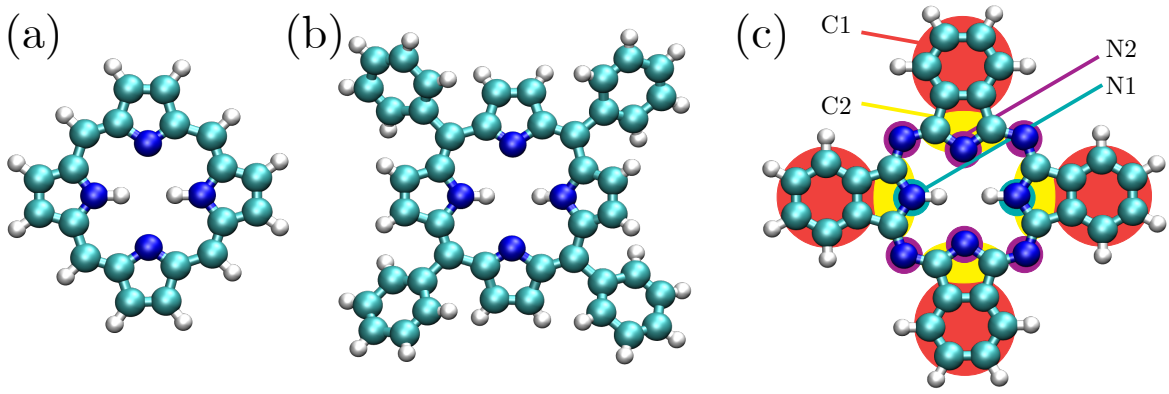

Figure 6.4: *Different tetrapyrrole-based molecules. A free base porphyrin (2H-P) is shown in* ***(a)****. In* ***(b)*** *and* ***(c)*** *a free base tetraphenylporphyrine (2H-TPP) and a free base phthalocyanine (2H-Pc) are shown, respectively. The colors represent different kinds of atoms: C - cyan, N - dark blue, H - white. The differently colored areas in (c) indicate the different groups of atoms in a 2H-Pc.*

Part IV.
Results

7. Charge state control of F_{16}CoPc on *h*BN/Cu(111)

This chapter includes content that has been published in:

Pörtner, M., Wei, Y., Riss, A., Seufert, K., Garnica, M., Barth, J. V., Diekhöner, L. & Auwärter, W., Charge state control of F_{16}CoPc on *h*BN/Cu(111). *Submitted.*

The modification of the molecular electronic structure at interfaces – such as level alignment, charging and charge transfer – by gating and screening, is highly relevant for potential applications of organic materials in solar cells, nano-electronics, sensing and quantum computing [13, 117–119]. The integral performance of such materials is determined by the molecular constituents and their interactions with each other. Furthermore, the influence of the substrate and the response to external stimuli, such as an applied electric field, can play a major role. Thus the control of the macroscopic properties of such materials relies on a fundamental microscopic understanding of the electronic properties of the molecular building blocks within their environment. Atomic-scale studies of molecular behavior have mostly been performed on metal substrates [40, 120], due to the facile application of STM and STS. However, the electronic interaction of the molecules with metals often leads to considerable hybridization, which can mask the intrinsic properties of the molecules. Thin films of decoupling layers with a band gap or low density of states around the Fermi energy grown on metal surfaces [38, 45, 46, 121] reduce the interaction between the substrate and the molecular adsorbates, but retain the possibility to perform STM/STS measurements. A particularly useful decoupling layer is one-atom-thick hexagonal boron nitride (*h*BN, see section 6.2). *h*BN layers are chemically inert, exhibit high temperature stability and most importantly, can be grown as full monolayers on metallic substrates [38], thus providing a suitable substrate for molecular adsorption. Molecular adsorbates have been shown to be influenced by the work function modulation of such substrates (associated with the formation of a moiré pattern [38, 55]), the screening by the substrate [41, 122, 123] and by neighboring molecules [124], as well as electric fields applied via back [125, 126] and top gating [127, 128]. Such effects – which can be strongly influenced by the molecular density – can lead to changes in the physicochemical behavior of the molecules, such as charging [126–130] and conformational or chemical switching [120]. Control of the molecular response therefore depends on the understanding of the complex interplay of these effects.

In this section the control of the molecular energy level alignment and the charge state of F_{16}CoPc molecules on *h*BN/Cu(111) will be analyzed. In particular, we investigate three crucial parameters: (i) the template induced gating due to the moiré-induced spatial variation of the work function of the *h*BN/Cu(111) substrate [38, 55], (ii) gating by the STM tip [57, 126–128, 131, 132] and (iii) the screening by neighboring molecules [41, 124]. A combination of these parameters can cause a change in the molecular charge state of F_{16}CoPc on *h*BN/Cu(111), *i.e.*, a shift of the molecular electronic level across the Fermi energy (E_F), which can be associated with sharp features in the dI/dV spectra of the respective molecules. In addition, AFM measurements, providing a way to probe charging at larger distances (even when the tunneling current is not detectable anymore) reveal the occurrence of multiple simultaneous charging events due to tip-induced gating.

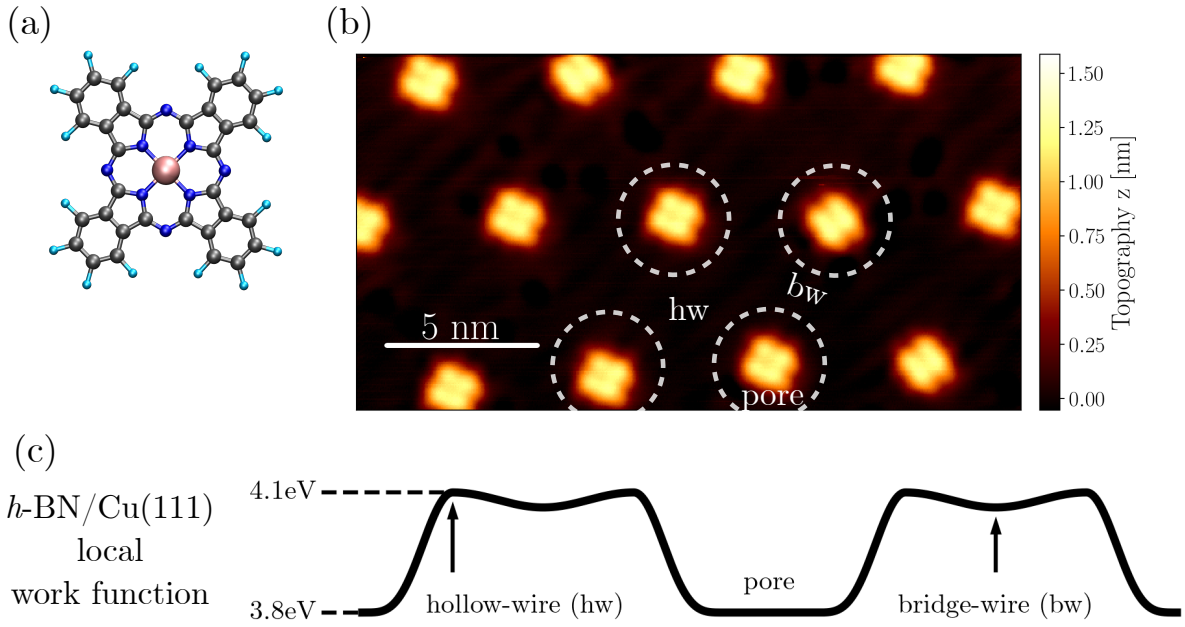

Figure 7.1: *Preferential adsorption of F_{16}CoPc on hBN/Cu(111).* ***(a)*** *Chemical structure model of F_{16}CoPc (light blue – fluorine, gray – carbon, dark blue – nitrogen, pink – cobalt).* ***(b)*** *STM topography image of 0.06 ML F_{16}CoPc on hBN/Cu(111) ($U = 1$ V, $I = 38$ pA). The molecules were evaporated at $T_{mol} = 420°C$ onto the room temperature sample for 3 min. Dashed white circles mark the pore areas of the hBN/Cu(111) moiré superstructure. The two types of wire regions are labeled with "hw" (hollow-wire) and "bw" (bridge-wire).* ***(c)*** *Schematic illustration of the local work function modulation of hBN/Cu(111), varying by 0.3 eV between the hollow-wire and the pore regions [55].*

Deposition of 0.06 ML of F_{16}CoPc (Fig. 7.1 (a)) onto *h*BN/Cu(111) held at room temperature and subsequent cooling to 5 K results in an adsorption of isolated molecules in a

superlattice. As seen in Fig. 7.1 (b) the molecules preferentially occupy the pore areas of the moiré pattern – formed by the lattice mismatch of the hBN layer and the underlying Cu(111) substrate – where the surface potential is lower. [38, 55]

7.1. Template induced gating

The work function modulation of the substrate – the pore areas exhibit a 0.3 eV lower local work function than the wire areas (Fig. 7.1 (c)) – is reflected in the molecular level alignment as probed by dI/dV spectroscopy. Spectra of molecules adsorbed on the pore areas (Fig. 7.2 (a)) are shown in Fig. 7.2 (d)-(f). In all cases a pronounced occupied-states feature at $U = -0.73\,\mathrm{V}$ (labeled "MO", molecular orbital) can be seen, while the unoccupied-states region at positive sample bias appears more or less featureless in the investigated range of up to 2 V. The asymmetry of the MO peak at $U = -0.73\,\mathrm{V}$ is due to side peaks at $U < -0.73\,\mathrm{V}$, which likely originate from vibronic excitations of the electronically decoupled molecules [114, 125, 127, 133, 134]. The resonance can be related to the LUMO of the free molecule, occupied upon adsorption resulting in negatively charged molecules. Indeed, taking into account the work function of the hBN/Cu(111) pore areas (3.8 eV) [55], the energy of the LUMO of the free F_{16}CoPc (−4.5 eV) [135] and assuming alignment of the vacuum levels of substrate and molecule, a resonance energy of −0.7 eV with respect to E_F would be expected – similar to what was observed in the spectra.
Lateral manipulation with the STM tip allows repositioning of the molecules from the pore regions (Fig. 7.2 (a)) onto different regions of the moiré pattern. In the first step molecule "1" (Fig. 7.2 (a)) was moved to a hollow-wire site (Fig. 7.2 (b)). Subsequently molecule "2" was moved to a bridge-wire site (Fig. 7.2 (c)), while molecule "3" in Fig. 7.2 (a) remained at its position at the pore region. This repositioning of the molecules gave rise to changes in the intramolecular resolution.
Before manipulation, each of the three molecules exhibited fourfold symmetry and comparable brightness. After manipulation, bright centers can be seen for the repositioned molecules 1 and 2, residing at the hollow-wire, bridge-wire regions. The dI/dV spectra of the molecules after manipulation are shown in Fig. 7.2 (g)-(i). The spectra of the molecules 1 and 2, repositioned to hollow-wire and bridge-wire sites, exhibit shifts of the MO peak from −0.73 V to −0.36 V and −0.38 V, respectively (Fig. 7.2 (g),(h)). The shifts agree well with change of the local work function across the moiré pattern ($\sim 0.3\,\mathrm{eV}$) [38, 55].

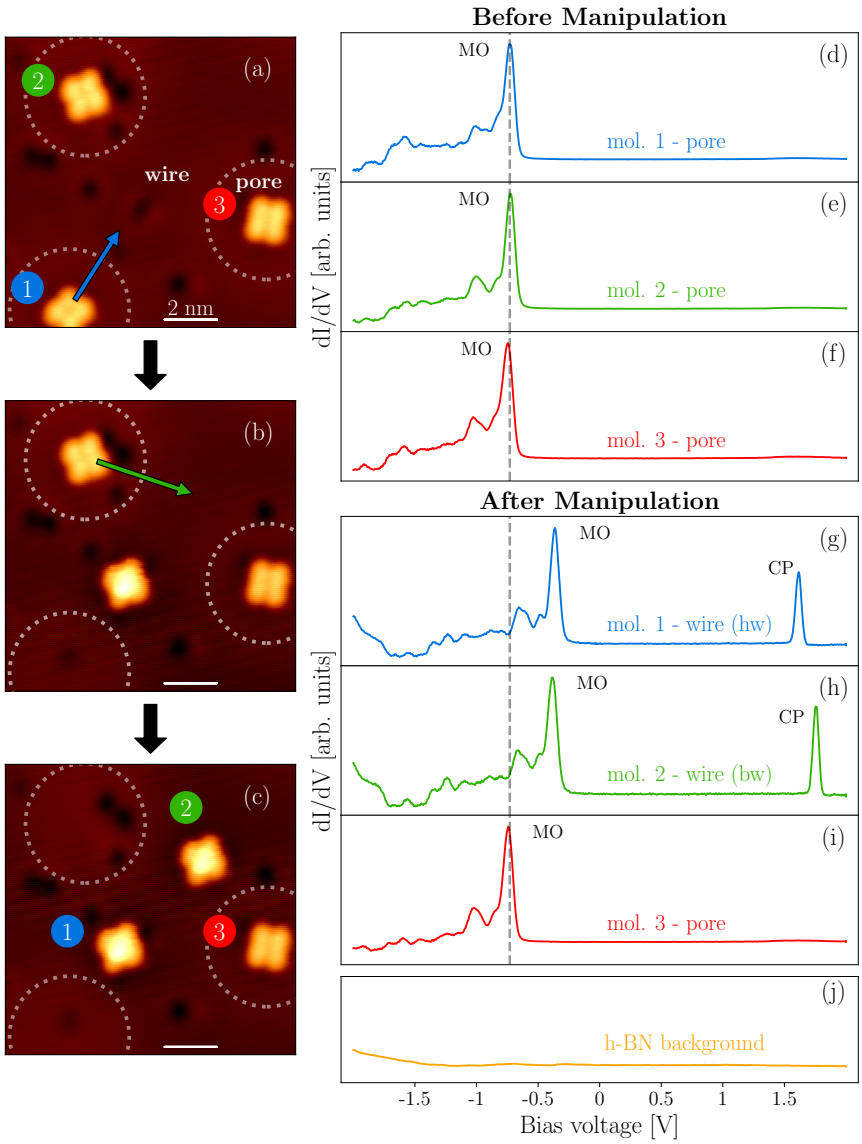

Figure 7.2: *Template induced gating of individual F_{16}CoPc molecules.* ***(a)*** *Three molecules adsorbed on moiré pore sites (dashed white circles).* ***(b)*** *Molecule 1 (blue) was moved from the pore to a hollow-wire region by LM.* ***(c)*** *Molecule 2 (green) was moved from the pore to a bridge-wire region.* ***(d)-(f)*** *dI/dV spectra of the three molecules before manipulation, i.e., adsorbed on the pore regions as shown in (a), show electronic resonances associated with a molecular orbital ("MO") at $U = -0.73$ V.* ***(g)-(i)*** *dI/dV spectra after manipulation. The energies of the molecular resonances are shifted for molecules 1 and 2 to -0.36 V and -0.38 V, respectively. In addition, charging peaks ("CP") appear at $U > 1.5$ V in the spectra for molecules 1 and 2.* ***(j)*** *Reference dI/dV spectrum taken on the hBN substrate. Scan and dI/dV stabilization parameters: $U = 1$ V, $I = 29$ pA. Spectra in (d)-(i) were taken with the tip positioned above the centers of the molecules.*

7.2. Tip induced gating

In addition to the shift of the MO, a sharp peak (denoted "CP", charging peak) appears at $U = 1.61\,\mathrm{V}$ and $U = 1.76\,\mathrm{V}$ in the spectra of the repositioned molecules 1 and 2. dI/dV maps taken at these energies show sharp ring-like features around the molecular center – seen in Fig. 7.4 – analogous to what has been observed for charging of adsorbates [57, 126–128, 130–132, 136].
In Fig. 7.3 (a),(b) dI/dV spectra for two molecules are shown, adsorbed at different positions of the hBN/Cu(111) moiré lattice. The spectrum in (a) shows a MO below E_F and a CP at 1.16 V, while the polarity of these two peaks is reversed in the spectrum in (b). The CP is at $-0.30\,\mathrm{V}$ and the MO is located above E_F. The color plots in Fig. 7.3 (c),(d) display the color-coded intensity of the spectra as a function of tip position (x-axis, along lines in insets of Fig. 7.3 (a),(b)) and sample bias (y-axis). Similar to the point spectra, the color plots portray the MO with additional vibronic peaks, as well as sharp parabola-like features, associated with the charging events [57, 126–128, 131, 132].
In addition to the distance dependency, the tip induced gating is also influenced by the applied bias voltage, as the charging is dictated by the electric field, shown in Fig. 7.4. The STM images (first and third column) and particularly the dI/dV maps (second and fourth column) show sharp ring-like features, associated with charging of the molecular species [57, 126–128, 131, 132, 136]. The radii of these rings strongly depend on the applied bias, as well as on the tip height.
To achieve an understanding of the dependency between the energies of CP and MO, the F_{16}CoPc/hBN/Cu(111) system needs to be treated as a double barrier tunneling junction (DBTJ) [57, 124, 127–129, 131, 134, 137]. Within this DBTJ-model the system consists of two tunneling junctions: the one between the metal substrate and the molecule, associated with a voltage drop of $U_{h\mathrm{BN}} = \gamma U$ [127, 131], and the vacuum tunneling junction between the molecule and the tip, associated with a voltage drop of $U_\mathrm{vac} = (1-\gamma)U$, where $0 \leq \gamma \leq 1$ is the bias fraction.

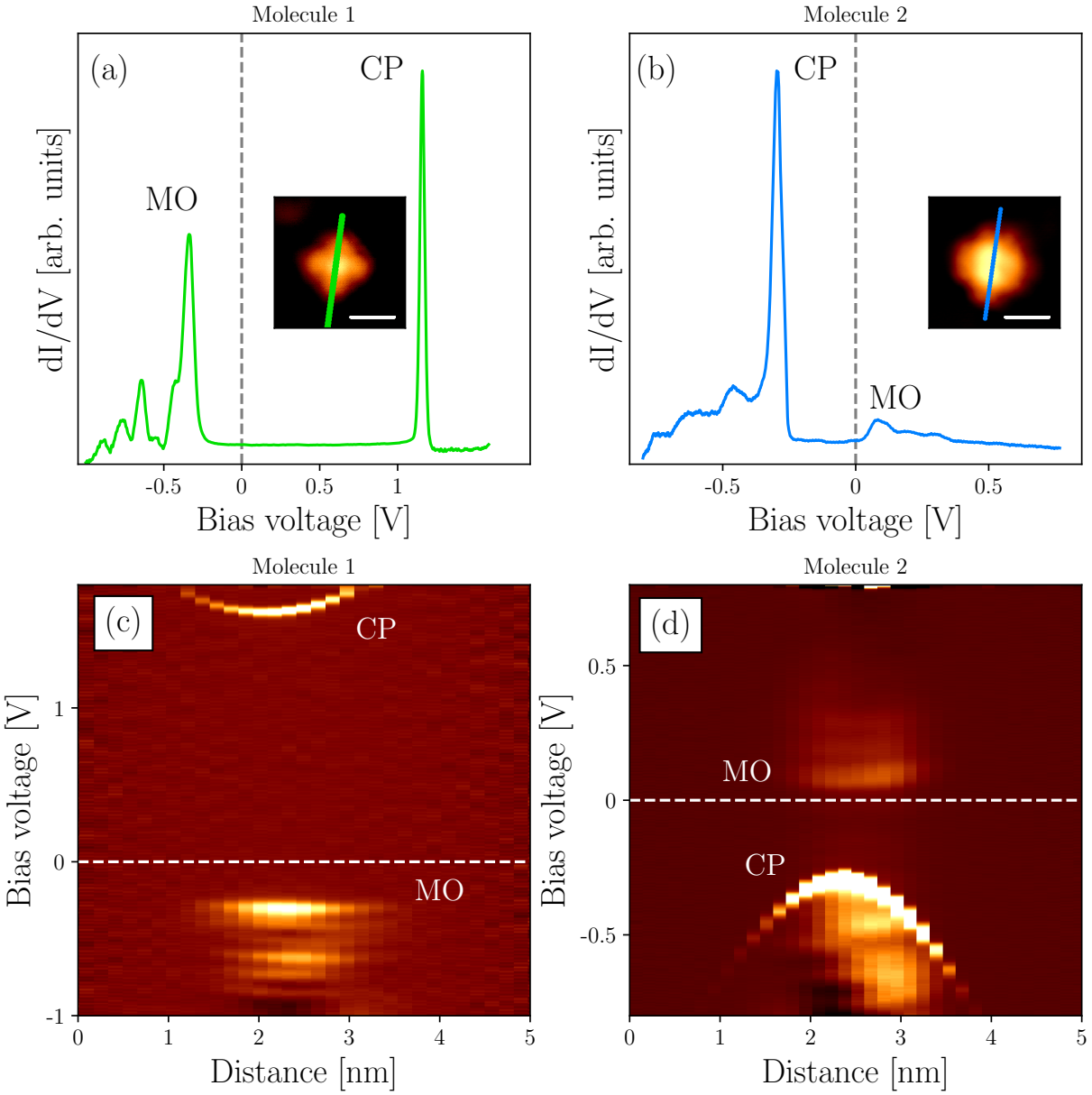

Figure 7.3: *Spatial dependence of dI/dV spectroscopy of $F_{16}CoPc$ molecules.* ***(a)***, ***(b)*** *dI/dV spectra of two molecules that are adsorbed at different positions of the hBN/Cu(111) moiré lattice. The spectrum in (a) shows a molecular resonance ("MO") below E_F and a charging peak ("CP") at 1.16 V, while (b) shows the peak associated with the molecular resonance above E_F and the charging peak at −0.30 V. (Tip stabilization parameters: (a) $U_{stab} = 1.6\,V$, $I_{stab} = 20\,pA$, (b) $U_{stab} = 0.8\,V$, $I_{stab} = 30\,pA$). The STM images of the molecules are shown in the insets (scan parameters: (a) $U = 1.0\,V$, $I = 20\,pA$, (b) $U = 1.7\,V$, $I = 30\,pA$).* ***(c)***, ***(d)*** *Color plots showing the color-coded spectral intensity as a function of tip position (x-axis, along the lines in the insets of (a), (b)) and sample bias (y-axis). The charging events are seen as sharp parabola-like features.*

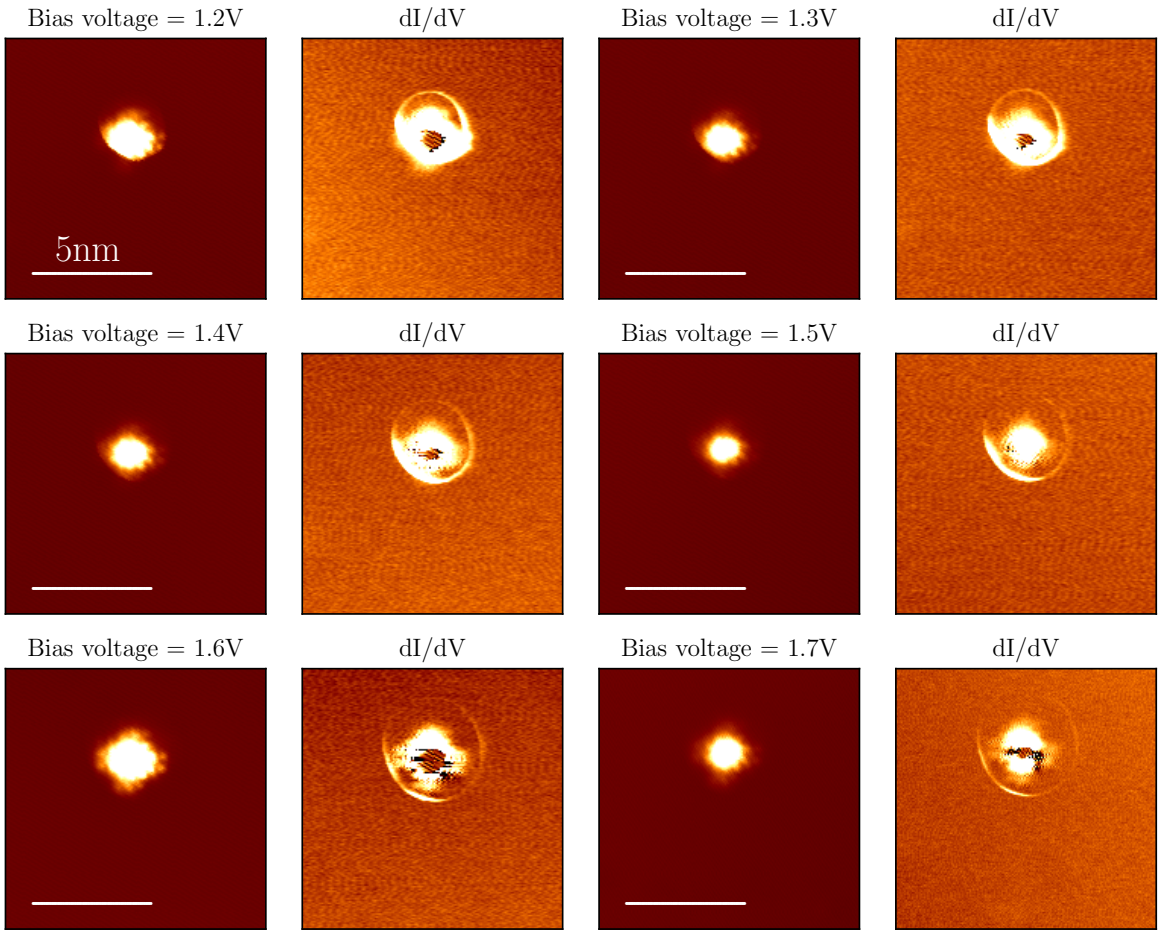

Figure 7.4: *Spatial dependence of the charging of $F_{16}CoPc$ on hBN/Cu(111). STM images (first and third column) and simultaneously recorded dI/dV maps (second and fourth column) for different bias voltages ($1.2\,\mathrm{V} \leq U \leq 1.7\,\mathrm{V}$, $I = 20\,\mathrm{pA}$). Sharp ring-like features around the molecule are associated with charging events. The size of these rings depends on the electric field between tip and sample.*

The sum of these two voltage drops equals the applied bias voltage:

$$U = U_{h\mathrm{BN}} + U_{\mathrm{vac}} = \gamma U + (1 - \gamma)U. \tag{7.1}$$

Due to gating, a shift of the MO energy is induced:

$$E_{\mathrm{MO}} = E^0_{\mathrm{MO}} + \Delta E_{\mathrm{MO}} \tag{7.2}$$

with $\Delta E_{\mathrm{MO}} = e\gamma U$, where E^0_{MO} (E_{MO}) is the energy of the MO without (with) an applied bias.

Two special cases can be considered. First, the shift of the MO peak (ΔE_{MO}) leads to alignment of the MO energy with the Fermi level of the substrate, *i.e.*,

$$E_{\mathrm{MO}} = E^0_{\mathrm{MO}} + \Delta E_{\mathrm{MO}} = 0 \Leftrightarrow E^0_{\mathrm{MO}} = -\gamma e U_{\mathrm{CP}} \tag{7.3}$$

In the spectrum this case is associated with the charging peak at $U = U_{\mathrm{CP}}$. This shifting of the molecular orbital across E_{F} reveals that the orbital changes its occupation, *i.e.*, the charge state at a bias voltage of U_{CP}.
In the second case, the MO energy aligns with the Fermi energy of the tip, *i.e.*,

$$E_{\mathrm{MO}} = E^0_{\mathrm{MO}} + \Delta E_{\mathrm{MO}} = eU_{\mathrm{MO}} \Leftrightarrow E^0_{\mathrm{MO}} = eU_{\mathrm{MO}} - e\gamma U_{\mathrm{MO}} \tag{7.4}$$

In the spectrum this case is associated with measurement of the MO-peak at $U = U_{\mathrm{MO}}$. Combination of Eq. 7.3 and Eq. 7.4 leads to

$$U_{\mathrm{CP}}/U_{\mathrm{MO}} = (\gamma - 1)/\gamma \tag{7.5}$$

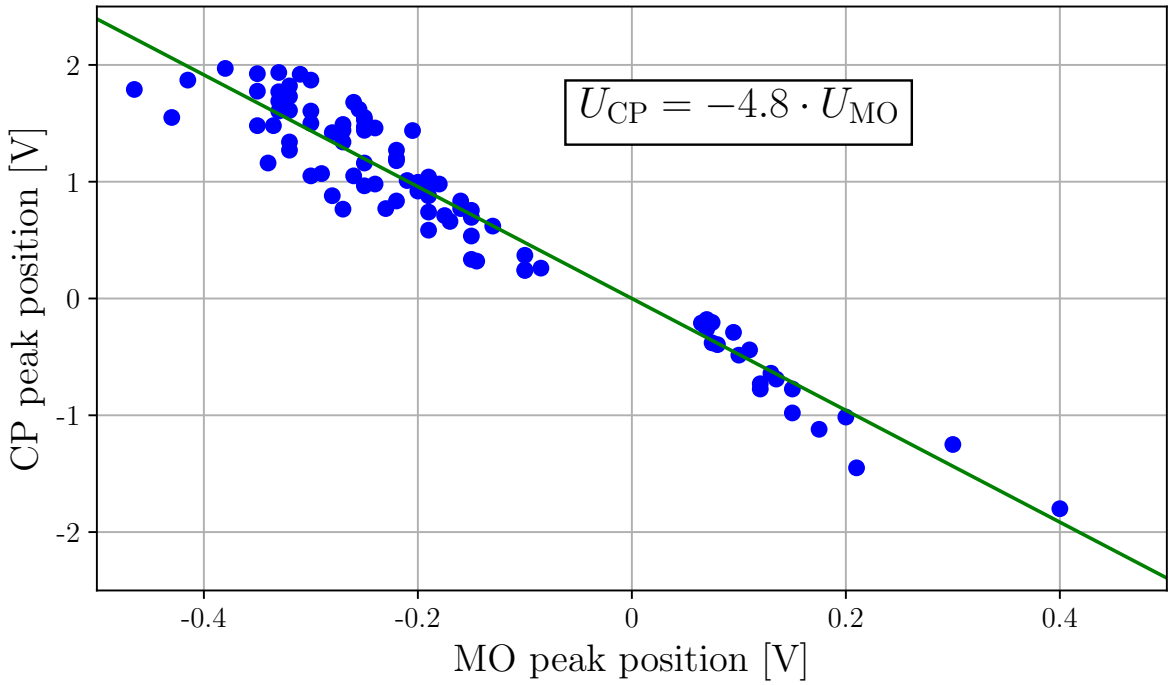

Figure 7.5: *Relation between CP and MO. Linear fitting for the ratio of energetic positions of the CP to those of the MO gives a value for the slope of $m = -4.8$.*

From the experimentally determined linear slope of U_{CP} vs. U_{MO} from 90 spectra, amounting to -4.8 (Fig. 7.5), γ can then be estimated to be 0.17.
This proportionality of $U_{\mathrm{CP}}/U_{\mathrm{MO}} = -4.8$ reveals that the initial unperturbed position of the MO will have a large impact on the bias threshold for charging.
The proportionality can also be modeled by estimating the voltage drops between tip and molecule and molecule and the metallic substrate, respectively to be $U_{\mathrm{CP}}/U_{\mathrm{MO}} = \epsilon Z/d$ [127, 129, 131, 132], where Z is the tip-molecule separation, d is the distance between the molecule and the Cu(111) substrate and ϵ is the dielectric constant, associated with the molecule-Cu(111) tunneling barrier including the hBN. A value of $\epsilon = 4$ [127, 138] yields a tip-molecule-distance, which is comparable to the molecule-metal-distance, *i.e.*, $\sim 0.5 - 0.6\,\mathrm{nm}$.

7.3. Screening

STM manipulation experiments display how the measured energy of the MO peak is affected by screening by neighboring molecules. For these experiments, we increased the molecular coverage, resulting in aggregates in the pore regions [38, 55]. The dI/dV spectrum, taken on the central molecule within a cluster of three molecules, reveals a molecular resonance at $-0.67\,\mathrm{V}$ (Fig. 7.6 (a)). Subsequent removal of its left neighbor (Fig. 7.6 (b)) and its right neighbor (Fig. 7.6 (c)) by LM shifts the position of the MO of the central molecule each time by $40 - 50\,\mathrm{mV}$ towards more negative energies, *i.e.*, away from E_{F}. This energy shift can be explained by reduced screening of the transiently charged central molecule by neighboring molecules. The polarization energy of a molecule i can be quantified by

$$E_i^P = \frac{\alpha e^2}{4\pi\epsilon_0} \sum_{j \neq i} R_{ij}^{-4} \tag{7.6}$$

and depends strongly on the distance R_{ij} to all surrounding molecules j [124]. e is the elementary charge and ϵ_0 is the vacuum permittivity. Considering only in-plane polarization, the polarizability tensor α can be approximated by a scalar for the C4-symmetric F_{16}CoPc molecules. Based on calculated values for Pc molecules, we use an estimate of the F_{16}CoPc polarizability of $\alpha = 137\,\mathrm{\AA}^3$ [139]. The calculated polarization energies (empty circles) and the measured shifts of the MO peaks (filled markers) are plotted in Fig. 7.6 (d) for the dimer/trimer (Fig. 7.6 (b)/(a)) and a molecular island, shown in the inset of Fig. 7.6 (d). For those molecules in the island, polarization effects can cause

large shifts of MO energies of a few hundred meV, in agreement with reports on a related system [124]. Despite the simplicity and limitations of the applied model, it creditably reflects the values and trends observed in the experiment (see summary section below). Discrepancies between experiment and calculation, particularly evident for some of the investigated molecules in the island, can occur due to the template induced gating (as discussed above). The gating effect is not taken into account in the calculation. For instance, molecule C6 is located close to a wire site causing an additional template induced shift towards positive energies in the experimental data.

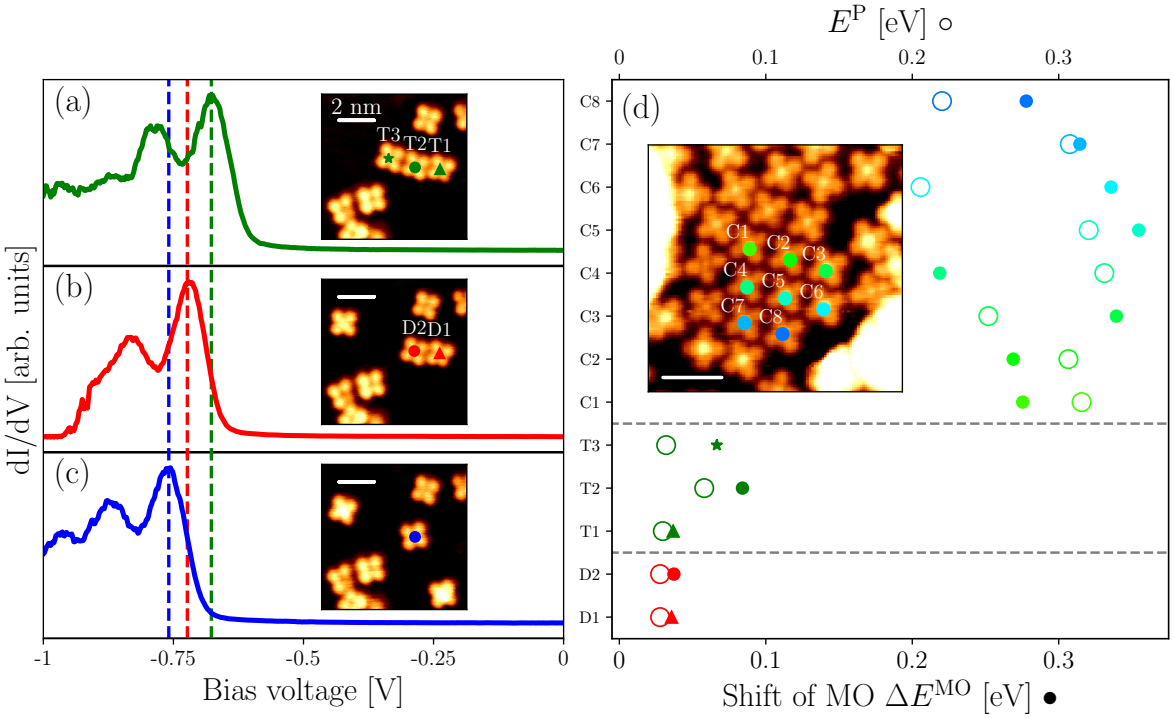

Figure 7.6: *Energy shift of the MO peaks due to polarization.* ***(a)-(c)*** *Removal of neighboring molecules by LM causes a 40−50 mV decrease of the MO position for the central molecule in the dI/dV measurements (tip stabilization parameters: $U = 1$ V, $I = 50$ pA).* ***(d)*** *Comparison of calculated polarization energies (empty circles, top x-axis) and measured shifts of MO peak energies with respect to an isolated $F_{16}CoPc$ (filled markers, bottom x-axis) for molecules in different assemblies: a cluster of two molecules (D1, D2), a cluster of three molecules (T1 to T3), and a island of molecules (C1 to C8, see STM image in the inset ($U = 1$ V, $I = 50$ pA)) (Tip stabilization parameters for dI/dV spectroscopy: $U_{stab} = 1$ V, $I_{stab} = 20$ pA, scalebars: 2 nm).*

7.4. High molecular coverage

At low coverage F_{16}CoPc molecules preferentially adsorb at the pore sites of the moiré lattice of *h*BN/Cu(111) (Fig. 7.7 (a)), as it was shown above.

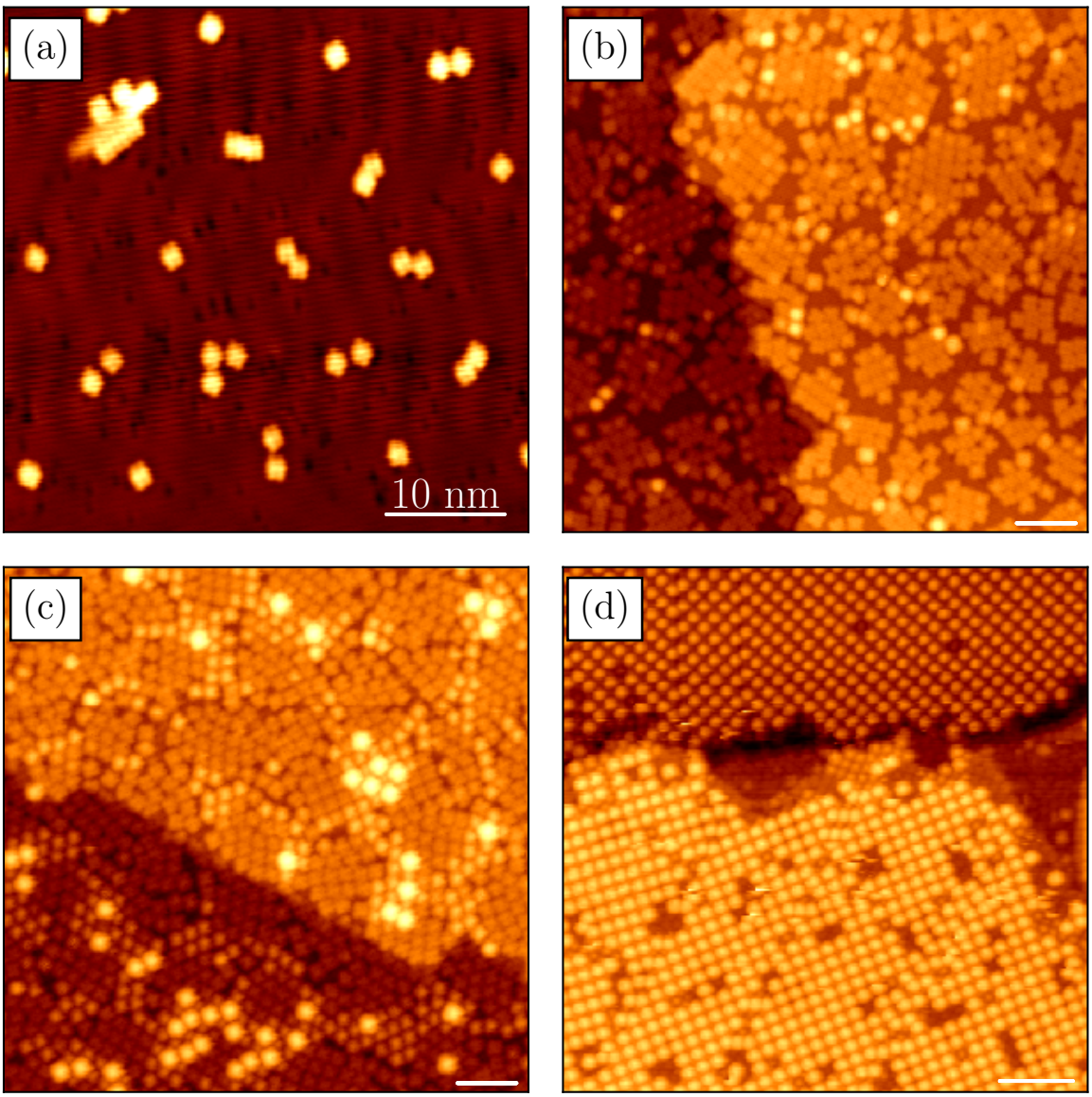

Figure 7.7: *Different coverages of F_{16}CoPc molecules on hBN/Cu(111).* ***(a)*** *0.06 ML,* ***(b)*** *0.69 ML,* ***(c)*** *0.89 ML,* ***(d)*** *1.8 ML ($U = 1$ V, $I = 40$ pA). First layer molecules preferentially adsorb in the pore regions of the hBN/Cu(111) moiré lattice, while the second layer growth starts at the wire regions. All scale bars represent 10 nm.*

At higher coverages the molecules also adsorb at the wire sites (Fig. 7.7 (b),(c)). Noticeably, the second layer molecules (bright features in Fig. 7.7 (c)) preferentially adsorb at the wire regions. The second layer grows as a quasi-square lattice [140], with a lower packing density, compared to the hexagonal close packed ordering of the first layer molecules (c.f. Fig. 7.7 (d),(e)). The second layer molecules adsorb on top of the first layer molecules near the center (c.f. Fig. 7.10).

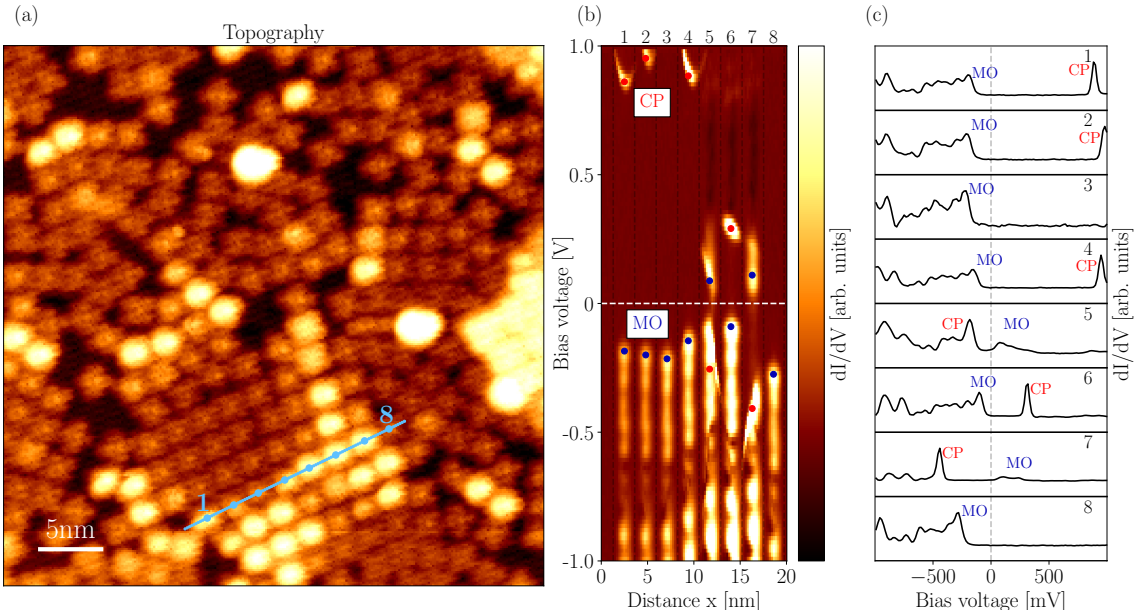

Figure 7.8: *Template induced shift of molecular levels, screening and charging for a sample with high $F_{16}CoPc$ coverage.* ***(a)*** *STM topography image of $F_{16}CoPc$ at 0.8 ML coverage ($U = 1$ V, $I = 20$ pA).* ***(b)*** *Visualization of the color coded intensity of dI/dV spectra along the light blue line in (a) as a function of lateral position (x-axis) and bias voltage (y-axis). The positions of the molecular resonances and charging features are marked with blue and red dots, respectively (tip stabilization parameters: $U_{stab} = 1$ V, $I_{stab} = 20$ pA).* ***(c)*** *Representative dI/dV spectra taken close to the center of each of the eight molecules. The spectra show molecular resonances, i.e., the energies of the molecules, affected by the modulation of the hBN/Cu(111) work function and screening by the neighboring molecules. For the molecules with MO peaks sufficiently close to E_F, charging peaks at the opposite polarity are observed.*

The STM image of a surface with ~ 0.8 ML molecular coverage in Fig. 7.8 (a) recorded at 1 V reveals a brighter appearance of molecules adsorbed at wire regions compared to the ones adsorbed at pore regions. This difference in contrast can be understood by analyzing the dI/dV spectra of the molecular layer. Fig. 7.8 (b) shows spectra taken along the solid blue line in Fig. 7.8 (a), in which the color-coded dI/dV intensity is plotted as a function

of position (x-axis) and bias voltage (y-axis). The color plot portrays separated features along the x-axis, corresponding to the eight molecules along the line. Representative dI/dV spectra for each of these molecules are shown in Fig. 7.8 (c), in which the molecular resonances and the charging peaks are labeled as "MO" and "CP", respectively. In the color plot, the charging-related features (red dots in Fig. 7.8 (b)) exhibit sharp parabola-like characteristics due to their strong energy-dispersion (c.f. Fig. 7.3), while the molecular resonances (blue dots in Fig. 7.8 (b)) give rise to a broader intensity distribution with side peaks. The energies of the MO peaks depend on the spatial position of the respective molecule on the moiré superlattice, *i.e.*, template induced gating (see Fig. 7.1 (c)) and on the molecular environment, *i.e.*, screening. For molecules 1, 2, 4, 5, 6, and 7, exhibiting MO energies close to E_F, charging peaks are observed at the opposite polarity of the MO peaks [57, 126–128, 130, 132]. The ratios between the absolute positions of the MO and CP peaks remain at about $|U_\mathrm{CP}|/|U_\mathrm{MO}| \approx 5$, regardless of whether the CP is observed at occupied or unoccupied states. The MO and CP positions in the spectra for molecule 6 show a deviation from the expected behavior based on the hBN/Cu(111) work function modulation, which might be due to an additional shift caused by impurities in the substrate.

In order to investigate how the charge states of adjacent molecules influence each other, the STM dI/dV and AFM frequency shift (Δf) signals for an island of molecules were spatially mapped (Fig. 7.9). Both channels, simultaneously recorded in constant-height mode at a sample bias $U = 2\,\mathrm{V}$, exhibit characteristic ring-like features, associated with the charging events [129, 130, 132, 141–143]. Both, the dI/dV and Δf vs. U point spectra, taken at the spot marked with a red cross in the maps show sharp features, *i.e.*, charging peaks and dips (labeled "CP"), at the same energy (insets in Fig. 7.9 (b) and (c)) [142]. Analogously, the charging rings coincide for both maps (dI/dV and Δf). A larger number of charging rings can be seen in the Δf channel due to the higher long-range sensitivity of AFM compared to STM. The rings do not exhibit a perfectly circular shape because of the asymmetry of the tip. The sizes of the rings vary – some exceed diameters of 10 nm [141] – depending on the energy position of the molecular resonances. For instance, the molecules marked with red dots exhibit relatively small charging rings that are visible in both the dI/dV and Δf vs. U maps. It is interesting to investigate the intersection of charging rings. A specific example of intersecting charging rings of neighboring molecules is marked by orange arrows in Fig. 7.9 (c) and schematically shown in Fig. 7.9 (d). Within the overlapping area of both charging rings, tip induced gating changes the charge states for both molecules simultaneously, associated with a subtle decrease of both ring radii.

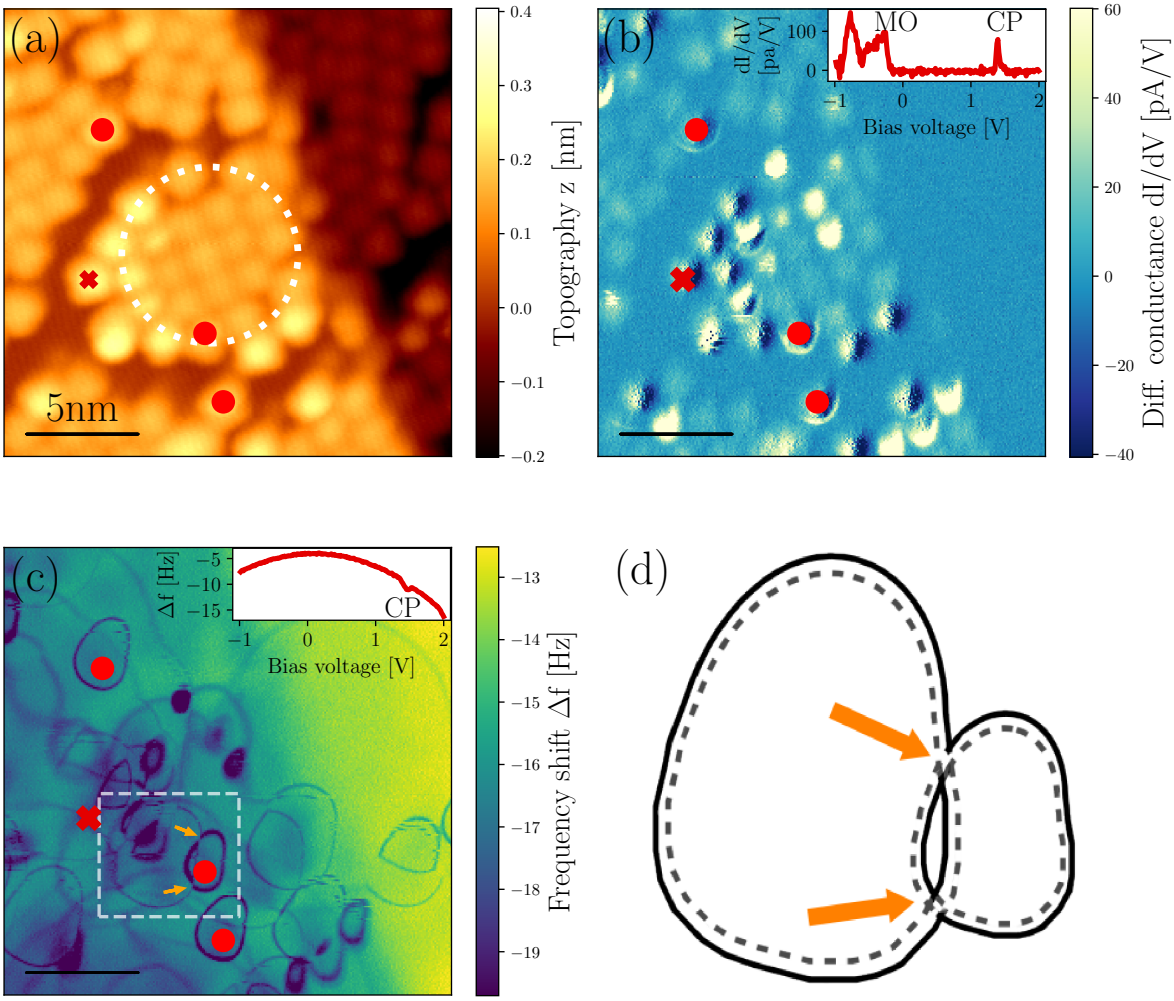

Figure 7.9: *Simultaneous charging events for a high coverage sample.* ***(a)*** *STM topography of a surface with 0.8 ML coverage. The dashed white circle marks the position of a pore area of the moiré lattice ($U = 2$ V, $I = 8$ pA).* ***(b)*** *Differential conductance (dI/dV) and* ***(c)*** *AFM frequency shift (Δf) maps, simultaneously acquired in constant height mode at $U = 2$ V, show charging rings for certain molecules. dI/dV and Δf vs. U spectra (insets in (b) and (c), taken at the position marked with the red cross) show sharp features (labeled "CP") at the same energy, related to charging events ($U_{stab} = 2$ V, $I_{stab} = 5$ pA). Red dots mark positions of three molecules, whose charging rings are visible in both maps in (b) and (c). Orange arrows in (c) mark the intersection of charging rings of two neighboring molecules. In the overlapping area the molecular orbitals of both molecules are shifted across E_F, leading to a small contraction of the ring radii because of an increase of the charging threshold. This effect, occurring in the area, marked with the white rectangle in (c) is schematically shown in* ***(d)****. The orange arrows in (c) and in (d) mark the same intersection.*

This observation indicates that the charging of one molecule increases the charging threshold of the other molecule, shifting the CP to higher energy and thus reducing the ring radius mapped at constant tip height. Nevertheless, this effect of charged neighbors appears to be weaker than template induced gating, tip induce gating or screening.

7.5. Second layer growth

The STM image in Fig. 7.10 (a) shows a bright appearance of second layer molecules with an apparent height of 0.3 nm (at $U = 2\,\mathrm{V}$) relative to the first layer molecules, nearly twice as much as the apparent height of the first layer molecules with reference to the *h*BN/Cu(111).

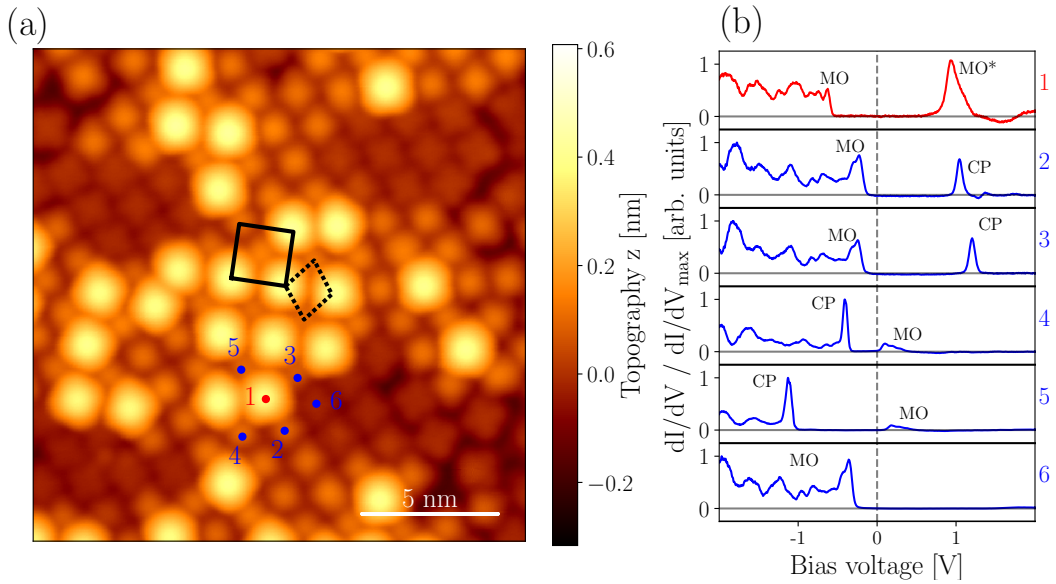

Figure 7.10: *Growth and electronic properties of >1 ML F_{16}CoPc on hBN/Cu(111).* ***(a)*** *Topography of the sample shows bright appearance of molecules adsorbed in the second layer ($U = 2\,V$, $I = 41\,pA$). The black dashed diamond marks the unit cell of the closed packed structure of the first layer molecules, while the black square shows the unit cell of the second layer islands.* ***(b)*** *dI/dV spectra taken at the spots marked in (a) by the colored dots ($U_{stab} = 2\,V$, $I_{stab} = 41\,pA$). The colors represent different types of molecules: red - second layer molecule exhibiting two peaks related to molecular resonances (labeled "MO" and "MO*"), blue - first layer molecules with charging peak ("CP") visible in the spectrum for molecules $2 - 5$.*

The packing density decreases in the second layer, as the second layer molecules adsorb in a quasi-square lattice, instead of a hexagonal closed packed lattice, as it is the case for the first layer (c.f. black square and black diamond in Fig. 7.10 (a)). dI/dV spectroscopy of

the first layer molecules reveals template and screening induced shifts of the MO-related peaks, as well as charging peaks for some of the molecules in the first layer (molecules $2-6$ in Fig. 7.10 (b)). The second layer molecule (molecule 1 in Fig. 7.10 (b)) exhibits two peaks (at $-0.7\,\mathrm{V}$ and at $\sim 1\,\mathrm{V}$) associated with molecular orbitals. This assignment is based on the absence of a significant dependence of the peak position on the tip-sample distance or applied bias – such a dispersion would be expected for charging peaks [57, 126–129, 131, 132, 136].

7.6. DFT calculations of CO adsorption on F_{16}CoPc

The nucleation of second layer F_{16}CoPc molecules starts on first layer molecules adsorbed on the wire regions of the *h*BN/Cu(111) moiré, shown in Fig. 7.7. This is in contrast to the adsorption of the first layer molecules, which prefer to adsorb on the pore regions. One reason for this could be the different charge states of the first layer molecules on the different sites of the moiré. To achieve a general idea about the adsorption energies of molecules on differently charged F_{16}CoPc, spin-polarized DFT calculations were performed. The projector-augmented plane wave method [144] and a plane wave basis set with maximum kinetic energy of 400 eV were used to relax the structures, until the acting forces were smaller than $0.05\,\mathrm{eV/Å}$ and the energy-change is less than $1\,\mu\mathrm{eV}$. The Perdew Burke Ernzerhof (PBE) exchange-correlation potential [94] (implemented in VASP [97, 145, 146]) was employed and long-range vdW interactions were included, as proposed by the DFT-D3 approach of Grimme *et al.* [147]. The optimization was executed at the gamma point of the Brillouin zone. The total tetragonal cell, used for the calculation, has a real-space size of $(20 \times 20 \times 25)\,\mathrm{Å}^3$.

The F_{16}CoPc was relaxed in the gas phase for two scenarios, as shown in Fig. 7.11. In the first scenario, a CO was placed far away from the F_{16}CoPc, with a C-Co distance of 1.1 nm, to exclude interactions between the CO and the F_{16}CoPc molecule. In the other scenario, the CO was placed close to the central Co, resulting in a C-Co distance was 0.2 nm, where the CO and the F_{16}CoPc molecule interact. These two scenarios were relaxed for three different numbers of electrons included in the system: a neutral system, a single negatively charged system and a single positively charged system.

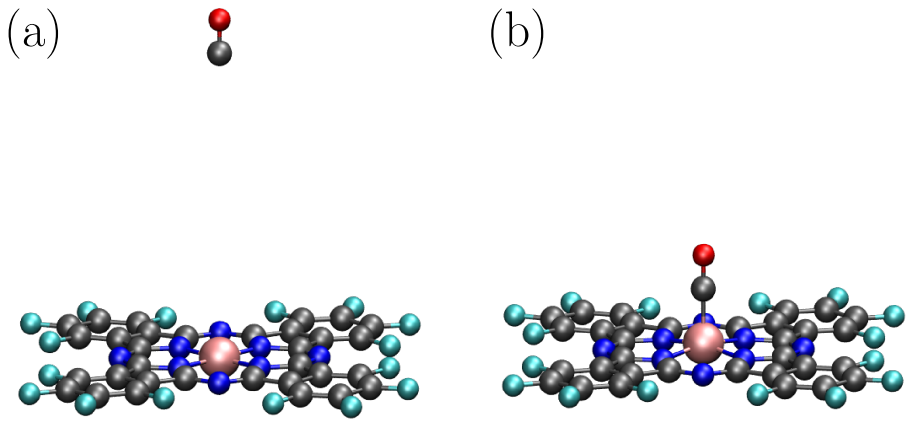

Figure 7.11: *Calculated adsorption of CO on F_{16}CoPc in the gas phase. In* ***(a)*** *the CO is far from the F_{16}CoPc, i.e., a C-Co distance of 1.1 nm and in* ***(b)*** *the C-Co distance between the CO and the F_{16}CoPc is reduced to 0.2 nm so that the CO can bind to the cobalt atom.*

Charge state [e]	Ground state energy [eV]		Adsorption energy [eV]
	CO far	CO close	
0	−439.230	−440.037	−0.806
+1	−433.429	−434.200	−0.771
-1	−443.425	−443.413	0.012

Table 7.1: *Ground state energies of the different scenarios (CO far, CO close) and the different charge states of the system (neutral, negatively charged, positively charged) and the resulting adsorption energy.*

The adsorption energy of the CO on the F_{16}CoPc can be calculated by the ground state energies of the two scenarios for each charge state of the system. These energies are listed in Tab. 7.1. It should be noted that an adsorption of CO on a neutral F_{16}CoPc is energetically much more favorable (energy gain of 0.81 eV) than on a negatively charged F_{16}CoPc (energy loss of 0.01 eV) and also favorable than on a positively charged F_{16}CoPc (energy gain of 0.77 eV). Since the LUMO of molecules, adsorbed on the wire regions, is unoccupied, these uncharged molecules are predicted to be the preferential sites for the adsorption of CO.

If this tendency pertains not only to small molecules like CO, but also for larger ones like a second F_{16}CoPc, than this could be a possible explanation for the nucleation of the second layer F_{16}CoPc molecules on the wire regions of the moiré.

7.7. Comparison to F_{16}CoPc on *h*BN/Ir(111)

While the moiré of *h*BN/Cu(111) shows a modulation of the work function between pore and wire regions from 3.8 eV to 4.1 eV [38, 56], a stronger modulation of the work functions between pore and wire is observed for *h*BN/Ir(111): 4.2 eV and 4.6 eV for pore and wire, respectively [38, 61]. Furthermore, there is also a stronger geometric corrugation of the *h*BN/Ir(111) compared to *h*BN/Cu(111). Different superstructure sizes are observed on *h*BN/Cu(111), depending on the angle between the *h*BN and the supporting Cu(111) surface [56], while for *h*BN/Ir(111) one superstructure size of 2.9 nm prevails [58]. This distance is large enough to separate F_{16}CoPc molecules, preferentially adsorbed on the pore regions of the moiré and therefore decreasing intermolecular interactions. Nonetheless, the superstructure size is still small enough that only one Pc-like molecule fits into one pore. As a result of this, for a coverage larger than one molecule per pore, the surplus molecules adsorb on the wire regions. Taking into account the vacuum level alignment of molecule and substrate, the F_{16}CoPc should be differently charged on the pore and wire regions, as the LUMO of the molecule, located at 4.5 eV below the vacuum level in the gas phase, would be occupied at the pore sites and unoccupied at the wire site [38, 61, 135].

Low coverage

The coverage of F_{16}CoPc on *h*BN/Ir(111) of $\sim 25\,\%$ is equal to ca. one molecule per pore (see Fig. 7.12). In the STM images of Fig. 7.12 (a)-(c) three different kinds of alignments are observed (blue, red, green), rotated by 30° with respect to each other. In these three alignments, one of the two molecular axes aligns with one of the three high symmetry directions of the moiré, as indicated by the colored crosses. Since the moiré lattice is aligned with the *h*BN lattice [58], the molecules are also aligned with the high symmetry directions of the *h*BN. The statistics regarding the total number of blue, red or green alignments in Fig. 7.12 (d) indicates a weak tendency, that one alignment, *i.e.*, the red marked one, is a bit more favored. Nevertheless, a random distribution of alignments is still more reasonable, since all three alignments should be energetically equal. This deviation from the random distribution could be explained by the number of considered areas and molecules, which might be too small. The averaged number of relatively aligned neighboring molecules in the different alignments is plotted in Fig. 7.12 (e). The correlation between the alignments of one molecule and the alignment of its adjacent molecules is tested. A weak correlation can be found: since most molecules are in a "red alignment", most neighboring molecules are also red aligned, independent of the alignment of

the central molecule. But in contrast to this, even though, for example, the blue aligned molecules are the least present on the surface, the number of equally aligned neighbors is relatively high. This can be observed in the relative number of neighboring molecules in Fig. 7.12 (f), representing the number of neighboring molecules divided by the relative amount of molecules in the respective alignment.

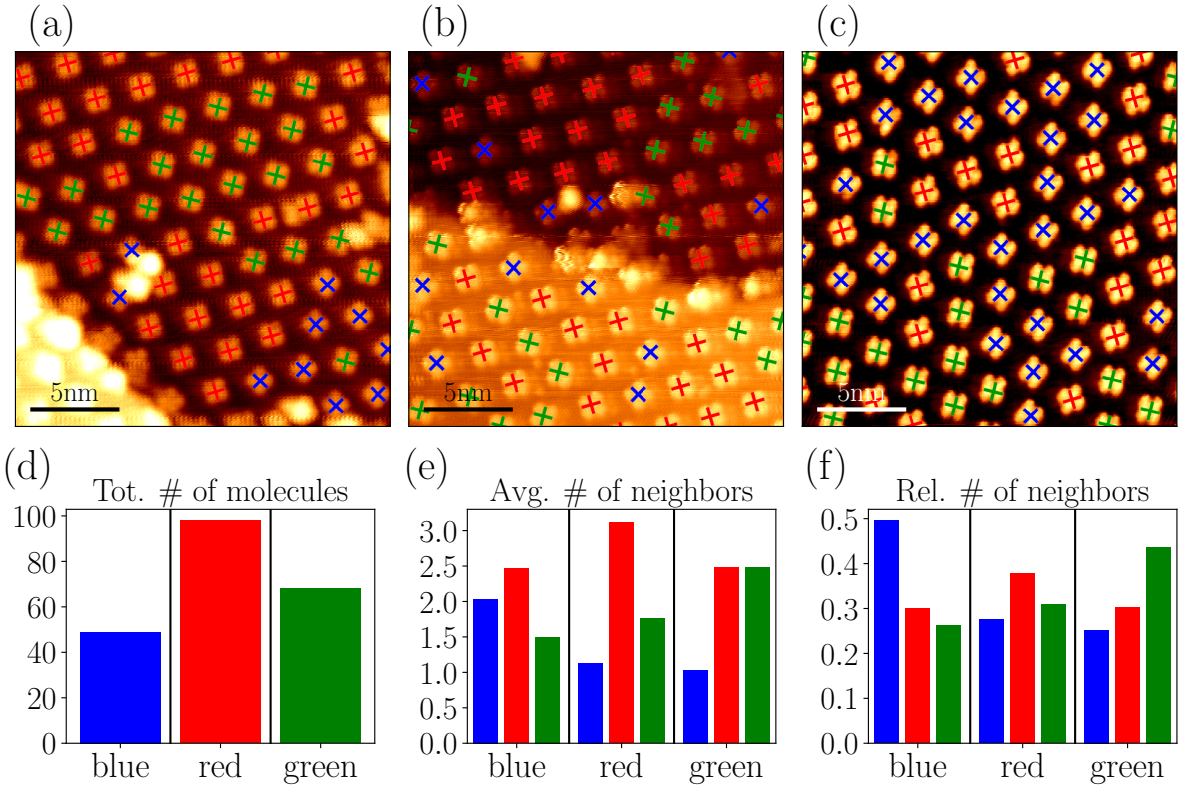

Figure 7.12: *Low coverage of F_{16}CoPc on hBN/Ir(111). The hBN/Ir(111) sample was prepared as described in section 6.2. The F_{16}CoPc molecules were evaporated via organic molecular beam epitaxy (OMBE) at $T_{mol} = 420°C$ for 26 min onto the room temperature hBN/Ir(111) sample, followed by a post-annealing to 150°C for 3 min. In* **(a)** *-* **(c)** *three STM topographies show the molecules, adsorbing on the pore regions of the moiré ($U = 1\,V$, $I = 0.1\,nA$). Three different alignments, i.e., blue, red and green, are observed, where one of the high symmetry axes of the molecule aligns with the high symmetry directions of the moiré. In* **(d)** *the statistics of the total number of molecules of each alignment is shown. The statistic in* **(e)** *shows the averaged number of adjacent molecules in the different alignments. The relative number of neighboring molecules in the different alignments in* **(f)**, *i.e., the averaged number of neighbors divided by the relative number of molecules in the respective alignment, shows the correlation between the alignment of a molecule and the alignments of the adjacent molecules.*

The same trend can be seen for the red and green aligned molecules, where the number of equally aligned neighbors is the highest. The relative number of equally aligned neighbors is in average 1.54 times larger than the number of differently aligned neighbors. This means that the interaction between the molecules is strong enough to still be present at the neighboring pore site and thus influencing the alignment of the molecule. This interaction could be a repulsive interaction between the outer fluorine atoms.

High coverage

An increase of the molecular coverage to $\sim 65\,\%$ leads to additional adsorption of molecules in the wire regions, shown in Fig. 7.13.

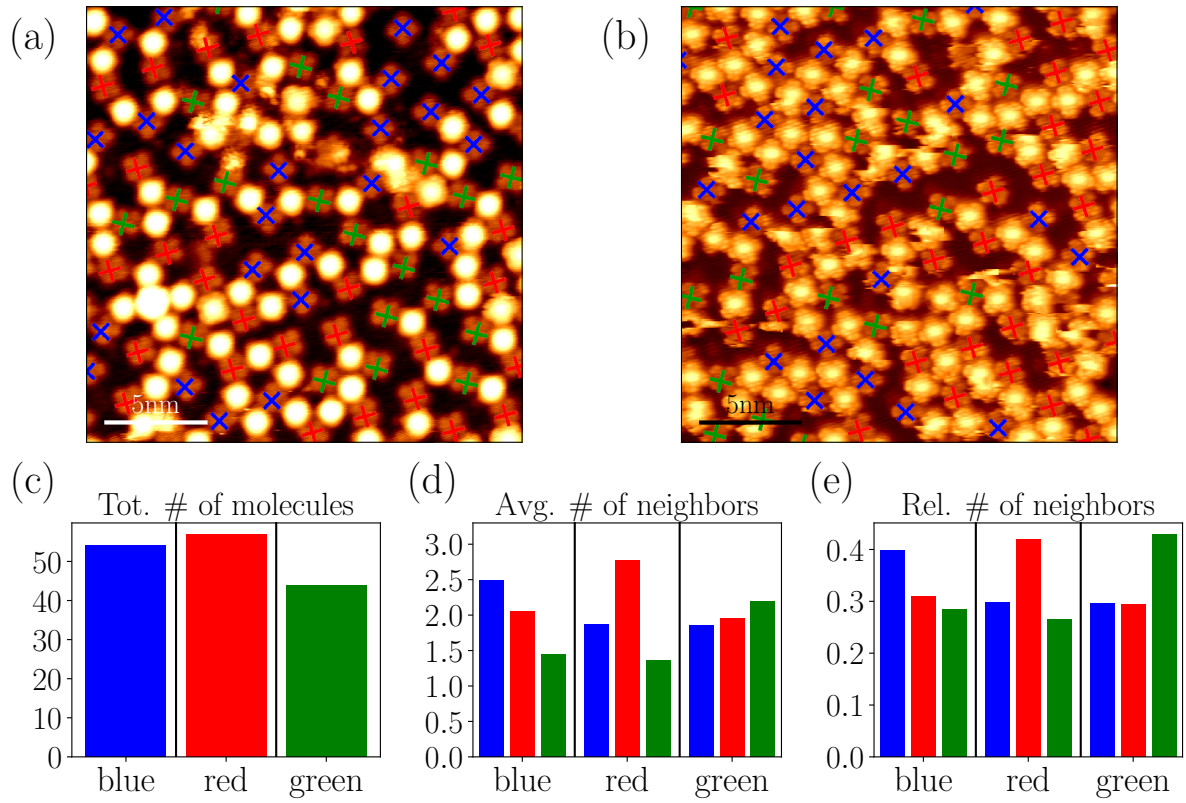

Figure 7.13: *High coverage of $F_{16}CoPc$ on hBN/Ir(111). In* **(a)** *and* **(b)** *it can be seen that the surplus molecules compared to Fig. 7.12 adsorb on the wire regions and are brighter in contrast ((a): $U = 1\,V$, $I = 0.1\,nA$; (b): $U = 1.5\,V$, $I = 0.1\,nA$). The statistic, regarding the total number of blue, red and green aligned molecules in the pore regions is shown in* **(c)** *and the averaged number of neighboring molecules with in the different alignments adsorbed in pore regions is shown in* **(d)**. *The relative number of adjacent molecules in the different alignments can be seen in* **(e)**, *showing the correlation between the alignment of the central molecule and the alignment of its neighbors.*

These additional molecules appear brighter as the ones adsorbed at the pore region (see Fig. 7.13 (a), (b)). This difference in appearance will be explained later. No dominant alignment is observed (c.f. Fig. 7.13 (c)), supporting the hypothesis of equal adsorption energies for the three alignments, as proposed for the low coverage. Furthermore, the correlation between the alignments of adjacent molecules adsorbed on pore regions – shown in Fig. 7.13 (d), (e) – is similar to the correlation observed for the low molecular coverage. The amount of neighboring molecules adsorbed in the pore is in all three cases, *i.e.*, blue, red or green alignment, the highest for the same alignment. Now the relative number of equally aligned molecules is in average only 1.43 times larger than the number of differently aligned neighbors, which can be explained by steric hindrance by the molecules adsorbed on the wire regions. Nevertheless, the correlation shows that the intermolecular interaction between the molecules adsorbed on the pore regions of the moiré is minimally reduced, due to an increased coverage.

Spectroscopy of F_{16}CoPc adsorbed on pore & wire

The difference in the appearance of the molecules adsorbed in pore and wire regions could origin either from a difference in geometry or from a difference in the LDOS. Since the same molecules were used in both experiments, a difference in the molecular geometry is unlikely. To understand this difference in appearance, arising from a difference in the molecular LDOS, STS measurements were conducted as shown in Fig. 7.14. The spectra of Fig. 7.14 (b), (c) were recorded at the spots marked with dots in the corresponding color in the STM topography in Fig. 7.14 (a). As a result the prominent resonance at occupied states of the molecule adsorbed on the pore site (blue, (b)), is far below E_F at $-0.81\,\mathrm{V}$ and is identified as the gas-phase LUMO (called "MO"). In comparison to this, the MO of the molecule adsorbed on the wire region (red, (c)) is located above E_F at $0.23\,\mathrm{V}$. Additionally to the MO feature a CP is observed at $\sim -1.1\,\mathrm{V}$. Since the position of the molecule on the moiré is not always exactly at the center of the pore/wire, the energetic position of the MOs can vary by $\sim 0.1\,\mathrm{V}$. The observed difference in the appearance in the STM images at the used bias voltage of $U = 1.5\,\mathrm{V}$ can now be explained by the presence or absence of a MO in the range of unoccupied states. The molecule on the wire region appears bright since the MO is in this case located above E_F. The molecule adsorbed on the pore region exhibits a lower intensity as a result of the MO being below E_F and due to a reduced DOS in the region of unoccupied states.
Due to this difference in the energetic position of the MO, the molecules adsorbed on the varying regions of the moiré are differently charged. By assigning this MO to the LUMO

of the gas phase molecule, as implemented for F_{16}CoPc/hBN/Cu(111), the molecule on the pore would be negatively charged and the one on the wire would be neutral [38, 61, 135]. This shift of $\sim 1.0\,\mathrm{V}$ can be partially explained by the template induced gating (c.f. section 7.1). Nevertheless, since the difference in the work function between pore and wire is only 0.4 V, the template induced gating can't induce such a huge difference in the positions of the MOs. Another effect, increasing this difference in the energetic positioning of the MOs is the charging energy. This additional energy depends on the interaction between the electrons in the molecule and an electron, added to or removed from the molecule. Since the molecular orbitals can respond differently to an added or removed charge, depending on the initial charge of the orbital, this charging energy can cause a non-linear change in the positions of MOs [57, 128, 148].
Schulz *et al.* demonstrated a very similar behavior for CoPc on hBN/Ir(111) [114]. The positions of the MOs depend on the adsorption site. A difference of the MO for the two adsorption sites of 1.1 V is reported. The difference to F_{16}CoPc/hBN/Ir(111) is the absolute position of the MOs. The orbitals of the unfluorinated CoPc molecule are located higher in energy ($U_{\mathrm{CoPc,MO,pore}} = -0.1\,\mathrm{V}$, $U_{\mathrm{CoPc,MO,wire}} = 0.9\,\mathrm{V}$ [114]) compared to the ones of the fluorinated molecule ($U_{\mathrm{F_{16}CoPc,MO,pore}} = -0.8\,\mathrm{V}$, $U_{\mathrm{F_{16}CoPc,MO,wire}} = 0.2\,\mathrm{V}$). This energetic shift of the orbitals, due to the fluorination, is in accordance with previous studies [135, 149].

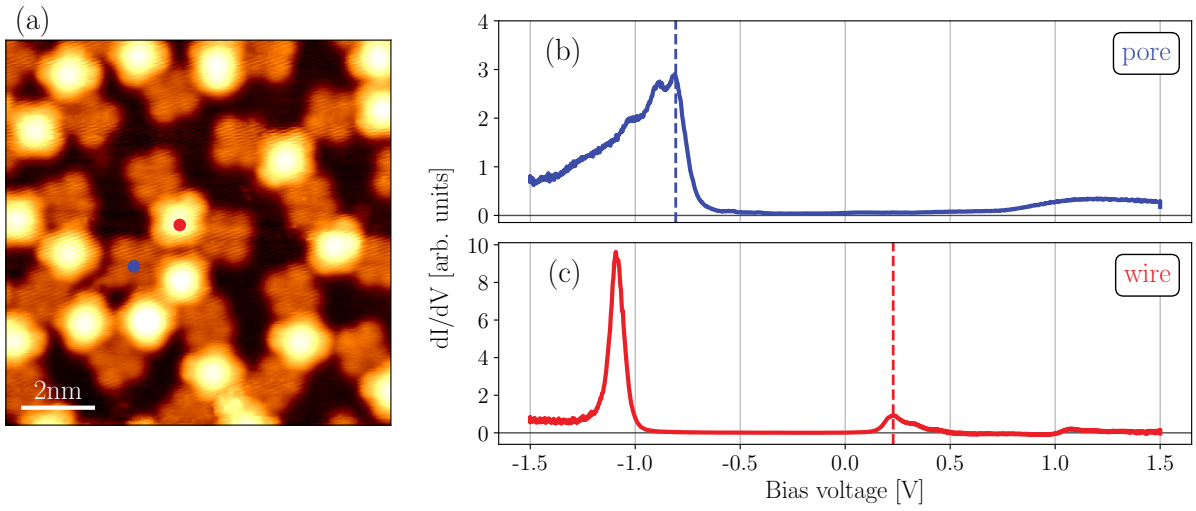

Figure 7.14: *STS measurements of F_{16}CoPc on pore and wire sites of the hBN/Ir(111) moiré. In* ***(a)*** *the topography of a sample with a coverage of $>$ 1 Molecule / pore is shown ($U = 1.5\,V$, $I = 0.3\,nA$). The spectra, taken at the blue (pore) / red (wire) marked positions in (a) are shown in* ***(b)/(c)****, respectively ($U_{\mathrm{stab}} = 1.5\,V$, $I_{\mathrm{stab}} = 0.3\,nA$). The MOs are marked in the spectra by dashed lines. In (c) a CP can be seen at $\sim -1.1\,V$ (c.f. section 7.2).*

7.8. Summary and outlook

The STM manipulation experiments presented in Fig. 7.2 display that the level alignment of an individual molecule can be changed by lateral repositioning on the *h*BN/Cu(111) work function template. This process is reversible. Previously, such pronounced energy shifts of MOs were only reported for molecular aggregates and films [38], without the possibility to induce and monitor template-induced modifications on the very same molecule. The magnitude of the MO shift on *h*BN/Cu(111) and, more noticeably, on *h*BN/Ir(111), exceeds the one reported for dense-packed F_{16}CoPc arrays on graphene/Ir(111) [149], reflecting distinct interface and template properties [38]. It should be pointed out that an unequivocal assignment of MO features, observed in STS measurements, to specific MOs, calculated for gas phase Pcs, is not straightforward, e.g. due to interface effects and many-body interactions [114, 150, 151]. Even with orbital-resolved STM imaging at hand, the assignment is hampered by the dependence of the calculated orbital sequence on subtle details of the employed theoretical method [149]. Nonetheless, as mentioned above, the energy position of the occupied MO of individual F_{16}CoPc units on *h*BN/Cu(111) and on *h*BN/Ir(111) indicate that this state is derived from the LUMO of the free molecule. This identification is also valid for a comparison of F_{16}CoPc/*h*BN/Ir(111) with CoPc/*h*BN/Ir(111) [114], where the observed MOs are rigidly shifted in energy with respect to the ones shown in this section due to the fluorination. An identification of the observed resonance with the highest occupied molecular orbital (HOMO) of the free molecule would request a pronounced interface dipole or unrealistic values of the $F_1$6CoPcs ionization potential. Thus, we assume electron transfer to F_{16}CoPc occurring upon adsorption on *h*BN/Cu(111), even though details of the process [152] (such as the amount of charge transferred) are elusive to our experimental observations (e.g. no resonances associated with singly (un)occupied MOs were identified by STS).

The effect of the local environment on the F_{16}CoPc's electronic signature, as resolved by STS, was modeled considering electrostatic screening of the charge (added/removed to the molecule during STS) by polarizable neighbors [124, 153]. Our model quantitatively agrees with the experimentally observed shifts of molecular resonance energies, even though additional parameters, such as the inhomogeneous charge distribution within the molecules, non-covalent intermolecular interactions, changes in adsorption geometry and distance, as well as interaction with the buried metal substrate, are not taken into account. Accordingly, this simple model captures the key findings of the experiments, in line with reports on related molecular systems on ultra-thin insulating supports [124, 151]. Additional and competing effects, such as a change in the local work function, induced

by adjacent molecules or a Coulombic field due to surrounding charges yield a shift of occupied MOs towards E_F with increasing number of molecular neighbors. All these effects would shift both occupied and unoccupied molecular resonances upwards (*i.e.*, occupied MOs towards E_F, unoccupied MOs away from E_F), in contrast to screening, yielding an inverted shift (*i.e.*, occupied and unoccupied MOs shift towards E_F). As we could not observe the first unoccupied MO in our experiment, we have no information of the evolution of the F_{16}CoPc's electronic gap with increasing number of neighbors. Thus, one cannot rule out a contribution of these effects.
Tip-induced gating, resulting in CP features in STS data of metal-organic complexes on ultra-thin spacer layers, is well documented in literature [57, 127–130, 134, 143]. Our results reveal how Δf mapping can be applied to study complex situations with multiple molecules charged by the electric field of a tip. Compared to template- and tip-induced gating, as well as screening by neighboring molecules, charging of adjacent molecules was found to exert a much smaller influence on the molecular level alignment. Such Δf mapping experiments open pathways to explore and control charging thresholds in molecular architectures.

To summarize, for the investigated system and the employed scan parameters, the three investigated effects – template induced gating, tip induced gating and screening – can cause shifts of the measured positions of the molecular resonances in the dI/dV spectra of up to 1 V on hBN/Cu(111). Each of these effects contributes additively and in an approximately similar amount ($\sim$ 0.3 V) to the cumulative shift. The relative contributions of template and tip induced gating can further be tuned by using a different substrate (such as hBN/Ir(111)) with a larger work function modulation [38], as well as by a change of tip height and sample bias (under the constraints of a stable tip-sample junction). Moreover, growth of additional layers of molecules is expected to further increase the screening by molecular neighbors. The molecular response to electrostatic gating can be controlled by the adsorption height (for molecules in additional layers, as well as by chemical functionalization). Additionally, the electronic modulation in F_{16}CoPc monolayers on hBN supports might result in a spatially patterned chemical reactivity (e.g. towards small gaseous adsorbates, as it was calculated for CO) and can template the growth of thin molecular films, as evidenced by the nucleation of second layer F_{16}CoPc in the wire regions of F_{16}CoPc/hBN/Cu(111).

To demonstrate the templating properties of the F_{16}CoPc on hBN/Cu(111) and on hBN/Ir(111) for adsorbates like CO or other tetrapyrrolic molecules, further experiments need to be done. In addition, the growth of a well ordered monolayer of molecules needs to be achieved, as this would lead to a larger shift of the molecular orbitals due to an enhanced screening.

8. Array formation of Ce-based multideckers on *h*BN/Ir(111)

Metal-organic multidecker molecules on surfaces have gained a lot of interest during the past years as these molecules can be used in applications such as organic solar cells, nano-electronics or single molecule magnets [6, 12, 13, 27, 64, 65, 154–163]. The use of individual spins of single molecules for data storage generated increasing interest in science as well as in the industry. Since the molecular magnetism is influenced by the supporting metal substrate upon adsorption induced hybridization [29], it is necessary to decouple these molecules from the metallic substrate to study their unperturbed (magnetic) properties. This decoupling from the metal – in this case Ir(111) – can, for example, be achieved by a single layer of *h*BN, resulting in a decreased influence of the substrate on the molecule in terms of a reduced hybridization [29, 38]. Another advantage of *h*BN/Ir(111) is its moiré pattern that can be used as a template, trapping one Pc per pore-site [38, 57, 58, 114, 115], leading to an array formation of molecules with the periodicity of the moiré superlattice (c.f. Fig. 7.12).

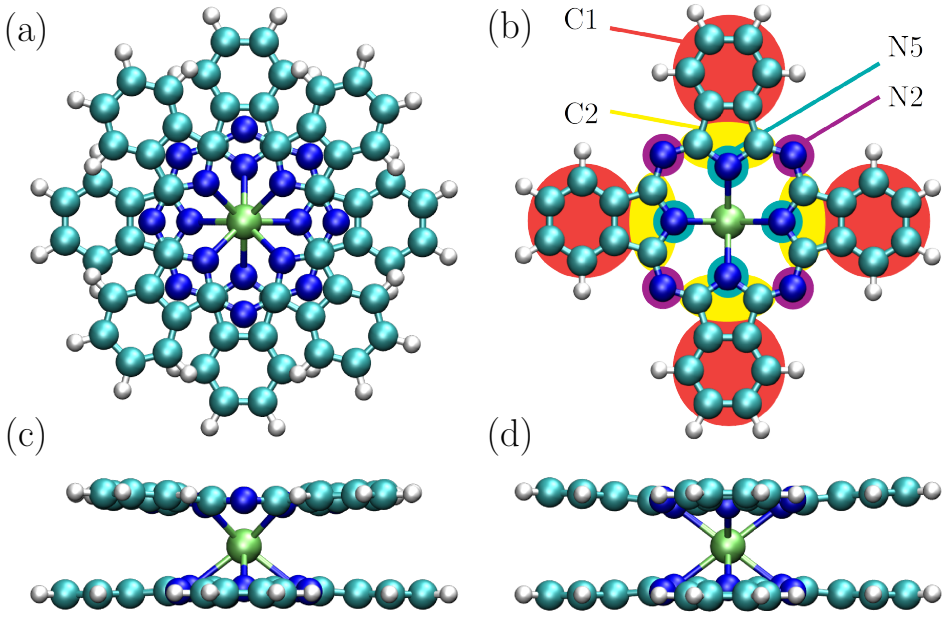

Figure 8.1: *Ball and stick model of $CePc_2$. The two main configurations of the $CePc_2$ are the following: the rotated one, shown in* **(a)**/**(c)** *with the top/side view and the parallel one, shown in* **(b)** *and* **(d)**. *In the top view of the parallel configuration in (b), the different types of carbon and nitrogen atoms are marked with different colors.*

Regarding multidecker compounds, we will focus on doubledecker complexes formed by two Pc molecules and a Ce atom in-between them. The choice of cerium as the central metal atom of these complexes is motivated by the two different oxidation states, this lanthanide can exhibit, *i.e.*, +III and +IV, influencing also the molecular magnetism. Since the dehydrogenated Pc has an oxidation state of -II, the total $CePc_2$ can be in a non-magnetic state, if the Ce is in the oxidation state +IV. If the oxidation state of the cerium is +III, one electron is unpaired, inducing a spin in the molecule. The Ce-based complexes were studied on the *h*BN/Ir(111) surface. Since the corrugation of the individual Pcs in such complexes was found to be rather small [65, 76], the low Pc-Pc interactions inside a doubledecker allows, in principle, multiple in plane rotations of the Pcs, with respect to each other (c.f. section 10.1). Two possible configurations of this molecule are illustrated in Fig. 8.1. In the first case the upper Pc is rotated by 45°, with respect to the bottom one (called rotated) and in the second case both Pcs are located on top of each other (called parallel). These two configurations will be implemented to define the molecular structure, especially in the theoretical DFT calculations, supporting the experimentally obtained results. In the first experiments, pre-synthesized molecules were evaporated onto the *h*BN/Ir(111) surface. For obtaining a more uniform and larger covered surface, Ce-based multidecker molecules were also synthesized in-situ.

8.1. Adsorption of pre-synthesized $CePc_2$ molecules on *h*BN/Ir(111)

The adsorbed molecules on the *h*BN/Ir(111) sample reveal two different appearances (see Fig. 8.2). (i) Rectangular shaped islands (Fig. 8.2 (a)) consisting of molecules, each exhibiting a 4-fold symmetry (c.f. zoom-in in Fig. 8.2 (d), showing a close-up of the grey marked area in (a) with the superimposed molecular models). Eight lobes are visible at the edge of the molecule and a cross-like structure in its center. The apparent height of these islands ($\sim 1.08\,\text{nm}$ at the used scanning parameters, see linescan in Fig. 8.2 (e)), indicates that they consist of Ce_2Pc_3 tripledeckers. The molecules arrange in a square lattice with a periodicity of $\sim 1.4\,\text{nm}$, as it is indicated by the faint green square in Fig. 8.2 (d). The molecules itself are rotated by $\sim 26°$ with respect to the square lattice. (ii) In addition to the islands, individual molecular units can be observed (see Fig. 8.2 (b), labeled as 1 in light-green). The apparent height of these units, adsorbed only in the pore regions of the moiré, of $\sim 0.69\,\text{nm}$ (c.f. Fig. 8.2 (f)), indicates that these molecular units are $CePc_2$ doubledeckers. The appearance of the doubledeckers, at a bias voltage of $|U| \geq 1.0\,V$, is

not as sharp as for the tripledeckers, indicating that these individual molecules feature dynamic effects at the time scale of the STM measurement. This movement could be a rotation of the upper Pc, leading to a dounut shaped form, as it is indeed observed. The bright outer rim is presumably a superposition of the bright lobes, which are illustrated in Fig. 8.2 (d).

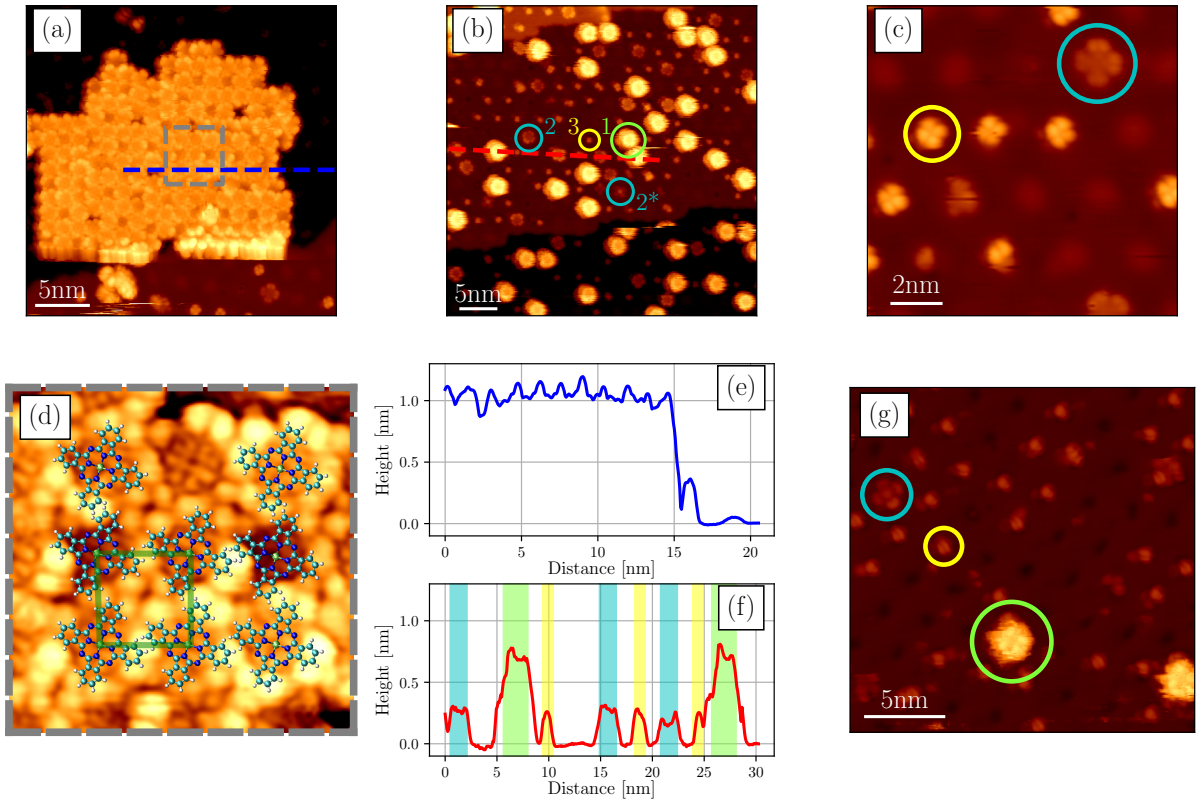

Figure 8.2: *Adsorption of $CePc_2$ on hBN/Ir(111). The $CePc_2$ molecules were deposited at $570-580°C$ for 60 min onto the hBN/Ir(111) sample (the hBN monolayer was grown as described in section 6.2), kept at 230°C. An island of Ce_2Pc_3 tripledeckers can be seen in* ***(a)*** *($U = 3\,V$, $I = 0.1\,nA$). The zoom-in of the grey marked area is shown with different contrast in* ***(d)*** *($U = 3\,V$, $I = 0.1\,nA$). The ball-and-stick models indicate the molecular orientation and the green square indicates the lattice, formed by the tripledeckers. Individual $CePc_2$ doubledecker, adsorbed on the pore regions of the moiré, are shown in* ***(b)*** *($U = 1.5\,V$, $I = 20\,pA$). Different types of molecules are present on the surface, labeled as 1: doubledecker (light green), 2/2*: Pc/CePc (cyan), 3: fragment (yellow). The linescans along the blue/red dashed lines in (a)/(b), are illustrated in* ***(e)/(f)****. In the linescan in (f) the different kinds of molecules are marked with the corresponding color. A close-up of the smaller fragments on the surface is shown in* ***(c)*** *($U = 3.5\,V$, $I = 50\,pA$). In* ***(g)*** *all three kinds of molecules are shown for a negative bias voltage of $U = -1\,V$ ($I = 0.1\,nA$).*

The fact that no doubledecker islands are observed indicates a stronger intermolecular interactions between the tripledeckers, overcoming the adsorption preferences on the templating substrate. This can be implied by the increased lateral, intermolecular vdW-interactions between the tripledeckers. The height based assignment of double- and tripledeckers is supported by literature values for different kind of tetrapyrrole-multideckers (see Tab. 8.1).

Molecule	Substrate	Height [nm]	Reference
$TbPc_2$	Ag(111)	0.62	[157]
$TbPc_2$	Ag(111)	0.4	[76]
$TbPc_2$	Cu(111)	0.3	[164]
$TbPc_2$	Au(111)	0.4	[160]
Tb_2Pc_3	Ag(111)	0.92	[157]
$CeTPP_2$	Ag(111)	0.6	[64]
Ce_2TPP_3	Ag(111)	0.94	[64]
YPc_2	Au(111)	0.46	[165]
Y_2Pc_3	Au(111)	0.55	[166]
$CePc_2$	*h*BN/Ir(111)	0.69	section 8.1
Ce_2Pc_3	*h*BN/Ir(111)	1.08	section 8.1
$CePc_2$	Ag(111)	0.63	section 8.2

Table 8.1: *Heights of double- and tripledecker molecules from literature and from the experiments shown in section 8.1 and section 8.2.*

Beside the double- and tripledeckers, additional species are also present on the surface, appearing less high and showing a smaller footprint than the multideckers. Species 2 and 2^* (colored in cyan) are identified as single Pc (dark center) and CePc (bright center) [76], respectively, with an apparent height of about 0.27 nm (see blue areas below the linescan in Fig. 8.2 (f)). The height difference between Pc and doubledecker can be calculated to $h_{CePc_2} - h_{Pc} = 0.42\,\text{nm}$ and between double- and tripledecker to $h_{Ce_2Pc_3} - h_{CePc_2} = 0.39\,\text{nm}$, thus corroborating the interpretation that the island in Fig. 8.2 (a) consists of tripledeckers, while the individual bright molecules in Fig. 8.2 (b) are doubledeckers. The second smaller species, labeled as 3 and colored in yellow, exhibts a comparable height as the Pc of about 0.23 nm. These molecules feature four individual lobes at the given bias voltage of 3.5 V (Fig. 8.2 (c)). The size of the molecules is roughly a quarter of a single Pc, leading to the assumption this species can be assigned to fragments of single Pcs. The reason for their presence on the surface could be the unusual high evaporation temperature of the $CePc_2$ doubledeckers of 580°C. At this temperature, the $CePc_2$ molecules could break apart and possibly fragment into units, even smaller than a Pc or a CePc. The resulting

fragments could be products of a decomposed Pc, as observed in mass spectrometry by Achar *et al.* [66]. These fragments will be reviewed in more detail in section 9. At a negative bias voltage, the molecules appear distinctly different (Fig. 8.2 (g)). The CePc (light blue) shows now four instead of eight outer lobes and a protrusion at the center. The $CePc_2$ (green) appears quite blurred but four lobes are discernible.

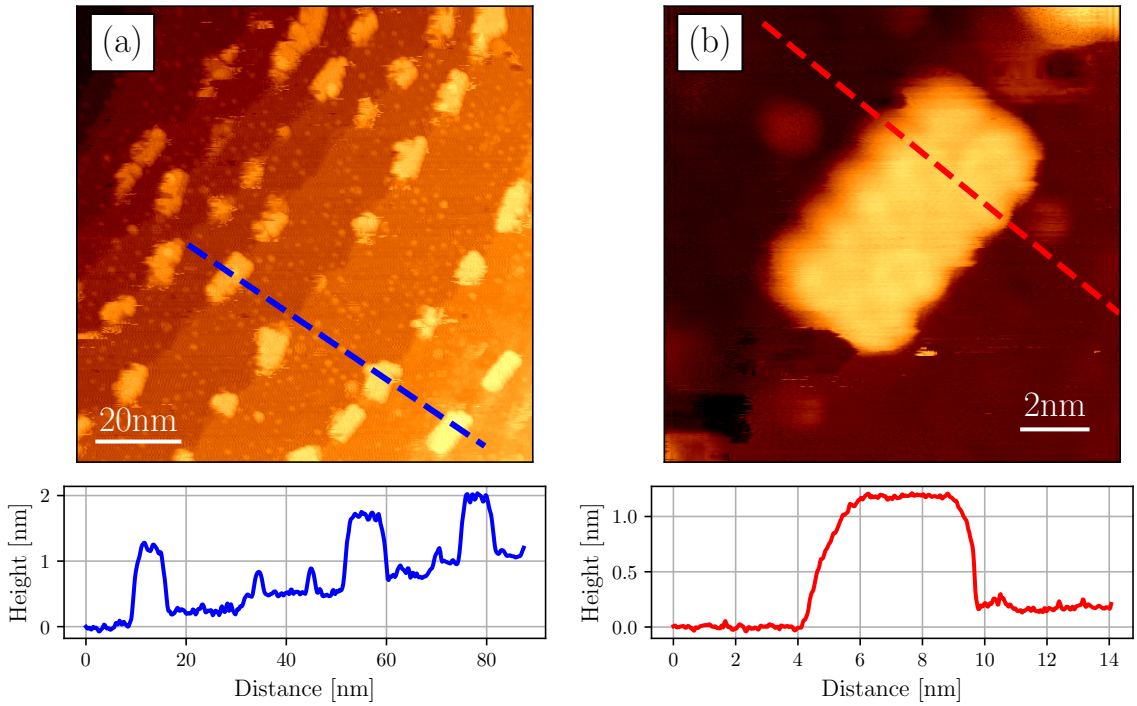

Figure 8.3: *Room temperature measurements of Ce-based multideckers on hBN/Ir(111). In* ***(a)*** *an overview with multiple terraces and Ce_2Pc_3 islands is shown ($U = 2.5\,V$, $I = 32\,pA$). A close-up of such an island is shown in* ***(b)*** *($U = 3\,V$, $I = 32\,pA$).*

To investigate the mobility of the observed molecules, *i.e.*, the double- and tripledeckers as well as the fragments on the *h*BN/Ir(111) at temperatures higher than 5 K, the sample was measured at room temperature. The result is illustrated in Fig. 8.3. An overview of the surface is shown in Fig. 8.3 (a) with multiple terraces and islands. The rectangular shaped islands are identified as Ce_2Pc_3 tripledecker islands based on their apparent height of about 1.14 nm. Similar to the findings at low temperatures, the intermolecular interaction in these islands is larger than the templating effect of the substrate. Beside the islands, the fragments (compare species 3 in Fig. 8.2) are still present on the surface (bright features in between the islands) and adsorb in the same positions as at low temperatures, *i.e.*, at the pore region of the moiré.

Surprisingly, no $CePc_2$ doubledeckers were found on the surface. Since desorption is unlikely at room temperature, considering the much higher evaporation temperature, one possible explanation could be a high mobility at room temperature. A measurement of the doubledeckers by STM would not be possible, since the STM tip would push them away instead of scanning across them. Another explanation could be an incorporation into the tripledecker islands. As it was shown by Hellerstedt *et al.*, doubledecker molecules might decompose at temperatures like the used evaporation temperature [157]. On the surface, the decomposed parts – mainly free-base Pcs and metalated Pcs – can form again multidecker complexes. Not only the initial doubledeckers can be formed on the surface, but also larger complexes, like tripledeckers [157]. Therefore, an absence of doubledeckers and the presence of mainly tripledecker complexes could be a result of the decomposition and reformation of the Ce-based multideckers.

8.2. Adsorption of $CePc_2$ on Ag(111)

As a reference experiment to study the structure, appearance and intermolecular interaction, $CePc_2$ molecules were deposited onto Ag(111). Large islands can be found on the sample (Fig. 8.4), assigned to $CePc_2$ doubledecker islands, based on their apparent height of $\sim 0.63\,\mathrm{nm}$ (see linescan). The reduced height compared to the doubledeckers on hBN/Ir(111) might be explained by the enhanced interaction between the $CePc_2$ and the Ag(111) [54, 167]. Those islands show the same rectangular shape as the tripledecker islands on hBN/Ir(111) with a periodicity of $\sim 1.3\,\mathrm{nm}$ (c.f. green square in Fig. 8.4 (c)). A dI/dV spectra, measured on the island (Fig. 8.4 (b), spot marked in with a red dot in (a)), shows a clear signal of the lowest unoccupied resonance at $\sim 1.4\,\mathrm{V}$. The onset at negative bias voltages of $\sim -1.7\,\mathrm{V}$ can be assigned to the signal of the highest occupied molecular resonance. The reference spectrum of the Ag(111) substrate in orange reveals a faint signal of the surface state at $\sim -50\,\mathrm{mV}$ as a step-like increase in the differential conductivity [168]. The feature at $\sim -1.5\,\mathrm{V}$ is attributed to the DOS of the tip, since it is also observed in the spectrum of the molecular island. In Fig. 8.4 (c)-(e) individual doubledeckers were extracted from the island by LM. This step-by-step removal is indicated by the green arrows, pointing from the initial position of the molecule to its final position after the manipulation. Here, the structure and size of a single $CePc_2$ becomes more obvious.

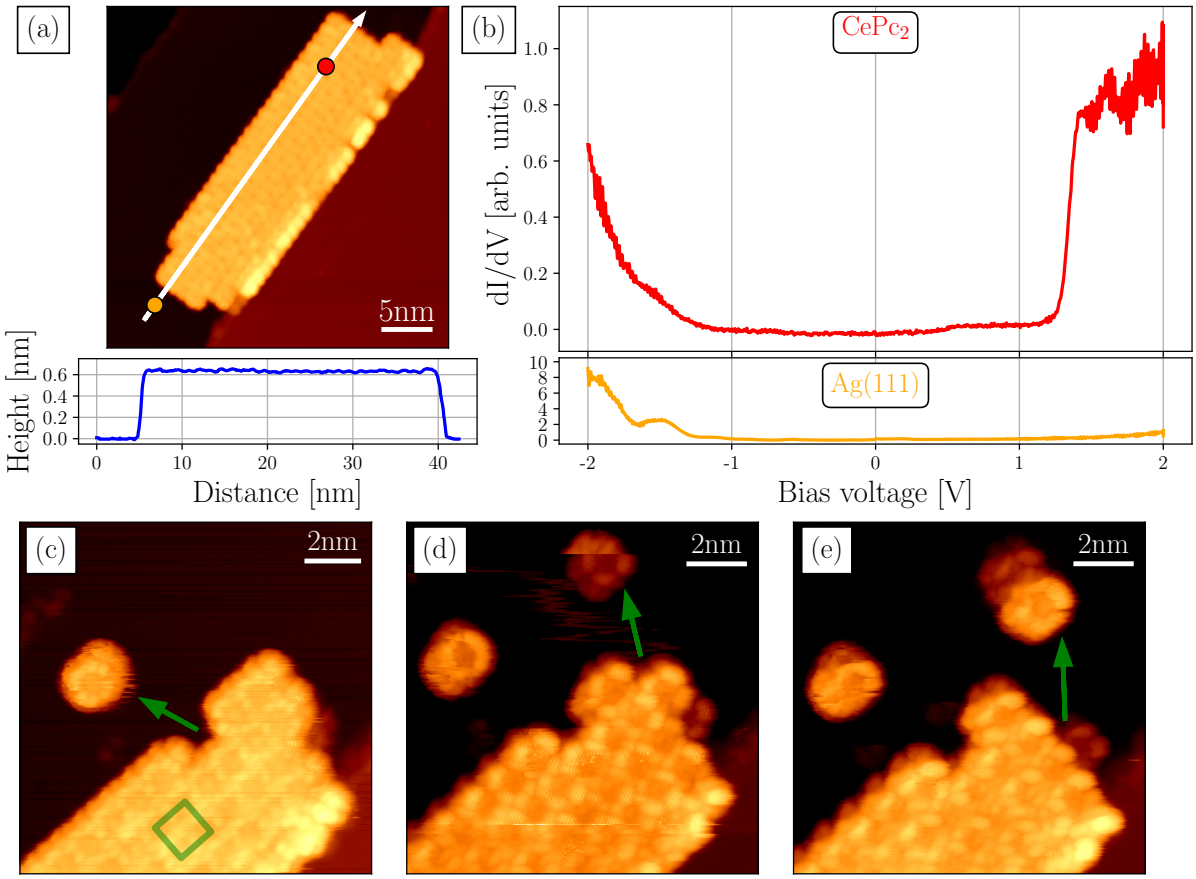

Figure 8.4: *Adsorption of $CePc_2$ on Ag(111). The $CePc_2$ molecules were evaporated at 570° C for 30 min onto the sample, kept at room temperature. In* ***(a)*** *an overview of a $CePc_2$ island can be seen with the linescan along the white arrow below (U = 2 V, I = 0.22 nA). The square lattice of the islands is indicated by the green square in (c). At the red/orange spots on the island/Ag(111) in (a) dI/dV spectra were taken and are illustrated in* ***(b)*** *as labeled. In* ***(c)*** *-* ***(e)*** *individual doubledeckers were removed from the island by LM, indicated by the green arrows (U = 2 V, I = 0.1 nA). The arrows point from the former position of the molecule to the position, where the molecules ended up after the manipulation.*

By comparing these measurements of the $CePc_2$ doubledeckers on Ag(111) with those on *h*BN/Ir(111), several differences and similarities can be found: (i) On Ag(111), neither tripledeckers nor fragments of $CePc_2$ molecules, *i.e.*, single Pcs or the smaller fragments (species 3 in Fig. 8.2) were found. (ii) In contrast to the doubledeckers on *h*BN/Ir(111), adsorbing as single molecules on the pore regions, they form islands on the bare metal. With LM it is possible to extract single molecular units, indicating a high stability of the complexes at low temperatures. (iii) The appearance of individual molecules in a doubledecker island on Ag(111), exhibiting eight lobes, is similar to the appearance of

individual molecules in a tripledecker island on hBN/Ir(111). (iv) The appearance of the single $CePc_2$ doubledeckers on Ag(111), extracted from an island, is similar to the appearance of the individual doubledeckers on hBN/Ir(111) in Fig. 8.2 (b) as the edge of the molecule appears as a smeared out rim and not as individual lobes, as in the islands. (v) The height of the doubledeckers on Ag(111) is reduced by 9 % in comparison to the doubledeckers on hBN/Ir(111). These observations imply a stronger molecular coupling to Ag(111) than to hBN/Ir(111). Nevertheless, the upper part of the molecule might be decoupled from the substrate, for example, due to the large distance of the upper Pc to the metal substrate, indicated by the similar appearances of the molecules in the doubledecker island on Ag(111) compared to the appearances of the molecules in the tripledecker islands on hBN/Ir(111), observed in section 8.1.

8.3. In-situ preparation of Ce-based multideckers on hBN/Ir(111)

In addition to the evaporation of the pre-synthesized $CePc_2$, multideckers were prepared in-situ. Similar to procedures of previous studies [64, 65], a multilayer of 2H-Pc molecules was deposited at $380 - 400$°C via OMBE for 180 min onto the room temperature hBN/Ir(111) surface. Subsequently cerium was evaporated from a home-build cell, containing a Ce ball enclosed by a W wire for resistive heating, into the multilayer. To synthesize the Ce-based multidecker complexes and desorb the surplus 2H-Pc molecules, the sample was heated to 300°C for 10 min. This procedure was monitored by XPS and is demonstrated for the main peaks, *i.e.*, C1s, N1s and $Ce3d_{5/2}$, in Fig. 8.5. The fit parameter are listed in Tab. 8.2. Before fitting the components of the core level features, measured by normal emission XPS, their background was subtracted. The background of the C1s signal is dominated by the nearby Ir4d peak and was modeled using two Gaussians and a linear slope. The N1s background was modeled by a Sigmoid step function. The background of the Ce3d peak on hBN/Ir(111) was modeled using a cubic polynomial. The fitting of the features was implemented by using Gaussians in a way that the width of peaks with the same origin were fixed to be equal. The height ratio of the peaks, resulting from the hBN layer was kept constant for all stages of the preparation.

The XPS measurement of the C1s signal of the 2H-Pc multilayer is shown in Fig. 8.5 (b). A clear feature consisting of three individual peaks, resulting from different types of carbon atoms in the 2H-Pc molecules, *i.e.*, the carbons in the phenyl rings (C1) and the carbons in the pyrrole rings (C2) (c.f. Fig. 6.4 (c) and Fig. 8.1 (b)), is observed. The peak SC2 is identified as a shake-up peak of the pyrrolic C2 peak and is located 1.67 eV higher in

energy than the C2 peak. This assignment and the binding energy difference are in good agreement with the energy shift of shake-up peaks found for other Pcs [169, 170]. The ratio of the area of the two peaks $A_{C1}/A_{C2} = 2.6$ fits the ration of 24/8, *i.e.*, the number of carbon atoms in phenyl and pyrrole rings, respectively (c.f. Fig. 6.4 (c), Fig. 8.1 (b)).

	Peak	Height [a.u.]	Center [eV]	HWHM [eV]	Area [a.u.]
C1s:	C1	5288.060	284.863	0.605	6815.6
2H-Pc/*h*BN/Ir(111)	C2	2041.640	286.350	0.605	2631.4
	SC2	378.226	288.017	0.605	487.5
	C1	3238.560	284.863	0.605	4174.1
C1s:	C2	1250.360	286.350	0.605	1611.5
Ce/2H-Pc/*h*BN/Ir(111)	SC2	231.637	288.017	0.605	298.5
heated	C3	1318.410	285.650	0.605	1699.3
	SC3	254.164	287.317	0.605	327.6
N1s:	N3	2204.070	397.909	0.706	3311.4
*h*BN/Ir(111)	N4	444.649	399.298	0.706	668.0
	N1	885.232	400.419	0.624	1176.1
N1s:	N2	1926.480	398.877	0.624	2559.4
2H-Pc/*h*BN/Ir(111)	N3	282.099	397.909	0.706	423.8
	N4	56.911	399.298	0.706	85.5
	N1	278.113	400.419	0.624	491.1
N1s:	N2	605.243	398.877	0.624	1068.7
Ce/2H-Pc/*h*BN/Ir(111)	N3	298.789	397.909	0.706	840.8
heated	N4	60.278	399.298	0.706	169.6
	N5	1029.940	398.962	0.624	1368.3
$Ce3d_{5/2}$:	Ce1	3058.470	886.633	1.845	12011.6
Ce/2H-Pc/*h*BN/Ir(111)	Ce2	952.788	882.617	1.845	3741.9
$Ce3d_{5/2}$: heated	Ce1	2187.450	886.633	1.845	8590.9
Ce/2H-Pc/*h*BN/Ir(111)	Ce2	1132.400	882.617	1.845	4447.3

Table 8.2: *Fit parameters of the in-situ preparation of Ce-Pc multideckers on hBN/Ir(111). The peak labeling of the C1s and the N1s peaks is done according to Fig. 6.4 (c) and Fig. 8.1 (b). The additional peak C3 stems from the interaction of the molecule with cerium. SC2 and SC3 are shake-up peaks of C2 and C3, respectively [170]. The peaks N3 and N4 result from the hBN layer (c.f. [58]). The peaks Ce1 and Ce2 correspond to clustered cerium and cerium, incorporated into the Pc macrocycle, respectively.*

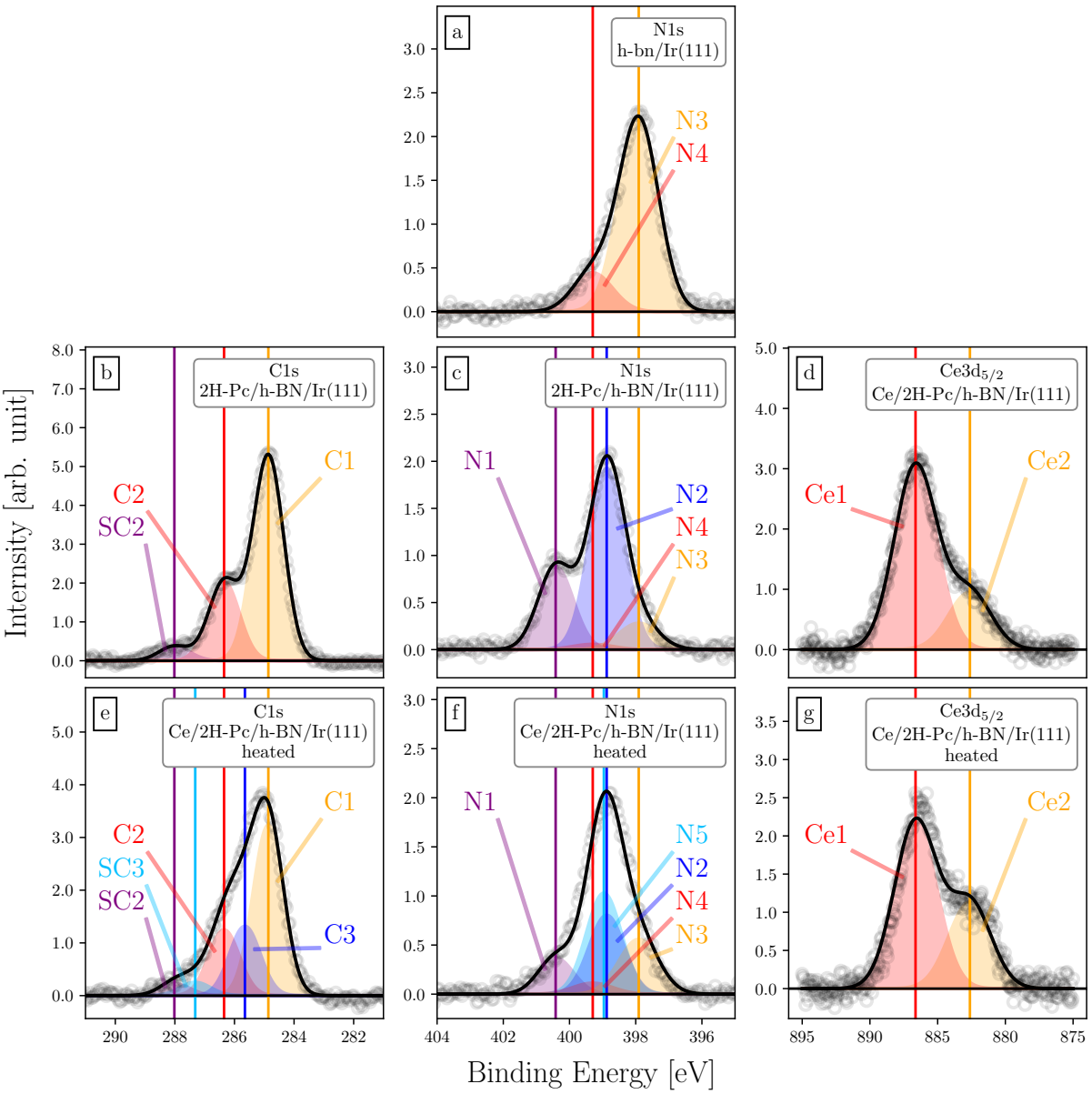

Figure 8.5: *XPS measurements of the in-situ growth of Ce-Pc multideckers on hBN/Ir(111). The three important peaks, i.e., the C1s, N1s and Ce3d$_{5/2}$, are monitored for the different stages of the growth:* ***(a)*** *– hBN/Ir(111);* ***(b)***, ***(c)*** *– multilayer 2H-Pc/hBN/Ir(111);* ***(d)*** *– Ce/2H-Pc/hBN/Ir(111);* ***(e)*** *-* ***(g)*** *– heated Ce/2H-Pc/hBN/Ir(111). Grey circles represent the measured data, colored areas indicate the peak components and the sum of the fits is shown by the black solid lines. The center of the Gaussians peaks are marked by the solid vertical lines with the corresponding color. The fit parameters of the peaks are listed in Tab. 8.2.*

The C1s signals, resulting from the evaporation of Ce into the multilayer of 2H-Pc and the heating induced formation of the multidecker complexes, accompanied by the desorption of the surplus 2H-Pc multilayer molecules [65] is shown in Fig. 8.5 (e). The magnitude of the peaks is decreased, due to the reduced amount of molecules on the surface. From the areas of the C1 peak before and after the multidecker formation, a desorption of 40 % of the multilayer molecules is observed. Two additional peaks appear in the C1s feature. These peaks are labeled C3 and SC3. The latter one is the shake-up peak of C3, exhibiting the same energetic distance to the main peak, as observed for the shake-up peak SC2. This implies that the peak C3 arises from a cerium induced change in the binding energy of the pyrrolic carbon atoms, leading to a downshift in energy of 0.7 eV. Additionally, the ratio between the areas of main and shake-up peaks are similar, supporting the hypothesis.

In Fig. 8.5 (a) the N1s signal on the *h*BN/Ir(111) surface is clearly dominated by two peaks (N3, N4), originating from the *h*BN layer. This occurrence of two peaks is expected, as it was observed by Farwick zum Hagen *et al.* and can be assigned to the strongly and weakly bound areas in the *h*BN moiré [58].
The deposition of the 2H-Pc multilayer changes the N1s signal significantly (see Fig. 8.5 (c)). The two peaks, originating from the *h*BN layer, are now clearly reduced, due to the coverage of the 2H-Pc. The presence of the molecules is reflected in the two additional components N1 and N2. These two peaks can be assigned to the two different kinds of nitrogens in the molecule, *i.e.*, the pyrrolic nitrogens (N1) and the iminic nitrogens (N2) – c.f. Fig. 6.4 [171–173]. The ratio of the areas $A_{\mathrm{N2}}/A_{\mathrm{N1}} = 2.6$ fits the expected ration of 6/2, *i.e.*, the number of iminic N with respect to the number of pyrrolic N.
The evaporation of cerium and the metalation of the 2H-Pc induce several changes in the N1s signal (see Fig. 8.5 (f)). The peaks, originating from the supporting *h*BN layer, are increased, since the thickness of the covering molecular layer is decreased. The molecular peaks N1 and N2 are both decreased, partially caused by the desorption of the surplus multilayer 2H-Pc, but also due to the metalation by cerium. In this metalation process the inner hydrogen atoms are replaced by one metal atom, in this case cerium. This results in the emergence of peak N5, located energetically in between N1 and N2 [171–173]. The presence of the N1 peak indicates that unmetalated 2H-Pc is also still present on the surface. The decrease of peak N2 can also be explained by the metalation. Since four nitrogen atoms per Pc bind to the inner Ce atom in Ce-based multideckers, the number of coordinated nitrogens in the center is doubled in comparison to 2H-Pc. Thereby, the number of iminic nitrogens (N2) is reduced by two per Pc. The energetic position of peak

N5 at $\sim$ 399 eV, originating from the metalated nitrogen atoms, is in accordance with other values of metalated tetrapyrrole-like molecules, found in literature [18, 23, 26, 171–174]. From the areas of the peaks N1 and N5, the amount of the Ce-based multideckers on the surface, with respect to the total number of Pc molecules, can be estimated to be $A_{\mathrm{N5}}/[2 \cdot A_{\mathrm{N1}} + A_{\mathrm{N5}}] \approx 60\,\%$.

The $\mathrm{Ce3d_{5/2}}$ signal in Fig. 8.5 (d) reveals a clear feature composed of two peaks Ce1 and Ce2. Overview spectra (not shown here) reveal the positions of the $\mathrm{Ce3d_{5/2}}$ and $\mathrm{Ce3d_{3/2}}$ peaks at binding energies of $\sim$ 886 eV and $\sim$ 905 eV, respectively, indicating an oxidation state of +III (c.f. [175]). Upon heating, the heights of the Ce1 and Ce2 peaks change in a way, that the Ce1 peak is reduced and the Ce2 peak is increased in intensity (c.f. Fig. 8.5 (g)). This change in intensity indicates that the Ce2 peak can be assigned to cerium, incorporated in the molecules, since the amount of metalated molecules should increased upon heating. The Ce1 peak could stem from clustered cerium. Upon heating, the cerium clusters could be partially involved in the metalation process but most of it could form even larger clusters. These cerium clusters can influence the molecules in a way that the binding energy of the pyrrolic carbon atoms is changed, yielding an explanation for the rise of the C3 peak. Regarding these measurements, the synthesis of Ce-based multideckers is likely to be successful. Nevertheless, since XPS is a surface-averaging technique, STM measurements are needed to confirm and characterize the synthesis of the Ce-based multideckers.

8.4. DFT calculations and STM simulations of $\mathrm{CePc_2}$ on *h*BN/Ir(111)

To support the experimental findings and get insights into other properties of the doubledecker molecules, like structure, adsorption energy or magnetism, DFT calculations were performed on the rotated and the parallel version of the $\mathrm{CePc_2}$ (c.f. Fig. 8.1). The projector-augmented plane wave method [144] and a plane wave basis set with maximum kinetic energy of 400 eV were used. The structures were relaxed until the acting forces were smaller than 0.05 eV/Å and the energy-change was less than 1 μeV. The PBE exchange-correlation potential [94] (implemented in VASP [97, 145, 146]) was employed. Long-range vdW interactions were included, as proposed by the DFT-D3 approach of Grimme *et al.* [147]. The optimization was enforced at the gamma point of the Brillouin zone. The f-electrons in the Ce were treated with the local spin density approximation

(LSDA), including on-site Coulomb interactions (LSDA+U), increasing the energy barrier for electron fluctuations in the d and f-orbitals by the value of U. The specific method, introduced by Dudarev *et al.*, was used [176]. In the gas phase, the molecules were calculated in a tetragonal unit cell with a size of $a \times b \times c = (25 \times 25 \times 20)\text{Å}^3$. The adsorption of the doubledeckers on the hBN/Ir(111) surface was calculated in a hexagonal cell, defined in real-space by the three vectors

$$\boldsymbol{a} = \begin{pmatrix} 29.862 \\ 0 \\ 0 \end{pmatrix} \text{Å}, \qquad \boldsymbol{b} = \begin{pmatrix} -14.931 \\ 25.861 \\ 0 \end{pmatrix} \text{Å}, \qquad \boldsymbol{c} = \begin{pmatrix} 0 \\ 0 \\ 28.650 \end{pmatrix} \text{Å}.$$

Calculations of the molecules in gas phase reveal, that both configurations (rotated and parallel) are quite similar in energy, but the rotated $CePc_2$, with a ground state energy of $E_{0,\text{rot,gas}} = -838.214\,\text{eV}$, is about 0.5 eV more stable than the parallel one ($E_{0,\text{para,gas}} = -837.780\,\text{eV}$). For both molecules an on-site Coulomb interaction of $U = 8\,\text{eV}$ was used. This value was determined by relaxing the molecule for different values of U, yielding $U = 8\,\text{eV}$ to be the value with the lowest ground state energy of the relaxed molecules. The structure of both configurations is shown in Fig. 8.1.

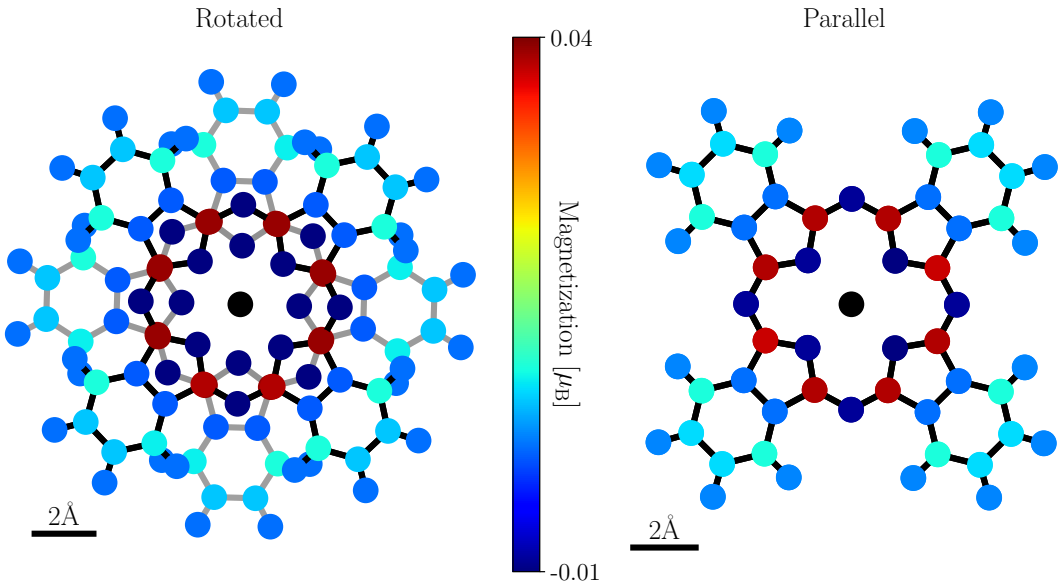

Figure 8.6: *Top view on the color-coded representation of the magnetization of the individual atoms in the $CePc_2$ molecules. The rainbow-like colorbar shows the magnetization of the ligands. The magnetization of the central cerium atom, colored in black, is not covered in the colorbar and amounts to $\sim 1\,\mu_B$.*

The height of the molecules, calculated by taking the difference between the averaged z-coordinate of the four inner N atoms of the top and the bottom Pc as indicated by the index $N4$, similar to the labeling in [177], is given by $\Delta h_{rot,N4} = 0.309$ and $\Delta h_{para,N4} = 0.302\,\mathrm{nm}$. This value is quite consistent with the experimentally measured height difference $h_{\mathrm{Ce_2Pc_3}} - h_{\mathrm{CePc_2}} = 0.39\,\mathrm{nm}$. The corrugation of the ligands (top and bottom Pc) of both molecules is $\Delta h_{Pc} = 0.05\,\mathrm{nm}$.
The molecules have a magnetic moment of $m_{\mathrm{rot,gas}} = 1.51\,\mu_{\mathrm{B}}$ and $m_{\mathrm{para,gas}} = 1.49\,\mu_{\mathrm{B}}$. As illustrated in the top view on the two different configurations of the molecule in Fig. 8.6, the spin is located at the ligands as well. The rainbow-like colorbar covers the magnetizations of the ligands, ranging from $-0.01\,\mu_{\mathrm{B}}$ (N atoms, dark blue) to $0.04\,\mu_{\mathrm{B}}$ (inner pyrrolic C atoms, dark red). The magnetization of the central cerium atom, colored in black, has a much larger value of $\sim 1\,\mu_{\mathrm{B}}$, that is not covered by the colorbar. The magnetization decreases with increasing distance from the molecular center.
Subsequently, the hBN/Ir(111) support was added to the model. The relaxation of this substrate was performed as described in detail in Appendix A. The molecules were adsorbed in a way that the central Ce-atom is positioned vertically above the reactive B atom of the pore of the moiré, *i.e.*, the closest atom to the underlying Ir(111) substrate. Furthermore, one of the main molecular axis of the bottom Pc is aligned with the high symmetry direction of the moiré and therefore also with the hBN lattice, shown in Fig. 8.7. The hBN layer is colorcoded to indicate the height in the z-direction (blue: far from Ir, red: close to Ir). Two different colors (green/yellow) indicate the two different Pc planes (top/bottom). From the ground state energies of the systems of the two adsorbed molecules ($E_{0,\mathrm{rot,ads}} = -6567.420\,\mathrm{eV}$, $E_{0,\mathrm{para,ads}} = -6567.050\,\mathrm{eV}$) the adsorption energies can be calculated by $\Delta E_{\mathrm{x,ads}} = E_{0,\mathrm{x,ads}} - E_{h\mathrm{BN/Ir(111)}} - E_{0,\mathrm{x,gas}}$ and amount to $\Delta E_{\mathrm{rot,ads}} = -3.795\,\mathrm{eV}$ and $\Delta E_{\mathrm{para,ads}} = -3.860\,\mathrm{eV}$. As for the gas phase calculation an on-site Coulomb interaction of $U = 8\,\mathrm{V}$ was used. The magnetization on the adsorbed $\mathrm{CePc_2}$ molecules ($m_{\mathrm{rot,ads}} = m_{\mathrm{para,ads}} = 1.17\,\mu_{\mathrm{B}}$) is reduced compared to the gas phase. As in the gas phase, the magnetism is mainly localized on the cerium atom, but now only the upper Pc shows a small magnetization, causing the reduction of the total magnetization. The energy difference of the ground states of the two adsorbed molecules of $\sim 0.4\,\mathrm{eV}$ is interesting, concidering the fuzzy appearance in STM (c.f. Fig. 8.2). The energy barrier, separating these two states, could be overcome by an excitation, induced by STM, presumably resulting in a rotation of the upper Pc (c.f. section 10.1). This induced switching between the parallel and the rotated configuration could be the reason for the blurred appearance, observed in Fig. 8.2.

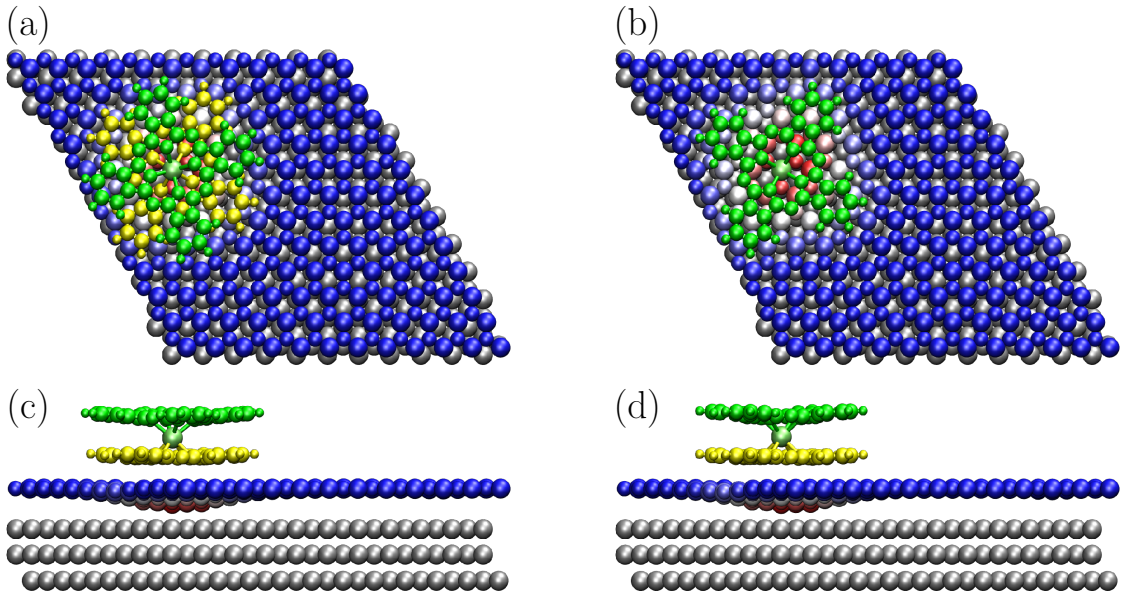

Figure 8.7: *Structure of the two different $CePc_2$ adsorbed on hBN/Ir(111). In* ***(a)/(b)*** *the top view is shown and in* ***(c)/(d)*** *the side view of the rotated/parallel $CePc_2$. The colorcode of the hBN indicates the height in z-direction (blue – far from the Ir, red – close to the Ir). The two different colors of the molecules are assigned to the top (green) and the bottom (yellow) Pc.*

Based on these relaxed structures of the adsorbed doubledeckers on the hBN/Ir(111) support, STM simulations were performed with an algorithm, based on the theory of Tersoff and Hamann [70, 178], introduced by Lorente and Persson [179, 180]. The simulations were periodically extended by a factor of three in both in-plane lattice directions of the moiré cell.

The STM simulations in Fig. 8.8 (a)-(d) show the two molecules for two different bias voltages, *i.e.*, $+1.5\,\mathrm{V}$ (left column) and $-1.5\,\mathrm{V}$ (right column). In addition, the superposition, *i.e.*, the average of the simulations of the two different molecules, for these two bias voltages can be observed in Fig. 8.8 (e),(f). At a positive bias voltage, eight lobes emerge at the edge of the molecule and a cross-like shape in the center of both the rotated and the parallel molecule (c.f. Fig. 8.8 (a),(c)). This appearance is very similar to the experimentally measured appearance of molecules in tripledecker islands (Fig. 8.2 (a)) and doubledecker islands (Fig. 8.4). By comparing the simulation with the appearance of the measured individual $CePc_2$ doubledeckers in Fig. 8.2 (b), it can be noted that the molecules in the experiment appear much more blurred. However, the simulation of the superposition of rotated and parallel $CePc_2$ appears more similar to the measured, in-

dividual $CePc_2$ doubledeckers on *h*BN/Ir(111). At negative bias voltages, the parallel and the rotated molecules show only four outer lobes and a depression in the center (c.f Fig. 8.8 (b),(d)). These four lobes were also observed experimentally for a single $CePc_2$ in Fig. 8.2 (d). Nevertheless, the doubledecker is very blurred in the STM image, implying that a rotation of the molecule can not be excluded.

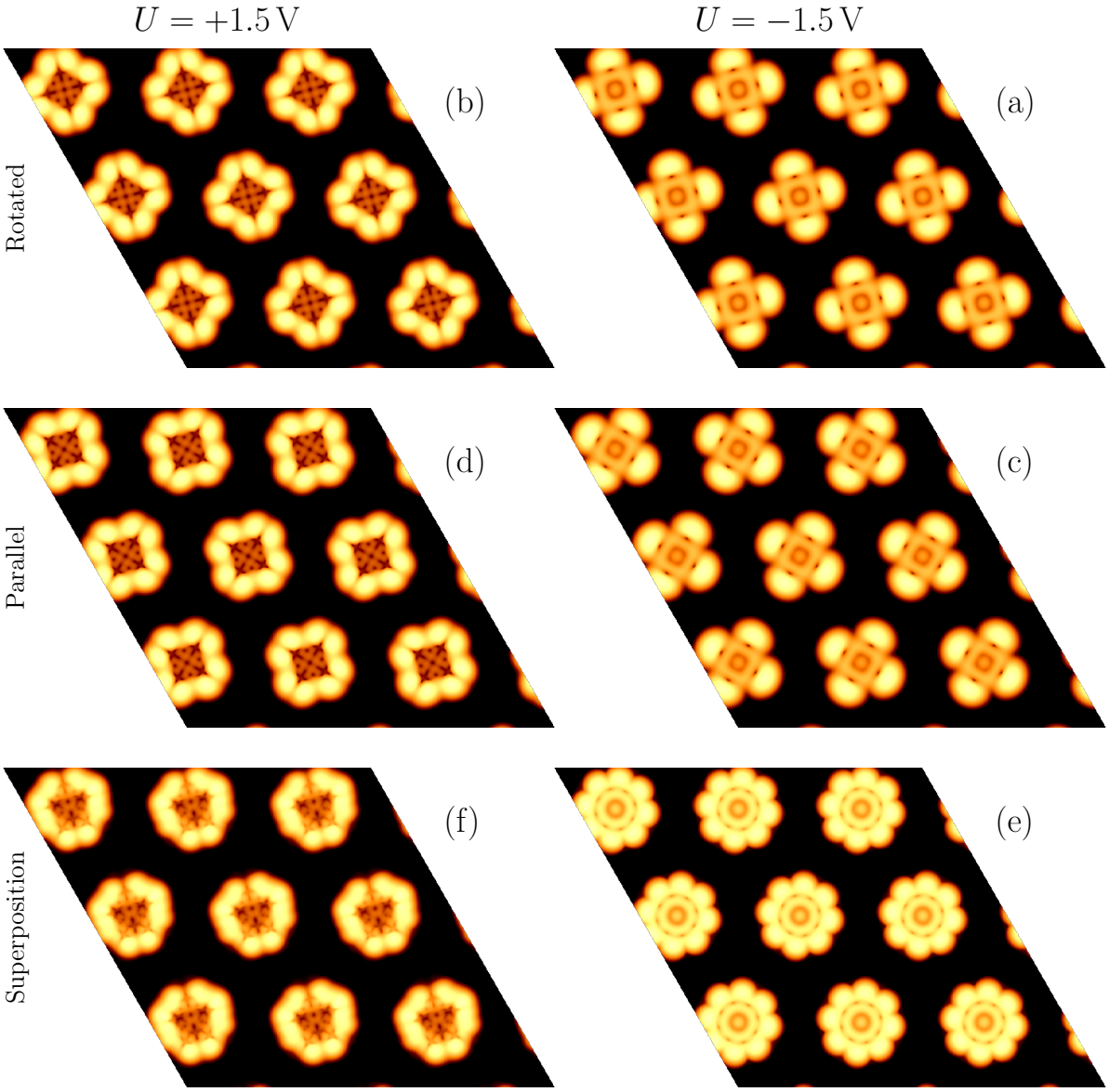

Figure 8.8: *STM simulations of $CePc_2$ on hBN/Ir(111). In the left column the simulations for the tunneling conditions of $U = 1.5\,V$, $I = 0.1\,nA$ are shown for the molecules indicated on the left. The right column shows the simulations for $U = -1.5\,V$, $I = 0.1\,nA$. The simulations in* ***(e)*** *and* ***(f)*** *show the superposition of the parallel and the rotated $CePc_2$ for the corresponding bias voltages.*

From these observation one could conclude that in individual $CePc_2$ on the hBN/Ir(111) surface a rotation of the upper Pc can be induced, causing the blurred appearance in the STM images. In contrast to this, the rotation of the upper Pc of the molecules in islands, both double- and tripledecker islands, is stabilized and the molecules show at positive bias voltages the typical appearance of the eight outer lobes.

8.5. Summary and outlook

A successful evaporation of intact $CePc_2$ doubledecker molecules on hBN/Ir(111), as well as an in-situ growth of Ce-based multideckers was achieved.
On the hBN/Ir(111) surface the molecules can be found in two different configuration, *i.e.*, in rectangular shaped Ce_2Pc_3 tripledecker islands and as individual $CePc_2$ doubledeckers, adsorbed in the pores of the hBN/Ir(111) moiré. The assignment to double- and tripledeckers was achieved by measuring the height of the structures and comparison with literature values (c.f. Tab. 8.1). The appearance of Ce_2Pc_3 molecules in the island is quite clear in STM, while the individual $CePc_2$ molecules are very blurred. This could be explained by a rotation of the upper Pc of the doubledecker. This hypothesis is supported by DFT calculations, showing a difference in the ground state energies of the two different $CePc_2$ configurations on the hBN/Ir(111) surface of 0.4 eV. The STM images, acquired at a bias voltage of $|U| \geq 1\,\mathrm{V}$ (see Fig. 8.2) might show the molecules with an induced rotation. Beside the $CePc_2$ and the Ce_2Pc_3, fragments of those are also found on the surface, *i.e.*, Pc, CePc and smaller molecules, identified as a quarter of a Pc. These small fragments are observed on the hBN/Ir(111) surface also at room temperature.
On the Ag(111) surface the molecules arrange in rectangular shaped $CePc_2$ doubledecker islands, where it is possible to remove individual molecules from this arrangement. Also, in this case, the appearance of the molecules in the island is rather sharp and similar to the appearance of the tripledecker islands on hBN/Ir(111). The absence of fragments of the $CePc_2$ complexes might be explained by a purification by degassing of the molecules between the experiments.
Beside the evaporation of pre-sythesized $CePc_2$ molecules, the in-situ preparation of Ce-based multideckers was executed on hBN/Ir(111). For this, a multilayer of 2H-Pc was deposited on the surface. Subsequently, cerium was evaporated into the multilayer followed by an annealing to 300°C, in order to metalate the molecules and to desorb the multilayer molecules [64, 65]. The XPS spectra of this procedure provided evidence for the metalation. Nevertheless, the $Ce3d_{5/2}$ signals, as well as the N1s signal, indicated that cerium, not included in the metalation process, as well as unmetalated 2H-Pc molecules,

are still present on the surface. Therefore, the Ce to Pc ratio needs to be adjusted systematically in future experiments, to obtain a fully reacted layer of Ce-based multideckers. In Addition, a microscopic surface analysis by STM/AFM seems mandatory to clarify the situation.

To support the experimental results, the molecules were modeled with DFT. These calculations in the gas phase and for the adsorption on *h*BN/Ir(111) yield properties, for example, the ground state energy, magnetism or the structure. The obtained magnetism of the doubledecker complexes is in agreement with the experimentally obtained oxidation state of +III of the cerium. By comparing the simulated STM images with the experimentally observed images, similarities could be found with the molecules in the islands. The blurred appearance of the single $CePc_2$ molecules in STM could be explained by a rotation of the upper Pc molecule, induced by STM, due to the small difference in the ground state energy of $\sim 0.4\,\mathrm{eV}$ and a possibly low energy barrier between these two states.

For a complete understanding of the molecules, additional measurements are necessary. To achieve a full array of individual doubledeckers on the *h*BN/Ir(111) moiré, a larger amount of molecules needs to be evaporated, while the amount of fragments needs to be reduced, as they could hinder the adsorption of the doubledeckers.

Alternatively, one could use the approach of in-situ growth of the Ce-based multideckers on *h*BN/Ir(111). In addition to the surface averaging XPS measurements, STM measurements of the surface are also required. A disadvantage of the in-situ growth could be the enhanced formation of multidecker islands instead of individual Ce-based multideckers at the pores of the moiré due to the enhanced intermolecular interactions with increasing size (c.f. [65]).

Important for further investigations with STM/AFM is the measurement of individual doubledeckers at low or even at zero bias voltage, to check whether the appearance changes below a certain bias voltage, thus supporting the hypothesis of the STM-induced rotation of the upper Pc.

After the structural classification, spectroscopic investigations are required to be performed by (spin-polarized) STS to obtain information regarding the electronic and magnetic properties of the doubledeckers. This information is crucial for future applications such as single molecular magnets for data storage [158, 181], light harvesting materials for solar cells [4, 6] or molecular building blocks for nano-electronics [155, 182].

9. Functionalization of *h*BN/Ir(111) by diiminoisoindoline

As it was shown in the previous section, *h*BN on Ir(111) is a suitable template for the separate adsorption of individual molecules [38, 114]. By functionalizing this insulating layer with molecules on the surface, new properties, like (photo-)catalytic reactivity or enhanced electric or thermal conductivity can emerge due to the added functional molecules [183]. Here, functionalization means a periodic, covalent binding of additional molecules to the *h*BN layer. Nevertheless, such a functionalization is not as easily achievable as on graphene, most probably due to the inert nature of *h*BN. It was reported that *h*BN and boron nitride nano tubes can be functionalized by oxygen and nitrogen radicals [184–188]. Sainsbury *et al.* observed a functionalization of *h*BN with nitrene radicals in solution [184]. The covalent bonding between the *h*BN sheet and the molecule was achieved via B-N bond formation. Since the results in the reported studies are all based on surface averaging techniques, a microscopic analysis of the functionalization of *h*BN is lacking.
In this section, the functionalization of *h*BN/Ir(111) by diiminoisoindoline ($C_8N_3H_7$, short 2III) will be demonstrated. The choice of this molecule was motivated by the observation of small units in section 8 (c.f. species 3 in Fig. 8.2), tentatively assigned to Pc fragments [66]. Since these fragments seem to be stably adsorbed in the pores of the *h*BN/Ir(111) moiré even at room temperature, despite their small mass and their naively assumed vdW-interaction with the supporting *h*BN, these molecules could thus be able to functionalize the *h*BN-layer. The 2III will be used as a model system for these fragments, since their appearance might indicate, that these fragments are about a quater of a Pc (c.f. Fig. 8.2 (c)). 2III is a molecule, composed of a phenyl ring attached to a pyrrole, at which two more NH groups are bound to the carbon atoms next to the pyrrolic nitrogen (c.f. inset in Fig 9.1).
The adsorption and modification of the molecules on the surface will be studied with STM and XPS as well as DFT calculations, supporting the experimental findings with the computation of ground state energies and simulations of STM images.

9.1. Adsorption of 2III on *h*BN/Ir(111)

To get insights into the interaction of the 2III with the *h*BN and to demonstrate that the Pc-fragments are derived from 2III, the molecules were deposited on the *h*BN/Ir(111) surface, prepared in the same way as described in section 8.1. The evaporation of 2III

was monitored with mass spectrometry, shown in Fig. 9.1. At evaporation temperatures $T \geq 110°C$ a peak at $m = (145.3 \pm 0.1)\,\mathrm{u}$ evolves, matching the mass of 2III given by $m_{2III} = 145.2\,\mathrm{u}$ [189]. The spectra were corrected by subtraction of a background spectrum, measured with a closed evaporator, while the molecules were kept at 110°C and subsequently fitted with Lorentzians. In the spectra at higher temperatures, *i.e.*, $T > 110°C$, the height of the peak increases. This increased intensity indicated a higher evaporation rate of still intact 2III molecules. Based on these measurements, an evaporation temperature of $110 - 115°C$ was used in the following experiments.

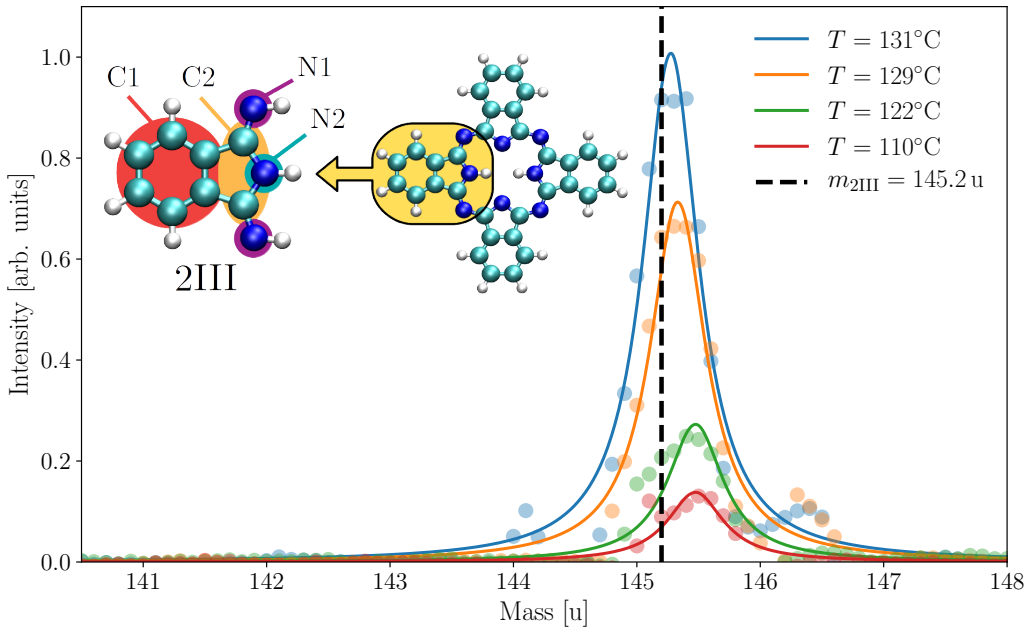

Figure 9.1: *Evaporation of 2III measured by mass spectrometry for different evaporation temperatures. Each spectra was corrected by subtraction of a background and fitted with a Lorentzian. For all fitted peaks the same width was used. The inset shows the molecular structure and its relation to a Pc. The different types of atoms are labeled: C1 – carbon atoms in phenyl, C2 – carbon atoms in pyrrole, N1 – iminic nitrogen, N2, pyrrolic nitrogen.*

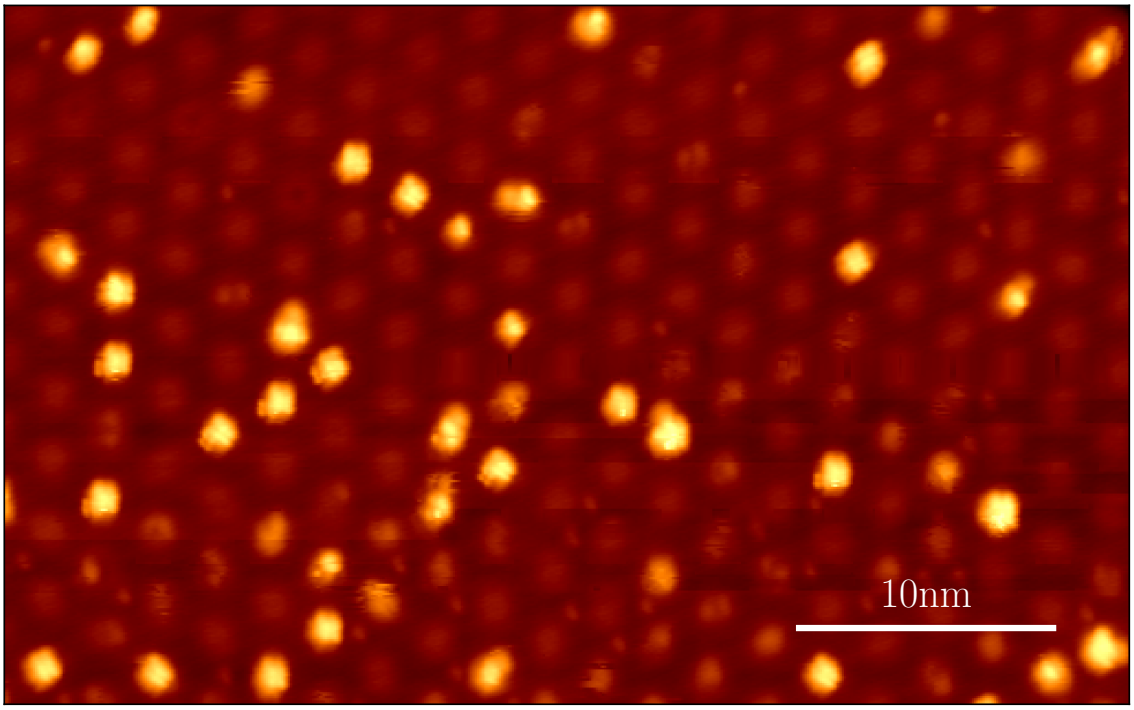

Figure 9.2: *Adsorption of 2III molecules on hBN/Ir(111). The 2III molecules were evaporated at $T_{\mathrm{mol}} = 110°C$ for 20 s onto the room temperature hBN/Ir(111) sample and adsorb in the pore regions of the moiré, which appear as protrusions at the bias voltage of $U = 0.5\,V$ ($I = 0.1\,nA$).*

The 2III, deposited on *h*BN/Ir(111) at room temperature, can be seen in Fig. 9.2. The molecules prefer to adsorb in the pore regions of the moiré of *h*BN/Ir(111) – shown as protrusions at a sample bias voltage of $U = 0.5\,\mathrm{V}$ – presumably, due to the lowered work function in this regions [38, 55, 57, 190].
By taking a closer look at an individual molecule, one can see a bias-dependent appearance (see Fig. 9.3). At positive voltages of $U \geq 1.1\,\mathrm{V}$, four lobes can be observed, which could be identified with the benzene ring on the one side (two smaller lobes) and with the diiminopyrrole on the other side (two larger lobes) as discussed later in section 9.7. At negative bias voltages the molecule appears as one bright protrusion. The apparent height of the molecule, illustrated in Fig. 9.3 (m), varies with the bias voltage. It increases from 0.19 nm at $-1.1\,\mathrm{V}$ to 0.26 nm at 1.3 V, matching the height measured in Fig. 8.2.

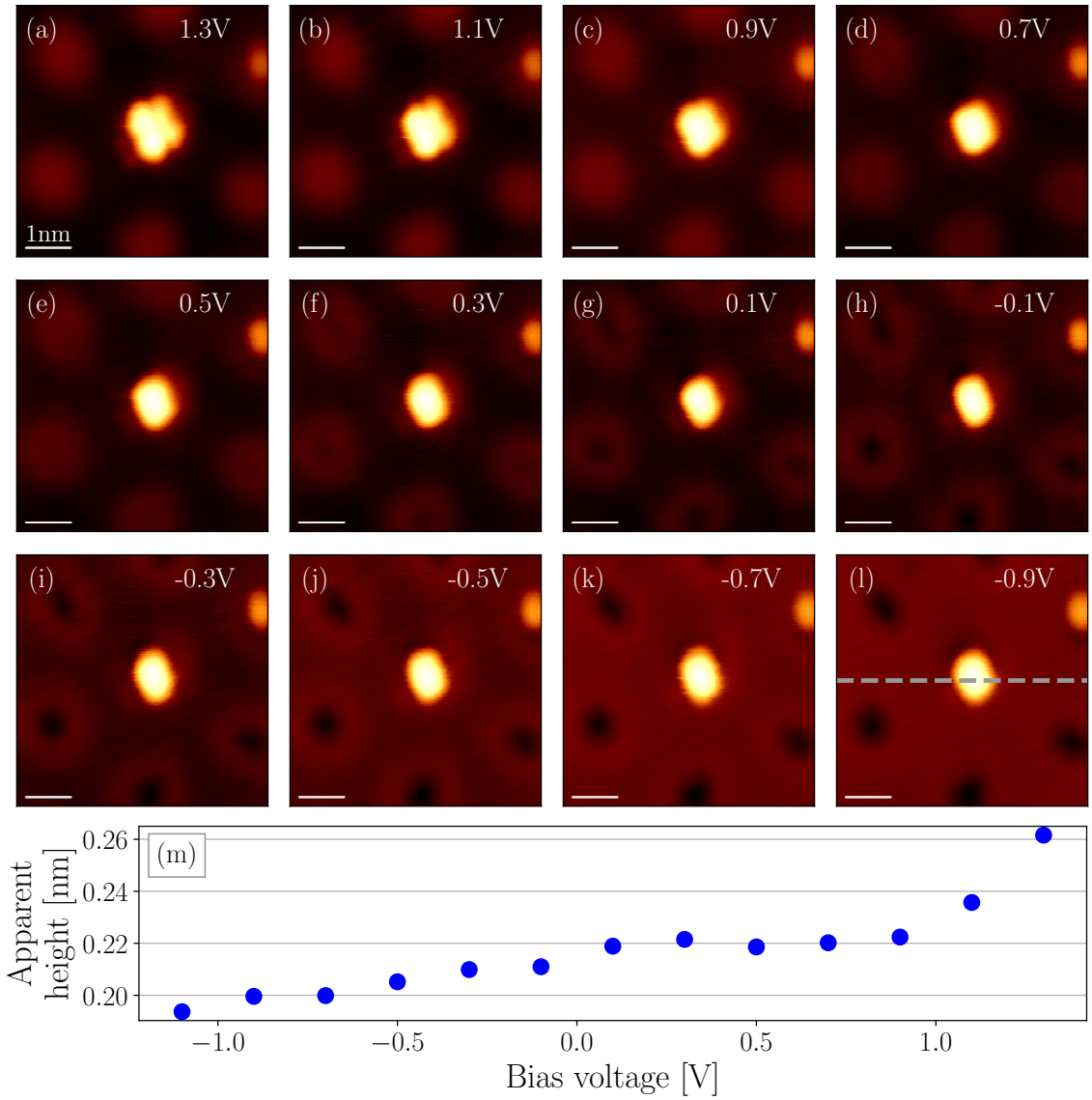

Figure 9.3: *Bias-voltage-dependent appearance of 2III/hBN/Ir(111). The bias voltages in each image in* ***(a)*** *-* ***(l)*** *are labeled ($I = 0.1\,nA$). The apparent heights are measured for each voltage along the grey line indicated in (l) and are shown in* ***(m)****.*

9.2. Irreversible modification of single 2III on *h*BN/Ir(111)

By measuring the electronic structure of the 2III/*h*BN/Ir(111) via STS at the center of the molecule, a jump in the current can be detected at $\sim 1.97\,V$. The spectrum was measured from $-1\,V$ to $+2\,V$. The drop in the current, as well as in the dI/dV signal, can be observed in Fig. 9.4 (b),(c) and can be assigned to a irreversible modification of the 2III.

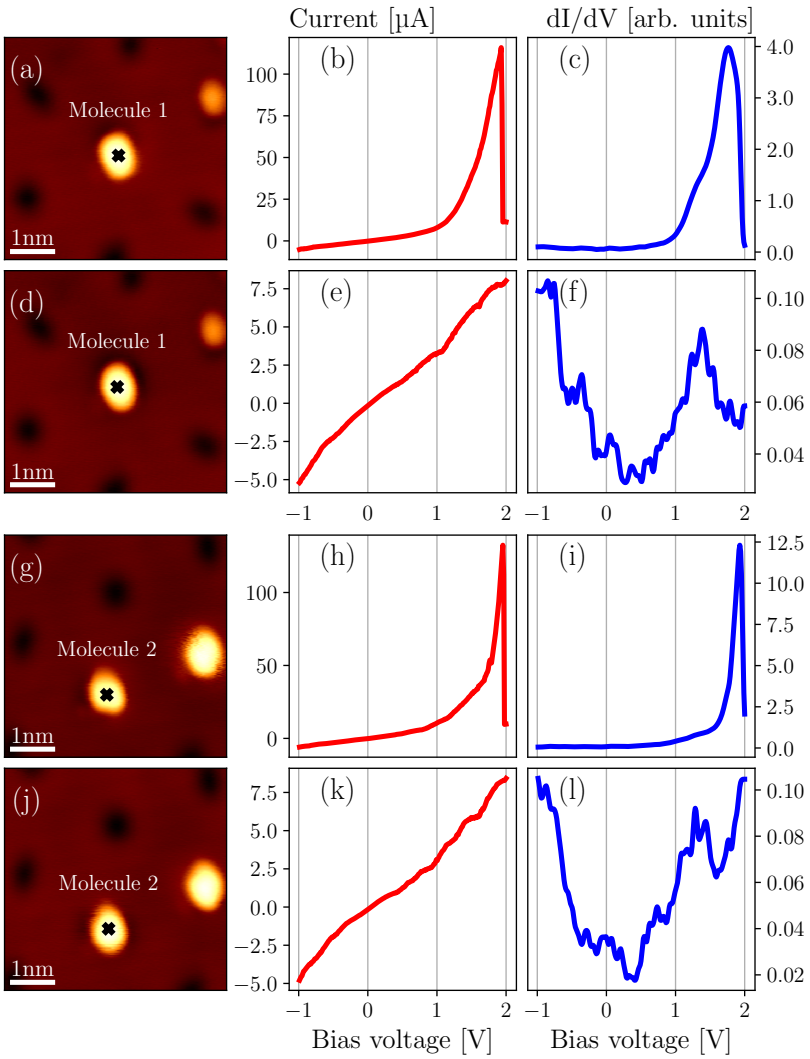

Figure 9.4: *Irreversible modification of 2III by STS. In* **(a)** *and* **(d)** *STM images before and after the modification of molecule 1 are shown ($U = -1\,V$, $I = 0.1\,nA$). In* **(b)**/**(e)** *the corresponding I(V) spectra and in* **(c)**/**(f)** *the corresponding dI/dV spectra are plotted ($U_{stab} = -1\,V$, $I_{stab} = 0.1\,nA$). Those spectra were taken at the spot, marked with black crosses in (a)/(d), respectively. In the spectra in (b) and (c) a drop in intensity at $\sim 1.97\,V$ is detected and assigned to the modification of the molecule. A change in the molecular appearance at $U = -1\,V$ is not observed after this modification. The same procedure is shown for a second molecule in* **(g)**-**(l)**.

In a second spectra, measured at the same position as the first one, a jump was not detectable (c.f. Fig. 9.4 (e), (f)). Now, the dI/dV spectrum shows a broad peak at $\sim 1.3\,V$ and a spectroscopic feature at $\sim -0.65\,V$, which could be assigned to the LUMO/HOMO of the molecule, respectively. The step-like increase at $\sim -0.3\,V$ originates from the Ir(111) surface state [191]. Both step-like features at negative bias voltages are observed

in the spectra, recorded prior to modification, but are not visible in comparison to the high amplitude of the feature at positive bias voltage. In contrast to the change in the spectrum, no difference in appearance at a bias voltage of $U = -1\,\mathrm{V}$ is observed, revealing the presence of the features at negative bias voltages before and after the modification. The same behavior was reproduced for other 2III molecules, as, for example, illustrated in Fig. 9.4 (g)-(l).

9.3. Temperature stability of the bond between 2III and *h*BN

To study the temperature stability of the binding between 2III and *h*BN/Ir(111), XPS measurements were conducted. For this purpose the C1s and the N1s features were investigated on bare Ir(111) and on *h*BN/Ir(111) (see Fig. 9.5). The fit parameters are listed in Tab. 9.1.

	Peak	Height [a.u.]	Center [eV]	HWHM [eV]	Area [a.u.]
C1s:	C1	268.712	284.759	0.913	522.42
2III/Ir(111)	C2	184.951	286.370	0.913	359.58
C1s:	C1	1686.300	285.896	0.710	2549.11
2III/*h*BN/Ir(111)	C2	339.076	287.884	0.710	512.57
N1s:	N1	226.544	398.895	0.813	392.28
2III/Ir(111)	N2	39.390	400.458	0.943	79.08
N1s:	N3	3224.030	398.064	0.707	4854.29
*h*BN/Ir(111)	N4	539.308	399.635	0.707	812.01
	N1	1731.850	398.312	0.711	2621.62
N1s:	N2	528.801	399.855	0.711	800.48
2III/*h*BN/Ir(111)	N3	778.772	398.064	0.707	1172.56
	N4	130.271	399.635	0.707	196.14

Table 9.1: *Fit parameters of the XPS measurements of 2III/Ir(111) and 2III/hBN/Ir(111). The peaks C1 and C2 origin from the two carbon atoms in the phenyl/pyrrole ring of the molecule, respectively. Peak N1/N2 stem from the iminic/pyrrolic nitrogen, as labeled in Fig. 9.1. The peaks N3 and N4 result from the hBN layer (c.f. [58]).*

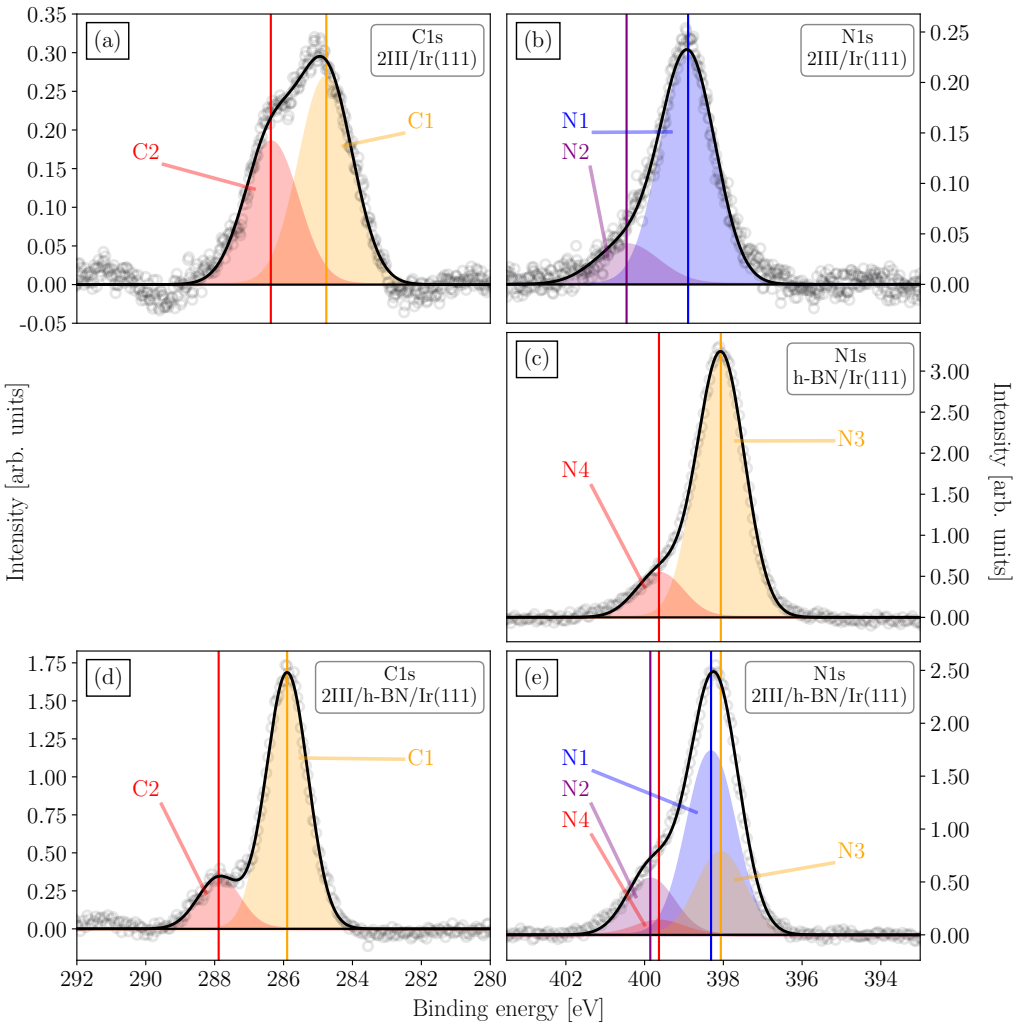

Figure 9.5: *XPS masurements of the C1s and the N1s signal on different surfaces. The 2III molecules were evaporated at 115°C for 1 min onto the room temperature samples. The monolayer hBN/Ir(111) was prepared as described in section 6.2. The spectra were recorded in 70° grazing emission.* ***(a)***, ***(b)*** *– 2III on Ir(111);* ***(c)*** *– hBN/Ir(111);* ***(d)***, ***(e)*** *– 2III on hBN/Ir(111). The backgrounds of the spectra, modeled as described in section 8.3, were subtracted before fitting. The grey circles show the measured data, the labeled, colored areas represent the peak components and the black solid lines resemble the sums of the fits. The center of the fitted Gaussians are indicated by the solid colored lines.*

As a reference, the XP-spectra of 2III were measured on Ir(111) (see Fig. 9.5 (a),(b)). The C1s feature of the multilayer of 2III molecules on Ir(111) can be modeled with two Gaussians (C1 and C2), originating from two different kinds of carbon atoms in the molecule, *i.e.*, the carbons in the phenyl (C1) and the carbon atoms in the pyrrole ring (C2) (c.f. inset in Fig. 9.1). The peak positions at 284.8 eV and 286.4 eV match the ones, observed

for the C1 and C2 peaks of the 2H-Pc multilayer on *h*BN/Ir(111), measured in section 8.3, indicating that the binding of the carbon atoms in the 2III is similar to the binding of those in 2H-Pc. The ratio of the areas of these two peaks should be 6/2, *i.e.*, the ratio of the number of the different carbon atoms in the molecule. However, this ratio is given by $A_{C1}/A_{C2} = 1.5$. An explanation could be, that the carbon atoms in the molecule bind differently in the multilayer, compared to the monolayer.
On *h*BN/Ir(111), the C1s signal can again be modeled by the two components C1 and C2 (c.f. Fig. 9.5 (d)). From the area of the peaks, a coverage, larger than one monolayer, can be estimated. The intensities and the peak position changed significantly compared to the 2III/Ir(111) measurements. The peaks shift both upwards as it could be expected [54, 167], but the magnitude of the shift (C1: 1.1 eV, C2: 1.5 eV) is rather large. Also the ratio of the peak areas changed drastically and amounts to $A_{C1}/A_{C2} = 5.0$. This difference to the expected value of 6/2 could again be explained by the different binding in the multilayer compared to the monolayer.

The N1s signal of 2III/Ir(111) in Fig. 9.5 (b) was fitted with two Gaussians (N1 and N2) originating from the two different types of nitrogen, *i.e.*, iminic and pyrrolic N, respectively. The peak positions of 398.9 eV and 400.5 eV match also those of the N1 and N2 peaks, observed for the 2H-Pc multilayer on *h*BN/Ir(111) in section 8.3. The ratio of the peak areas of $A_{N1}/A_{N2} = 5.0$ is 2.5 times larger, than it should be from the ratio of iminic to pyrrolic nitrogens (2/1). An explanation could be as well the different binding in the 2III multilayer compared to the monolayer.
For the N1s signal of *h*BN/Ir(111) a prominent feature is observed, consisting of two peaks (N3 and N4), resulting from the strongly and weakly bound areas of the moiré [58] (c.f. Fig. 9.5 (c)).
Due to the adsorption of 2III, this N1s signal changes (Fig. 9.5 (e)). In addition to the two components of the *h*BN layer (N3 and N4), two peaks, resulting from the 2III, were observed. The intensity of N3 and N4 is drastically reduced due to the 2III overlayer.[5] The energetic shift of the molecular peaks N1 and N2 towards lower binding energies (N1: 0.6 eV, N2: 0.7 eV) is in accordance with the shift of the N1s core level of other tetrapyrrole-based molecules for a compared adsorption on metal and *h*BN [54, 167]. The ratio between the areas of the two peaks – on this substrate given by $A_{N1}/A_{N2} = 3.3$ – is closer to the expected value but still exceeds the ratio of 2/1.

[5] This reduction in intensity is enhanced by the use of a grazing emission angle of 70°.

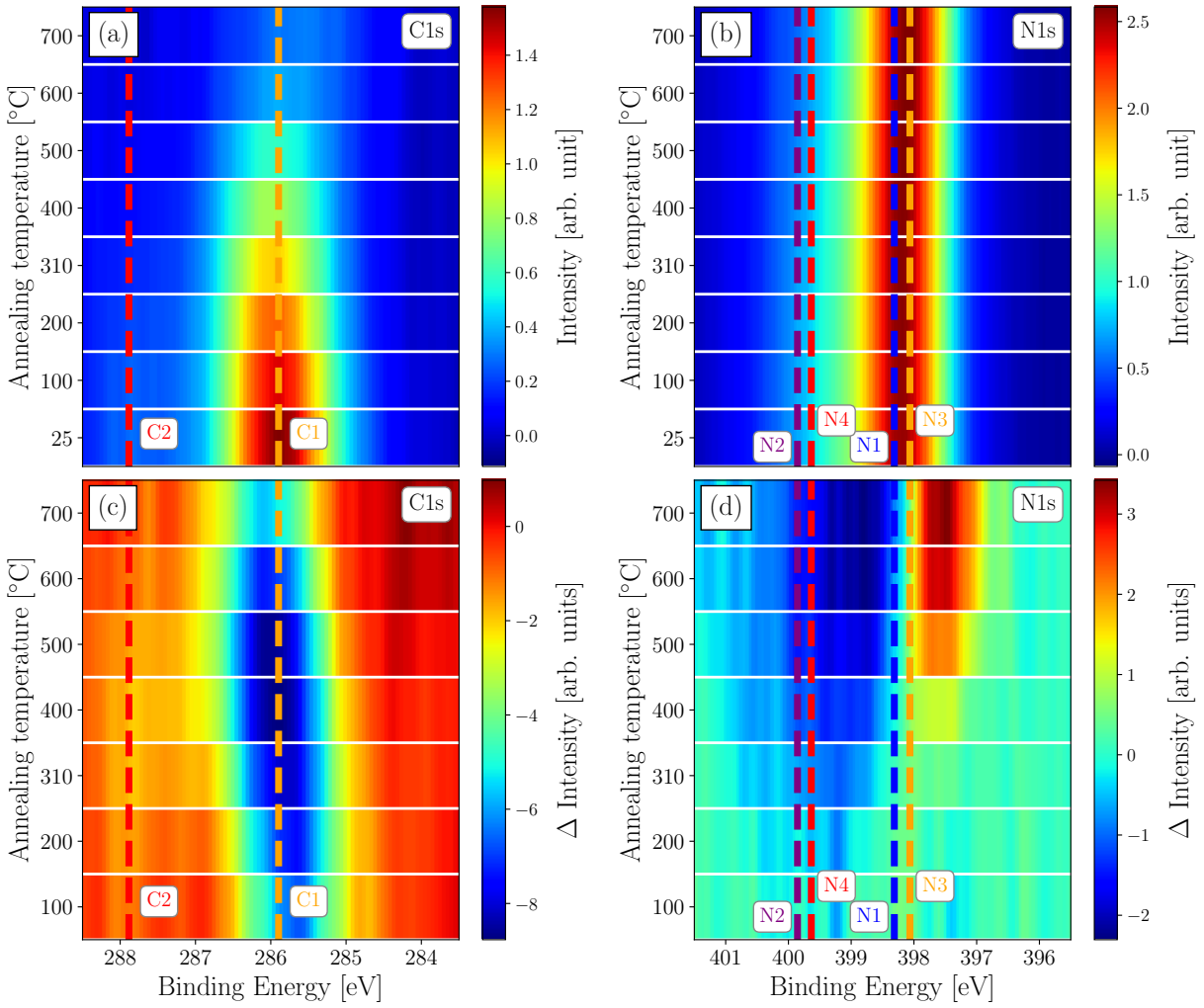

Figure 9.6: *XPS measurements of the thermal stability of 2III/hBN/Ir(111). The spectra of the C1s in* ***(a)*** *and of the N1s in* ***(b)*** *are plotted for different temperatures, indicated along the y-axis. The intensity, a function of the binding energy (x-axis) and the temperature (y-axis), is color coded, as the color bars indicate. The relative changes at each temperature step, with respect to the previous step, are illustrated in* ***(c)*** *and* ***(d)****. The vertical colored lines represent the fitted energetic positions of the peak components of Fig. 9.5 (d),(e).*

The temperature stability of the bond between 2III molecules and *h*BN/Ir(111) was studied by annealing the sample in 100°C steps from room temperature (25°C) to 700°C for 5 min at each step. After each heating step, the sample was checked with XPS at room temperature. The result is illustrated in Fig. 9.6. The horizontal bars, separated by white lines, represent one measurement at the temperature indicated along the y-axis. The intensity at the corresponding binding energy (x-axis) is color coded as indicated by the

color bars on the right. The vertical, dashed lines indicate the fitted positions of the peak components highlighted in Fig. 9.5 (d),(e). It can be observed that the C1s signal in Fig. 9.6 (a) decreases with increasing temperature and is strongly reduced after heating to 500°C. The difference in intensity, with respect to the spectrum of the next lower temperature step, is illustrated in Fig. 9.6 (c). The strongest reduction in intensity of the C1s signal at 285.9 eV, *i.e.*, the energetic position of peak C1, is observed at $T = 400$°C, which could be assigned to the desorption of the multilayer 2III molecules. The molecules in the monolayer, which bind stronger to the substrate, desorb at higher temperatures (~ 500°C).

The N1s signal in Fig. 9.6 (b) doesn't change significantly up to 400°C, better visible in the intensity difference in Fig. 9.6 (d). For higher temperatures the onset towards higher binding energies of the feature decreases (blue color in (d)). At the same time the onset towards lower binding energies of the feature gains intensity. Since the peak positions of the molecular nitrogens (N1 and N2) are close to the positions of the peaks originating from the *h*BN layer (N3 and N4), it is difficult to differentiate between a change in the binding energy of the molecule, caused, for example, by a modification, and a reduction in the coverage (c.f. Fig. 9.6 (c)), leading both to a shift in intensity. Nevertheless, the change in the spectra at temperatures, up to 400°C can be attributed to a desorption of the 2III multilayer molecules. The reduction of the molecular peaks at higher temperatures seems to be compensated by the increasing peaks originating from the *h*BN layer. Thus, a prominent change is not clearly visible.

These temperature dependent measurements reveal a strong binding of the 2III molecules to the *h*BN/Ir(111) substrate. The molecules are present on the surface up to a temperature of 500°C. This is quite astonishing, considering the evaporation temperature of 110°C (see Fig. 9.1) and desorption temperatures of other small π-conjugated molecules on surfaces [192–194].

9.4. Dimer formation on *h*BN/Ir(111)

Since the 2III are stable on the surface for temperatures up to $400 - 500$°C, the molecules were measured in STM after heating the low covered 2III/*h*BN/Ir(111) sample of Fig. 9.2 to 410°C for 5 min in order to observe if the molecules change upon heating. As a result, the molecular coverage did not change significantly, which could support the hypothesis that up to 400°C only multilayer 2III desorb, as discussed for the XPS measurements in

section 9.3. In addition, some molecules accumulated in pore regions, shown in Fig. 9.7. For a bias voltage of −1.0 V the monomer molecules in Fig. 9.7 (a) appear unchanged as single protrusions (c.f. Fig. 9.3). In addition, there is a new species appearing more elongated and exhibiting two protrusions. This can be observed better in Fig. 9.7 (b) and in the zoom-ins in Fig. 9.7 (c)-(f) by measuring these molecules at a bias voltage of +1.5 V. The molecule $m^{(i)}$ in Fig. 9.7 (f) has four lobes, as it was observed in Fig. 9.3. This molecule is identified as a monomer. The molecules $d^{(i)}$-$d^{(iii)}$ show a different appearance. Molecules $d^{(i)}$ (Fig. 9.7 (c)) and $d^{(ii)}$ (Fig. 9.7 (d)) look quite similar by exhibiting two rows of three lobes each. The protrusions in the center of each row are the ones with the highest intensities. Molecule $d^{(ii)}$ tends to have a point symmetry with respect to its center. The appearance of molecule $d^{(iii)}$ (Fig. 9.7 (e)) deviates from the appearance of molecules $d^{(i)}$ and $d^{(ii)}$. The lobes are ordered from left to right in alternating columns of two and one individual protrusions (: · : ·). The central single protrusion between the double-protrusions shows the largest apparent height.

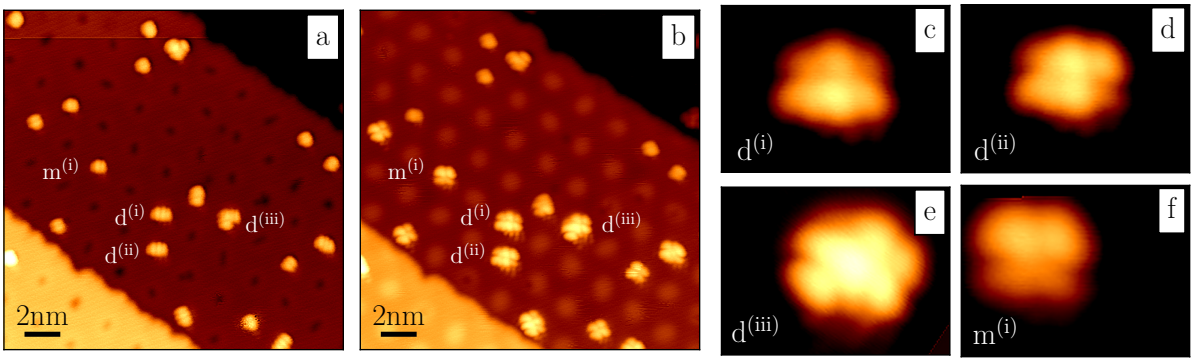

Figure 9.7: *Dimer formation of 2III on hBN/Ir(111) by heating the sample to 410°C for 5 min. In* ***(a)*** *an overview image is shown at the tunneling conditions of $U = -1.0\,V$, $I = 0.1\,nA$.* ***(b)*** *shows the same area at a different voltage of $U = +1.5\,V$, $I = 0.1\,nA$. Zoom-ins of the molecules $d^{(i)}$-$d^{(iii)}$ and $m^{(i)}$, labeled in (a) and (b), can be seen in* ***(c)*****-****(f)*** *($U = +1.5\,V$, $I = 0.1\,nA$). The molecules show two different appearances, i.e., four lobes, as it was seen before for the single molecules (c.f. Fig. 9.3) and six lobes. Molecules with the latter amount of lobes are identified as 2III-dimers.*

A possible explanation for these different species is a dimerization of the 2III molecules due to the elevated temperature during heating. Since the appearance of the observed dimers in Fig. 9.3 varies, different configurations seem to be possible, as it will be discussed in the following section.

In STS reproducibly no modification of monomers could be observed after heating the sample to 410°C, as it was measured in Fig. 9.4. In combination with the measurements in Fig. 9.6 on might propose that the irreversible modification, induced by the change of the bias voltage in STS, can also be achieved by heating.

9.5. Adsorption of 2III on a submonolayer *h*BN/Ir(111)

The binding energy of molecules on metals is usually higher than on *h*BN, resulting in a higher molecular coverage on the bare metal, if the molecules are able to diffuse from an *h*BN island to the metal. If the interaction between the molecule and the *h*BN is large enough, the diffusion will be reduced, *i.e.*, the molecule will stick to the *h*BN surface. This interaction between the 2III and the *h*BN substrate will be analyzed by adsorbing the molecules on a submonolayer of *h*BN/Ir(111) at room temperature.

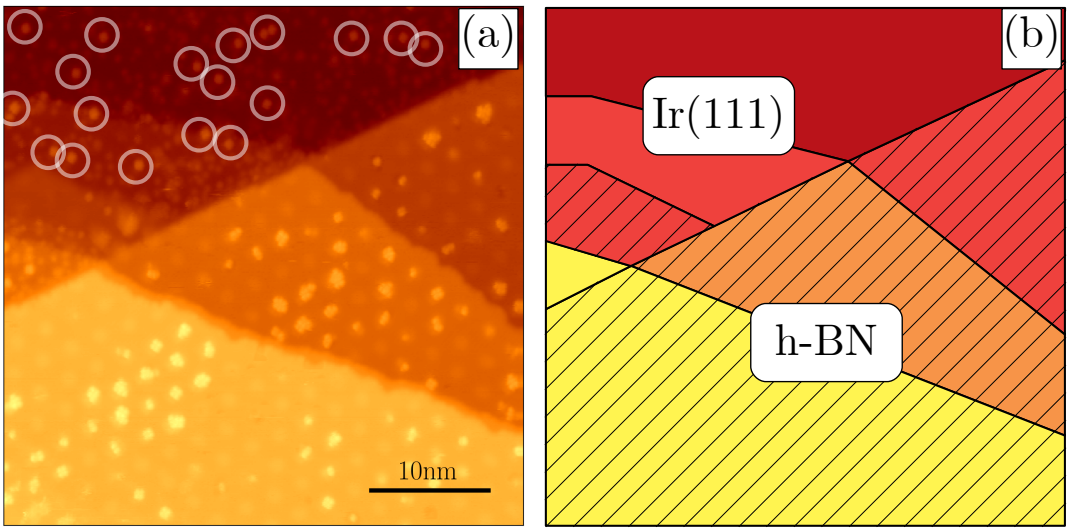

Figure 9.8: *Adsorption of 2III on a submonolayer hBN/Ir(111). The molecules, evaporated at 120°C for 30 s onto the 0.6 ML hBN/Ir(111) surface at room temperature, can be found on both hBN and Ir(111). The submonolayer hBN/Ir(111) sample was prepared as described in section 6.2. The different regions and terraces of the STM image in* ***(a)*** *($U = 1$ V, $I = 0.2$ nA) are sketched in* ***(b)****.*

The surface, covered with ~ 0.6 ML *h*BN, is shown in Fig. 9.8 (a). The molecules adsorb on the *h*BN as well as on the bare metal surface (the different areas are sketched in (b)), meaning that the binding energy of the molecules to the *h*BN is at room temperature, high enough to avoid diffusion onto the metal. On the metal surface, only the bright protrusions, marked by white circles, are 2III molecules, while the rest is contamination

of the metal substrate (see Fig. 9.8 (a)). The measured densities of molecules on the two different substrates are $\rho_{\mathrm{2III/Ir(111)}} = (0.047 \pm 0.005)\,\mathrm{nm}^{-2}$ on the metal and $\rho_{\mathrm{2III/BN/Ir(111)}} = (0.044 \pm 0.009)\,\mathrm{nm}^{-2}$ on the hBN, meaning the coverage of molecules on both substrates is roughly the same and adsorption is not preferred on either of them over the other.

9.6. DFT calculations of the molecular energies

To get a better understanding of the 2III in gas phase and of the molecular adsorption on hBN/Ir(111), DFT calculations were conducted. For this, the projector-augmented plane wave method [144] was used with a plane wave basis set with maximum kinetic energy of 400 eV. The convergence criteria were set to 0.05 eV/Å for the acting forces and 1 μeV for the energy changes. The PBE exchange-correlation potential [94], as implemented in VASP [97, 145, 146], was employed and long-range vdW interactions were included by the DFT-D3 approach, proposed by Grimme *et al.* [147]. The optimization was done at the gamma point of the Brillouin zone. The calculations of the gas phase molecules were performed in an tetragonal cell with a size of $a \times b \times c = (22 \times 22 \times 12)\,\mathrm{Å}^3$. The adsorbed molecules on hBN/Ir(111) were calculated in a hexagonal cell, defined be the three vectors

$$\boldsymbol{a} = \begin{pmatrix} 29.862 \\ 0 \\ 0 \end{pmatrix} \text{ Å}, \qquad \boldsymbol{b} = \begin{pmatrix} -14.931 \\ 25.861 \\ 0 \end{pmatrix} \text{ Å}, \qquad \boldsymbol{c} = \begin{pmatrix} 0 \\ 0 \\ 28.650 \end{pmatrix} \text{ Å}.$$

The energy levels of different modifications of the 2III molecule, *i.e.*, the monomer (M), radicals (R1, R2), biradicals (B1, B2), triradical (T) and dimers (D1 - D3), were calculated for three aspects, *i.e.*, the relative gas phase energy, the adsorption energy on hBN/Ir(111) and the formation energy on hBN/Ir(111). These energies are indicated as horizontal lines – with the corresponding model of the molecule next to it – in Fig. 9.9 and listed in Tab. 9.2. The monomer M is the initial molecule, whose energy is set to 0 eV, shown in Fig. 9.9 (a) and (c). For the formation of a radical by removing one hydrogen, two configurations are possible. The first possibility is the removal of one hydrogen of the iminic nitrogens, resulting in the radical R1 and the second possibility is the removal of the hydrogen of the pyrrolic nitrogen, resulting in radical R2. The removal of a second hydrogen results again in two possible configurations: biradical B1 (only one iminic N binds to an H) and biradical B2 (only the pyrrolic N binds to an H). Removing the last hydrogen bound to a nitrogen results in the triradical T.

Based on these building blocks, numerous variations of dimers are possible. The most probable ones are the dimers D1 - D3 (see models in Fig. 9.9). Dimer D1 is formed by attaching two biradicals B1 with the unsaturated nitrogens together, while the two remaining iminic nitrogens point into opposite directions, *i.e.*, outwards of the resulting molecule. Dimer D2 is also composed of two biradicals B1, where the remaining iminic nitrogens are located on the same side of the resulting dimer. For dimer D3 two triradicals T are attached "head-to-head" with the unsaturated nitrogens.
For a better comparison of the calculated energies, the amount of atoms in each calculation were adjusted in a way that the total number of each atom type is the same for every calculation, *i.e.*, the total number of atoms of two 2III monomers.

The relative ground state energies in the gas phase with respect to the monomer, $\Delta E_{\mathrm{x,gas}}$, of the different molecules x are illustrated in Fig. 9.9 (a). These energies were calculated via the following equation

$$\Delta E_{\mathrm{x,gas}} = \alpha \cdot E_{\mathrm{x,gas-phase}} + \beta \cdot E_{\mathrm{H_2}} - 2 \cdot E_{\mathrm{M,gas-phase}}, \tag{9.1}$$

where the variable x represents the different molecular configurations. The absolute ground state energies of the individual gas phase molecules are given by $E_{\mathrm{x,gas-phase}}$ and the energy of a H_2 atom in gas phase is given by $E_{\mathrm{H_2}}$. By using the coefficients α and β the amount of atoms in the calculation can be adjusted. α adjusts the number of whole molecules and β adjusts the number of additional H_2 molecules, added to the calculation to compensate the hydrogen atoms, removed by radical-formation. The used values for these coefficients are listed in Tab. 9.2.

	M	R1	R2	B1	B2	T	D1	D2	D3
α	2	2	2	2	2	2	1	1	1
β	0	1	1	2	2	3	2	2	3
$\Delta E_{\mathrm{x,gas}}$ [eV]	0.00	4.15	4.27	8.35	8.47	12.70	2.88	3.75	5.98
$E_{\mathrm{x,ads}}$ [eV]	−1.31	−2.78	-	−4.57	-	-	−2.27	−2.36	−2.23
$\Delta E_{\mathrm{x,form}}$ [eV]	0.00	1.22	-	1.84	-	-	3.23	4.02	6.38

Table 9.2: *List of the coefficients α and β used in and Eq. 9.1 and Eq. 9.3 and the resulting energies, shown in Fig. 9.9.*

As a result, the ground state energy of a dehydrogenated molecule is located $\sim 2\,\mathrm{eV}$ (half the value showed in Fig. 9.9 (a) due to the value of $\alpha = 2$ in this case) higher in energy, than its hydrogenated configuration. This energetic difference is the same for the removal

of the first hydrogen (M → R1, R2) as for the second hydrogen (R1, R2 → B1, B2) or the third hydrogen (B1, B2 → T).
The ground state energies of the dimers (shorter green lines in Fig. 9.9) D1, D2 are below the energy of two radicals, meaning that a formation of a dimer (D1, D2) is more favorable, starting from two radicals. The energy of dimer D3 is also lower than the energy of two biradicals, *i.e.*, the two suitable educts to form the dimer D3. Nevertheless, since the energies for the dehydrogenations are very high, even if no energy barriers for these reactions are taken into account, the formation of the different radicals in the gas phase is not very likely.

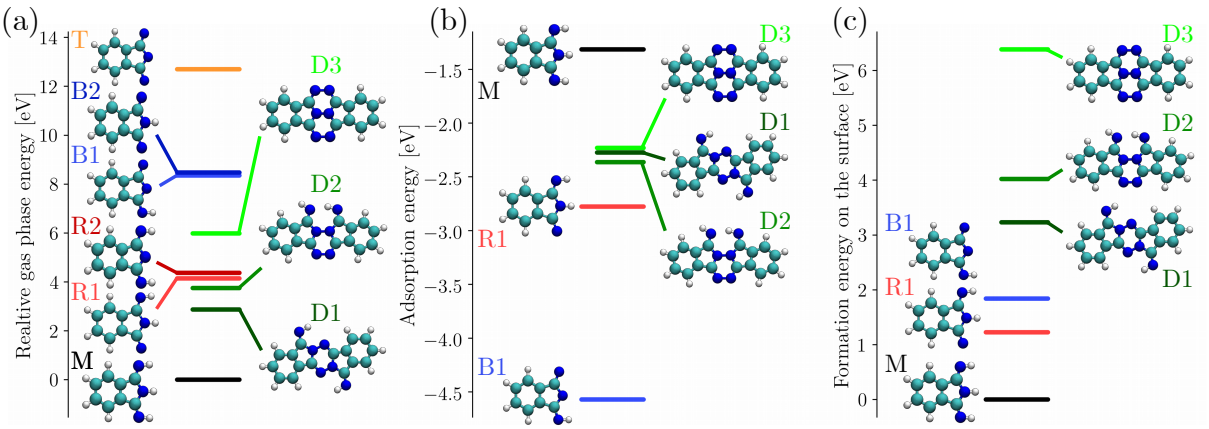

Figure 9.9: *DFT calculations of energetic levels of the different molecular configurations. The configurations are the initial 2III monomer (M), its radicals (R1, R2), its biradicals (B1, B2), its triradical (T) and possible dimers (D1 - D3). In* ***(a)*** *the energies of the individual molecules in the gas phase are calculated with respect to the monomer. The adsorption energies on hBN/Ir(111) are plotted in* ***(b)*** *and the formation energies of the certain products from the monomers on hBN/Ir(111) are shown in* ***(c)****.*

In addition to the gas phase calculations, the molecules were relaxed on the *h*BN/Ir(111) surface. This substrate was relaxed in advance and will be discussed in Appendix A. The adsorption site was chosen to be the pore region of the moiré of *h*BN/Ir(111), since the molecules were found to adsorb there in experiments (c.f. Fig 9.2). Even more precise: the pyrrolic nitrogen atom of the monomer and the radicals was placed initially above the reactive B atom of the *h*BN layer, since the interaction between the molecule and the *h*BN is there presumably the strongest. For the dimers one of the pyrrolic nitrogen atoms were located initially above the reactive B atom of the pore site. The orientation was chosen in a way that one axis of the molecule is aligned with the high symmetry axis of the *h*BN. STM simulations of the adsorbed molecules will be discussed in section 9.7.

From the calculations of the adsorbed molecules, the adsorption energies on hBN/Ir(111) can be determined via

$$E_{\mathrm{x,ads}} = E_{\mathrm{x}/h\mathrm{BN/Ir(111)}} - E_{h\mathrm{BN/Ir(111)}} - E_{\mathrm{x,gas-phase}}. \tag{9.2}$$

Fig. 9.9 (b) illustrates the adsorption energies of some of the previously calculated species. Radical R2 and biradical B2 were not considered for adsorption, since they are energetically less favorable than R1/B1, respectively. Due to the high formation energy, also the triradical T was not considered for adsorption. It should be noted that the adsorption energies are all negative, meaning that the adsorption is favorable. The highest calculated energy gain is observed for the biradical B1, explainable based on the unpaired electrons of the biradical, which can be screened by the substrate after the adsorption.[6] The adsorption energies of the dimers are all in a comparable regime of $\sim -2.3\,\mathrm{eV}$.

With the calculated energies of the adsorbed molecules, the formation of the radicals and the dimers on the surface can also be calculated. This formation energy reflects the difference of the ground state energies of the individual adsorbed molecules. Energy barriers for the corresponding reactions are not taken into account, meaning that energies, most likely higher than the calculated formation energies, are required to trigger the reaction. The calculation of the formation energies was conducted with the following equation

$$\begin{aligned}\Delta E_{\mathrm{x,form}} = \alpha \cdot (E_{\mathrm{x}/h\mathrm{BN/Ir(111)}} - E_{h\mathrm{BN/Ir(111)}}) \\ - 2 \cdot (E_{\mathrm{M}/h\mathrm{BN/Ir(111)}} - E_{h\mathrm{BN/Ir(111)}}) + \beta \cdot E_{\mathrm{H_2}}\end{aligned} \tag{9.3}$$

By comparing these energies (Fig. 9.9 (c)) with the ground state energies of the gas phase molecules (Fig. 9.9 (a)), it turns out that the on-surface formation energies are much lower. For example, the radical R1, resulting from the dehydrogenation of the monomer, is energetically located $\sim 0.6\,\mathrm{eV}$ higher than the monomer itself (again, the listed value needs to be divided by $\alpha = 2$). This difference is 1.5 eV smaller than in the gas phase. Another difference to the gas phase scenario is apparent in the formation energy of the dimers. Neither of them is energetically more favorable than the educts of the dimerisation, *i.e.*, two radicals R1 or two biradicals B1. The formation energy of the most favorable dimer (D1) is located $\sim 2\,\mathrm{eV}$ higher in energy than its educts (R1).

[6] It can be assumed that the adsorption energy of the triradical T is even more negative than that of B1, even though it was not calculated.

9.7. STM simulations of the different molecular species

To compare the different species of the molecule with the experimental results, STM simulations were performed for the molecules adsorbed on the *h*BN/Ir(111) surface. For this an algorithm was implemented, based on the theory of Tersoff and Hamann [70, 178], introduced by Lorente and Persson [179, 180].

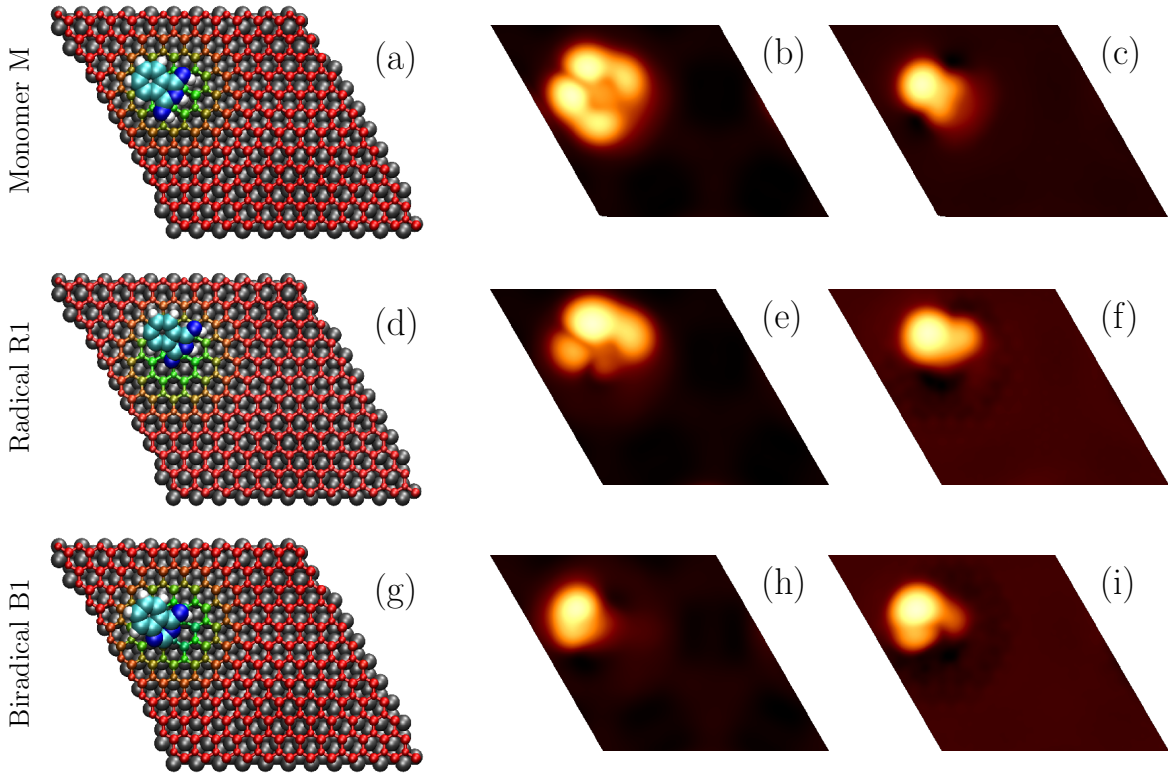

Figure 9.10: *STM simulations of different monomolecular configurations. The monomer M is shown in* ***(a)-(c)****, the radical R1 in* ***(d)-(f)*** *and the biradical B1 in* ***(g)-(i)****. In the left column the adsorbed molecules on the hBN/Ir(111) surface are schematically shown. The supporting hBN layer is color-coded to indicate the height of the B (larger) and N (smaller) atoms (red – far from the Ir(111), green – close to the Ir(111)). In the middle column the simulated STM topographies for the tunneling conditions of* $U = +1.5\ V$, $I = 0.1\ nA$ *can be seen and in the right column for the conditions of* $U = -1.0\ V$, $I = 0.1\ nA$.

The simulations of the monomer M, the radical R1 and the biradical B1 are illustrated in Fig. 9.10 (a)-(c), (d)-(f) and (g)-(i), respectively. In the left column the relaxed models are shown schematically. The color of the supporting *h*BN-layer represent the z-position of the B (larger spheres) and N (smaller spheres) atoms (red – far from the Ir(111), green – close to the Ir(111)). In the center column the simulation for the tunneling conditions

of $U = +1.5\,\mathrm{V}$ and $I = 0.1\,\mathrm{nA}$ are shown, while in the right column the simulation for $U = -1.0\,\mathrm{V}$ and $I = 0.1\,\mathrm{nA}$ can be seen.
By comparing the simulations with the STM images of the single molecules in Fig. 9.3, one can observe that the best agreement is achieved for the monomer. The molecule is aligned with the high symmetry axis of the moiré, and thus with the high symmetry direction of the *h*BN lattice. In the simulation at a bias voltage of $U = +1.5\,\mathrm{V}$, four lobes are visible, as in the experimental image. A deviation from the experiment can be observed regarding the intensity of the lobes. In the experiment the laterally more extended lobes are more intense than the smaller ones. This is reversed in the simulation. A possible explanation could be the tilting angle of $\sim 5°$, with respect to the surface plane, observed in the simulation. If this angle is overestimated in the relaxation, the intensity could be misleading, as well. At the negative voltage of $U = -1\,\mathrm{V}$ the molecular appearance of a single protrusion in the simulation reflects the experimental contrast.
The radical R1 was adsorbed in a way, that the outer N atom, where the hydrogen atom was removed, was initially located vertically above the reactive B atom. The appearance in the STM simulations of this species at positive bias voltage does not correspond to the experimentally observed appearance, while it could still match the experiments at negative voltages.
This applies also to the biradical B1, where the hydrogens of the pyrrolic and one iminic nitrogen are removed and the pyrrolic N was placed initially above the reactive B. A closer observation reveals that the molecule changed its structure during the relaxation. The pyrrole ring was opened and the unsaturated iminic N atom was incorporated into the ring structure to form a six-membered ring. This reaction is quite unlikely, since the energy barriers for such a reaction are quite high [195, 196]. The STM simulation of this configuration at positive bias voltage does not correlate with the experimentally obtained data.

The simulations of the dimers are shown in Fig. 9.11. By comparing them with the experiments, illustrated in Fig. 9.7, a possible assignment of the molecules could be conducted as such: Dimer $\mathrm{d}^{(\mathrm{i})}$ and $\mathrm{d}^{(\mathrm{ii})}$ of Fig. 9.7 have the best correlation with dimer D1 in Fig. 9.11 (a)-(c). At a positive bias voltage of $U = 1.5\,\mathrm{V}$, the six lobes are separated in two rows with different brightness. For the negative bias voltage of $U = -1\,\mathrm{V}$, the two molecules $\mathrm{d}^{(\mathrm{i})}$ and $\mathrm{d}^{(\mathrm{ii})}$ appear as two protrusions with a bit of additional finer structure in between, matching the simulation of Dimer D1 (c.f. Fig. 9.7 (a) and Fig. 9.11 (c)). By taking a closer look at the zoom-ins Fig. 9.7 (c),(d), the appearance of $\mathrm{d}^{(\mathrm{ii})}$ fits better to

D1, because of the tendency towards a point-symmetric object. This can be even better observed by the model of this dimer with its perfect point-symmetry in the gas phase (c.f. model of D1 in Fig. 9.9 (a)). The simulation, correlating the best with dimer $d^{(iii)}$ in Fig. 9.7 is observed for the simulated dimer D2. For the positive bias voltage of $U = 1.5\,\mathrm{V}$, the lobes are also alternately ordered ($\because$) from bottom-left to top-right (c.f. D2 in Fig. 9.9 (e)). The central lobe in the simulation is not as pronounced as in the experiment but is still in correlation. At $U = -1\,\mathrm{V}$ the molecule shows a kinked form in Fig. 9.7 (a). The simulation in Fig. 9.11 (f) only shows two lobes with a very faint additional intensity at the bottom-right side of the molecule. The dimer D3 does not correspond to the measured data. The pronounced lobe, as it can be seen in Fig. 9.11 (h) could not be observed.

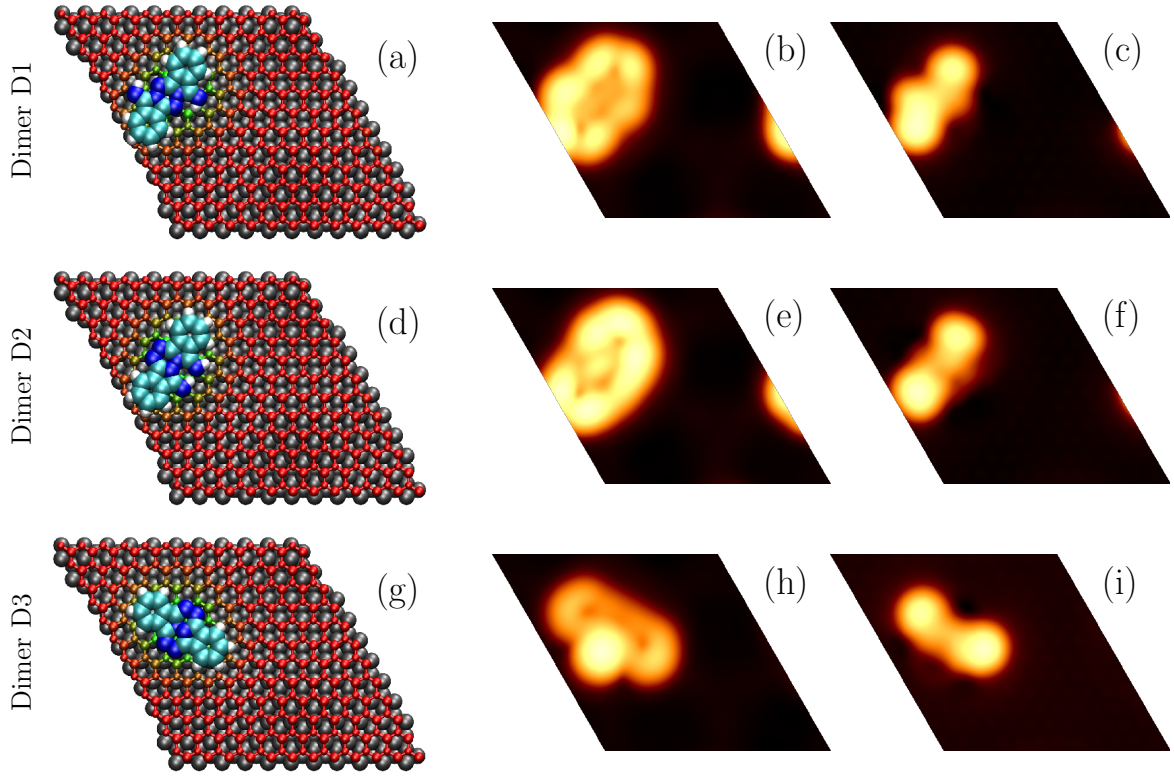

Figure 9.11: *STM simulations of the different dimers. The names of the dimers are labeled on the left. In the left column the adsorbed molecules on the hBN/Ir(111) surface are schematically shown. The supporting hBN-layer is color-coded to indicate the height of the B (larger) and N (smaller) atoms (red – far from the Ir(111), green – close to the Ir(111)). In the middle column the simulated STM-topographies for the tunneling conditions of $U = +1.5\,V$, $I = 0.1\,nA$ can be seen and in the right column for the conditions of $U = -1.0\,V$, $I = 0.1\,nA$.*

9.8. Summary and outlook

In summary, the functionalization of *h*BN/Ir(111) by the small molecule 2III, a model system for a Pc-fragment [66], was observed. It was concluded that the small molecules observed in the experiments of $CePc_2$/*h*BN/Ir(111) in section 8 are indeed derived from 2III. The 2III molecules adsorb in the pore regions of the moiré of *h*BN/Ir(111) and are quite strongly bound there, since they are not mobile enough to make it out of the pores at room temperature, despite their small size. The strong binding was experimentally demonstrated by measuring the temperature induced desorption of the 2III from the surface by XPS. The molecules were still present on the surface even after heating the sample to 410°C, yielding an indication for a covalent bonding. A consequence of this heating is the dimerization of the molecules, noticed by the change in the appearance in STM. These dimers are not identical, but have different forms. By measuring STS on the single 2III, a irreversible modification of the molecule was observed. After heating the sample to 410°C, this modification by STS was not observed anymore. Based on these results, one might propose a molecular adsorption in two phases: in phase (i) the molecule should be bound relatively weakly to the *h*BN but still strong enough to stick to the pore sites of the moiré. Upon heating or by increasing the bias voltage, the molecule might be irreversibly modified, resulting in an adsorption in phase (ii). The molecule could form a covalent bond between a nitrogen and a boron atom of the *h*BN layer in phase (ii). This could be achieved by a dehydrogenation of the molecule [25, 184, 197–200]. Therefore, a hydrogen would be removed from one of the nitrogen atoms. Another possible modification could be a change in the electronic structure of the molecule, *i.e.*, a breaking of the iminic C=N double bond, resulting in a covalent, thus more stable bond to the underlying B atom.
For a better understanding of the energetics and to simulate topographic STM images, DFT calculations were conducted. These calculation provided insights into the adsorption and formation energies of the different molecular species, *i.e.*, the single molecule, its dehydrogenated forms and suitable dimers. Since the DFT simulated STM images of the radical R1 (H was removed from the iminic N) and the biradical B1 (an additional H was removed from the pyrrolic N) show no similarities with the experimentally observed molecules, as it is the case for the monomer M, the hypothesis of dehydrogenation remains questionable. It is still possible that the radical R2, missing a H at the pyrrolic N, which was not simulated, fits to the experimentally obtained data. Nevertheless, a change in the electronic structure in form of a bond rearrangement seems more likely. Another possible modification could be a dehydrogenation of the carbon atoms in the phenyl ring. However, by comparing the experimental data with the simulated ones, most of the molecules could

be identified and potential dimer configurations could be assigned. The small differences in the appearance between simulation and experiment could be explained by different adsorption sites, leading to a slightly different twisting or tilting of the molecule. Since STM is very sensitive to small height deviations, this effect could influence the appearance immensely.

To obtain an extensive understanding of the system and especially of the 2III-dimers, high resolution AFM measurements would be helpful in analyzing the structure of these molecules. With this, an unambiguous assignment of the dimers to the models could be achieved. In the future, the 2III molecules could be chemically modified in a way that additional molecules could be attached at the backbone, *i.e.*, the benzene ring. Based on the strong binding and the thermal stability of these molecule on the *h*BN/Ir(111) they could be used to functionalize the *h*BN. As these molecules favor an adsorption on the pore sites of the moiré, an array formation of the desired molecule could be possible for future applications as for example organic solar cells [182] or nano-electronics [201].

10. DFT calculations on novel tetrapyrrol-based double- and multidecker complexes

In this section different tetrapyrrolic-multidecker complexes were investigated theoretically with DFT to support experimental data. This data was acquired by others, named in detail in the corresponding subsection. These calculations can provide additional insights into molecular properties like the structure and magnetism and to compare them with the experimentally obtained results.
The following DFT calculations were performed using the projector-augmented plane wave method [144, 146]. A plane wave basis set with a maximum kinetic energy of 400 eV was used. Structures were relaxed until the acting forces were smaller than 0.05 eV/Å and energy differences were smaller than 1 μeV. The PBE exchange-correlation potential [94] as implemented in VASP [97, 98, 145, 146] was employed. If it is specified, long-range vdW interactions were taken into account by the DFT-D3 approach proposed by Grimme *et al.* [147]. All structures were optimized at the gamma point of the Brillouin zone. For STM-simulations an algorithm, based on the theory of Tersoff and Hamann [70, 178] and introduced by Lorente and Persson [179, 180], was used.

10.1. Structural analysis of $Gd_{x-1}Pc_x$ multideckers

This section includes content that has been published in:

Urgel, J. I., Ecija, D., Vijayaraghavan, S., Pörtner, M., Bocquet, M.-L., Auwärter, W. & Barth, J. V. In-Situ Growth of Gadolinium Phthalocyaninato Sandwich Complexes on the Ag(111) Surface. *ChemPhysChem Commun* **20**, 1–5. (2019). [65], Copyright by John Wiley & Sons, Inc.

As a support for the experimental study of $Gd_{x-1}Pc_x$ by STM, done by J. I. Urgel, D. Ecija, S. Vijayaraghavan, W. Auwärter and J. V. Barth, $Gd_{x-1}Pc_x$ multideckers were theoretically modeled. The goal of this analysis was to find the most stable structure of $Gd_{x-1}Pc_x$ concerning the in-plane rotation angles of all individual Pc molecules. Due to the π-bonding-systems of the Pcs, vdW interactions were considered in the calculations. The f-electrons of the Gd atoms were included in the core so that the non-magnetic calculations were conducted. The cubic unit cell of the calculation has a size of 25 Å^3.

For the construction of a multidecker a single dehydrogenated Pc was used as the base molecule. The Gd atom was then placed 0.18 nm above the center of this first Pc. To calculate the energetically most favorable rotation of the upper Pc, in each multidecker, the topmost Pc was placed 0.18 nm above the last Gd atom and rotated in four different angles, *i.e.*, $\phi(x) \in [35°, 45°, 55°, 65°]$ for odd values of x and $\phi(x) \in [-10°, 0°, 10°, 20°]$ for even values of x. The angle dependent ground state energies of the relaxed multideckers were than fitted to a cosine function $E(\phi) = E' \cdot \cos[4 \cdot (\phi - \phi_0)] + E_0$. After obtaining the optimal rotation of the upper Pc of the first multidecker, *i.e.*, for $x = 2$, the same procedure was applied for $x = 3$, $x = 4$ and $x = 5$, consecutively. Gradually, the properties of the multideckers with $x \in [2, 5]$ were calculated and are listed in Tab. 10.1. The fitting of the angle dependent energies is shown in Fig. 10.1. Based on the fitted angles it is to be observed that the topmost Pc is rotated by $\sim 45°/\sim 0°$ with respect to the bottom Pc if the number of Pcs is even/odd, which can be explained by the reduced repulsive interaction between the benzene rings of the adjacent Pcs.

Molecule	ϕ [°]	$E(\phi)$ [eV]	h_{N4} [nm]	Molecule	ϕ [°]	$E(\phi)$ [eV]	h_{N4} [nm]
$GdPc_2$	35.708	-838.913	0.305	Gd_3Pc_4	35.036	-1690.323	0.973
$x = 2$	44.883	−839.030	0.304	$x = 4$	44.884	−1690.345	0.976
	54.222	−838.914	0.306		54.839	−1690.311	0.973
	63.954	−838.628	0.310		64.859	−1690.271	0.975
Gd_2Pc_3	0	−1265.151	0.635	Gd_4Pc_5	0	−2115.488	1.313
$x = 3$	9.870	−1265.082	0.637	$x = 5$	9.830	−2115.451	1.308
	19.852	−1264.579	0.667		19.896	−2115.425	1.307
	80.101	−1265.120	0.634		80.096	−2115.465	1.307

Table 10.1: *Obtained values for rotation angle, energy and height of the relaxed $Gd_{x-1}Pc_x$ complexes. The height was calculated by taking the difference between the averaged z-coordinates of the four inner N atoms of the topmost and the bottom Pc as indicated by the index $N4$, similar the labeling in [177].*

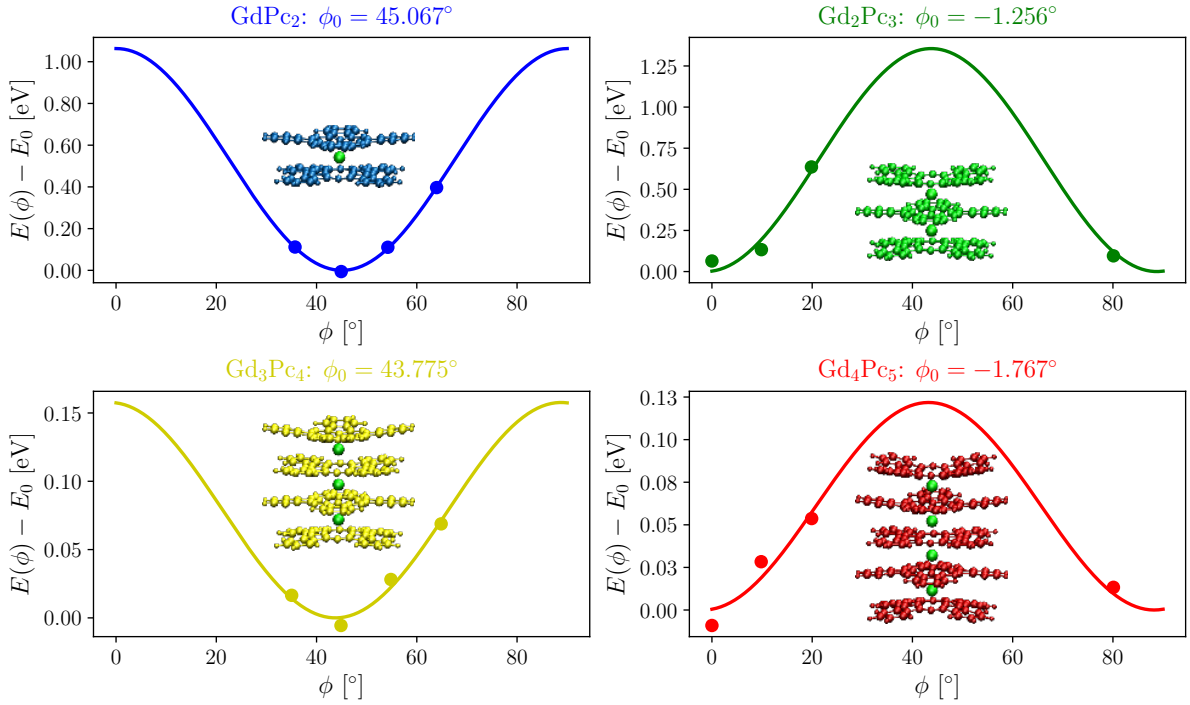

Figure 10.1: *Fitting of the rotation angles of $Gd_{x-1}Pc_x$ multideckers. The shifted ground state energy $E(\phi) - E_0$ depends on the rotation angles of the upper Pcs in each molecule. The insets show models of the relaxed molecules with the lowest energy.*

Based on observations of the rotation of all Pcs in the complexes, illustrated in Fig. 10.2 (a), the same trend of alternating rotation can be noted in the middle Pcs. The corrugation of each Pc molecule in each complex is shown in Fig. 10.2 (b). As a result, the corrugation of the outer Pcs is the largest as the repulsive force between the Pcs is now only acting in one direction. The corrugation decreases from the outer Pcs to the central ones.
A comparison of the optimal, theoretically obtained rotation angles with the experimentally found rotation angles of the topmost Pc, with respect to the bottom one, is illustrated in Fig. 10.3. The areas reflect the range of the experimentally measured angles. The lines indicate the fitted values for the different multideckers. The results are in good agreement, since the theoretic rotation angles are all in the error range of the experimentally obtained ones.

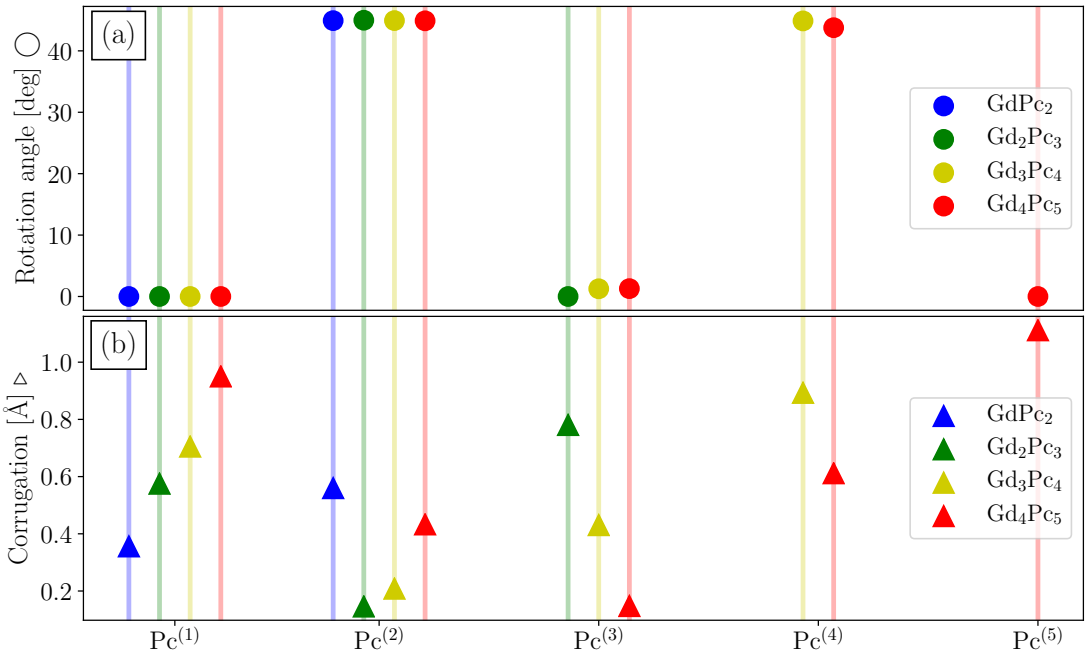

Figure 10.2: *Rotation angles and corrugations of all Pcs. The rotation angles of all Pcs in the complexes with the lowest calculated energy are shown in* ***(a)*** *and the corrugation is shown in* ***(b)****.*

To analyze how much energy is gained by the formation of a multidecker is calculated, *i.e.*, the difference between the energy of a certain multidecker and the sum of energies of the next smaller complex, a single Pc and one Gd-atom:

$$\Delta E_x = E_{\mathrm{Gd}_{x-1}\mathrm{Pc}_x} - \left[E_{\mathrm{Gd}_{x-2}\mathrm{Pc}_{x-1}} + E_{\mathrm{Pc}} + E_{\mathrm{Gd}}\right], \tag{10.1}$$

where $E_{\mathrm{Pc}} = -410.198\,\mathrm{eV}$ is the energy of a single Pc and $E_{\mathrm{Gd}} = -0.064\,\mathrm{eV}$ is the energy of a single Gd-atom.

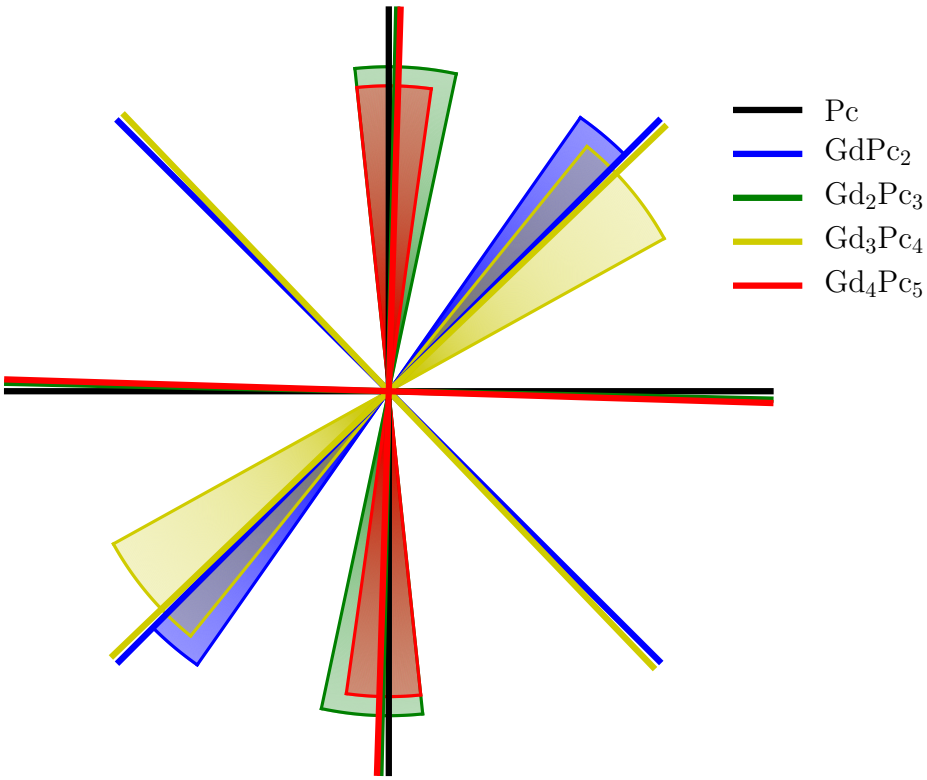

Figure 10.3: *Comparison of theoretical and experimentally obtained rotation angles. The lines indicate the calculated rotation angles between the topmost and the bottom Pc and the areas show the experimentally obtained ones.*

The energy gain for values of $x \in [2, 5]$ is shown in Fig. 10.4. The formation of any complex out of its parts is energetically more favorable, since their formation energy is negative. Nevertheless, more energy is gained by the formation of $GdPc_2$ from two Pcs and a Gd ($-18.563\,\text{eV}$), than by the formation of a Gd_4Pc_5 from a Gd_3Pc_4, a Pc and a Gd ($-14.876\,\text{eV}$). The trend shows that the energy gain converges for $x \geq 4$, meaning that as soon as all molecules on the surface consist out of more than four Pcs, there is no preferred position to continue the growth of a multidecker.

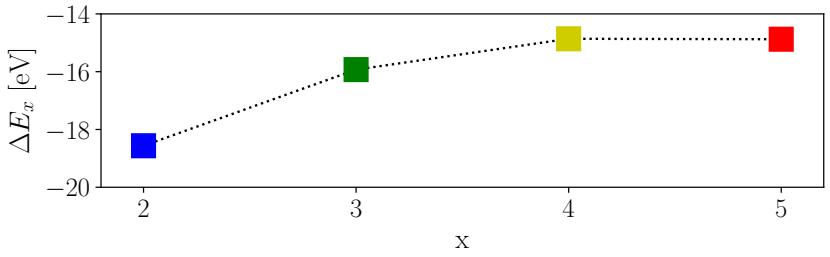

Figure 10.4: *Energy gain for the formation of a multidecker. The formation energy of a multidecker is calculated from the next smaller complex, a Pc and a Gd-atom. The values were calculated by Eq. 10.1.*

In summary, the rotational alignment of Pcs in multideckers, proposed based on experimental observations could be confirmed. The calculatons provided additional insight to rationalize the experiments and the resulting multidecker structures. Also the calculated formation energies of the multideckers matches the measured surface coverage of $Gd_{x-1}Pc_x$ /Ag(111), where the number of observed molecules decreases with the size (see Fig. 3 in [65]). Discrepancies between calculations and experiments occurred regarding the height of the multideckers, which were larger in the calculations. An explanation for this could be the supporting Ag(111) substrate in the experiments. Due to the interaction of the bottom Pc with the silver substrate, the corrugation of this Pc could be reduced, resulting in a smaller total size of the molecule. Another explanation could be the underestimation of the attractive vdW interactions between the Pcs by the DFT calculations, resulting in larger distances between these planes.

10.2. Adsorption of $Th(TPP)_2$ doubledeckers on Ag(111)

To support the experimental STM studies of $Th(TPP)_2$/Ag(111) by Erik Rheinfrank [202], DFT calculations of this molecule were performed. As the molecule physisorbs on the surface, vdW interactions need to be taken into account in this calculation. To treat possible magnetic properties of the f-electrons, spin-polarization was also included in the calculations. The gas phase molecule, adapted from $Ce(TPP)_2$ (c.f. Supporting information in [191]) by replacing the Ce-atom with Th, was calculated in a tetragonal unit cell with a real space size of $a \times b \times c = 25\,\text{Å} \times 25\,\text{Å} \times 20\,\text{Å}$. The adsorption of the $Th(TPP)_2$ was done on a $8 \times 8 \times 4$ Ag(111) slab in an hexagonal unit cell spanned by the real-space lattice vectors

$$\boldsymbol{a} = \begin{pmatrix} 23.027 \\ 0 \\ 0 \end{pmatrix} \text{Å}, \qquad \boldsymbol{b} = \begin{pmatrix} -11.514 \\ 19.942 \\ 0 \end{pmatrix} \text{Å}, \qquad \boldsymbol{c} = \begin{pmatrix} 0 \\ 0 \\ 36.096 \end{pmatrix} \text{Å}.$$

The relaxed gas phase molecule, shown in Fig. 10.5 has a ground state energy of $-1079.5\,\text{eV}$ and carries no magnetic moment. This non-magnetic behavior was determined, even when using the LSDA+U method with values for the on site Coulomb interaction of $2\,\text{eV} \leq U \leq 10\,\text{eV}$. The ground state energy of the molecules with a fixed spin of $s = 1/2$ is $\sim 0.7\,\text{eV}$ higher, than the ground state energy of the non-magnetic molecule, making it less favorable.

An interesting aspect pertaining to this structure, is the tilting of the phenyl and pyrrole moieties, shown in Tab. 10.2. In the upper TPP two phenyl rings, called ph-u1, are almost perpendicular to the plane spanned by the N-atoms. The other two phenyl rings, called ph-u2, are rotated a bit more towards the plane. These different phenyl groups are marked in Fig. 10.5 (a). All pyrrole groups of the upper layer are tilted approximately by the same angle with respect to the N-plane. The angles of the pyrroles were calculated via $\alpha_{\text{py}} = 90° - 0.5 \cdot \arccos\left(\frac{\boldsymbol{a}\cdot\boldsymbol{b}}{|\boldsymbol{a}||\boldsymbol{b}|}\right)$, where $\boldsymbol{a} = (\boldsymbol{a}_1 - \boldsymbol{a}_2) \times (\boldsymbol{a}_1 - \boldsymbol{a}_3)$ and $\boldsymbol{b} = (\boldsymbol{b}_1 - \boldsymbol{b}_2) \times (\boldsymbol{b}_1 - \boldsymbol{b}_3)$ are the normal vectors of opposite pyrrole planes, defined by the N atom and the two opposite C atoms ($\boldsymbol{a}_i$, $\boldsymbol{b}_i$). The tilting angle of the phenyl groups are calculated via $\alpha_{\text{ph}} = 0.5 \cdot \arccos\left(\frac{\boldsymbol{a}\cdot\boldsymbol{b}}{|\boldsymbol{a}||\boldsymbol{b}|}\right)$, where $\boldsymbol{a} = (\boldsymbol{a}_1 - \boldsymbol{a}_2) \times (\boldsymbol{a}_1 - \boldsymbol{a}_3)$ and $\boldsymbol{b} = (\boldsymbol{b}_1 - \boldsymbol{b}_2) \times (\boldsymbol{b}_1 - \boldsymbol{b}_3)$ are the normal vectors of the phenyl planes, defined by three C atoms ($\boldsymbol{a}_i$, $\boldsymbol{b}_i$).

The tilting of the ligands in the bottom TPP varies. The phenyls are all tilted with a similar angle but the pyrrols are tilted differently. Two of them are lying flat in the N-plane but the other two, called py-b and marked in Fig. 10.5 (b), are tilted more downwards.

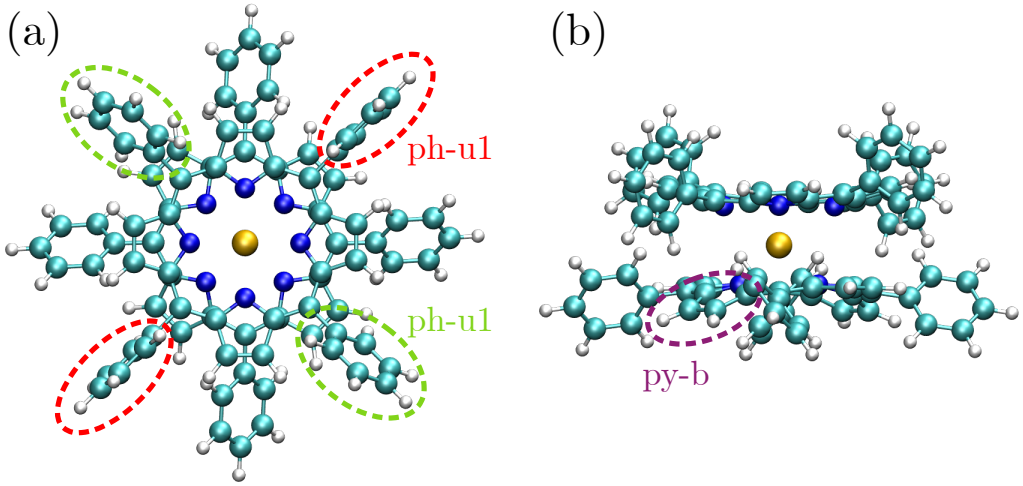

Figure 10.5: *Molecular structure of Th(TPP)$_2$ in the gas phase. The top view is shown in* **(a)** *with the two differently tilted type of phenyls in the upper TPP marked with red (ph-u1) and green (ph-u2) and the side view in* **(b)** *with the stronger tilted pyrrol groups marked with purple (py-b). Atom colors: C - light blue, H - white, N - dark blue, Th - yellow.*

In general, one would expect a symmetric tilting of both ligands, since in gas phase there is no difference between the "upper" and the "bottom" TPP. The difference originates from the used adapted configuration, *i.e.*, the configuration of the adsorbed Ce(TPP)$_2$ [191]. In the optimization process, this configuration converges in a local minimum. In the adsorbed molecule, there is a difference between the ligands, since one of them interacts with the substrate.

	Rotation-/tilting angle	
Ligand	gas phase	adsorbed on Ag(111)
Pyrrole upper TPP	18.34°	13.27°
Pyrrole bottom TPP – py-b	25.73°	25.78°
Phenyl bottom TPP	49.85°	42.69°
Phenyl upper TPP – ph-u1	86.42°	86.40°
Phenyl upper TPP – ph-u2	66.16°	66.18°

Table 10.2: *Tilting of the ligands in the gas-phase Th(TPP)$_2$ and the adsorbed molecule on Ag(111). The tilting angle of the two pyrroles of the bottom TPP (not listed) are tilted with a negligible angle with respect to the N plane.*

Due to adsorption of the $Th(TPP)_2$ on Ag(111) (see Fig. 10.6) some tilting angles change. The largest change can be observed by the phenyl groups of the bottom TPP. They adapt a smaller rotation angle, as they interact with the surface. Therefore, the repulsion between the bottom phenyl and the upper pyrrole groups is reduced, leading to a flattening of the pyrrol groups of the upper TPP. The resulting rotation angles are also listed in Tab. 10.2.

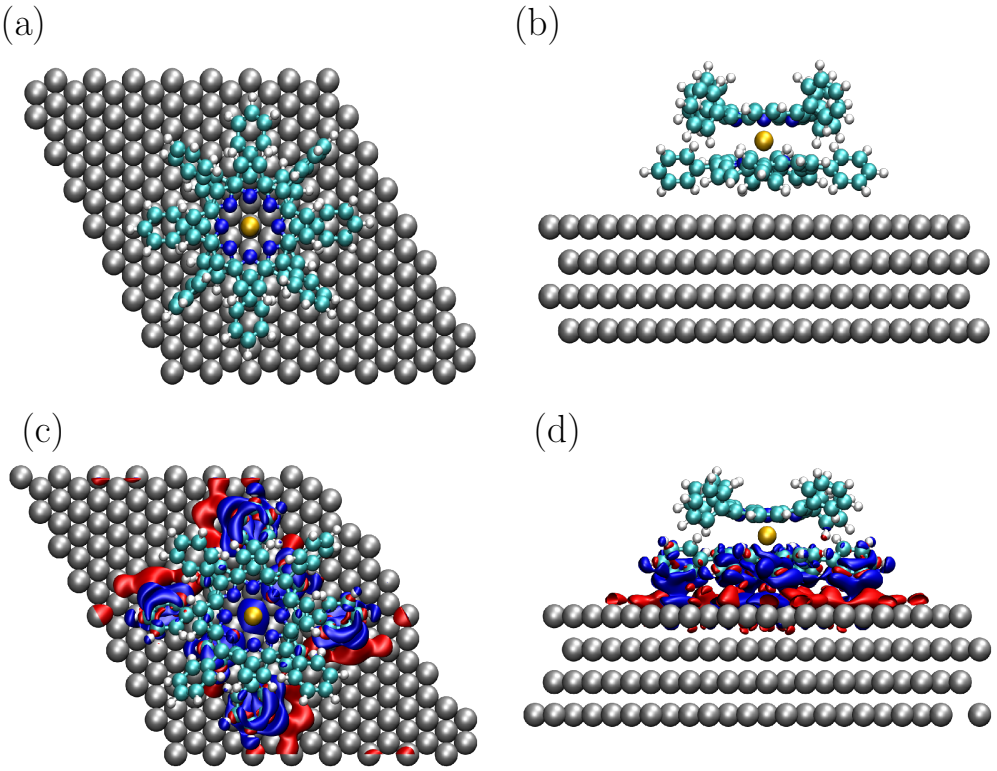

Figure 10.6: *Adsorption of $Th(TPP)_2$ on Ag(111). The top view is shown in* ***(a)*** *and from the side in* ***(b)****. The colors are the same as in Fig. 10.5 with Ag - silver. In* ***(c)*** *and* ***(d)*** *the charge density difference can be seen from top and side view, respectively. The red color shows an electron accumulation and the blue color shows an electron depletion.*

In the process of adsorption, the energy of the system is lowered by $-3.479\,\text{eV}$ and the charge density changes. This is portrayed in the charge density difference in Fig. 10.6 (c) and (d), reflecting the difference of the whole system compared to the two separated subsystems ($Th(TPP)_2$ and Ag(111) substrate). The red color represents an electron accumulation, mainly found on the surface. The complementary electron depletion (blue color) can be found on the bottom TPP of the molecule and its interface with the surface. The upper TPP is not involved in the process of adsorption as the charge there is not changed significantly.

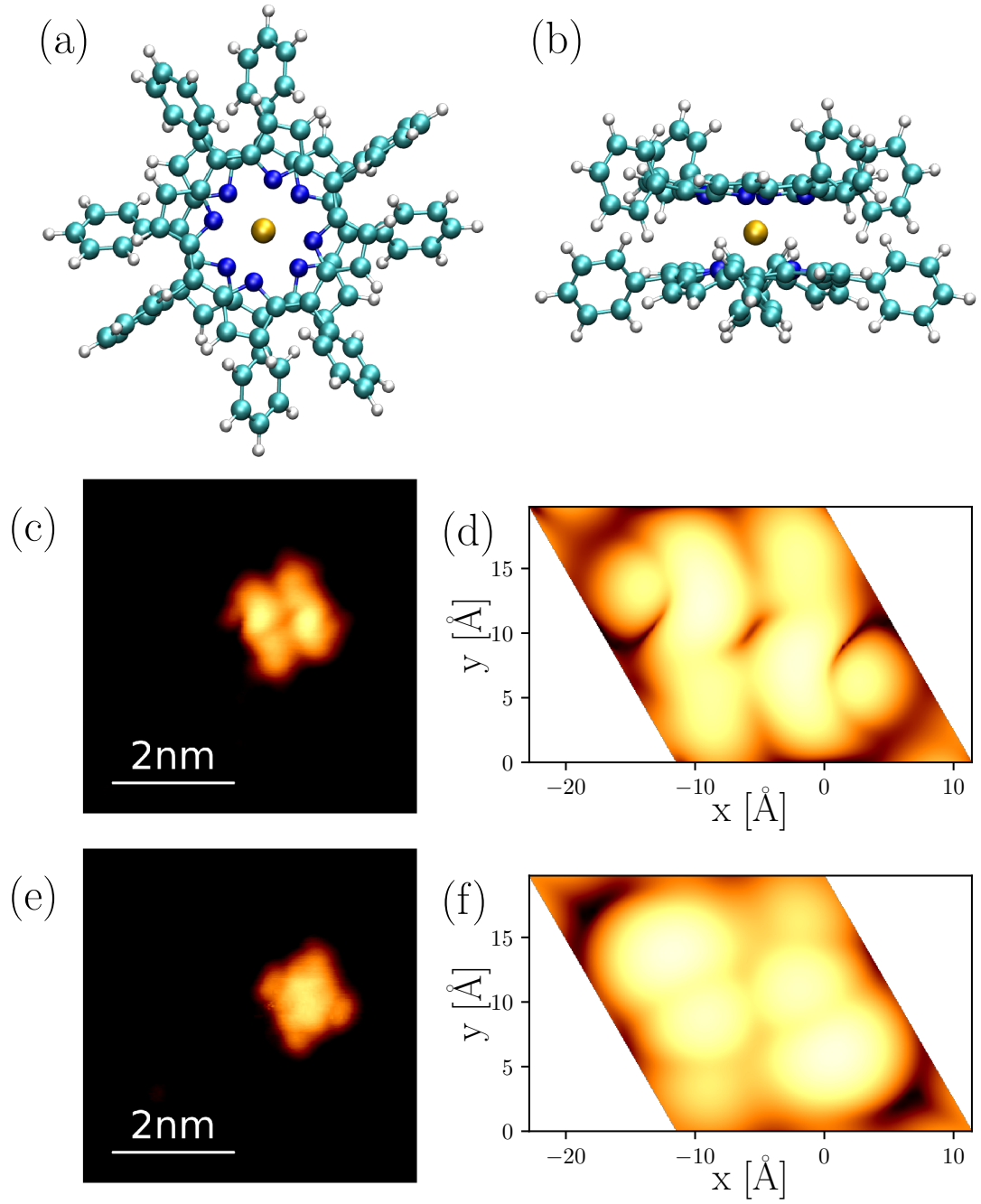

Figure 10.7: *STM simulation of $Th(TPP)_2$. Gas phase and adsorbed $Th(TPP)_2$ molecules, whose upper TPP is rotated by 33° with respect to the bottom one. In* ***(a)*** *and* ***(b)*** *the top and side view of the gas phase molecule are shown.* ***(c)*** *and* ***(e)*** *show the measured STM images of the double-decker,* ***(d)*** *and* ***(f)*** *the simulations. The scanning/simulation conditions are: (c): $U = 0.9\,V$, $I = 0.11\,nA$, (d): $U = 1.0\,V$, $I = 1\,pA$, (e): $U = -1.5\,V$, $I = 0.11\,nA$, (f): $U = -2.0\,V$, $I = 1\,pA$.*

Experimentally another configuration of the molecule was observed, where the upper TPP is rotated by $\sim 33°$ with respect to the bottom one (c.f. [203]). The calculated ground state energy of this molecule, shown in the gas phase in Fig. 10.7 (a), (b), turned out to be $-1079.480\,\text{eV}$, almost identical to the one with a 45° angle between the two TPPs. By adsorbing this molecule on Ag(111) the calculated adsorption energy is $-3.534\,\text{eV}$ and is therefore more favorable compared to the one, where the TPPs are 45° rotated with respect to each other. For a comparison of the experimental and the theoretical results, STM images of the molecule, with the upper TPP, rotated by 33°, were simulated and compared with the measured ones as shown in Fig. 10.7. In Fig. 10.7 (c) the molecule scanned at a bias voltage of 0.9 V is shown. The simulated image at 1.0 V in Fig. 10.7 (d) looks very similar concerning the two pronounced opposite legs (top left and bottom right). At negative voltages the agreement is not as optimal as for positive voltages. Fig. 10.7 (e) portrays the molecule, scanned at $-1.5\,\text{V}$. The simulation at $-2.0\,\text{V}$ shows also a pronounced feature in the center, as it can be seen in the STM image, but the intensity at two opposite corners of the molecule is not observed in experiment. A reason for the deviation might be that the measured double-decker is embedded in a monolayer of 2H-TPPs in experiment, which could lead to additional features in the appearance. In the simulation, a single double-decker was placed on the Ag(111) substrate, without neighboring 2H-TPPs. In addition, the structure of the molecule could be close to the simulated one but may differ for the rotation/tilting of some subgroups. This would have a small influence on the energetics, but since STM is very sensitive to height changes, this could modify the appearance of the molecule.
Nevertheless, these calculations gave additional insights into the intramolecular structure and the energetics of the $ThTPP_2$ in the gas phase and upon adsorption on Ag(111).

Part V.
Summary and outlook

In this thesis phthalocyanine-complexes, adsorbed on hBN templates, were studied. This decoupling layer reduces the influence of the metal substrates, so that electronic states of the molecules do not hybridize strongly with the metal [38]. Additionally, adsorbed molecules can follow the hBN/metal superlattice, resulting in a periodic arrangement of molecules on the surface. As the hBN layer is only one atom thick, an analysis with surface sensitive techniques, such as STM or STS, is still possible. The experimental results were supported by theoretical simulations with DFT.

In section 7 the charge state control of F_{16}CoPc on hBN/Cu(111) by three crucial parameters was demonstrated. These parameters are the template induced gating, based on the electronic corrugation of the underlying substrate [38, 56], the tip induced gating, due to the electric field between the STM tip and the sample [57, 126–128, 131, 132] and the screening by neighboring molecules [41, 124]. As a result, the LUMO of the molecule, becoming occupied upon adsorption at the pore regions of the hBN/Cu(111) moiré [56, 135], can be shifted by each of these three parameters by $\sim 0.3\,\mathrm{eV}$. As the orbital is initially located at $\sim -0.7\,\mathrm{eV}$, the LUMO can be shifted across E_F, thus changing the charge state of the molecule. This change of the charge state, actively induced by the field of the STM-tip, can be detected in STS by a sharp feature at the opposite polarity compared to the molecular orbital. AFM measurements revealed that a simultaneous charging of multiple molecules at the same time is possible. The influence of the simultaneously charged molecules on each other is rather small compared to the three main parameters that control the charge state. A comparison with F_{16}CoPc adsorbed on hBN/Ir(111) showed two main differences: the template induced gating is with 0.4 eV slightly stronger than on hBN/Cu(111) [38, 61], leading to a larger energetic shift of the molecular orbital for molecules adsorbed on different sites of the moiré. Further the size of the moiré leads to

an adsorption of only one F_{16}CoPc per pore site [58], meaning that additional molecules automatically adsorb on the wire regions, where the molecules exhibit a different charge state. Therefore, the pattern of differently charged sites on the surface is more dense than on *h*BN/Cu(111). DFT calculation showed that an adsorption of small gas molecules is favored on neutral molecules over negatively charged molecules. This tendency can also be seen for the growth of the second layer of F_{16}CoPc/*h*BN/Cu(111), starting in contrast to the first layer at the wire regions of the moiré, where the first layer molecules are in some instances not negatively charged anymore, but neutral.
This molecular adsorption on F_{16}CoPc/*h*BN needs to be studied in more detail to prove the templating nature of this system for additionally adsorbed molecules.
These results of the charge state control indicate the potential of this system, since the understanding of the molecular charging is key for future applications such as solar cells, catalysts or microelectronics.

Section 8 presented the results of Ce-Pc multideckers on *h*BN/Ir(111). The evaporation of intact $CePc_2$ doubledecker molecules could be demonstrated, resulting in an adsorption of single $CePc_2$ on pore regions of the *h*BN/Ir(111) moiré. The unstable appearance of these single $CePc_2$ in STM raises the hypothesis that the upper Pc of those molecules is not static but exhibits a STM-induced switching. Beside the single $CePc_2$ doubledeckers, Ce_2Pc_3 tripledecker islands were also observed on the surface. In these islands the appearance of the molecules is no longer unstable, leading to the conclusion that the rotation of the upper Pcs in the island is suppressed. Simulated STM images were compared to the experimental data. The appearance of the measured tripledecker molecules in the island correlated quite well the appearance of the simulated doubledeckers. By superimposing the simulated images of two $CePc_2$ with different rotations of the upper Pc, with respect to the bottom one, *i.e.*, 0° (called parallel) and 45° (called rotated), the appearance matches better the one observed for the single $CePc_2$/*h*BN/Ir(111). The growth of Ce-Pc multideckers was achieved in-situ by the metalation of a 2H-Pc multilayer, followed by an desorption of the surplus 2H-Pc multilayer molecules upon annealing [64, 65]. This procedure was monitored by XPS.
To obtain an array of $CePc_2$ molecules, covering every pore of the *h*BN/Ir(111) moiré, the evaporation of the pre-synthesized $CePc_2$ needs to be optimized in future experiments. Alternatively, the in-situ grown Ce-Pc multideckers need to be measured with STM or AFM to proof the successful growth of these multideckers, since XPS is only a surface averaging technique. Additionally, a study of the appearance of single $CePc_2$ at low or

even zero bias voltages needs to be conducted to clarify, whether the rotation of the upper Pc in the doubledecker complex can be switched off at a sufficiently low bias voltage. The array formation of these single molecular magnets on an insulator-metal-interface indicates the potential of this system for applications in data-storage devices.

In addition to the $CePc_2$ doubledeckers, smaller fragments of those were observed on the *h*BN/Ir(111) surface. As a suitable model system for these fragments, diiminoisoindoline (2III) was investigated, since the size of the fragments could be estimated to be about a quater of a Pc, based on their appearance in STM [66]. The characterization of these molecules and their functionalization of the *h*BN layer was reported in section 9. STM measurements of the 2III molecules could proof that the small fragments, found on the surface along the $CePc_2$ doubledeckers, are derived from the 2III. They adsorb at the pore regions of the *h*BN/Ir(111) moiré and show a bias-voltage dependent appearance, *i.e.*, four lobes at positive and a single protrusion at negative voltage. The molecules bind quite strongly to the supporting *h*BN, since they do not diffuse out of the pore areas of the moiré, even at room temperature. The temperature stability of the bond between molecule and *h*BN was analyzed by XPS measurements of the sample, heated to temperatures of up to 700°C. Despite the small size of the molecules, they stay on the surface up to a temperature of at least 410°C before they desorb – a much higher temperature, than their evaporation temperature of 110°C. In STS experiments an irreversible change in the molecule could be detected. The absence of this feature in STS, after heating the sample to 410°C, supports a hypothesis of two phases of molecular adsorption: In phase (i) the molecules adsorb on the surface and bind there relatively strong. Either due to heating or due to the electric field of the STM tip, the molecule can be modified to end up in an adsorption in phase (ii), thus forming an even stronger, covalent bond between the a nitrogen of the molecule and a boron of the *h*BN. Possible modification of the molecule could either be a dehydrogenation [25, 197–200] or a rearrangement of the bonds in the molecule. The latter modification could be achieved by a breaking of an iminic C=N doublebond and a formation of a covalent bond to the underlying *h*BN layer. Upon heating, some molecules dimerize, observed in the appearance of molecules with six lobes, instead of four at positive bias voltages. The energetics of the 2III, its dehydrogenated forms and three possible dimers were theoretically calculated with DFT. By comparing the simulated STM images with the experimental ones, the appearance of the simulated monomer matched the appearance of the experimental measurements of a single 2III. Also some experimentally measured dimers could be assigned to different structures by comparing

them with the simulated STM images. In additional experiments, the structure of the molecules needs to be studied in more detail by AFM. With this technique, it is possible to obtain more insight into the dimer formation and which structures are really present on the surface [91]. For possible future applications of this system, the functionalization of the *h*BN surface could be used by attaching different kinds of molecules to the substrate in a regular way, *i.e.*, along the moiré. Therefore the desired molecules need to be attached chemically to the backbone of the 2III, *i.e.*, the benzene ring.
The demonstrated functionalization of the inert *h*BN layer by a small molecule opens pathways to use this system for light harvesting or catalysis, since the properties of this insulator-metal-interface could be modified.

To support experimental projects on tetrapyrrolic multidecker complexes, DFT calculations were conducted and are presented in section 10.
The growth of $Gd_{x-1}Pc_x$ multideckers on Ag(111) showed a rotation of the upper Pc, depending on the number of Pc ligands. This dependency was fitted for the gas phase molecules with values of $x \in [2, 5]$ and displayed that each additional layer of Pc is rotated by 45° with respect to the next lower one. This observation correlates with the experimentally observed data [65]. Additionally, the corrugations of the individual Pc planes were analyzed, decreasing towards the center of the molecule. The energy gain for the addition of extra Gd and Pcs saturates for a values of $x \geq 4$, which could be one reason why the amount of molecules on the surface decreases with their size.
The metalation of 2H-TPP with thorium was experimentally studied on Ag(111). The geometric and electronic changes of the $ThTPP_2$ molecule upon adsorption were analyzed, revealing that mainly the bottom TPP is changed in the adsorption process. STM simulations were compared with experimental STM images, where consistencies were found. Deviations might be explained by the rotation of the phenyl groups and the tilting of the pyrrole groups of the upper Pc, which strongly influences the appearance in the simulation.

The presented results of phthalocyanine-based complex, adsorbed on *h*BN templates gave insights into various properties like charge state, structure, adsorption pattern, adsorption motives or magnetism of the molecules. These parameters are decisive for the use of such systems in future applications. Since surface-based technologies gained huge interest in the past years, this thesis gives an important overview about the potential of phthalocyanine molecules on insulator-metal interfaces.

Part VI.
Appendix

A. Calculation of the moiré-pattern of *h*BN/Ir(111)

To simulate the adsorption of molecules on *h*BN/Ir(111), first, the substrate needs to be modeled. For this, the results of Farwick zum Hagen *et al.* [58] were reproduced.
As in the publication, vdW interactions were included but in this case the DFT-D3 method [147] was used instead of DFT-D2. An Ir(111) slab consistent of $11 \times 11 \times 3$ Ir atoms was used with a sheet of 12×12 unit cells *h*BN on top, positioned with a z-offset of 0.31 nm above the upper most Ir layer. The total cell, used for the calculation, has a hexagonal shape and is described in real-space by the thee vectors

$$\boldsymbol{a} = \begin{pmatrix} 29.863 \\ 0 \\ 0 \end{pmatrix} \text{Å}, \qquad \boldsymbol{b} = \begin{pmatrix} -14.931 \\ 25.861 \\ 0 \end{pmatrix} \text{Å}, \qquad \boldsymbol{c} = \begin{pmatrix} 0 \\ 0 \\ 28.650 \end{pmatrix} \text{Å}.$$

The relaxed structure has a ground state energy of $E_{h\text{BN/Ir(111)}} = -5725.410\,\text{eV}$ and is illustrated in Fig. A.1 with a top view of the structure in Fig. A.1 (a). The different colors represent the different kinds of atoms, *i.e.*, the boron atoms are colored in turquoise and the nitrogen atoms in dark-blue. The three Ir layers are colored from bottom to top in grey, yellow and green. A cut along the $(1\bar{1}0)$-plane of Fig. A.1 (a), marked by the dark-grey line, is shown in Fig. A.1 (b). The corrugation of the *h*BN-layer can be clearly seen and is additionally represented by the color scale, shown on the right. To distinguish the two atom types, the B atoms are shown larger in size than the N atoms. The corrugation of the sheet varies in a range of $0.209\,\text{nm} - 0.350\,\text{nm}$. The corrugation of the topmost Ir layer is 0.7 pm. By taking a look at the pore region, *i.e.*, the valley in the *h*BN, it is to be observed that the lowest atom is the B, siting in the hcp-position of the supporting Ir(111) slab and is surrounded by N atoms, sitting in the top position.
The top view on a periodically extended cell in Fig. A.1 (c), with the same color code for the *h*BN-layer as in Fig. A.1 (b), portrays the moiré structure with the three highlighted high-symmetry positions. The pore region with the $B_{hcp}N_{top}$-configuration is marked in grey and the two hollow-wire regions with the $B_{top}N_{fcc}$- and $B_{fcc}N_{hcp}$-structure are marked green and yellow, respectively. The region in between these two hollow-wire region is called bridge-wire.

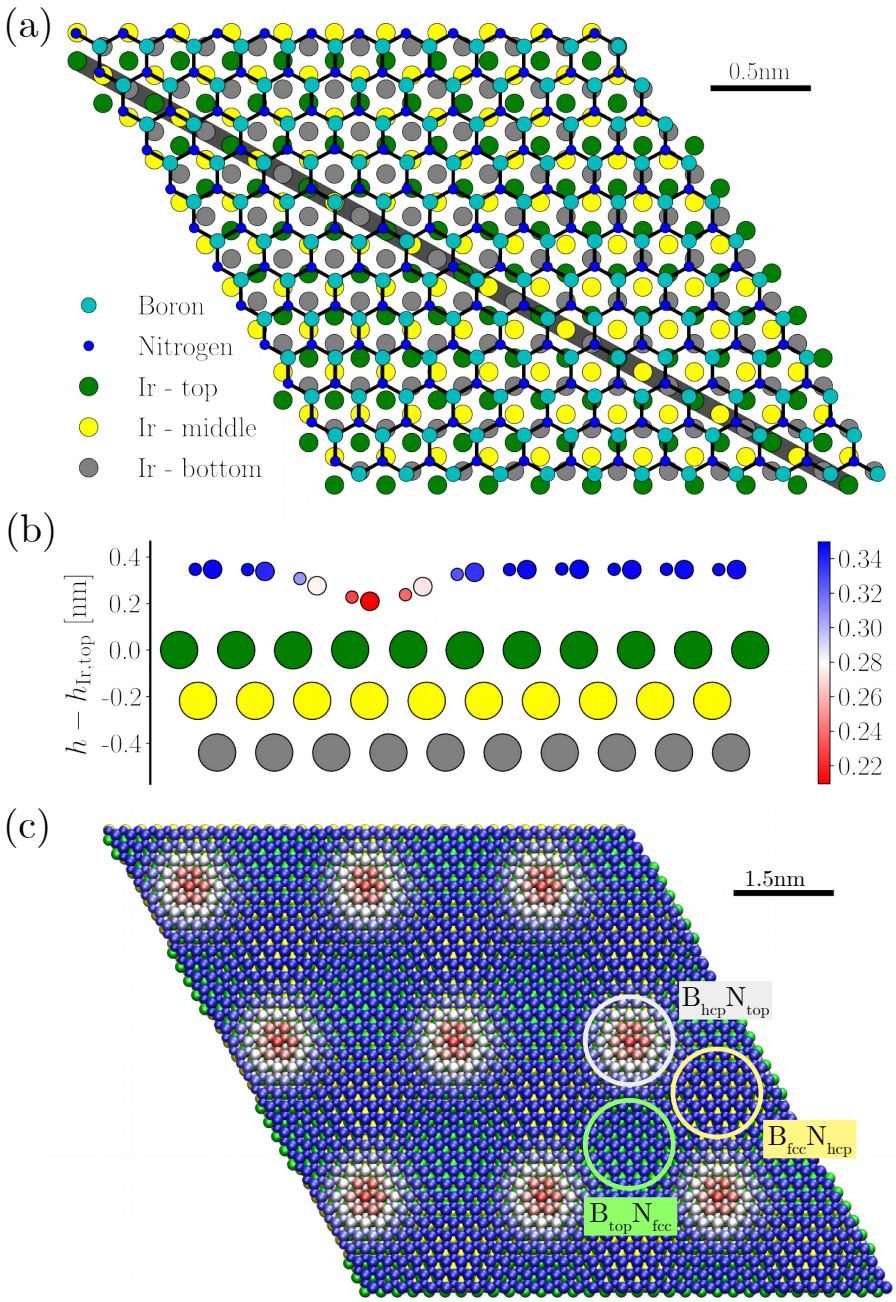

Figure A.1: *Calculated structure of hBN/Ir(111). In* ***(a)*** *one moiré cell of the structure is shown, where the different atoms have different colors as labeled. In* ***(b)*** *a cut along the* $(1\bar{1}0)$*-plane, i.e., the black line in (a), is shown. The color code of the hBN shows the height above the upper Ir layer as indicated by the colorbar on the right. The B/N atoms are represented by the larger/smaller spheres.* ***(c)*** *shows the top view onto a periodically enlarged cell with the same color code as in (b).*

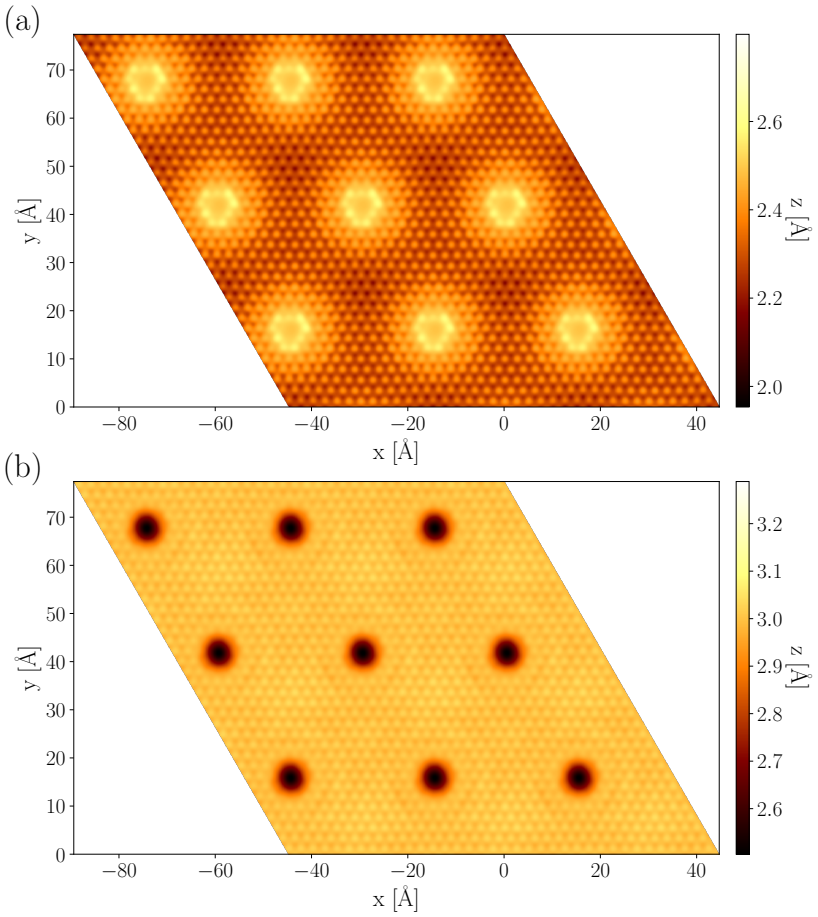

Figure A.2: *STM simulation of hBN/Ir(111). The topography is shown in* ***(a)*** *for* $U = 1\ V$, $I = 1\,\mu A$ *and in* ***(b)*** *for* $U = -1\ V$, $I = 1\,\mu A$.

For comparison with real STM measurements, as they were shown in Fig. 1 in [58], STM-images were simulated and shown in Fig. A.2. For a positive bias voltage of $U = 1\,\mathrm{V}$ (c.f. Fig. A.2 (a)), the pore regions appear higher with a depression in the middle. For negative bias voltages of $U = -1\,\mathrm{V}$ (c.f. Fig. A.2 (b)), they appear as depressions. The same behavior is found by Farwick zum Hagen *et al.* [58].

B. Hexagonal boron nitride on Cu(100)

The adsorption of a thin layer, such as graphene or *h*BN, on a metal substrate can result in a moiré lattice, induced, e.g., by a lattice mismatch, a different symmetry of rotational alignment of support and overlayer and depend also on their chemical interaction [38, 56, 58, 204].
Thin layers with a 3-fold symmetry are mainly grown on the 3-fold symmetric (111)-surfaces of fcc-metals (c.f. section 6.1) [38, 56, 58, 59, 204]. The resulting moiré lattice is again 3-fold and the lattice parameter depend on the mismatch of the lattice parameter of the constituents.
By using a 4-fold symmetric substrate, such as the (100)-surface of fcc-metals, the resulting moiré lattice can be 2-fold symmetric [38, 205–207].
Such a surface with a striped superstructure, *i.e.*, showing a 2-fold symmetry, is a suitable template for the growth of 1D-structures [208]. In addition the *h*BN layer might reduce the electric coupling of adsorbate structures to the metal [38].
To ensure spectroscopic investigations, minimal influenced by the metallic substrate, those structures are required to be decoupled from the metal-surface. These two demands are fulfilled by the one-dimensional moiré lattice of *h*BN adsorbed on a (100) metals surface, since *h*BN is a large bandgap material [38].

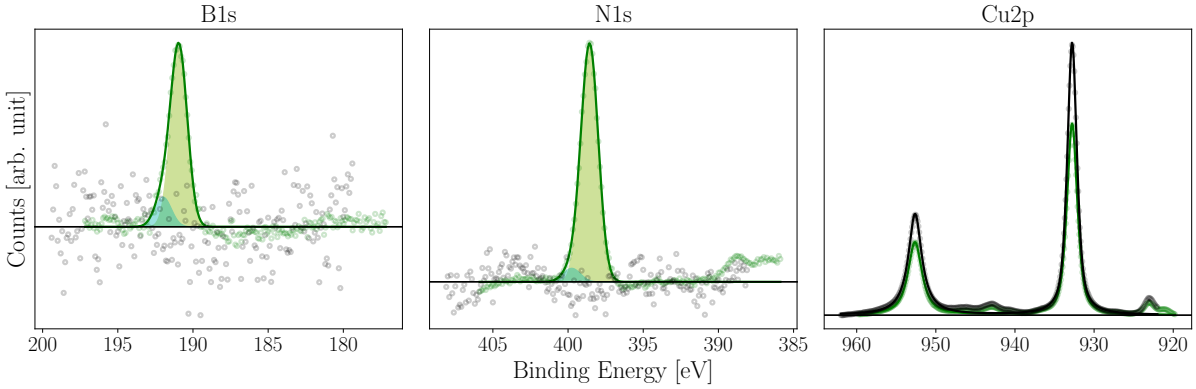

Figure B.1: *XPS measurements of the growth of hBN/Cu(100). The three peaks of interest, i.e., B1s, N1s and Cu2p, are shown before (black) and after (green) the growth of hBN. For both the B1s and the N1s signal a clear peak is visible after the growth. Also a reduction in intensity of the Cu2p peak is observed.*

The growth of *h*BN on Cu(100) was performed via CVD of borazine as a precursor (c.f. section 6.2) and characterized by XPS (see Fig. B.1). The sample was heated to a temperature of 750°C and borazine was dosed for 5 min at a background pressure of

$p_{\text{borazine}} = 9 \times 10^{-7}$ mbar, at this temperature. After dosing the borazine, the sample was kept at the growth temperature for one more minute. The XPS measurements of the B1s, N1s and Cu2p peaks before (black) and after (green) the growth show clear boron and the nitrogen signals as well as a reduction of the copper signal. The B1s and the N1s features consist of two peak components, indicated by the filled areas in Fig. B.1 (a),(b). The binding energies of the B1s and the N1s peaks were fitted and are shown together with literature values for other *h*BN/metal systems in Tab. B.1. The obtained binding energies of the B1s and the N1s features are in agreement with the values of other *h*BN/metal-interfaces, found in literature.

Substrate	B1s [eV]	N1s [eV]	Reference
Ir(111)	189.9	397.6	[58]
Ni(100)	190.2	398.5	[209]
Ni(111)	190.5	398.5	[210]
Pd(111)	190.5	398.1	[211]
Cu(111)	190.5	398.0	[212]
Rh(111)	190.7	398.3	[211]
Cu(100)	190.9	398.6	Fig. B.1

Table B.1: *Binding energies of the B1s and the N1s peaks of different hBN/metal interfaces. The listed binding energies refer to the main component of the feature, if consisting of multiple peaks.*

The structure of *h*BN/Cu(100) was characterized by STM, illustrated in Fig. B.2. The stripes on the large flake indicate the 1D moiré pattern as it can also be seen in the linescans of two differently oriented domains ((b) and (c)) along the blue and green lines in (a). A periodicity of $a_{\text{M}} = 2.13\,\text{nm}$ ($a_{\text{M}} = 2.26\,\text{nm}$) was measured for the blue (green) linescan. This indicates that the size of the moiré can depend on the rotation of the *h*BN with respect to the substrate. The two domains are separated by a domain wall, marked with black arrows in (a). Nevertheless, since the difference of the periodicities is quite small, it could also be an artifact of the measurement.

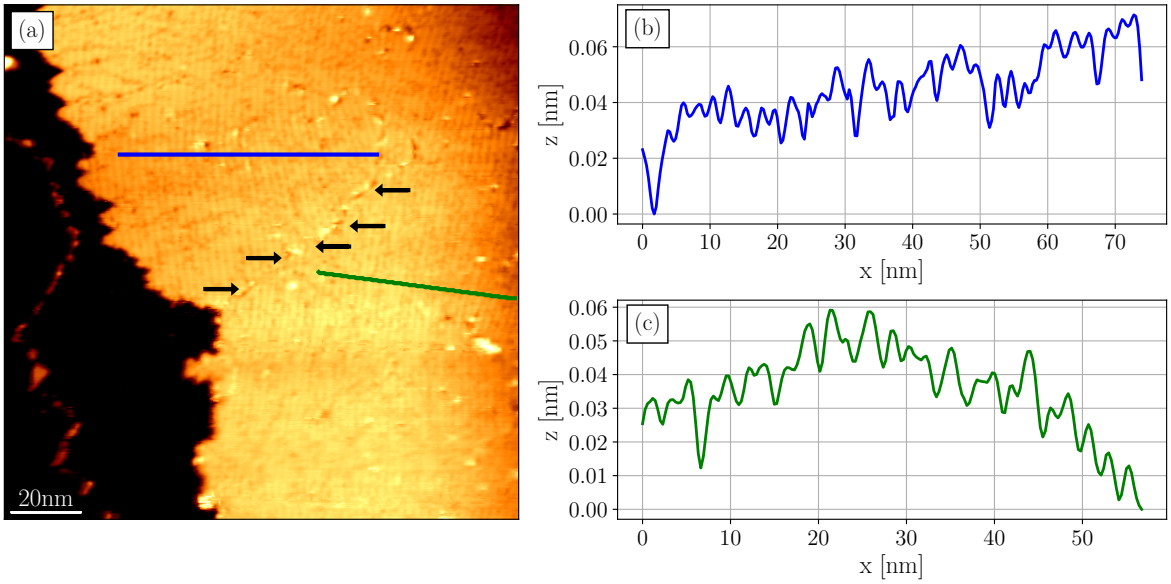

Figure B.2: *STM image of hBN/Cu(100). In* **(a)** *the topography of the sample is shown with the two linescans marked with a blue and a green line, shown in* **(b)** *and* **(c)** *($U = 2.575\,V$, $I = 1.3\,nA$). The black arrows indicate a domain wall between two differently oriented domains.*

With these results, the 2-fold symmetric structure of hBN/Cu(100) was briefly characterized. Based on these experiments, this substrate can be used as a promising template for the growth of 1D nanostructures on an insulator-metal-interface in the future.

C. Vacuum distillation of borazine

To avoid contamination of air the distillation of borazine is done in vacuum with the setup shown in Fig. C.1 by the following procedure:

1. Attach the borazine tube to the refill line and open the red valve on top.
2. Attach He gas to refill line and close the He gas valve.
3. Attach the borazine dewar to the refill line.
4. Freeze the borazine dewar with LN_2.
5. Pump the whole refill line with the TP.
6. Flush the refill line $2-3$ times with He:
   a) Let the TP reach full speed.
   b) Close the valve to the TP and stop the TP.
   c) Open the valve to the He gas for $2-3\,\mathrm{s}$.
   d) Close the valve to He gas.
   e) Open the valve to the TP slowly when its speed is below $500\,\mathrm{Hz}$.
   f) Start the TP. The valve to it is completely open.
7. Open the green marked valve of the borazine dewar, still frozen.
8. Flush the refill line $2-3$ times with He.
9. Unfreeze the borazine dewar by removing the LN_2 and start freezing the borazine tube with LN_2. The refilling starts.
10. Check that the white seeling of borazine tube does not freeze.
11. After filling the tube with $\sim 3-5\,\mathrm{mm}$ close the red valve of the borazine tube, while keeping the borazine tube frozen.
12. Freeze the borazine dewar with LN_2 and wait for $\sim 15\,\mathrm{min}$.
13. Close the green valve at the borazine dewar.
14. Stop the TP and vent the refill line.

15. Unmount the borazine dewar and put it back in the freezer.
16. Unmount the borazine tube and the TP and mount them at the chamber.
17. Pump the borazine tube for $\sim 15\,\text{min}$ with the red valve open and still frozen.
18. Close the red valve of the borazine tube and close the valve to the TP.

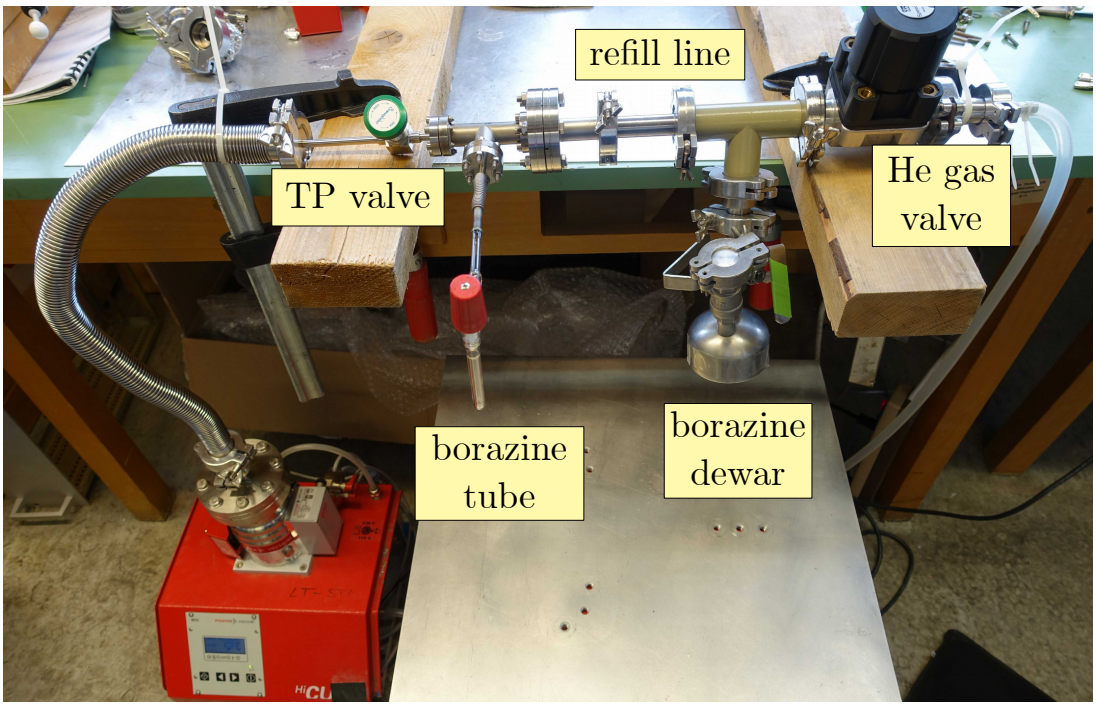

Figure C.1: *Setup for refilling borazine. The borazine tube with the red valve, the borazine dewar with the green valve, the green TP valve and the black He gas valve are connected to the refilling line.*

After refilling the borazine and mounting it at the chamber a mass spectrum can be measured to ensure the quality of the borazine. An example spectrum is shown in Fig. C.2 in orange (reference spectrum without dosing borazine in blue). Clear signals of the masses around 81 u = (3·11+3·14+6·1) u are observed while dosing borazine. The increased peaks $< 81\,\text{u}$ can be explained by fragments of borazine, produced in the mass spectrometer. The presence of these peaks does not indicate a decomposition of the borazine in the reservoir.

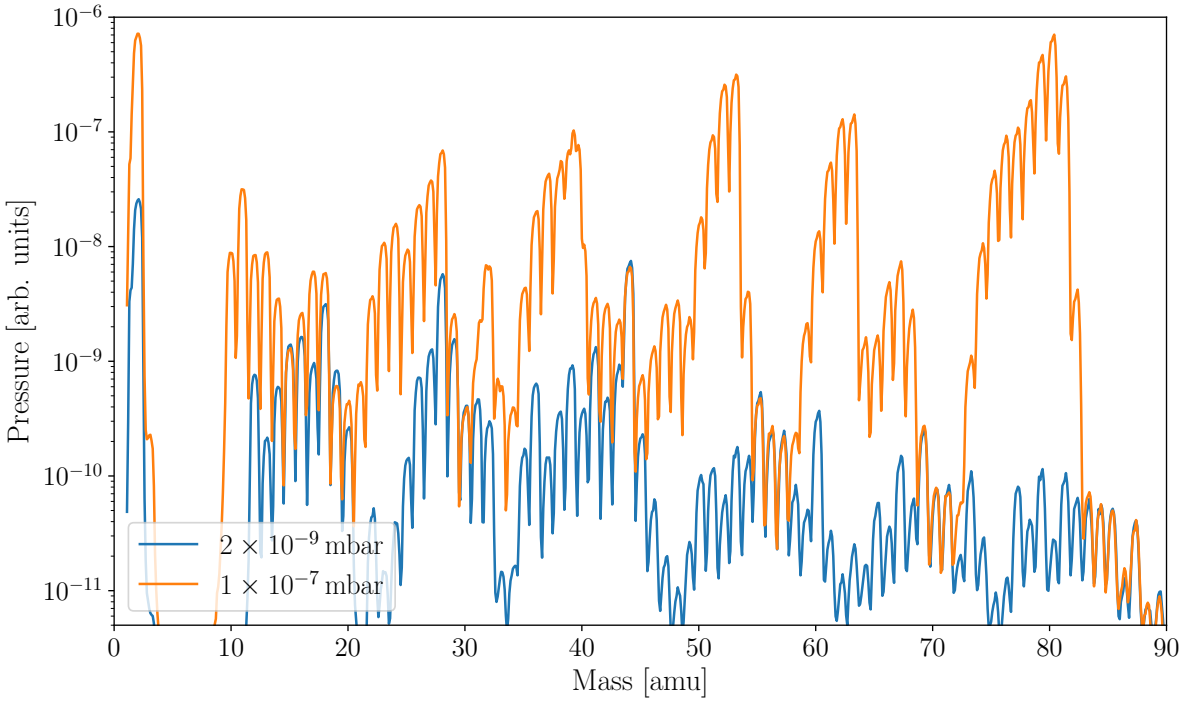

Figure C.2: *Mass spectrum of Borazine. In blue the background spectrum at a pressure of* 2×10^{-9} *mbar and in orange the spectrum while dosing borazine at a pressure of* 1×10^{-7} *mbar is shown.*

D. Lab automatization

In order to get a better overview of the status of the machines, a program for monitoring and logging the status of experimental key parameters was written. This program collects the information of the following sensors:

- Pressures from MaxiGauge
- Temperatures from cryo, STM, manipulator via diodes
- Temperature of sample, OMBE via temperature chip (K-type thermocouple)
- Currents of the ion pumps
- Helium level

The second crucial part beside the software is the hardware, consisting of a RaspberryPi 3b [213], two AD-converter chips and a temperature chip, which is shown with its wiring in a schematic drawing in Fig. D.2.
In addition to these devices, the pressure gauge and the ion pumps are connected via RS232, coupled to USB-adapters.
The incoming status information were displayed on a graphical user interface (GUI) (see Fig. D.1) and also stored on the server, every two seconds.

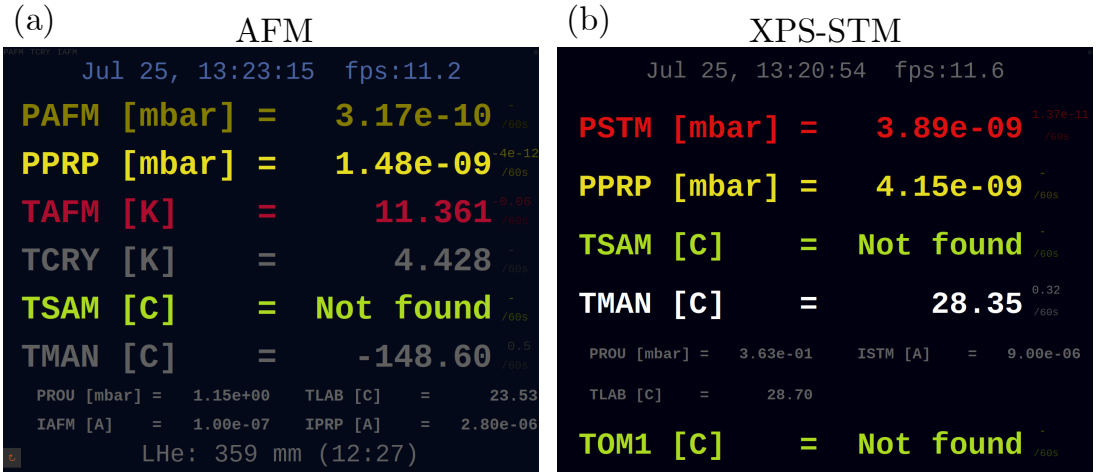

Figure D.1: *Screenshots of the graphical user interface of the lab automatization software. In* ***(a)****/****(b)*** *the GUI of the "AFM"/"XPS-STM"-setup is shown, respectively.*

The program can be modified for each machine, *i.e.*, the "LT-STM", the "AFM" and the "XPS-STM", to track different kinds of sensors and input information. The helium level

of the cryostat, for example, needs to be measured for the “LT-STM” and the “AFM”, but not for the “XPS-STM”.

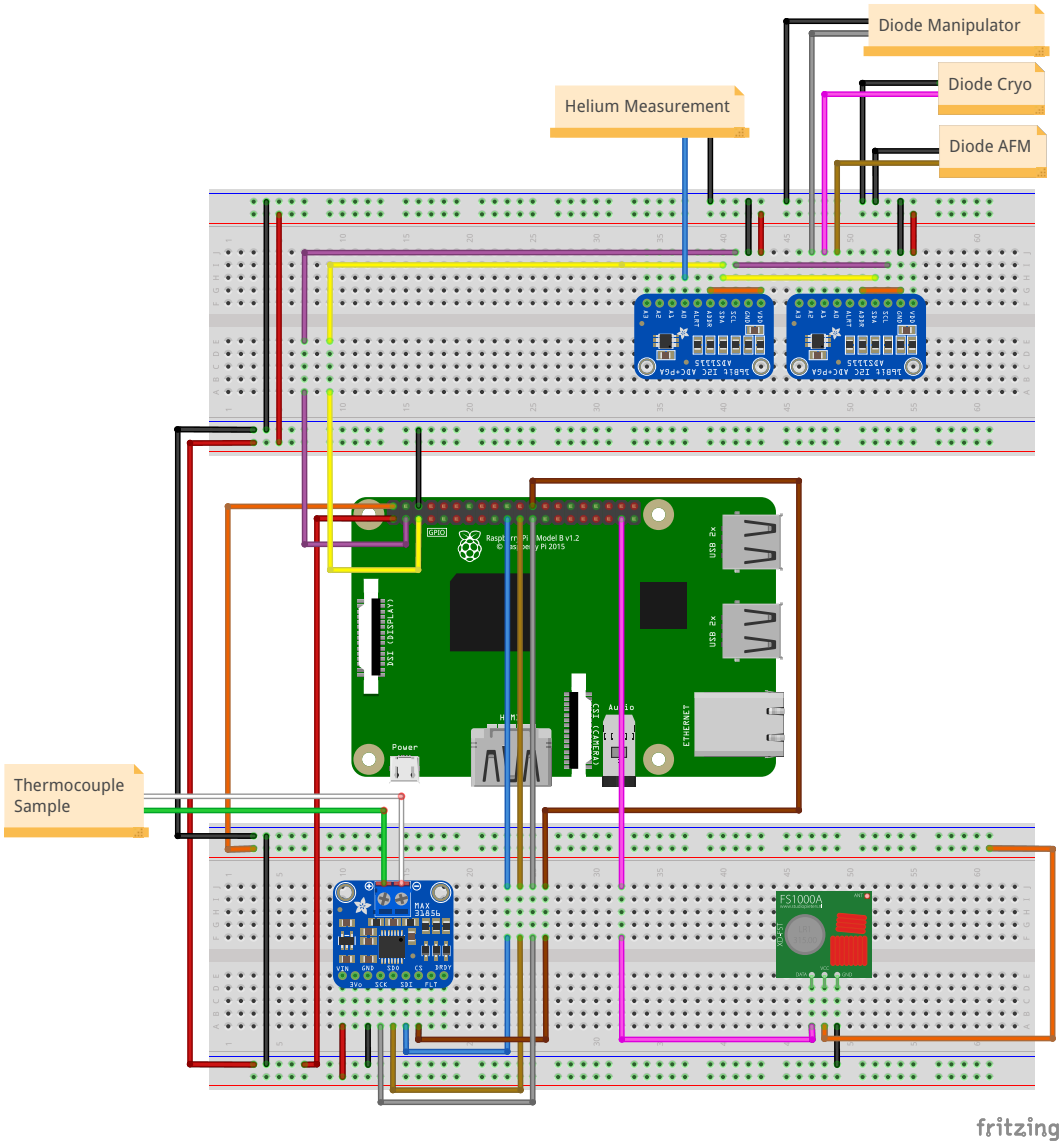

Figure D.2: *Connecting scheme for the lab automatization of the “AFM” setup. The scheme, optimized for the “AFM”-setup shows the connection of the different chips with the RaspberryPi [213].*

E. Data processing

The acquired data was analyzed with Python [214], using Numpy [215], SciPy [216] and Matplotlib [217]. For analyzing STM and AFM images, Gwyddion [218] and the CreaTec Software STMAFM [106] were used. Only subtle processing, for example, line subtraction, gaussian filtering, leveling or 2D fast Fourier Transformations were conducted. XP-spectra were fitted using the fityk software [219]. The backgrounds were fitted with linear slopes, cubic polynomials or Sigmoid functions and peaks were fitted with either Gaussians, Lorentzians or a mixture using Pseudo-Voigt functions. The simulated STM images, calculated by DFT were interpolated to smooth them out. Molecular models were created using Avogadro [220] and visualized using VMD [221].

The calibration of the piezo constants in the room temperature measurements in section 8.1 was done by comparing the Ir(111) step edges for the z-direction to literature values and the intermolecular distance of the Ce_2Pc_3-tripledecker islands for the x- and y-direction with the low-temperature measurements.

F. List of publications

Urgel, J. I., Ecija, D., Vijayaraghavan, S., Pörtner, M., Bocquet, M.-L., Auwärter, W. & Barth, J. V. In-Situ Growth of Gadolinium Phthalocyaninato Sandwich Complexes on the Ag(111) Surface. *ChemPhysChem Commun* **20**, 1–5. (2019). [65]

Pörtner, M., Wei, Y., Riss, A., Seufert, K., Garnica, M., Barth, J. V., Diekhöner, L. & Auwärter, W., Charge state control of F_{16}CoPc on *h*BN/Cu(111). *Submitted*.

G. References

1. Moore, G. E. Cramming more components onto integrated circuits, Reprinted from Electronics, volume 38, number 8, April 19, 1965, pp.114 ff. *IEEE J Solid-St Circ* **11,** 33–35. doi:10.1109/N-SSC.2006.4785860 (2006).
2. Taniguchi, N., Arakawa, C. & Kobayashi, T. *On the basic concept of 'nano-technology'* in *Proceedings of the International Conference on Production Engineering* **2** (1974), 18–23.
3. Barth, J. V., Costantini, G. & Kern, K. Engineering atomic and molecular nanostructures at surfaces. *Nature* **437,** 671–679. doi:10.1038/nature04166 (2005).
4. Gusain, A., Faria, R. M. & Miranda, P. B. Polymer Solar Cells - Interfacial Processes Related to Performance Issues. *Front Chem* **7.** doi:10.3389/fchem.2019.00061 (2019).
5. Grätzel, M. Dye-sensitized solar cells. *J Photochem Photobio C* **4,** 145–153. doi:10.1016/S1389-5567(03)00026-1 (2003).
6. Li, Y., Bian, Y., Yan, M., Thapaliya, P. S., Johns, D., Yan, X., Galipeau, D. & Jiang, J. Mixed (porphyrinato)(phthalocyaninato) rare-earth(III) double-decker complexes for broadband light harvesting organic solar cells. *J Mater Chem* **21,** 11131. doi:10.1039/c1jm11246e (2011).
7. Wiesendanger, R. Nanoscale magnetic skyrmions in metallic films and multilayers: a new twist for spintronics. *Nat Rev Mat* **1,** 16044. doi:10.1038/natrevmats.2016.44 (2016).
8. Natterer, F. D., Yang, K., Paul, W., Willke, P., Choi, T., Greber, T., Heinrich, A. J. & Lutz, C. P. Reading and writing single-atom magnets. *Nature* **543,** 226–228. doi:10.1038/nature21371 (2017).
9. Donati, F., Rusponi, S., Stepanow, S., Wackerlin, C., Singha, A., Persichetti, L., Baltic, R., Diller, K., Patthey, F., Fernandes, E., Dreiser, J., Sljivancanin, Z., Kummer, K., Nistor, C., Gambardella, P. & Brune, H. Magnetic remanence in single atoms. *Science* **352,** 318–321. doi:10.1126/science.aad9898 (2016).
10. Liu, Z., Yasseri, A. A., Lindsey, J. S. & Bocian, D. F. Molecular Memories That Survive Silicon Device Processing and Real-World Operation. *Science* **302,** 1543–1545. doi:10.1126/science.1090677 (2003).

11. Leuenberger, M. N. & Loss, D. Quantum computing in molecular magnets. *Nature* **410,** 789–793. doi:10.1038/35071024 (2001).

12. Clemente-Juan, J. M., Coronado, E. & Gaita-Arino, A. Magnetic polyoxometalates: from molecular magnetism to molecular spintronics and quantum computing. *Chem Soc Rev* **41,** 7464. doi:10.1039/c2cs35205b (2012).

13. Gaita-Arino, A., Luis, F., Hill, S. & Coronado, E. Molecular spins for quantum computation. *Nat Chem* **11,** 301–309. doi:10.1038/s41557-019-0232-y (2019).

14. Peter, L. M. Towards sustainable photovoltaics: the search for new materials. *Philos T Roy Soc A* **369,** 1840–1856. doi:10.1098/rsta.2010.0348 (2011).

15. Son, I. H., Park, J. H., Park, S., Park, K., Han, S., Shin, J., Doo, S.-G., Hwang, Y., Chang, H. & Choi, J. W. Graphene balls for lithium rechargeable batteries with fast charging and high volumetric energy densities. *Nat Commun* **8,** 1561. doi:10.1038/s41467-017-01823-7 (2017).

16. Hills, G., Lau, C., Wright, A., Fuller, S., Bishop, M. D., Srimani, T., Kanhaiya, P., Ho, R., Amer, A., Stein, Y., Murphy, D., Arvind, Chandrakasan, A. & Shulaker, M. M. Modern microprocessor built from complementary carbon nanotube transistors. *Nature* **572,** 595–602. doi:10.1038/s41586-019-1493-8 (2019).

17. Battersby, A. R. Tetrapyrroles: the pigments of life. *Nat Prod Rep* **17,** 507–526. doi:10.1039/b002635m (2000).

18. Gottfried, J. M. Surface chemistry of porphyrins and phthalocyanines. *Surf Sci Rep* **70,** 259–379. doi:10.1016/j.surfrep.2015.04.001 (2015).

19. Auwärter, W., Ecija, D., Klappenberger, F. & Barth, J. V. Porphyrins at interfaces. *Nat Chem* **7,** 105–120. doi:10.1038/nchem.2159 (2015).

20. Mathew, S., Yella, A., Gao, P., Humphry-Baker, R., Curchod, B. F. E., Ashari-Astani, N., Tavernelli, I., Rothlisberger, U., Nazeeruddin, K., Grätzel, M., Nazeeruddin, M. K., Grätzel, M., Nazeeruddin, K. & Grätzel, M. Dye-sensitized solar cells with 13% efficiency achieved through the molecular engineering of porphyrin sensitizers. *Nat Chem* **6,** 242–247. doi:10.1038/nchem.1861 (2014).

21. Senge, M. O. in *The Porphyrin Handbook* 239–347 (Academic Press, 2000).

22. Buchner, F., Schwald, V., Comanici, K., Steinrück, H.-P. & Marbach, H. Microscopic Evidence of the Metalation of a Free-Base Porphyrin Monolayer with Iron. *ChemPhysChem* **8,** 241–243. doi:10.1002/cphc.200600698 (2007).

23. Gottfried, J. M., Flechtner, K., Kretschmann, A., Lukasczyk, T. & Steinrück, H.-P. Direct Synthesis of a Metalloporphyrin Complex on a Surface. *J Am Chem Soc* **128,** 5644–5645. doi:10.1021/ja0610333 (2006).

24. Auwärter, W., Weber-Bargioni, A., Brink, S., Riemann, A., Schiffrin, A., Ruben, M. & Barth, J. V. Controlled Metalation of Self-Assembled Porphyrin Nanoarrays in Two Dimensions. *ChemPhysChem* **8,** 250–254. doi:10.1002/cphc.200600675 (2007).

25. Sperl, A., Kröger, J. & Berndt, R. Controlled Metalation of a Single Adsorbed Phthalocyanine. *Angew Chem Int Edit* **50,** 5294–5297. doi:10.1002/anie.201100950 (2011).

26. Diller, K., Klappenberger, F., Allegretti, F., Papageorgiou, A. C., Fischer, S., Wiengarten, A., Joshi, S., Seufert, K., Ecija, D., Auwärter, W. & Barth, J. V. Investigating the molecule-substrate interaction of prototypic tetrapyrrole compounds: Adsorption and self-metalation of porphine on Cu(111). *J Chem Phys* **138,** 154710. doi:10.1063/1.4800771 (2013).

27. Inose, T., Tanaka, D., Liu, J., Kajihara, M., Mishra, P., Ogawa, T. & Komeda, T. Coordination structure conversion of protonated bisporphyrinato terbium(III) double-decker complexes and creation of a Kondo assembly by electron injection on the Au(111) surface. *Nanoscale* **10,** 19409–19417. doi:10.1039/c8nr04630a (2018).

28. Komeda, T., Isshiki, H., Liu, J., Zhang, Y. F., Lorente, N., Katoh, K., Breedlove, B. K. & Yamashita, M. Observation and electric current control of a local spin in a single-molecule magnet. *Nat Commun* **2.** doi:10.1038/ncomms1210 (2011).

29. Wäckerlin, C., Donati, F., Singha, A., Baltic, R., Rusponi, S., Diller, K., Patthey, F., Pivetta, M., Lan, Y., Klyatskaya, S., Ruben, M., Brune, H. & Dreiser, J. Giant Hysteresis of Single-Molecule Magnets Adsorbed on a Nonmagnetic Insulator. *Adv Mater* **28,** 5195–5199. doi:10.1002/adma.201506305 (2016).

30. Brede, J., Atodiresei, N., Kuck, S., Lazic, P., Caciuc, V., Morikawa, Y., Hoffmann, G., Blügel, S. & Wiesendanger, R. Spin- and Energy-Dependent Tunneling through a Single Molecule with Intramolecular Spatial Resolution. *Phys Rev Lett* **105,** 047204. doi:10.1103/PhysRevLett.105.047204 (2010).

31. Godfrin, C., Ferhat, A., Ballou, R., Klyatskaya, S., Ruben, M., Wernsdorfer, W. & Balestro, F. Operating Quantum States in Single Magnetic Molecules: Implemen-

tation of Grover's Quantum Algorithm. *Phys Rev Lett* **119,** 187702. doi:10.1103/PhysRevLett.119.187702 (2017).

32. Binnig, G. & Rohrer, H. Das Raster-Tunnel-Mikroskop. *Physik Journal* **39,** 16–17. doi:10.1002/phbl.19830390107 (1983).

33. Binnig, G., Frank, K. H., Fuchs, H., Garcia, N., Reihl, B., Rohrer, H., Salvan, F. & Williams, A. R. Tunneling spectroscopy and inverse photoemission: Image and field states. *Phys Rev Lett* **55,** 991–994. doi:10.1103/PhysRevLett.55.991 (1985).

34. Crommie, M. F., Lutz, C. P. & Eigler, D. M. Confinement of electrons to quantum corrals on a metal surface. *Science* **262,** 218–220. doi:10.1126/science.262.5131.218 (1993).

35. Eigler, E. K. & Schweizer, D. K. Positioning single atoms with a scanning tunneling microscop. *Nature* **344,** 524–525. doi:10.1038/344524a0 (1990).

36. Novoselov, K. S., Geim, A. K., Morozov, S. V., Jiang, D., Zhang, Y., Dubonos, S. V., Grigorieva, I. V. & Firsov, A. A. Electric Field Effect in Atomically Thin Carbon Films. *Science* **306,** 666–9. doi:10.1126/science.1102896 (2004).

37. Novoselov, K. S., Mishchenko, A., Carvalho, A. & Castro Neto, A. H. 2D materials and van der Waals heterostructures. *Science* **353,** aac9439. doi:10.1126/science.aac9439 (2016).

38. Auwärter, W. Hexagonal boron nitride monolayers on metal supports: Versatile templates for atoms, molecules and nanostructures. *Surf Sci Rep* **74,** 1–95. doi:10.1016/j.surfrep.2018.10.001 (2019).

39. Wang, Q. H., Kalantar-Zadeh, K., Kis, A., Coleman, J. N. & Strano, M. S. Electronics and optoelectronics of two-dimensional transition metal dichalcogenides. *Nat Nanotechnol* **7,** 699–712. doi:10.1038/nnano.2012.193 (2012).

40. Barth, J. V. Molecular Architectonic on Metal Surfaces. *Annu Rev Phys Chem* **58,** 375–407. doi:10.1146/annurev.physchem.56.092503.141259 (2007).

41. Fernandez-Torrente, I., Franke, K. J. & Pascual, J. I. Spectroscopy of C_{60} single molecules: the role of screening on energy level alignment. *J Phys-Condens Mat* **20,** 184001. doi:10.1088/0953-8984/20/18/184001 (2008).

42. Mugarza, A., Robles, R., Krull, C., Korytar, R., Lorente, N. & Gambardella, P. Electronic and magnetic properties of molecule-metal interfaces: Transition-metal phthalocyanines adsorbed on Ag(100). *Phys Rev B* **85,** 155437. doi:10.1103/PhysRevB.85.155437 (2012).

43. Kahle, S., Deng, Z., Malinowski, N., Tonnoir, C., Forment-Aliaga, A., Thontasen, N., Rinke, G., Le, D., Turkowski, V., Rahman, T. S., Rauschenbach, S., Ternes, M. & Kern, K. The Quantum Magnetism of Individual Manganese-12-Acetate Molecular Magnets Anchored at Surfaces. *Nano Lett* **12,** 518–521. doi:10.1021/nl204141z (2012).

44. Repp, J., Meyer, G., Stojković, S. M., Gourdon, A. & Joachim, C. Molecules on insulating films: Scanning-tunneling microscopy imaging of individual molecular orbitals. *Phys Rev Lett* **94.** doi:10.1103/PhysRevLett.94.026803 (2005).

45. Repp, J. & Meyer, G. Scanning Tunneling Spectroscopy of Molecules on Insulating Films. *Chimia* **64,** 370–375. doi:10.2533/chimia.2010.370 (2010).

46. Kumar, A., Banerjee, K. & Liljeroth, P. Molecular assembly on two-dimensional materials. *Nanotechnology* **28,** 082001. doi:10.1088/1361-6528/aa564f (2017).

47. Kim, G., Jang, A.-R., Jeong, H. Y., Lee, Z., Kang, D. J. & Shin, H. S. Growth of High-Crystalline, Single-Layer Hexagonal Boron Nitride on Recyclable Platinum Foil. *Nano Lett* **13,** 1834–1839. doi:10.1021/nl400559s (2013).

48. Orofeo, C. M., Suzuki, S., Kageshima, H. & Hibino, H. Growth and low-energy electron microscopy characterization of monolayer hexagonal boron nitride on epitaxial cobalt. *Nano Res* **6,** 335–347. doi:10.1007/s12274-013-0310-1 (2013).

49. Blase, X., Rubio, A., Louie, S. G. & Cohen, M. L. Quasiparticle band structure of bulk hexagonal boron nitride and related systems. *Phys Rev B* **51,** 6868–6875. doi:10.1103/PhysRevB.51.6868 (1995).

50. Simonson, R. J., Paffett, M. T., Jones, M. E. & Koel, B. E. A vibrational study of borazine adsorbed on Pt(111) and Au(111) surfaces. *Surf Sci* **254,** 29–44. doi:10.1016/0039-6028(91)90635-6 (1991).

51. Paffett, M. T., Simonson, R. J., Papin, P. & Paine, R. T. Borazine adsorption and decomposition at Pt(111) and Ru(001) surfaces. *Surf Sci* **232,** 286–296. doi:10.1016/0039-6028(90)90121-N (1990).

52. He, J.-W. & Goodman, D. W. Interaction of borazine with a Re(0001) surface, studied by LEED, TDS, AES and ELS. *Surf Sci* **232,** 138–148. doi:10.1016/0039-6028(90)90594-X (1990).

53. Koitz, R., Seitsonen, A. P., Iannuzzi, M. & Hutter, J. Structural and electronic properties of a large-scale Moiré pattern of hexagonal boron nitride on Cu(111) studied with density functional theory. *Nanoscale* **5,** 5589. doi:10.1039/c3nr00709j (2013).

54. Schwarz, M., Duncan, D. A., Garnica, M., Ducke, J., Deimel, P. S., Thakur, P. K., Lee, T.-L., Allegretti, F. & Auwärter, W. Quantitative determination of a model organic/insulator/metal interface structure. *Nanoscale* **10,** 21971–21977. doi:10.1039/C8NR06387G (2018).

55. Joshi, S., Bischoff, F., Koitz, R., Ecija, D., Seufert, K., Seitsonen, A. P., Hutter, J., Diller, K., Urgel, J. I., Sachdev, H., Barth, J. V. & Auwärter, W. Control of Molecular Organization and Energy Level Alignment by an Electronically Nanopatterned Boron Nitride Template. *ACS Nano* **8,** 430–442. doi:10.1021/nn406024m (2014).

56. Joshi, S., Ecija, D., Koitz, R., Iannuzzi, M., Seitsonen, A. P., Hutter, J., Sachdev, H., Vijayaraghavan, S., Bischoff, F., Seufert, K., Barth, J. V. & Auwärter, W. Boron Nitride on Cu(111): An Electronically Corrugated Monolayer. *Nano Lett* **12,** 5821–5828. doi:10.1021/nl303170m (2012).

57. Schulz, F., Drost, R., Hämäläinen, S. K. & Liljeroth, P. Templated Self-Assembly and Local Doping of Molecules on Epitaxial Hexagonal Boron Nitride. *ACS Appl Mater Inter* **7,** 11121–11128. doi:10.1021/nn404840h (2013).

58. Farwick zum Hagen, F. H., Zimmermann, D. M., Silva, C. C., Schlueter, C., Atodiresei, N., Jolie, W., Martinez-Galera, A. J., Dombrowski, D., Schröder, U. A., Will, M., Lazic, P., Caciuc, V., Blügel, S., Lee, T. L., Michely, T. & Busse, C. Structure and Growth of Hexagonal Boron Nitride on Ir(111). *ACS Nano* **10,** 11012–11026. doi:10.1021/acsnano.6b05819 (2016).

59. Corso, M., Auwärter, W., Muntwiler, M., Tamai, A., Greber, T. & Osterwalder, J. Boron Nitride Nanomesh. *Science* **303,** 217–220. doi:10.1126/science.1091979 (2004).

60. Iannuzzi, M., Tran, F., Widmer, R., Dienel, T., Radican, K., Ding, Y., Hutter, J. & Gröning, O. Site-selective adsorption of phthalocyanine on h-BN/Rh(111) nanomesh. *Phys Chem Chem Phys* **16,** 12374–12384. doi:10.1039/C4CP01466A (2014).

61. Schulz, F., Drost, R., Hämäläinen, S. K., Demonchaux, T., Seitsonen, A. P. & Liljeroth, P. Epitaxial hexagonal boron nitride on Ir(111): A work function template. *Phys Rev B* **89,** 235429. doi:10.1103/PhysRevB.89.235429 (2014).

62. Schwarz, M., Riss, A., Garnica, M., Ducke, J., Deimel, P. S., Duncan, D. A., Thakur, P. K., Lee, T. L., Seitsonen, A. P., Barth, J. V., Allegretti, F. & Auwärter, W. Corrugation in the Weakly Interacting Hexagonal-BN/Cu(111) System: Structure Deter-

mination by Combining Noncontact Atomic Force Microscopy and X-ray Standing Waves. *ACS Nano* **11,** 9151–9161. doi:10.1021/acsnano.7b04022 (2017).

63. Preobrajenski, A. B., Vinogradov, A. S., Ng, M. L., Cavar, E., Westerström, R., Mikkelsen, A., Lundgren, E. & Martensson, N. Influence of chemical interaction at the lattice-mismatched h-BN/Rh(111) and h-BN/Pt(111) interfaces on the overlayer morphology. *Phys Rev B* **75,** 245412. doi:10.1103/PhysRevB.75.245412 (2007).

64. Ecija, D., Auwärter, W., Vijayaraghavan, S., Seufert, K., Bischoff, F., Tashiro, K. & Barth, J. V. Assembly and manipulation of rotatable cerium porphyrinato sandwich complexes on a surface. *Angew Chem Int Edit* **50,** 3872–3877. doi:10.1002/anie.201007370 (2011).

65. Urgel, J. I., Ecija, D., Vijayaraghavan, S., Pörtner, M., Bocquet, M.-L., Auwärter, W. & Barth, J. V. In-Situ Growth of Gadolinium Phthalocyaninato Sandwich Complexes on the Ag(111) Surface. *ChemPhysChem Commun* **20,** 1–5. doi:10.1002/cphc.201900253 (2019).

66. Achar, B. N., Fohlen, G. M., Lokesh, K. S. & Mohan Kumar, T. M. GC-MS studies on degradation of copper phthalocyanine sheet polymer. *Int J Mass Spectrom* **243,** 199–204. doi:10.1016/j.ijms.2005.03.001 (2005).

67. Nobelprize.org. *The Nobel Prize in Physics* https://www.nobelprize.org/prizes/physics/1986/summary/ (2019-09-26).

68. Gamov, G. Zur Quantentheorie des Atomkerns. *Z Phys* **51,** 204–212. doi:10.1007/BF01343196 (1928).

69. Bardeen, J. Tunnelling from a many-particle point of view. *Phys Rev Lett* **6,** 57–59. doi:10.1103/PhysRevLett.6.57 (1961).

70. Tersoff, J. & Hamann, D. R. Theory of the scanning tunneling microscope. *Phys Rev B* **31,** 805–813. doi:10.1103/PhysRevB.31.805 (1985).

71. Stroscio, J. A. & Kaiser, W. J. *Scanning Tunneling Microscopy* 27th ed., 459 (Academic Press, inc, 1993).

72. Chen, C. J. *Introduction to Scanning Tunneling Microscopy* 2nd ed., 489. doi:10.1093/acprof:oso/9780199211500.001.0001 (Oxford University Press, 2007).

73. Selloni, A., Carnevali, P., Tosatti, E. & Chen, C. D. Voltage-dependent scanning-tunneling microscopy of a crystal surface: Graphite. *Phys Rev B* **31,** 2602–2605. doi:10.1103/PhysRevB.31.2602 (1985).

74. Hamers, R. J. Atomic-Resolution Surface Spectroscopy with the Scanning Tunneling Microscope. *Annu Rev Phys Chem* **40,** 531–559. doi:10.1146/annurev.pc.40.100189.002531 (1989).

75. IEEE. *Recommended Unit Symbols, SI Prefixes, and Abbreviations* https://www.ewh.ieee.org/soc/ias/pub-dept/abbreviation.pdf (2019-08-30).

76. Katoh, K., Yoshida, Y., Yamashita, M., Miyasaka, H., Breedlove, B. K., Kajiwara, T., Takaishi, S., Ishikawa, N., Isshiki, H., Yan, F. Z., Komeda, T., Yamagishi, M. & Takeya, J. Direct observation of lanthanide(III)-phthalocyanine molecules on Au(111) by using scanning tunneling microscopy and scanning tunneling spectroscopy and thin-film field-effect transistor properties of Tb(III)- and Dy(III)-phthalocyanine molecules. *J Am Chem Soc* **131,** 9967–9976. doi:10.1021/ja902349t (2009).

77. Uphoff, M. *Atomistic Investigations and Control of Novel Quantum Materials: Lanthanide-Organic Nano-Architectures at Well-Defined Substrates and the Iron Silicide (110) Facet* PhD thesis (Technical University Munich, 2019).

78. Stroscio, J. A. & Eigler, D. M. Atomic and molecular manipulation with the scanning tunneling microscope. *Science* **254,** 1319–1326. doi:10.1126/science.254.5036.1319 (1991).

79. Giessibl, F. J. Forces and frequency shifts in atomic-resolution dynamic-force microscopy. *Phys Rev B* **56,** 16010–16015. doi:10.1103/PhysRevB.56.16010 (1997).

80. Giessibl, F. J. Advances in atomic force microscopy. *Rev Mod Phys* **75,** 949–983. doi:10.1103/RevModPhys.75.949 (2003).

81. Morita, S., Giessibl, F. J., Meyer, E. & Wiesendanger, R. *Noncontact Atomic Force Microscopy* doi:10.1007/978-3-319-15588-3 (Springer International Publishing, 2015).

82. Bischoff, F. *Scanning probe microscopy studies of surface confined molecules and (metal-organic) nanostructures* PhD thesis (Technical University Munich, 2017).

83. Schwarz, M. *Assembly and Characterization of Hybrid Nanomaterials on Noble Metal Surfaces* PhD thesis (Technical University Munich, 2018).

84. Rugar, D. & Hansma, P. *Atomic Force Microscopy* tech. rep. (1990), 23–30.

85. Israelachvili, J. N. in *Intermolecular and Surface Forces* 3rd ed., 107–132 (Elsevier, 2011). doi:10.1016/B978-0-12-375182-9.10006-5.

86. London, F. & Polanyi, M. Über die atomtheoretische Deutung der Adsorptionskritfte. *Naturwissenschaften* **18,** 1099–1100. doi:10.1007/BF01492533 (1930).

87. Hamaker, H. C. The London-van der Waals attraction between spherical particles. *Physica* **4,** 1058–1072. doi:10.1016/S0031-8914(37)80203-7 (1937).

88. Bargeman, D. & van Voorst Vader, F. Van der waals forces between immersed particles. *J Electroanal Chem* **37,** 45–52. doi:10.1016/S0022-0728(72)80213-4 (1972).

89. Nonnenmacher, M., O'Boyle, M. P. & Wickramasinghe, H. K. Kelvin probe force microscopy. *Appl Phys Lett* **58,** 2921–2923. doi:10.1063/1.105227 (1991).

90. Mohn, F., Gross, L., Moll, N. & Meyer, G. Imaging the charge distribution within a single molecule. *Nat Nanotechnol* **7,** 227–231. doi:10.1038/nnano.2012.20 (2012).

91. Gross, L., Mohn, F., Moll, N., Liljeroth, P. & Meyer, G. The chemical structure of a molecule resolved by atomic force microscopy. *Science* **325,** 1110–1114. doi:10.1126/science.1176210 (2009).

92. March, N. H. The Thomas-Fermi approximation in quantum mechanics. *Adv Phys* **6,** 1–101. doi:10.1080/00018735700101156 (1957).

93. Hohenberg, P. & Kohn, W. Inhomogeneous Electron Gas. *Phys Rev* **136,** B864–B871. doi:10.1103/PhysRev.136.B864 (1964).

94. Perdew, J. P., Burke, K. & Ernzerhof, M. Generalized Gradient Approximation Made Simple. *Phys Rev Lett* **77,** 3865–3868. doi:10.1103/PhysRevLett.77.3865 (1996).

95. Casida, M. E., Jamorski, C., Casida, K. C. & Salahub, D. R. Molecular excitation energies to high-lying bound states from time-dependent density-functional response theory: Characterization and correction of the time-dependent local density approximation ionization threshold. *J Chem Phys* **108,** 4439–4449. doi:10.1063/1.475855 (1998).

96. Lusk, M. T. & Mattsson, A. E. High-performance computing for materials design to advance energy science. *MRS Bull* **36,** 169–174. doi:10.1557/mrs.2011.30 (2011).

97. Kresse, G. & Furthmüller, J. Efficient iterative schemes for ab initio total-energy calculations using a plane-wave basis set. *Phys Rev B* **54,** 11169–11186. doi:10.1103/PhysRevB.54.11169 (1996).

98. Hafner, J. Ab-initio simulations of materials using VASP: Density-functional theory and beyond. *J Comput Chem* **29,** 2044–2078. doi:10.1002/jcc.21057 (2008).

99. Einstein, A. Über einen die Erzeugung und Verwandlung des Lichtes betreffenden heuristischen Gesichtspunkt. *Annalen der Physik* **322,** 132–148. doi:10.1002/andp.19053220607 (1905).

100. Nobelprize.org. *The Nobel Prize in Physics* https://www.nobelprize.org/prizes/physics/1921/summary/ (2019-09-26).

101. Alford, T. L., Feldman, L. C. & Mayer, J. W. *Fundamentals of nanoscale film analysis* (Springer, New York and London, 2007).

102. He, Y. *Bottom-up Construction and Direct Characterization of Porphyrin- and Graphene-based Nanostructures* PhD thesis (Technical University Munich, 2017).

103. VAb Vakuum-Anlagenbau GmbH. *Marie-Curie-Straße 11, 25337 Elmshorn, Germany* https://www.vab-vakuum.com/ (2019-09-12).

104. Giessibl, F. J. High-speed force sensor for force microscopy and profilometry utilizing a quartz tuning fork. *Appl Phys Lett* **73,** 3956–3958. doi:10.1063/1.122948 (1998).

105. CreaTec Fischer & Co. GmbH. *Manual: How to install the LT-STM head* 2013.

106. CreaTec Fischer & Co. GmbH. *Industriestr. 9, 74391 Erligheim, Germany* https://createc.de/ (2019-09-12).

107. Ducke, J. *Scanning Probe Microscopy Investigation of Hybrid Nano Systems Comprising Functional Molecules and Two-Dimensional Layers* PhD thesis (Technical University Munich, 2018).

108. Zöphel, S. *Der Aufbau eines Tieftemperatur-Rastertunnelmikroskops und Strukturuntersuchungen auf vicinalen Kupferoberflächen* PhD thesis (Freie Universität Berlin, 2000).

109. Wiengarten, A. C. *Scanning tunneling microscopy investigation of structure and electronic properties of surface-confined tetrapyrrolic species* PhD thesis (Technical University Munich, 2015).

110. Liu, L., Feng, Y. P. & Shen, Z. X. Structural and electronic properties of h-BN. *Phys Rev B* **68,** 104102. doi:10.1103/PhysRevB.68.104102 (2003).

111. Novoselov, K. S., Jiang, D., Schedin, F., Booth, T. J., Khotkevich, V. V., Morozov, S. V. & Geim, A. K. Two-dimensional atomic crystals. *P Natl A Sci* **102,** 10451–10453. doi:10.1073/pnas.0502848102 (2005).

112. Alem, N., Erni, R., Kisielowski, C., Rossell, M. D., Gannett, W. & Zettl, A. Atomically thin hexagonal boron nitride probed by ultrahigh-resolution transmission electron microscopy. *Phys Rev B* **80.** doi:10.1103/PhysRevB.80.155425 (2009).

113. Valerius, P., Herbig, C., Will, M., Arman, M. A., Knudsen, J., Caciuc, V., Atodiresei, N. & Michely, T. Annealing of ion-irradiated hexagonal boron nitride on Ir(111). *Phys Rev B* **96,** 235410. doi:10.1103/PhysRevB.96.235410 (2017).

114. Schulz, F., Ijäs, M., Drost, R., Hämäläinen, S. K., Harju, A., Seitsonen, A. P. & Liljeroth, P. Many-body transitions in a single molecule visualized by scanning tunnelling microscopy. *Nature Physics* **11,** 229–234. doi:10.1038/nphys3212 (2015).

115. Will, M., Atodiresei, N., Caciuc, V., Valerius, P., Herbig, C. & Michely, T. A Monolayer of Hexagonal Boron Nitride on Ir(111) as a Template for Cluster Superlattices. *ACS Nano* **12,** 6871–6880. doi:10.1021/acsnano.8b02127 (2018).

116. Moser, F. H. & Thomas, A. L. Phthalocyanine compounds. *J Chem Educ* **41,** 245. doi:10.1021/ed041p245 (1964).

117. Lu, L., Zheng, T., Wu, Q., Schneider, A. M., Zhao, D. & Yu, L. Recent Advances in Bulk Heterojunction Polymer Solar Cells. *Chem Rev* **115,** 12666–12731. doi:10.1021/acs.chemrev.5b00098 (2015).

118. Xin, N., Guan, J., Zhou, C., Chen, X., Gu, C., Li, Y., Ratner, M. A., Nitzan, A., Stoddart, J. F. & Guo, X. Concepts in the design and engineering of single-molecule electronic devices. *Nat Rev Phys* **1,** 211–230. doi:10.1038/s42254-019-0022-x (2019).

119. Samori, P. & Biscarini, F. Nanomaterials properties tuned by their environment: integrating supramolecular concepts into sensing devices. *Chem Soc Rev* **47,** 4675–4676. doi:10.1039/C8CS90066C (2018).

120. Grill, L. Functionalized molecules studied by STM: motion, switching and reactivity. *J Phys-Condens Mat* **20,** 053001. doi:10.1088/0953-8984/20/05/053001 (2008).

121. Swart, I., Gross, L. & Liljeroth, P. Single-molecule chemistry and physics explored by low-temperature scanning probe microscopy. *Chem Commun* **47,** 9011. doi:10.1039/c1cc11404b (2011).

122. Neaton, J. B., Hybertsen, M. S. & Louie, S. G. Renormalization of Molecular Electronic Levels at Metal-Molecule Interfaces. *Phys Rev Lett* **97,** 216405. doi:10.1103/PhysRevLett.97.216405 (2006).

123. Hollerer, M., Lüftner, D., Hurdax, P., Ules, T., Soubatch, S., Tautz, F. S., Koller, G., Puschnig, P., Sterrer, M. & Ramsey, M. G. Charge Transfer and Orbital Level Alignment at Inorganic/Organic Interfaces: The Role of Dielectric Interlayers. *ACS Nano* **11,** 6252–6260. doi:10.1021/acsnano.7b02449 (2017).

124. Cochrane, K. A., Schiffrin, A., Roussy, T. S., Capsoni, M. & Burke, S. A. Pronounced polarization-induced energy level shifts at boundaries of organic semiconductor nanostructures. *Nat Commun* **6.** doi:10.1038/ncomms9312 (2015).

125. Riss, A., Wickenburg, S., Tan, L. Z., Tsai, H.-Z., Kim, Y., Lu, J., Bradley, A. J., Ugeda, M. M., Meaker, K. L., Watanabe, K., Taniguchi, T., Zettl, A., Fischer, F. R., Louie, S. G. & Crommie, M. F. Imaging and Tuning Molecular Levels at the Surface of a Gated Graphene Device. *ACS Nano* **8,** 5395–5401. doi:10.1021/nn501459v (2014).

126. Wickenburg, S., Lu, J., Lischner, J., Tsai, H., Omrani, A. A., Riss, A., Karrasch, C., Bradley, A. J., Jung, H. S., Khajeh, R., Wong, D., Watanabe, K., Taniguchi, T., Zettl, A., Neto, A. H. C., Louie, S. G. & Crommie, M. F. Tuning charge and correlation effects for a single molecule on a graphene device. *Nat Commun* **7,** 13553. doi:10.1038/ncomms13553 (2016).

127. Liu, L., Dienel, T., Widmer, R. & Gröning, O. Interplay between Energy-Level Position and Charging Effect of Manganese Phthalocyanines on an Atomically Thin Insulator. *ACS Nano* **9,** 10125–10132. doi:10.1021/acsnano.5b03741 (2015).

128. Swart, I., Sonnleitner, T. & Repp, J. Charge state control of molecules reveals modification of the tunneling barrier with intramolecular contrast. *Nano Lett* **11,** 1580–1584. doi:10.1021/nl104452x (2011).

129. Nazin, G. V., Qiu, X. H. & Ho, W. Charging and Interaction of Individual Impurities in a Monolayer Organic Crystal. *Phys Rev Lett* **95,** 166103. doi:10.1103/PhysRevLett.95.166103 (2005).

130. Brar, V. W., Decker, R., Solowan, H.-M. M., Wang, Y., Maserati, L., Chan, K. T., Lee, H., Girit, C. O., Zettl, A., Louie, S. G., Cohen, M. L. & Crommie, M. F. Gate-controlled ionization and screening of cobalt adatoms on a graphene surface. *Nat Phys* **7,** 43–47. doi:10.1038/nphys1807 (2011).

131. Fernandez-Torrente, I., Kreikemeyer-Lorenzo, D., Strozecka, A., Franke, K. J. & Pascual, J. I. Gating the charge state of single molecules by local electric fields. *Phys Rev Lett* **108.** doi:10.1103/PhysRevLett.108.036801 (2012).

132. Hauptmann, N., Hamann, C., Tang, H. & Berndt, R. Switching and charging of a ruthenium dye on Ag(111). *Phys Chem Chem Phys* **15,** 10326–10330. doi:10.1039/c3cp51023a (2013).

133. Nazin, G. V., Wu, S. W. & Ho, W. Molecular Electronics Special Feature: Tunneling rates in electron transport through double-barrier molecular junctions in a scanning tunneling microscope. *P Natl A Sci* **102,** 8832–8837. doi:10.1073/pnas.0501171102 (2005).

134. Wu, S. W., Nazin, G. V., Chen, X., Qiu, X. H. & Ho, W. Control of relative tunneling rates in single molecule bipolar electron transport. *Phys Rev Lett* **93.** doi:10.1103/PhysRevLett.93.236802 (2004).

135. Toader, M., Gopakumar, T. G., Shukrynau, P. & Hietschold, M. Exploring the F_{16}CoPc/Ag(110) Interface Using Scanning Tunneling Microscopy and Spectroscopy. 2. Adsorption-Induced Charge Transfer Effect. *J Phys Chem C* **114,** 21548–21554. doi:10.1021/jp1078295 (2010).

136. Teichmann, K., Wenderoth, M., Loth, S., Ulbrich, R. G., Garleff, J. K., Wijnheijmer, A. P. & Koenraad, P. M. Controlled charge switching on a single donor with a scanning tunneling microscope. *Phys Rev Lett* **101,** 076103. doi:10.1103/PhysRevLett.101.076103 (2008).

137. Järvinen, P., Hämäläinen, S. K., Banerjee, K., Häkkinen, P., Ijäs, M., Harju, A. & Liljeroth, P. Molecular self-assembly on graphene on SiO_2 and h-BN substrates. *Nano Lett* **13,** 3199–3204. doi:10.1021/nl401265f (2013).

138. Arya, S. & D'Amico, A. Preparation, properties and applications of boron nitride thin films. *Thin Solid Films* **157,** 267–282. doi:10.1016/0040-6090(88)90008-9 (1988).

139. Ramprasad, R. & Shi, N. Polarizability of phthalocyanine based molecular systems: A first-principles electronic structure study. *Appl Phys Lett* **88,** 222903. doi:10.1063/1.2209197 (2006).

140. Scarfato, A., Chang, S. H., Kuck, S., Brede, J., Hoffmann, G. & Wiesendanger, R. Scanning tunneling microscope study of iron(II) phthalocyanine growth on metals and insulating surfaces. *Surf Sci* **602,** 677–683. doi:10.1016/j.susc.2007.11.011 (2008).

141. Cockins, L., Miyahara, Y., Bennett, S. D., Clerk, A. A., Studenikin, S., Poole, P., Sachrajda, A. & Grutter, P. Energy levels of few-electron quantum dots imaged and characterized by atomic force microscopy. *P Natl A Sci* **107,** 9496–9501. doi:10.1073/pnas.0912716107 (2010).

142. Kocic, N., Weiderer, P., Keller, S., Decurtins, S., Liu, S. X. & Repp, J. Periodic Charging of Individual Molecules Coupled to the Motion of an Atomic Force Microscopy Tip. *Nano Lett* **15,** 4406–4411. doi:10.1021/acs.nanolett.5b00711 (2015).

143. Pradhan, N. A., Liu, N., Silien, C. & Ho, W. Atomic scale conductance induced by single impurity charging. *Phys Rev Lett* **94.** doi:10.1103/PhysRevLett.94.076801 (2005).

144. Blöchl, P. E. Projector augmented-wave method. *Phys Rev B* **50,** 17953–17979. doi:10.1103/PhysRevB.50.17953 (1994).

145. Kresse, G. & Furthmüller, J. Efficiency of ab-initio total energy calculations for metals and semiconductors using a plane-wave basis set. *Comp Mater Sci* **6,** 15–50. doi:10.1016/0927-0256(96)00008-0 (1996).

146. Kresse, G. & Joubert, D. From ultrasoft pseudopotentials to the projector augmented - wave method. *Phys Rev B* **59,** 1758–1775. doi:10.1103/PhysRevB.59.1758 (1999).

147. Grimme, S., Antony, J., Ehrlich, S. & Krieg, H. A consistent and accurate ab initio parametrization of density functional dispersion correction (DFT-D) for the 94 elements H-Pu. *J Chem Phys* **132,** 154104. doi:10.1063/1.3382344 (2010).

148. Lu, X., Grobis, M., Khoo, K. H., Louie, S. G. & Crommie, M. F. Charge transfer and screening in individual C_{60} molecules on metal substrates: A scanning tunneling spectroscopy and theoretical study. *Phys Rev B* **70,** 115418. doi:10.1103/PhysRevB.70.115418 (2004).

149. Järvinen, P., Hämäläinen, S. K., Ijäs, M., Harju, A. & Liljeroth, P. Self-Assembly and Orbital Imaging of Metal Phthalocyanines on a Graphene Model Surface. *J Phys Chem C* **118,** 13320–13325. doi:10.1021/jp504813v (2014).

150. Uhlmann, C., Swart, I. & Repp, J. Controlling the Orbital Sequence in Individual Cu-Phthalocyanine Molecules. *Nano Lett* **13,** 777–780. doi:10.1021/nl304483h (2013).

151. Cochrane, K. A., Roussy, T. S., Yuan, B., Tom, G., Marsell, E. & Burke, S. A. Molecularly Resolved Electronic Landscapes of Differing Acceptor–Donor Interface Geometries. *J Phys Chem C* **122,** 8437–8444. doi:10.1021/acs.jpcc.8b01396 (2018).

152. Hofmann, O. T., Rinke, P., Scheffler, M. & Heimel, G. Integer versus Fractional Charge Transfer at Metal(/Insulator)/Organic Interfaces: Cu(/NaCl)/TCNE. *ACS Nano* **9,** 5391–5404. doi:10.1021/acsnano.5b01164 (2015).

153. Hesper, R., Tjeng, L. H. & Sawatzky, G. A. Strongly reduced band gap in a correlated insulator in close proximity to a metal. *Europhys Lett* **40,** 177–182. doi:10.1209/epl/i1997-00442-2 (1997).

154. Amokrane, A., Klyatskaya, S., Boero, M., Ruben, M. & Bucher, J. P. Role of π-Radicals in the Spin Connectivity of Clusters and Networks of Tb Double-Decker Single Molecule Magnets. *ACS Nano* **11,** 10750–10760. doi:10.1021/acsnano.7b05804 (2017).

155. Chen, Y., Su, W., Bai, M., Jiang, J., Li, X., Liu, Y., Wang, L. & Wang, S. High performance organic field-effect transistors based on amphiphilic tris(phthalocyaninato) rare earth triple-decker complexes. *J Am Chem Soc* **127,** 15700–15701. doi:10.1021/ja054343e (2005).

156. He, Y., Zhang, Y., Hong, I. P., Cheng, F., Zhou, X., Shen, Q., Li, J., Wang, Y., Jiang, J. & Wu, K. Low-temperature scanning tunneling microscopy study of double-decker $DyPc_2$ on Pb Surface. *Nanoscale* **6,** 10779–10783. doi:10.1039/c4nr02863e (2014).

157. Hellerstedt, J., Cahlik, A., Svec, M., de la Torre, B., Moro-Lagares, M., Chutora, T., Papouskova, B., Zoppellaro, G., Mutombo, P., Ruben, M., Zboril, R. & Jelinek, P. On-surface structural and electronic properties of spontaneously formed Tb_2Pc_3 single molecule magnets. *Nanoscale* **10,** 15553–15563. doi:10.1039/C8NR04215B (2018).

158. Ishikawa, N., Sugita, M., Ishikawa, T., Koshihara, S. Y. & Kaizu, Y. Lanthanide double-decker complexes functioning as magnets at the single-molecular level. *J Am Chem Soc* **125,** 8694–8695. doi:10.1021/ja029629n (2003).

159. Katoh, K., Komeda, T. & Yamashita, M. The Frontier of Molecular Spintronics Based on Multiple-Decker Phthalocyaninato Tb^{III} Single-Molecule Magnets. *Chem Rec* **16,** 987–1016. doi:10.1002/tcr.201500290 (2016).

160. Komeda, T., Katoh, K. & Yamashita, M. Double-decker phthalocyanine complex: Scanning tunneling microscopy study of film formation and spin properties. *Prog Surf Sci* **89,** 127–160. doi:10.1016/j.progsurf.2014.03.001 (2014).

161. Serrano, G., Velez-Fort, E., Cimatti, I., Cortigiani, B., Malavolti, L., Betto, D., Ouerghi, A., Brookes, N. B., Mannini, M. & Sessoli, R. Magnetic bistability of a $TbPc_2$ submonolayer on a graphene/SiC(0001) conductive electrode. *Nanoscale* **10,** 2715–2720. doi:10.1039/c7nr08372f (2018).

162. Takami, T., Ye, T., Arnold, D. P., Sugiura, K., Wang, R., Jiang, J. & Weiss, P. S. Controlled Adsorption Orientation for Double-Decker Complexes. *J Phys Chem C* **111,** 2077–2080. doi:10.1021/jp063309z (2007).

163. Zhang, Y., Wang, Y., Liao, P., Wang, K., Huang, Z., Liu, J., Chen, Q., Jiang, J. & Wu, K. Detection and Manipulation of Charge States for Double-Decker $DyPc_2$ Molecules on Ultrathin CuO Films. *ACS Nano* **12,** 2991–2997. doi:10.1021/acsnano.8b00751 (2018).

164. Vitali, L., Fabris, S., Conte, A. M., Brink, S., Ruben, M., Baroni, S. & Kern, K. Electronic structure of surface-supported bis(phthalocyaninato) terbium(lll) single molecular magnets. *Nano Lett* **8,** 3364–3368. doi:10.1021/nl801869b (2008).

165. Zhang, Y. F., Isshiki, H., Katoh, K., Yoshida, Y., Yamashita, M., Miyasaka, H., Breedlove, B. K., Kajiwara, T., Takaishi, S. & Komeda, T. Low-Temperature Scanning Tunneling Microscopy Investigation of Bis(phthalocyaninato)yttrium Growth on Au(111): From Individual Molecules to Two-Dimensional Domains. *J Phys Chem C* **113,** 9826–9830. doi:10.1021/jp902410q (2009).

166. Isshiki, H., Liu, J., Katoh, K., Yamashita, M., Miyasaka, H., Breedlove, B. K., Takaishi, S. & Komeda, T. Scanning tunneling microscopy investigation of Tris (phthalocyaninato) yttrium triple-decker molecules deposited on Au(111). *J Phys Chem C* **114,** 12202–12206. doi:10.1021/jp101349v (2010).

167. Schwarz, M., Garnica, M., Duncan, D. A., Perez Paz, A., Ducke, J., Deimel, P. S., Thakur, P. K., Lee, T.-L., Rubio, A., Barth, J. V., Allegretti, F. & Auwärter, W. Adsorption Conformation and Lateral Registry of Cobalt Porphine on Cu(111). *J Phys Chem C* **122,** 5452–5461. doi:10.1021/acs.jpcc.7b11705 (2018).

168. Li, J., Schneider, W.-D., Berndt, R., Bryant, O. R. & Crampin, S. Surface-State Lifetime Measured by Scanning Tunneling Spectroscopy. *Phys Rev Lett* **81,** 4464–4467. doi:10.1103/PhysRevLett.81.4464 (1998).

169. Dufour, G., Poncey, C., Rochet, F., Roulet, H., Sacchi, M., De Santis, M. & De Crescenzi, M. Copper phthalocyanine on Si(111)-7 × 7 and Si(001)-2 × 1 surfaces: an X-ray photoemission spectroscopy and synchrotron X-ray absorption spectroscopy study. *Surf Sci* **319,** 251–266. doi:10.1016/0039-6028(94)90592-4 (1994).

170. Ottaviano, L., Lozzi, L., Ramondo, F., Picozzi, P. & Santucci, S. Copper hexadecafluoro phthalocyanine and naphthalocyanine: The role of shake up excitations in the interpretation and electronic distinction of high-resolution X-ray photoelectron spectroscopy measurements. *J Electron Spectrosc* **105,** 145–154. doi:10.1016/S0368-2048(99)00064-X (1999).

171. Bai, Y., Buchner, F., Wendahl, M. T., Kellner, I., Bayer, A., Steinrück, H.-P., Marbach, H. & Gottfried, J. M. Direct Metalation of a Phthalocyanine Monolayer on Ag(111) with Coadsorbed Iron Atoms. *J Phys Chem C* **112,** 6087–6092. doi:10.1021/jp711122w (2008).

172. Chen, M., Röckert, M., Xiao, J., Drescher, H.-J., Steinrück, H.-P., Lytken, O. & Gottfried, J. M. Coordination Reactions and Layer Exchange Processes at a Buried Metal–Organic Interface. *J Phys Chem C* **118,** 8501–8507. doi:10.1021/jp5019235 (2014).

173. Smykalla, L., Shukrynau, P., Zahn, D. R. T. & Hietschold, M. Self-Metalation of Phthalocyanine Molecules with Silver Surface Atoms by Adsorption on Ag(110). *J Phys Chem C* **119,** 17228–17234. doi:10.1021/acs.jpcc.5b04977 (2015).

174. Di Santo, G., Castellarin-Cudia, C., Fanetti, M., Taleatu, B., Borghetti, P., Sangaletti, L., Floreano, L., Magnano, E., Bondino, F. & Goldoni, A. Conformational Adaptation and Electronic Structure of 2H-Tetraphenylporphyrin on Ag(111) during Fe Metalation. *J Phys Chem C* **115,** 4155–4162. doi:10.1021/jp111151n (2011).

175. Praline, G., Koel, B., Hance, R., Lee, H.-I. & White, J. X-Ray photoelectron study of the reaction of oxygen with cerium. *J Electron Spectrosc* **21,** 17–30. doi:10.1016/0368-2048(80)85034-1 (1980).

176. Dudarev, S. L., Botton, G. A., Savrasov, S. Y., Humphreys, C. J. & Sutton, A. P. Electron-energy-loss spectra and the structural stability of nickel oxide: An LSDA+U study. *Phys Rev B* **57,** 1505–1509. doi:10.1103/PhysRevB.57.1505 (1998).

177. Bian, Y., Li, L., Wang, D., Choi, C.-F., Cheng, D. Y. Y., Zhu, P., Li, R., Dou, J., Wang, R., Pan, N., Ng, D. K. P., Kobayashi, N. & Jiang, J. Synthetic, Structural, Spectroscopic, and Electrochemical Studies of Heteroleptic Tris(phthalocyaninato) Rare Earth Complexes. *Eur J Inorg Chem* **2005,** 2612–2618. doi:10.1002/ejic.200400920 (2005).

178. Tersoff, J. & Hamann, D. R. Theory and Application for the Scanning Tunneling Microscope. *Phys Rev Lett* **50,** 1998–2001. doi:10.1103/PhysRevLett.50.1998 (1983).

179. Lorente, N. & Persson, M. Theoretical aspects of tunneling-current-induced bond excitation and breaking at surfaces. *Faraday Discuss* **117,** 277–290. doi:10.1039/b002826f (2000).

180. Bocquet, M.-L., Lesnard, H., Monturet, S. & Lorente, N. in *Computational Methods in Catalysis and Materials Science* 199–219 (Wiley-VCH Verlag GmbH & Co. KGaA, Weinheim, Germany, 2009). doi:10.1002/9783527625482.ch11.

181. Gonidec, M., Biagi, R., Corradini, V., Moro, F., De Renzi, V., Del Pennino, U., Summa, D., Muccioli, L., Zannoni, C., Amabilino, D. B. & Veciana, J. Surface supra-molecular organization of a terbium(III) double-decker complex on graphite and its single molecule magnet behavior. *J Am Chem Soc* **133,** 6603–6612. doi:10.1021/ja109296c (2011).

182. Sun, Y., Liu, Y. & Zhu, D. Advances in organic field-effect transistors. *J Mater Chem* **15,** 53. doi:10.1039/b411245h (2005).

183. Weng, Q., Wang, X., Wang, X., Bando, Y. & Golberg, D. Functionalized hexagonal boron nitride nanomaterials: emerging properties and applications. *Chem Soc Rev* **45,** 3989–4012. doi:10.1039/C5CS00869G (2016).

184. Sainsbury, T., Satti, A., May, P., O'Neill, A., Nicolosi, V., Gun'ko, Y. K. & Coleman, J. N. Covalently Functionalized Hexagonal Boron Nitride Nanosheets by Nitrene Addition. *Chem-Eur J* **18,** 10808–10812. doi:10.1002/chem.201201734 (2012).

185. Sainsbury, T., Satti, A., May, P., Wang, Z., McGovern, I., Gun'ko, Y. K. & Coleman, J. Oxygen Radical Functionalization of Boron Nitride Nanosheets. *J Am Chem Soc* **134,** 18758–18771. doi:10.1021/ja3080665 (2012).

186. Ikuno, T., Sainsbury, T., Okawa, D., Frechet, J. M. J. & Zettl, A. Amine - functionalized boron nitride nanotubes. *Solid State Commun* **142,** 643–646. doi:10.1016/j.ssc.2007.04.010 (2007).

187. Nazarov, A. S., Demin, V. N., Grayfer, E. D., Bulavchenko, A. I., Arymbaeva, A. T., Shin, H.-J., Choi, J.-Y. & Fedorov, V. E. Functionalization and Dispersion of Hexagonal Boron Nitride (h-BN) Nanosheets Treated with Inorganic Reagents. *Chem-Asian J* **7,** 554–560. doi:10.1002/asia.201100710 (2012).

188. Zhi, C. Y., Bando, Y., Terao, T., Tang, C. C., Kuwahara, H. & Golberg, D. Chemically Activated Boron Nitride Nanotubes. *Chem-Asian J* **4,** 1536–1540. doi:10.1002/asia.200900158 (2009).

189. Sigma-Aldrich. *1,3-Diiminoisoindoline 97%* https://www.sigmaaldrich.com/catalog/product/aldrich/279528?lang=de&region=DE (2019-10-07).

190. Kumar, A., Banerjee, K., Dvorak, M., Schulz, F., Harju, A., Rinke, P. & Liljeroth, P. Charge-Transfer-Driven Nonplanar Adsorption of F_4TCNQ Molecules on Epitaxial Graphene. *ACS Nano* **11,** 4960–4968. doi:10.1021/acsnano.7b01599 (2017).

191. Vijayaraghavan, S., Ecija, D., Auwärter, W., Joshi, S., Seufert, K., Seitsonen, A. P., Tashiro, K. & Barth, J. V. Selective supramolecular fullerene-porphyrin interactions and switching in surface-confined C_{60}-Ce(TPP)$_2$ dyads. *Nano Lett* **12,** 4077–4083. doi:10.1021/nl301534p (2012).

192. Duncan, D. A., Pfisterer, J. H. K., Deimel, P. S., Acres, R. G., Fritton, M., Feulner, P., Barth, J. V. & Allegretti, F. Formation of a thermally stable bilayer of coadsorbed intact and deprotonated thymine exploiting the surface corrugation of rutile TiO_2(110). *Phys Chem Chem Phys* **18,** 20433–20442. doi:10.1039/C6CP02541B (2016).

193. Chakradhar, A., Trettel, K. & Burghaus, U. Benzene adsorption on Ru(0001) and graphene/Ru(0001)—How to synthesize epitaxial graphene without STM or LEED? *Chem Phys Lett* **590,** 146–152. doi:10.1016/j.cplett.2013.10.069 (2013).

194. Komarneni, M., Sand, A., Goering, J., Burghaus, U., Lu, M., Monica Veca, L. & Sun, Y.-P. Possible effect of carbon nanotube diameter on gas–surface interactions – The case of benzene, water, and n-pentane adsorption on SWCNTs at ultra-high vacuum conditions. *Chem Phys Lett* **476,** 227–231. doi:10.1016/j.cplett.2009.05.072 (2009).

195. Blank, D. A., North, S. W. & Lee, Y. T. The ultraviolet photodissociation dynamics of pyrrole. *Chem Phys* **187,** 35–47. doi:10.1016/0301-0104(94)00230-4 (1994).

196. Bacskay, G. B., Martoprawiro, M. & Mackie, J. C. The thermal decomposition of pyrrole: an ab initio quantum chemical study of the potential energy surface associated with the hydrogen cyanide plus propyne channel. *Chem Phys Lett* **300,** 321–330. doi:10.1016/S0009-2614(98)01388-8 (1999).

197. Baadji, N., Kuck, S., Brede, J., Hoffmann, G., Wiesendanger, R. & Sanvito, S. Controlled sequential dehydrogenation of single molecules by scanning tunneling microscopy. *Phys Rev B* **82,** 115447. doi:10.1103/PhysRevB.82.115447 (2010).

198. Neel, N., Lattelais, M., Bocquet, M.-L. & Kröger, J. Depopulation of Single - Phthalocyanine Molecular Orbitals upon Pyrrolic - Hydrogen Abstraction on Graphene. *ACS Nano* **10,** 2010–2016. doi:10.1021/acsnano.5b06153 (2016).

199. Pham, V. D., Repain, V., Chacon, C., Bellec, A., Girard, Y., Rousset, S., Smogunov, A., Dappe, Y. J. & Lagoute, J. Control of Molecule–Metal Interaction by Hydrogen Manipulation in an Organic Molecule. *J Physi Chem Lett* **7,** 1416–1421. doi:10.1021/acs.jpclett.6b00476 (2016).

200. Auwärter, W., Seufert, K., Bischoff, F., Ecija, D., Vijayaraghavan, S., Joshi, S., Klappenberger, F., Samudrala, N. & Barth, J. V. A surface-anchored molecular four-level conductance switch based on single proton transfer. *Nat Nanotechnol* **7,** 41–46. doi:10.1038/nnano.2011.211 (2012).

201. Katz, H. E., Bao, Z. & Gilat, S. L. Synthetic Chemistry for Ultrapure, Processable, and High-Mobility Organic Transistor Semiconductors. *Accounts Chem Res* **34,** 359–369. doi:10.1021/ar990114j (2001).

202. Rheinfrank, E. *On-Surface Synthesis and Characterization of Actinide Tetrapyrrole Complexes* (Master Thesis, Technical University Munich, 2019).

203. Girolami, G. S., Gorlin, P. A., Milam, S. N., Suslick, K. S. & Wilson, S. R. Bis (porphyrin) actinide complexes and their radical cations and dications. *J Coord Chem* **32,** 173–212. doi:10.1080/00958979408024247 (1994).

204. Coraux, J., N'Diaye, A. T., Busse, C. & Michely, T. Structural Coherency of Graphene on Ir(111). *Nano Lett* **8,** 565–570. doi:10.1021/nl0728874 (2008).

205. Rasool, H. I., Song, E. B., Mecklenburg, M., Regan, B. C., Wang, K. L., Weiller, B. H. & Gimzewski, J. K. Atomic-Scale Characterization of Graphene Grown on Copper (100) Single Crystals. *J Am Chem Soc* **133,** 12536–12543. doi:10.1021/ja200245p (2011).

206. Song, X., Gao, J., Gao, T., Nie, Y., Sun, J., Chen, Y., Jin, C., Ding, F., Zhang, Y. & Liu, Z. Wafer-scale CVD Growth of Monolayer Hexagonal Boron Nitride with Large Domain Size by Cu Foil Enclosure Approach. *arXiv,* 1–20 (2015).

207. Ma, C., Park, J., Liu, L., Kim, Y. S., Yoon, M., Baddorf, A. P., Gu, G. & Li, A. P. Interplay between intercalated oxygen superstructures and monolayer h-BN on Cu(100). *Phys Rev B* **94,** 1–8. doi:10.1103/PhysRevB.94.064106 (2016).

208. Tait, S. L., Langner, A., Lin, N., Stepanow, S., Rajadurai, C., Ruben, M. & Kern, K. One-Dimensional Self-Assembled Molecular Chains on Cu(100): Interplay between Surface-Assisted Coordination Chemistry and Substrate Commensurability. *J Phys Chem C* **111,** 10982–10987. doi:10.1021/jp071100v (2007).

209. Desrosiers, R. M., Greve, D. W. & Gellman, A. J. Nucleation of boron nitride thin films on Ni(100). *Surf Sci* **382,** 35–48. doi:10.1016/S0039-6028(97)00092-7 (1997).

210. Späth, F., Gebhardt, J., Düll, F., Bauer, U., Bachmann, P., Gleichweit, C., Görling, A., Steinrück, H.-P. & Papp, C. Hydrogenation and hydrogen intercalation of hexagonal boron nitride on Ni(1 1 1): reactivity and electronic structure. *2D Materials* **4,** 035026. doi:10.1088/2053-1583/aa7d6b (2017).

211. Corso, M. *Boron nitride nanostructures on transition metals: flat layers and nanomesh* PhD thesis (University of Zurich, 2006). doi:10.5167/uzh-163626.

212. Preobrajenski, A. B., Vinogradov, A. S. & Martensson, N. Monolayer of h-BN chemisorbed on Cu(111) and Ni(111): The role of the transition metal 3d states. *Surf Sci* **582,** 21–30. doi:10.1016/j.susc.2005.02.047 (2005).

213. Raspberry Pi Foundation. *RaspberryPi* https://www.raspberrypi.org/ (2019-09-12).

214. Python Software Foundation. *Python* https://www.python.org/ (2019-09-24).

215. Van der Walt, S., Colbert, S. C. & Varoquaux, G. The NumPy Array: A Structure for Efficient Numerical Computation. *Comput Sci Eng* **13,** 22–30. doi:10.1109/MCSE.2011.37 (2011).

216. Jones, E., Oliphant, T., Peterson, P., *et al. SciPy: Open source scientific tools for Python* http://www.scipy.org/.

217. Hunter, J. D. Matplotlib: A 2D Graphics Environment. *Comput Sci Eng* **9,** 90–95. doi:10.1109/MCSE.2007.55 (2007).

218. Necas, D. & Klapetek, P. Gwyddion: an open-source software for SPM data analysis. *Open Phys* **10,** 181–188. doi:10.2478/s11534-011-0096-2 (2012).

219. Wojdyr, M. Fityk : a general-purpose peak fitting program. *J Appl Crystallogr* **43,** 1126–1128. doi:10.1107/S0021889810030499 (2010).

220. Hanwell, M. D., Curtis, D. E., Lonie, D. C., Vandermeersch, T., Zurek, E. & Hutchison, G. R. Avogadro: an advanced semantic chemical editor, visualization, and analysis platform. *J Cheminformatics* **4,** 17. doi:10.1186/1758-2946-4-17 (2012).

221. Humphrey, W., Dalke, A. & Schulten, K. VMD: Visual molecular dynamics. *J Mol Graphics* **14,** 33–38. doi:10.1016/0263-7855(96)00018-5 (1996).

H. List of Figures

1.1. Principle of scanning tunneling microscopy . . . 6
1.2. Electron tunneling . . . 9
1.3. STM modes . . . 13
2.1. AFM model . . . 16
2.2. AFM Potential & Force . . . 19
3.1. Electron cloud approximation . . . 21
3.2. Flowchart of iteration in DFT . . . 22
4.1. Principle of XPS . . . 23
5.1. Setup of the UHV system . . . 26
5.2. Setup of the cryogenic system . . . 29
5.3. Schematic drawing of the SPM scanner . . . 30
5.4. Piezo movement . . . 31
6.1. High symmetry planes of a fcc crystal . . . 33
6.2. Schematic structure of hexagonal boron nitride (hBN) . . . 34
6.3. Chemical vapor deposition of borazine . . . 35
6.4. Different tetrapyrrole-based molecules . . . 37
7.1. Adsorption of F_{16}CoPc on hBN/Cu(111) . . . 42
7.2. Template induced gating of F_{16}CoPc . . . 45
7.3. Spatial dependence of dI/dV spectroscopy of F_{16}CoPc . . . 47
7.4. Spatial dependence of the charging of F_{16}CoPc . . . 48
7.5. Dependency between the energetic position of MO and CP . . . 49
7.6. Energy shift of the MO peaks of F_{16}CoPc due to polarization . . . 51
7.7. Different coverages of F_{16}CoPc on hBN/Cu(111) . . . 52
7.8. Spectroscopic study of the surface with a high coverage of F_{16}CoPc . . . 53
7.9. AFM measurements on F_{16}CoPc . . . 56
7.10. Growth and electronic properties of the 2nd layer F_{16}CoPc/hBN/Cu(111) . . . 57
7.11. Calculated adsorption of CO on F_{16}CoPc . . . 59
7.12. Statistics on the alignments of F_{16}CoPc/hBN/Ir(111) at low coverage . . . 61
7.13. Statistics on the alignments of F_{16}CoPc/hBN/Ir(111) at high coverage . . . 62
7.14. STS measurements of F_{16}CoPc on hBN/Ir(111) . . . 65
8.1. Structure model of $CePc_2$ . . . 70
8.2. Adsorption of $CePc_2$ on hBN/Ir(111) . . . 72
8.3. Room temperature measurements of Ce-based multideckers on hBN/Ir(111) 74
8.4. Adsorption of $CePc_2$ on Ag(111) . . . 76

8.5. XPS measurements of the in-situ growth of Ce-based multideckers 79
8.6. Calculated magnetization of the individual atoms in the $CePc_2$ molecules . 83
8.7. Structure of the adsorbed $CePc_2$ molecules on hBN/Ir(111) 84
8.8. STM simulations of $CePc_2$/hBN/Ir(111) 86
9.1. Evaporation of 2III measured by mass spectrometry 90
9.2. Adsorption of 2III on hBN/Ir(111) 91
9.3. Bias-voltage-dependent appearance of 2III on hBN/Ir(111) 92
9.4. Irreversible modification of 2III by STS 93
9.5. XPS measurements of 2III on Ir(111) and on hBN/Ir(111) 95
9.6. XPS measurements of thermal stability of 2III/hBN/Ir(111) 97
9.7. Dimer formation of 2III on hBN/ Ir(111) 99
9.8. Adsorption of 2III on a submonolayer hBN/Ir(111) 100
9.9. Energetic levels of 2III molecules calculated by DFT 103
9.10. STM simulation of the monomer, radical and biradical 105
9.11. STM simulation of the dimers 107
10.1. Fitting rotation angles of $Gd_{x-1}Pc_x$ 113
10.2. Rotation angles and corrugation of all Pcs 114
10.3. Comparison of theoretical and experimentally obtained rotation angles . . 115
10.4. Formation energy for different multideckers 116
10.5. Molecular structure of $Th(TPP)_2$ 118
10.6. Adsorption of $Th(TPP)_2$ on Ag(111) 119
10.7. $Th(TPP)_2$ with upper TPP rotated by 33° 120
A.1. Calculated structure of hBN/Ir(111) 131
A.2. STM simulation of hBN/Ir(111) 132
B.1. XPS measurement of the growth of hBN on Cu(100) 133
B.2. STM measurements of the moiré of hBN/Cu(100) 135
C.1. Setup borazine refill 138
C.2. Mass spectrum of borazine 139
D.1. Screenshots of the graphic user interface of lab automatization software . . 141
D.2. Connecting scheme for the lab automatization of the “AFM” setup 142

I. List of Tables

6.1. Annealing temperatures for metals 34
7.1. Ground state energies of differently charged systems of $CO/F_{16}CoPc$ 59
8.1. Heights of double- and tripledecker molecules 73
8.2. XPS measurement fit parameters of Ce-based multideckers 78
9.1. XPS measurement fit parameters of 2III/Ir(111) & 2III/hBN/Ir(111) . . . 94
9.2. List of the calculated energies for different 2III molecules 102
10.1. Calculated values for $Gd_{x-1}Pc_x$ multideckers 112
10.2. Tilting of the ligands in $Th(TPP)_2$ 118
B.1. Binding energies of B1s and N1s peaks of hBN 134

J. Acknowledgment

At the end of this thesis I would like to thank all those who have contributed to it. Particularly I would like to express my gratitude to the following people:
First of all I would like to thank Prof. Willi Auwärter for giving me the opportunity to join his group and for supervising me during my PhD. A lot of thanks also to Dr. Alex Riss and Dr. Knud Seufert, who helped me a lot in the lab by setting up the experiments and with the analysis of the data.
A great thanks goes to the staff of E20, *i.e.*, Dr. Martin Uphoff, Aleksandr Baklanov, Andi Walz, Eduardo Rascon, Dr. Knud Seufert, Dr. Alex Riss, Dr. Tobias Paintner, Dr. Jacob Ducke, Sabine Synkule, Karolina Steuber, Dr. Felix Bischoff, Domenik Zimmermann, Dr. Martin Schwarz and Prof. Peter Feulner who supported me on the one hand with scientific discussion and on the other hand with important time of distraction from work by cooking or playing darts!
Many thanks also to Karl Eberle, Reinhold Schneider and Prof. Peter Feulner for fixing, repairing or building a lot of lab equipment and for their support concerning technical questions. Furthermore, I thank Viktoria Blaschek for her excellent help with organizational issues and challenges.
Thanks also to Prof. Marie-Laure Bocquet and the theoretical chemistry group at the ENS Paris for hosting me during my stay in Paris and for giving me a great time there.
I would like to thank Dr. Knud Seufert, Dr. Alex Riss and Erik Schönemann for proof reading my thesis.
Thankfully I want to mention of course also my family for supporting me all the time during the last eight years of study and PhD. You helped me in a lot of tough times and gave me confidence! Especially, I would like to mention my cousins Sabrina and Veronika, as I promised to do so.
Finally, I want to express a big thank you to my fiancée Jessica for supporting me, criticizing me and most importantly standing by my side all the way.